Designing a Robust Pitch Angle Controller for a 2-Motor-Pitch-System in a Large Wind Turbine

Dissertation zur Erlangung des akademischen Grades

Doktor der Ingenieurwissenschaften (Dr. –Ing.)

Vorgelegt im Fachbereich Elektrotechnik/Informatik

der Universität Kassel

Dipl. –Ing. Jungchul Choi

Kassel, February 21. 2014

Erklärung

Hiermit versichere ich, dass ich die vorliegende Dissertation selbstständig, ohne unerlaubte Hilfe Dritter angefertigt und andere als die in der Dissertation angegebenen Hilfsmittel nicht benutzt habe. Alle Stellen, die wörtlich oder sinngemäß aus veröffentlichen oder unveröffentlichten Schriften entnommen sind, habe ich als solche kenntlich gemacht. Dritte waren an der inhaltlich-materiellen Erstellung der Dissertation nicht beteiligt; insbesondere habe ich hierfür nicht die Hilfe eines Promotionsberaters in Anspruch genommen. Kein Teil dieser Arbeit ist in einem anderen Promotions- oder Habilitationsverfahren verwendet worden.

Die vorliegende Arbeit wurde vom Fachbereich Elektrotechnik/Informatik der Universität Kassel als Dissertation zur Erlangung des akademischen Grades eines Doktors der Ingenieurwissenschaften (Dr. –Ing.) angenommen.

Erster Gutachter: Prof. Dr.-Ing. Habil. Peter Zacharias

Zweiter Gutachter: Dr.-Ing. Boris Fischer

Tag der mündlichen Prüfung: 21. Februar 2014

This work has been accepted by the Faculty of Electrical Engineering and Computer Science of the University of Kassel as a thesis for acquiring the academic degree of Doktor der Ingenieurwissenschaften (Dr. –Ing.)

1st Supervisor: Prof. Dr.-Ing. Habil. Peter Zacharias, University of Kassel

2nd Supervisor: Dr.-Ing. Boris Fischer, Fraunhofer IWES

Examiner: Prof. Dr.-Ing. Albert Claudi, University of Kassel

Examiner: Prof. Dr.-Ing. Martin Braun, University of Kassel

Defense Date: February 21, 2014

Acknowledgements

Many colleagues at the division *Control Engineering and Energy Storage Systems* in *Fraunhofer institute for wind energy and energy systems (IWES)* helped me in the good achievement of this work. My daily supervisor Martin Shan and Peter Caselitz supported me in many ways since the very first days at Fraunhofer IWES. I am grateful to Jochen Giebhard und Mattias Wecker who took part in installation and operation of the test rig. Daniel Duckwitz guided me how to formulate my research results more explicitly.

Thanks are given to Prof. Dr. –Ing. habil. Peter Zacharias in the University of Kassel for his scientific advice, personal encouragement and vision since 2008. I would also like to thank Dr.-Ing. Boris Fischer for taking his time to evaluate my doctorial thesis.

Prof. Dr. –Ing. Albert Claudi and Prof. Dr. –Ing. Martin Braun are also thanked for their attention to this thesis as a member of the Doctoral Examination Committee.

Greatest thanks are due to my parents, whose endless love and encouragement have supported me for many years. Finally, I wish to thank my wife, Jiyoon Lee. Without her patience and encouragement, completion would never have been reached.

Zusammenpassung

Für große Windenergieanlagen werden neue Pitchregler wie Einzelblattregler oder Turmdämpfungsregler entwickelt. Während diese neuen Pitchregler die Elemente der Windenergieanlagen entlasten, wird das Pitchantriebssystem stärker belastet. Die Pitchantriebe müssen weitaus häufiger bei höherer Amplitude arbeiten. Um die neuen Pitchregler nutzen zu können, muss zunächst das Problem der Materialermüdung der Pitchantriebssysteme gelöst werden. Das Getriebespiel in Getrieben und zwischen Ritzeln und dem Zahnkranz erhöht die Materialermüdung in den Pitchantriebssystemen.

In dieser Studie werden als Lösung zwei Pitchantriebe pro Blatt vorgeschlagen. Die beiden Pitchantriebe erzeugen eine Spannung auf dem Pitchantriebssystem und kompensieren das Getriebespiel. Drehmomentspitzen, die eine Materialermüdung verursachen, treten bei diesem System mit zwei Pitchmotoren nicht mehr auf. Ein Reglerausgang wird via Drehmomentverteiler auf die beiden Pitchantriebe übertragen. Es werden mehrere Methoden verglichen und der leistungsfähigste Drehmomentverteiler ausgewählt. Während die Pitchantriebe in Bewegung sind, ändert sich die Spannung auf den Getrieben.

Die neuen Pitchregler verstellen den Pitchwinkel in einer sinusförmigen Welle. Der Profilgenerator, der derzeit als Pitchwinkelregler verwendet wird, kann eine Phasenverzögerung im sinusförmigen Pitchwinkel verursachen. Zusätzlich erzeugen große Windenergieanlagen eine hohe Last, die sich störend auf die Pitchbewegung auswirkt. Änderungen der viskosen Reibung und Nichtlinearität der Gleitreibung bzw. Coulombsche Reibung des Pitchregelsystems erschweren zudem die Entwicklung eines Pitchwinkelreglers. Es werden zwei robuste Regler (H_∞ und μ–synthesis) vorgestellt und mit zwei herkömmlichen Reglern (PD und Kaskadenregler) verglichen.

Zur Erprobung des Pitchantriebssystems und des Pitchwinkelreglers wird eine Prüfanordnung verwendet. Da der Kranz nicht mit einem Positionssensor ausgestattet ist, wird ein Überwachungselement entwickelt, das die Kranzposition meldet. Neben den beiden Pitchantrieben sind zwei Lastmotoren mit dem Kranz verbunden. Über die beiden Lastmotoren wird das Drehmoment um die Pitchachse einer Windenergieanlage simuliert.

Das Drehmoment um die Pitchachse setzt sich zusammen aus Schwerkraft, aerodynamischer Kraft, zentrifugaler Belastung, Reibung aufgrund des Kippmoments und der Beschleunigung bzw. Verzögerung des Rotorblatts. Das Blatt wird als Zweimassenschwinger modelliert.

Große Windenergieanlagen und neue Pitchregler für die Anlagen erfordern ein neues Pitchantriebssystem. Als Hardware-Lösung bieten sich zwei Pitchantriebe an mit einem robusten Regler als Software.

Summary

New pitch controllers such as individual pitch control or tower damping control are developed for large wind turbines. Whereas the new pitch controllers reduce load on the elements of wind turbines, more load is added onto the pitch actuation system. Pitch actuators must operate much more frequently and in higher amplitude. In order to adopt the new pitch controllers, fatigue of the pitch actuation system has to be solved first. Gear plays in gearboxes and between pinions and blade rings increases fatigue on pitch actuation systems.

Two pitch actuators per blade were suggested as a solution in the project '*Lastreduzierende Regelungssysteme für Multimegawatt-Windkraftanlagen im Offshore-Bereich*' [11]. The two pitch actuators create tension on the pitch actuation system and compensate for gear play. Torque peak, which causes fatigue, is no longer found with the two-pitch-motor-system. A test rig was made for the two-motor-pitch-system.

In this research, new pitch angle controllers are developed for the proposed two-motor-pitch-system. A test rig modeling, parameter estimation and load simulation are performed prior to the controller design. A controller output is transferred to the two pitch actuators via a torque distributor. Several methods are compared and the best performing torque distributor is chosen.

A test rig is used for the experimentation of the pitch actuator system and the pitch angle controllers. Since a position sensor is not equipped on the ring, an observer is designed to provide feedback regarding the ring position. Besides two pitch actuators, two load motors are connected to the ring. Simulated torque around the pitch axis on a wind turbine is transferred to the two load motors.

Torque around the pitch axis contains gravity, aerodynamic force, centrifugal loading, friction due to overturning moment and accelerating and decelerating rotor blade. The blade is modeled as a two-mass-spring-damper system.

New pitch controllers adjust the pitch angle in sinusoidal wave. The profile generator, which is used currently as a pitch angle controller, can cause phase delay in sinusoidal shape pitch angle. In addition, large wind turbines create a large load which interferes with pitch action. Nonlinear Coulomb/sliding friction and viscous friction change of the pitch actuation system are also hindrance to making a pitch angle controller. Two robust controllers (H_∞ and μ–synthesis) are suggested to handle the four problems. The robust controllers are compared with two classical controllers (PD and cascade). Tracking performances of the pitch angle controllers are verified with root-mean-square (RMS) of errors between reference and actual angles. In case of a collective pitch control, RMS of errors is reduced by 49% with a μ–synthesis in comparison to a PD-controller. The RMS with a μ–synthesis is 72% less than the RMS with a cascade controller if an individual controller is used as a pitch controller.

Large wind turbines and new pitch controllers for the turbines require a new pitch actuation system. The hardware solution is a 2-motor-pitch-system and the software is a robust controller.

Table of Contents

1. Introduction

1.1. Wind turbine control

A wind turbine is a device which converts wind energy to mechanical energy. The mechanical energy is converted again to electricity in most modern wind turbines. Below rated wind speed, the wind turbine tries to gain as much energy as can, thus the pitch angle does not vary. Above rated wind speed, a wind turbine is designed to choose one of the three options: Pitch control, active stall control and stall control

Pitch control is the mostly used concept in modern wind turbines. Increasing pitching angle reduces the angle of attack and hence the lift coefficient. Above rated wind speed, pitch control regulates the aerodynamic power and loads by increasing pitch angle so that design limits of the components such as generator speed and torque are not exceeded.

Current blade pitch control focuses on limiting generator speed and power. However, as wind turbine size increases, loads on the elements of the turbine become more critical than generator power. For example, if power is increased by four times as the rotor diameter doubles, bending moment on the blade root is increased by eight times.

Several kinds of technologies are developed to reduce load on wind turbines. The technologies are categorized into a blade profile and a pitch action. Development in the blade profile implies blade with bend-twist-coupling effect, variable diameter rotor, active flow control, and plasma actuator. Individual pitch control and tower damping control are the representative pitch action to alleviate load on wind turbines.

A blade which has bend-twist-coupling effect can be used to reduce load on the blade [3]. The blade is designed so that the twist distribution changes as the blade bends [4]. The blade is twisted toward lower angle of attack, thus the load is mitigated.

Variable diameter rotor has a tip blade which is extended in lower wind speed and retracted in higher wind speed (see Figure 1-1). Excessive load can be avoided in higher wind speed with the variable diameter rotor.

Active flow control uses various shapes of blade to reduce load. Figure 1-2 shows a compliant wing is bended up and down.

Individual pitch control and tower damping control are developed for load alleviation with a pitch control. These are explained in the next section.
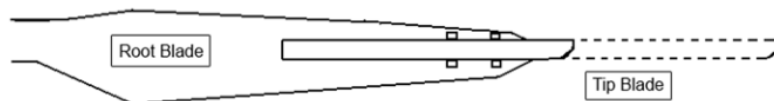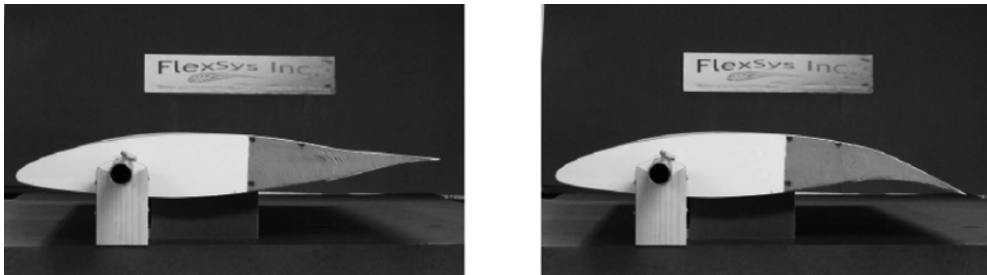
Figure 1-2: adaptive compliant wing for active flow control [4]

1.2. Pitch control for load reduction

1.2.1. Individual pitch control

On large wind turbines, each blade experiences different wind conditions due to gusts, wind shear and turbulence (see Figure 1-3 for wind shear). Independent control of each blade is an effective solution to compensate for loads due to asymmetrical wind conditions. The basic idea for individual pitch control came from helicopter technology. The most significant aerodynamic load takes place once per revolution, *1P*, which is mainly caused by wind shear. Harmonics of the frequency, i.e. *2P*, *3P*, *4P*, etc are to be considered, but their amplitude is smaller than *1P*. Harmonics at *3P*, *6P* and so on are also significant with three-bladed rotors. The asymmetrical aerodynamic force affects loads on yaw bearing, shafts and especially blade roots.

Since *1P* is the most significant frequency in asymmetrical aerodynamic force, individual pitch controllers can be simply designed based on the rotor azimuth angle. Tilt and yaw moment at the rotor center are calculated from flap and edgewise blade root bending moments of three blades. Cyclic pitch variation with a 120° phase is used to alleviate tilt and yaw moment. This method is called cyclic pitch control and it is used to reduce loads caused by aerodynamic wind shear, tower shadow and yaw misalignment [2]. However, this is not useful in practice because wind speed variation is dominated by stochastic variations due to turbulence [5].

Another way of compensating for loads is measuring asymmetrical loads and feeding back to controller to build individual pitch controllers. Flap and edgewise blade root bending moment is transformed into a mean value and variations on two orthogonal axes using "d-q axis transformation" [2].

Traditional strain gauges are not suitable because of weakness on fatigue and short lifetime. Advanced sensors such as optical strain gauges and solid strain measurement devices make this approach feasible [5].

As seen in Figure 1-4, individual pitch control can be operated independently from collective pitch control and implemented in different hardware platforms which have advantages in signal transfer and safety [6]. M. Geyler [6] proposed a H$_\infty$ controller as well as a PI controller with a 1st order low

pass filter. Both controllers are stable and able to tolerate uncertainty. The flapwise blade bending moment is diminished by individual pitch control as seen in Figure 1-5. However, larger amplitude and more reversal of pitch angle increase load on the pitch actuator. Lifetime of the pitch actuation system has to be considered first before adopting individual pitch controller.
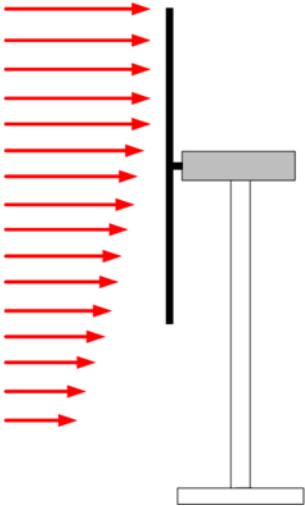
Figure 1-3: Wind shear
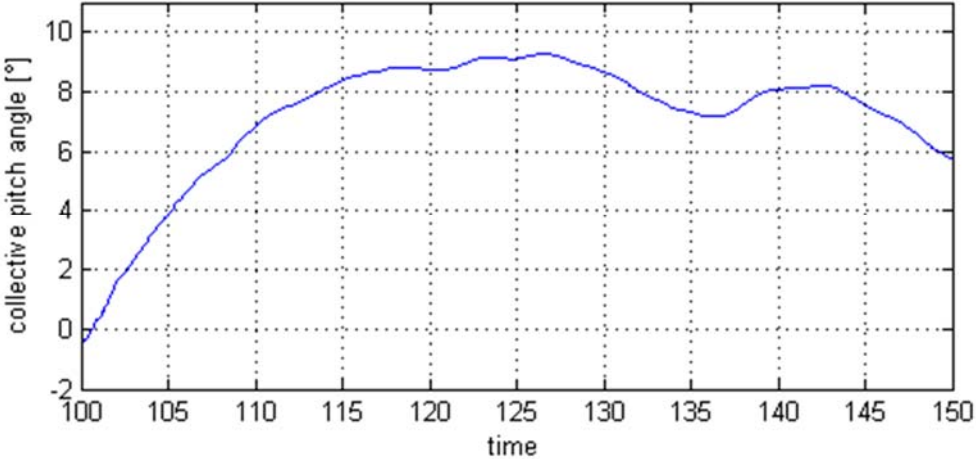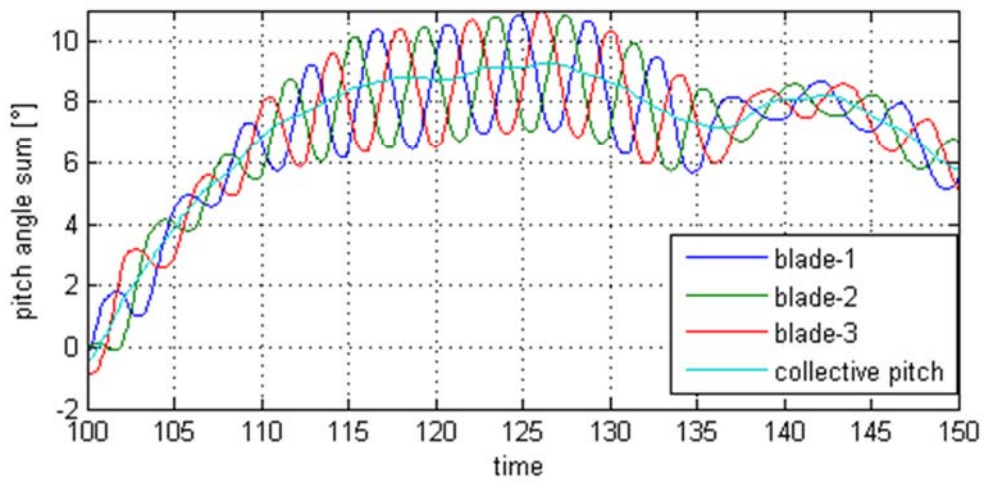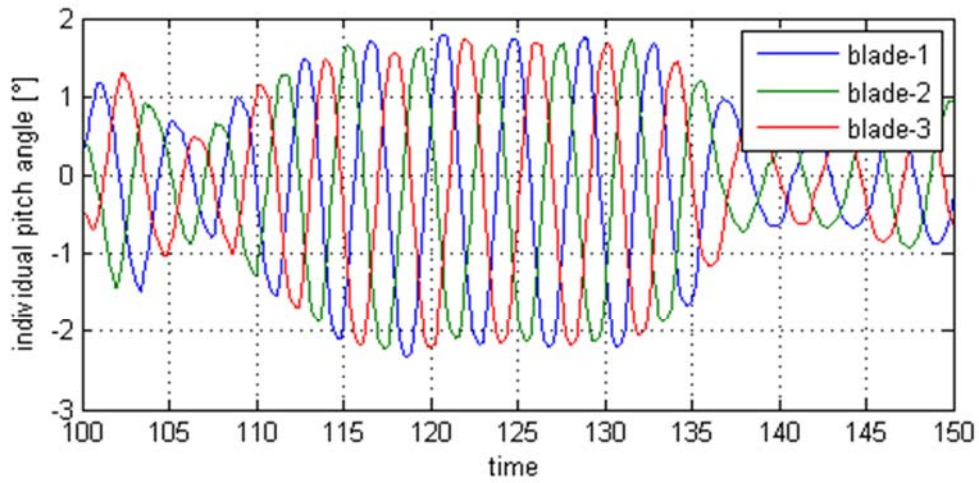
Figure 1-4: Pitch angles – collective, individual, sum
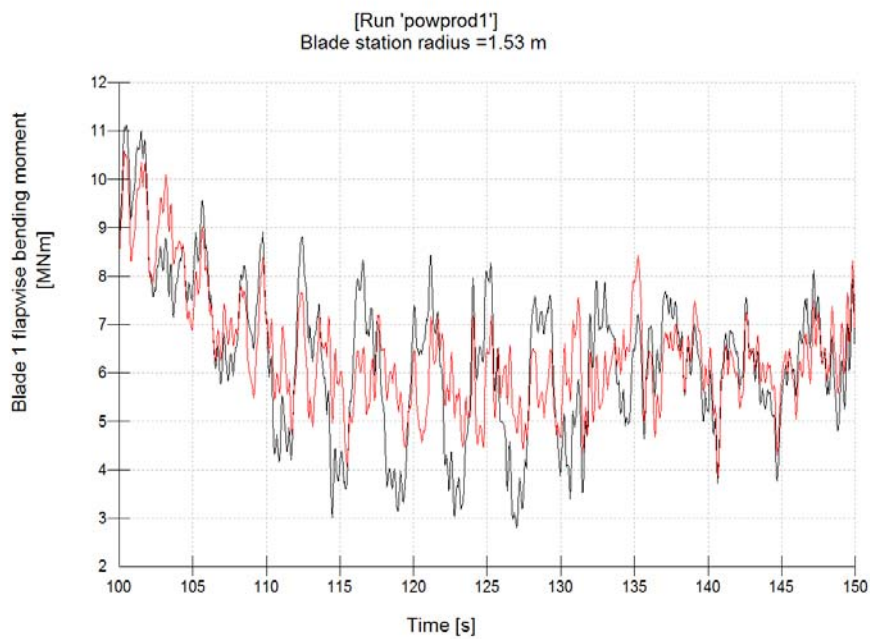
Figure 1-5: flapwise bending moment without (black)/with (red) individual pitch control

1.2.2. Tower damping control

Wind energy forces not only rotate rotor blades but also to push turbine structure behind. Even though wind turbine blades are slender, thrust force on the turbine occurs in about 80% of the cases where a circular plate with the same rotor diameter is equipped [7]. As rotor blades pass in front of the tower, aerodynamic force is diminished. The variation of aerodynamic force causes tower vibration in an axial direction. As the turbine moves opposite to wind direction, relative wind speed and rotor angular speed increase. The wind turbine controller increases pitch angle to reduce rotor speed. Increasing pitch angle reduces not only rotor speed but also thrust force so that the turbine moves further to upwind. The process leads to large tower vibration [8] (see Figure 1-6). Tower vibration affects fatigue on tower bottom.

In order to lessen vibration, an acceleration sensor can be mounted on the nacelle and its signal is fed back to the wind turbine controller. Signals of the acceleration sensor must pass a filter in order to avoid interaction with the blade's natural frequencies. Pitch angles of the three blades can be the same and it lessens tower bending moment (see Figure 1-7, Figure 1-8).

Figure 1-6: Tower vibration

[Run 'powprod1']
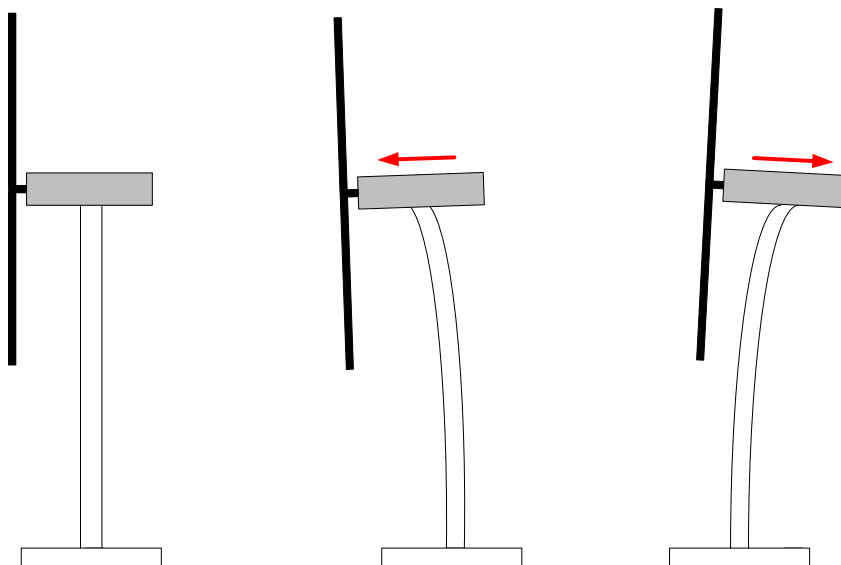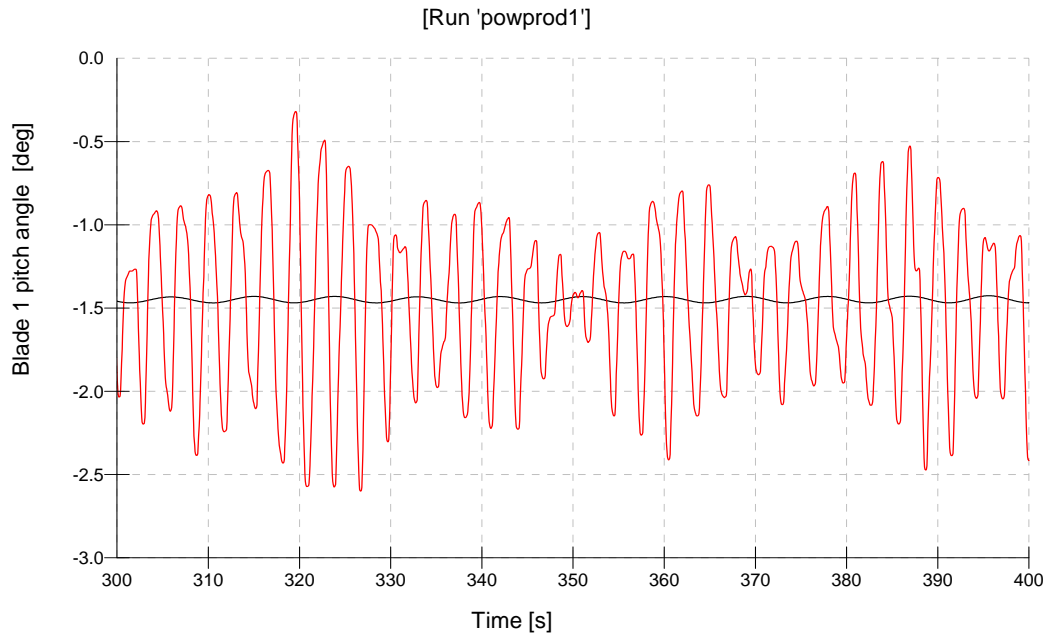
Figure 1-7: Pitch angles without (black)/with (red) tower damping control

[Run 'powprod1']
Tower station height =4.5 m
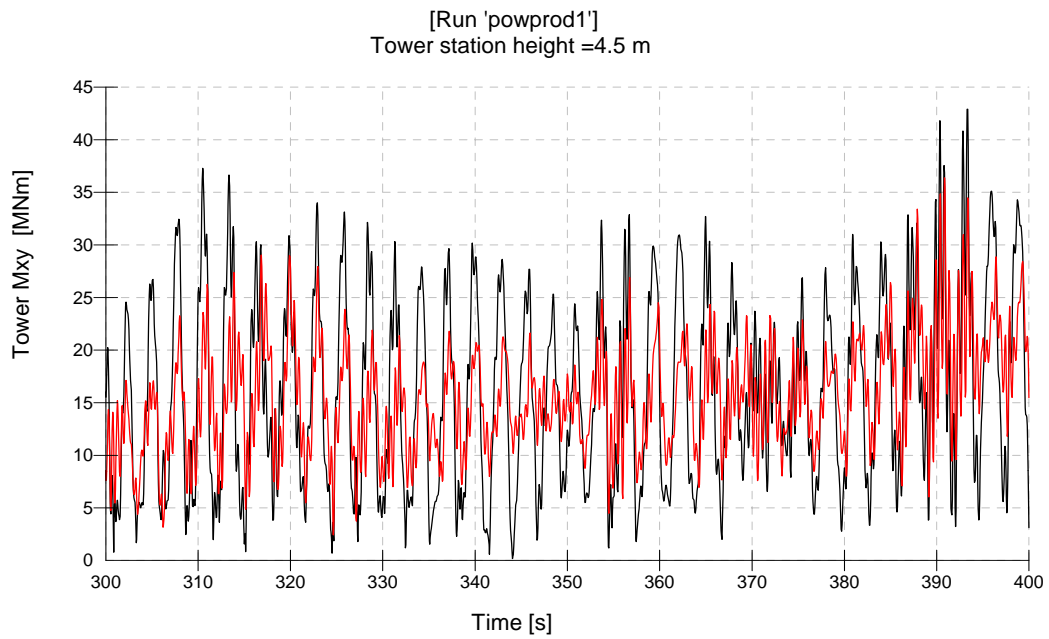
Figure 1-8: tower load without (black)/with (red) tower damping control

2. Overview of the research

The new developed pitch controls for load reduction in section 1.2 require more pitch actions and reversals to the pitch actuators. Fatigue on the pitch actuation system increases in contrast to that of other parts, such as blade bearing and main bearing. A two-motor-pitch-system is suggested in this research to reduce fatigue on the pitch actuation system (see section 2.1).

As the size of the wind turbine increases, nonlinear friction on the blade bearing and external load such as gravity increase, too. The suggested two-motor-pitch-system also makes pitch angle control design hard because of increased sliding friction. Uncertainty of viscous friction coefficient in the pitch actuation system is another hindrance to pitch angle control. Robust controllers are designed to overcome these difficulties (see section 2.2).

2.1. Fatigue on the pitch actuation system

2.1.1. Problem statement

An electrical motor or a hydraulic cylinder is used for pitch action (see Figure 2-1). A hydraulic drive was commonly used in early wind turbines. A pitch actuator controlled all the blades and an electric motor with mechanical links was relatively complex and cost-intensive [9]. However, as the size of wind turbine increases, shaft brakes for central electrical drives become more expensive. It can be avoided by adopting separate actuators per blade. Separate actuators guarantee safety since two actuators can provide enough aerodynamic braking torque even if one motor fails.
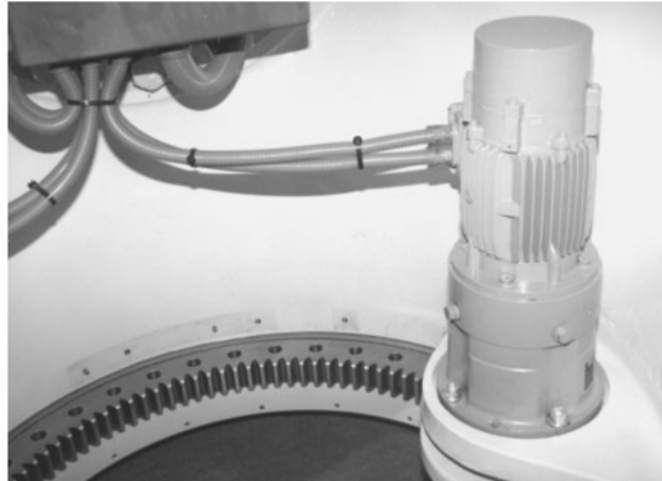
Figure 2-1: Hydraulic actuator and electric actuator [1]

Electric motors rotate fast with low torque compared to required pitching characteristics on blades, so a gearbox is mounted between the motor and blade bearing. The gearbox is composed of many gear teeth which have gear play. Gear play is a gap between a gear tooth and mating gear tooth. Gear play is essential for lubricant oil which is located in the gap and prevents excessive heat and wear. In addition, gear play gives a mechanical tolerance and allows thermal expansion. Gear play interferes with accurate positioning and induces high torque as gear teeth 'hit' each other when the direction of rotation changes. Gear play exists also between the gear ring and pinion.

Gear play is not so important if a machine normally rotates in one direction. A precise positioning application such as a robot changes its direction frequently so that high torque is experienced in the element. It increases fatigue and reduces its lifetime. Current wind turbine control operates only in high wind speed. However, new pitch controls in section 1.2 requires pitch action also in low wind speed. In addition, pitching direction changes to a great degree with the new pitch control. Figure 2-2 shows pitch rate with different controllers. As pitch rate passes zero, pitching direction changes and torque peak occurs in the gearbox. In particular, individual pitch control results in very frequent pitch direction change and it leads to fatigue increase.

Gear play cannot be neglected anymore. A new method has to be designed to avoid torque peak and fatigue due to gear play.

[Run 'powprod1']
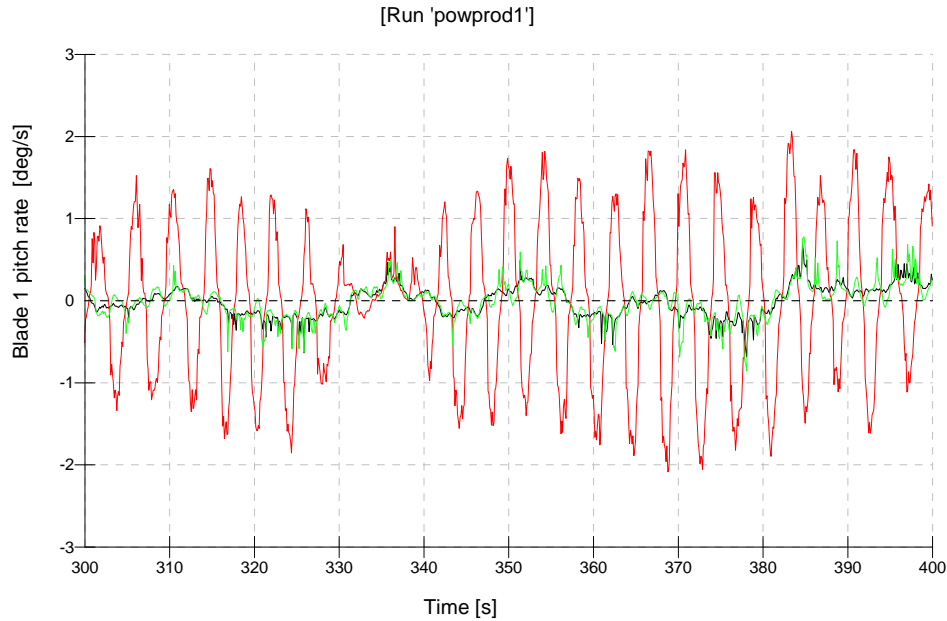
Figure 2-2: Pitch rate – baseline (black), individual pitch (red), tower damping (green) control

2.1.2. State of the art

Gear play in section 2.1.1 raises large torque peak when pitch direction changes. The large torque increases fatigue which reduces lifetime of the pitch actuation system. With the current control system, pitching action is performed only above the rated wind speed. However, new developing individual pitch control and tower damping control require steady pitch actions in the whole wind speed range. Fatigue of the pitch actuation system is the inevitable problem if the individual pitch control or tower damping control is used for the wind turbines.

About gear play or backlash compensation, most of the scientific researches focused on tracking problem e.g. [17], [18]. The studies help designing controllers, but cannot avoid torque peak on the gear teeth.

The following two inventions are designed for other purposes, but they can also reduce or avoid torque peak.

The first invention is on the emergency pitch actuation system for a wind turbine by P. Rogall et al. [16]. Beside a pitch drive, an additional emergency drive is mounted on a blade root (see Figure 2-3). The emergency drive is driven by spring force in order to enhance safety. Number 8 of the figure refers to the spring. It would be complex if the spring is equipped in a pitch drive which works in normal conditions. An electric motor with battery backup for emergency is fault-prone in case of damage to electrical parts, thus the spring is used as a drive force. He mentioned a hydraulic element may substitute for spring for mechanical energy storage. The risk that the emergency drive cannot operate because of gearbox failure in the pitch drive can be avoided. As one or more emergency

drives are equipped, the requirements for the pitch drive do not need to be very high. A small failure in the pitch drive is acceptable.

Whereas P. Rogall et. al. invented the pitch actuation system to avoid failure in emergency, this invention compensates for gear play additionally. The spring gives a steady torque to the blade bearing and the pitch motor gives torque to overcome the spring torque. Gear play compensation was not written in his report.
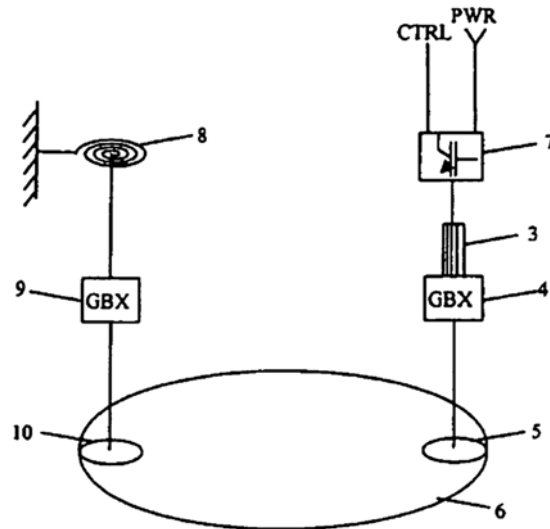
Figure 2-3: Pitch drive system by P.Rogall et.al [16]

Another method to avoid torque peak was invented for vehicles by M. Hackl at Robert Bosch GmbH [13]. The invention is designed for a "steer-by-wire" steering drive mechanism. In the classical way, a vehicle is steered by the force which a driver gives the handle. Modern vehicles are steered by a motor with the "steer-by-wire" system. The motor torque is amplified by a gearbox. Because a gearbox has a gear play, gear teeth are bumped against each other every time the handling direction changes. The invention compensates for gear play using two motors with the opposite torque direction (see Figure 2-4). M. Hackl invented the system in order to reduce noise which is occurred on the gear play whereas the purpose of this research is to lengthen the lifetime of the pitch actuation system.

M. Hackl mentioned that the braking moment may be adapted according to different types of driving or road conditions. He suggested a method to reduce vibrations which arise from elasticity in motors and gears as:

$$F_1' = F_1 + K \cdot (\omega_2 - \omega_1)$$
$$F_2' = F_2 - K \cdot (\omega_2 - \omega_1)$$

in which F_1' and F_2' are the actual forces of the motor-1 and 2. F_1 and F_2 are the original force component of the motor-1 and 2. ω_1 and ω_2 are rotary speeds of the motors and K is an

amplification factor. Since such a two-motor-system reduces fatigue, a gearbox with larger tolerances can be used. Hence the cost for the gearbox can be saved [13].
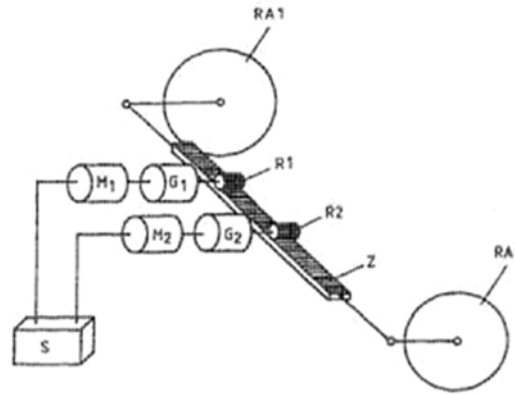
Figure 2-4: Method for actuating a steer-by-wire steering device [13]

The following two inventions do not handle gear play compensation. However, these inventions use two or more motors in a blade thus the suggested solution in this research should consider the following studies.

A. Wobben [14] invented a pitch actuation system which is composed of at least two motors in a rotor blade. A large pitching torque can be fulfilled with several small motors. If three motors are equipped for a blade, each motor has only to bring one third of the required power. Even though one motor fails, the wind turbine does not need to be stopped because the other two motors can perform pitch action. The maximum power of each motor has to be set by considering the scenario that one motor is out of order. The motors are situated the same distance from one another in order not to damage the rotor blades. Because directions of torque out of motors are the same, gear play cannot be compensated for.

The invention was also developed by using a case to connect at least two motors [15] (see Figure 2-5). The purpose is to enlarge output torque by means of several motors. By using several motors, length of the motors can be shortened and their moments of inertias decrease. An additional gearbox to the set of motors and gearbox can be built in order to increase gear ratio. As seen in Figure 2-5, a cooling system is enough for the two motors. It reduces weight and cost in comparison with two separate cooling systems. Since the two motors rotate in an opposite direction to each other, the gear teeth are designed to consider their directions. As only one gearbox is equipped in a blade, gear play is not compensated for.
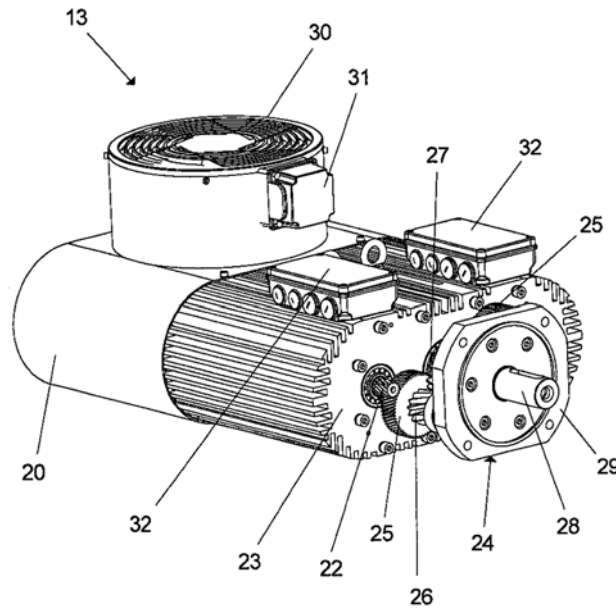
Figure 2-5: Pitch drive system with two motors in a case [15]

2.1.3. Suggested solution in this research

Since the gear play is the place where large torque peak takes place, gear play has to be eliminated or reduced. Gear play can be compensated for by replacing one pitch motor with two motors which generate tension on each other (see Figure 2-6). This idea was invented by M. Hackl [13] on steering mechanism in order to reduce noise. His idea was applied to wind turbine pitch actuators in the project '*Lastreduzierende Regelungssysteme für Multimegawatt-Windkraftanlagen im Offshore-Bereich*' [11]. However, the aim of the application in this project is not noise alleviation but fatigue reduction. A test rig was built to test the invention in the project. Parameters for the test rig are measured later in this research.

With a two-motor-pitch-system, large torque peak is also avoided because the gear play is eliminated. Since their torque direction is opposite, one motor attaches its right gear surface to the blade root bearing and the other motor attaches its left gear surface. Even though pitch direction changes, the gear surfaces are not detached. Thus neither gear play nor torque peak occur with a two-motor-pitch-system.

Figure 2-7 compares a 1- and two-motor-pitch-system. One-motor-pitch-system shows torque peak shortly after the torque direction changes. As the torque direction changes, gear teeth are detached in a short time and 'hit' each other. The torque soars on the point as seen at 0.3 seconds and 2.2 seconds of the figure. Two-motor-pitch-system does not have a gear play in the gearbox. Thus two-motor-pitch-system does not include torque peak which is seen in the one-motor-pitch-system.

Figure 2-6: current pitch actuation system (left) and the suggested pitch actuation system (right)
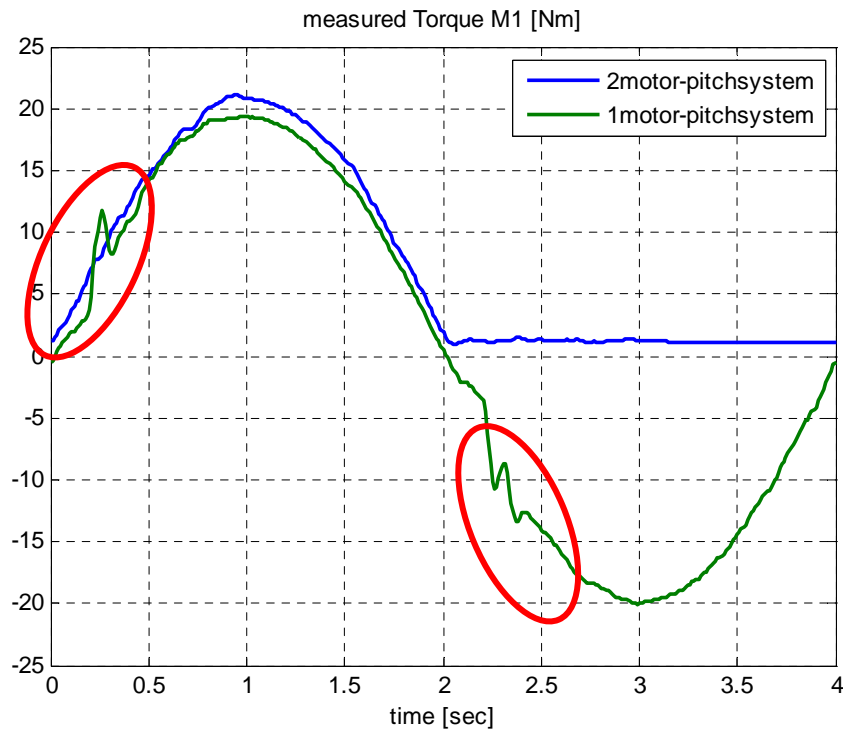
Figure 2-7: Motor torque with one- and two-motor-pitch-system (measured in the test rig)

As the two-motor-pitch-system eliminates torque peaks, lifetime of the pitch actuation system increases. Gear teeth in the gearbox, pinion and ring may have larger tolerance, thus the manufacturer can save cost by use of the two-motor-pitch-system. On the other hand, sliding friction due to tension (see section 4.3.1), the additional inertia and additional Coulomb and viscous friction require more electricity consumption. Let the pitch torque is $T(t)$, the energy consumption is determined as:

$$E = \int_{t_1}^{t_2} |T(t)| dt$$

In case of the two-motor-pitch system, the pitch torque, $T(t)$, is determined from the torque sum of the two motors. Figure 2-8 shows simulated pitch power of one- and two-motor-pitch-system if the reference signal is the same as Figure 6-47. The energy consumption in this period is 143Nms and 318Nms in one- and two-motor-pitch-system. Thus the two-motor-pitch-system requires around two times more energy than the current one-motor-pitch-system.
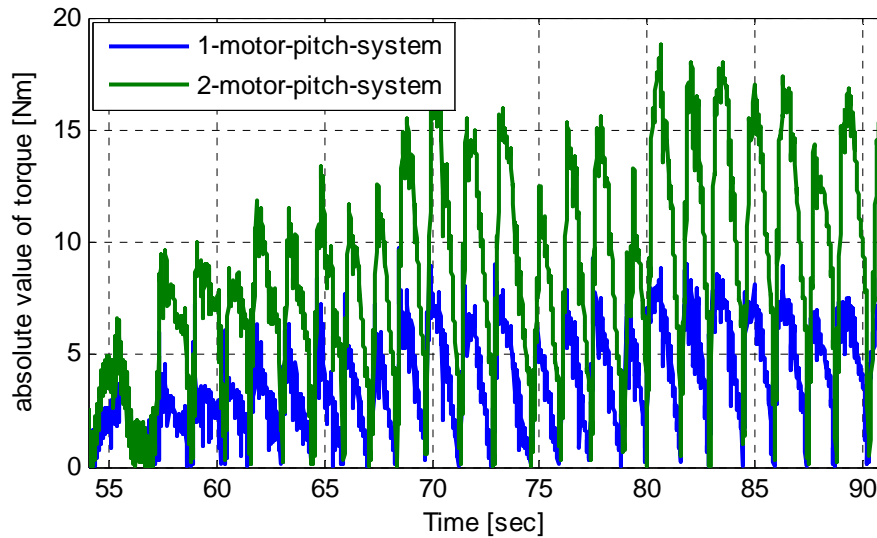
Figure 2-8: Demanded power with one- and two-motor-pitch-system (simulation)

Since two motors are used in a closed-loop-system, a torque distributor is necessary to control the two motors. The two-motor-pitch-system is made as a test rig in section 4.

2.2. Pitch angle controller

2.2.1. Problem statement

A wind turbine controller is composed of a torque controller and a pitch controller. A torque controller adjusts generator speed and torque to obtain the maximum power from wind. A pitch controller is active above rated wind speed to limit generator speed and power. A pitch controller operates also in case of starting at low wind speed or emergency stop.

The pitch angle from the pitch controller is not transferred directly to the pitch motor. The pitch angle is changed to the pitch moment which drives the pitch actuator. This process is performed by a pitch angle controller (see Figure 2-9). The currently used pitch angle controller is profile generator.

In the profile generator, acceleration is limited and the shape of the velocity graph becomes trapezoid if a reference pitch angle is stepwise [10]. The profile generator performs well for collective pitch control, but is not suitable for individual pitch control or tower damping control because of

phase delay (see Figure 2-11). As the reference pitch angle changes all the time with individual pitch control or tower damping control, pitch angle controller does not settle but track the reference pitch angle. Instead of a profile generator, another pitch angle controller has to be designed for individual pitch control or tower damping control.

Designing of a pitch angle controller should consider pitch actuation system characteristics. The pitch actuation system consists of the motor, gearbox, pinion and ring which is connected to a blade. The pitch actuation system can be modeled with linear parameters, e.g. moment of inertia, viscous friction, damping and stiffness. However, the four effects make control design difficult – sinusoidal reference value, blade's load around pitch axis, Coulomb and sliding friction, and viscous friction coefficient change.
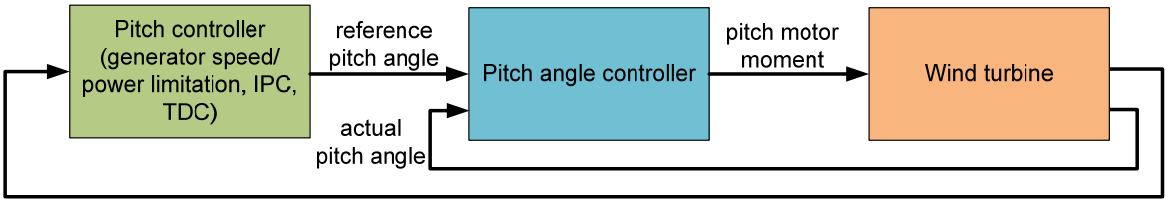
Figure 2-9: Pitch angle controller

Sinusoidal reference value

A profile generator is used currently for the pitch angle controller. The profile generator controls servo motor position by limiting acceleration. Velocity and position are decided by the acceleration characteristic, which is either rectangular or trapezoid [10]. Figure 2-10 shows acceleration, velocity and position graphs of emergency stops where pitch position is increased from 0° to 90°. The pitch position graph approaches reference position smoothly.

However, if the reference position is sinusoidal, the phase shift is found in the position of the profile generator [11] (see Figure 2-11). Individual pitch control or tower damping control uses sinusoidal functions as reference positions. Thus, the profile generator is not suitable for individual pitch control or tower damping control.
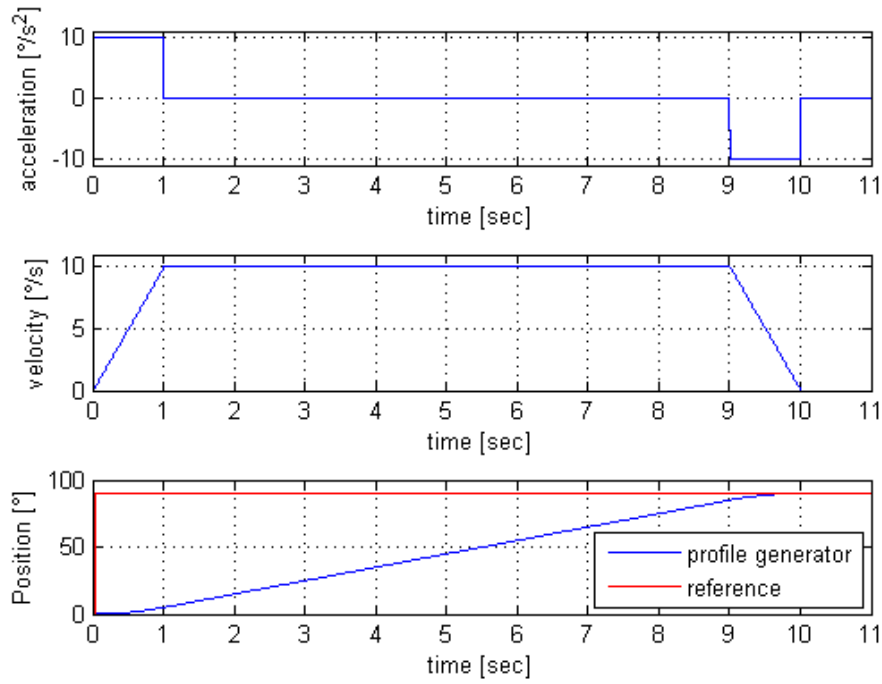
Figure 2-10: acceleration, velocity and position with profile generator
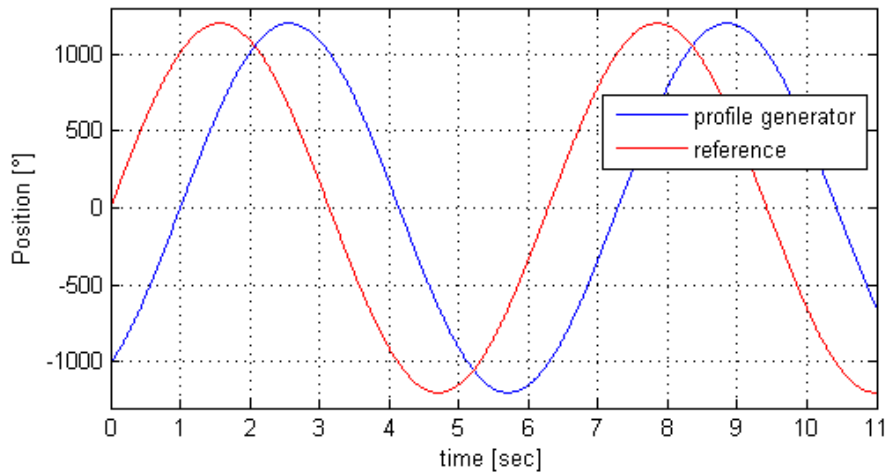
Figure 2-11: sine position with profile generator

Blade's load around pitch axis

Gravity, aerodynamic force, centrifugal force, and friction due to overturning moment of the blade make pitch control challenging (see section 5 for detail). The biggest load is friction due to overturning moment [30]. A long and heavy blade is mounted to a ring bearing and the blade's load, such as gravity or thrust force, is transferred to the overturning moment on the bearing.

The forces have been neglected in the pitch angle controller design due to large gear ratio of the pitch actuation system. However, large wind turbines are developed and load increase is higher than power increase as the turbine size grows. Thus the loads on the blade have to be considered in the designing of pitch angle controller.

Nonlinearities of the pitch actuation system

Coulomb friction is constant, thus is nonlinear and cannot be contained in a linear model (see section 4.3.1 for more in detail). In two-motor-pitch-system, if two motors operate in opposite directions, more torque is needed than if only one motor is active. The increment is called sliding friction and has the same effect as Coulomb friction. The sum of Coulomb and sliding friction may not be neglected in a two-motor-pitch-system.

Viscous friction coefficient change

The viscous friction coefficient changes dependent on temperature in the gearbox. The viscous friction coefficient is high in low temperatures and low in high temperatures. Although the viscous friction is linear, its changes interfere with control design. Viscous friction coefficient change is seen in Figure 4-16 of section 4.3.1.

2.2.2. State of the art

A profile generator is currently used as the pitch angle controller. Since the profile generator is not suitable for individual pitch control or tower damping control, a new pitch angle controller has to be developed. The following four problems in designing the pitch angle controller were researched separately in literatures.

Sinusoidal reference value

D. Limon et. al. [48] suggested a model predictive control for a reference signal which is periodic and whose period is known. The proposed model predictive controller has the future sequence of inputs and an artificial reference as decision variables. The controlled system with the model predictive control is asymptotically stable and converges to the best possible reachable trajectory.

A feed-forward ($H_0(s)$ in Figure 2-12) is appropriate in the case when the reference is fairly arbitrary [49]. Reference input is incorporated into the feed-back controller ($C(s)$ in Figure 2-12). This method

generates good tracking only for slowly changing references. Feed-forward improves performance significantly as seen in Figure 2-13.
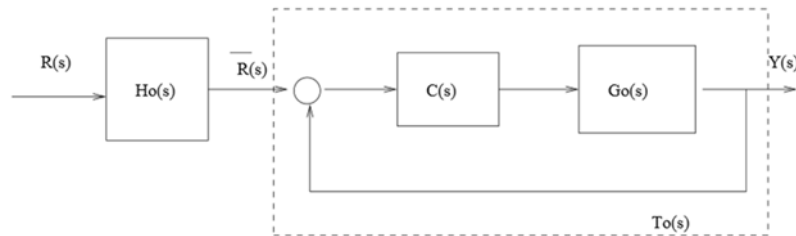
Figure 2-12: Feed-forward control concept [49]
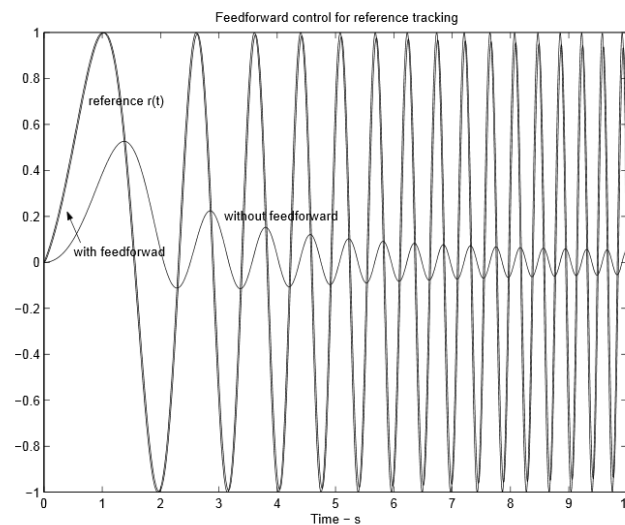
Figure 2-13: reference tracking with and without feed-forward control [49]

Blade's load around pitch axis

There is no controller developed for blade's load around pitch axis. Blade's load is composed of several forces such as gravity, aerodynamic force, centrifugal force and friction due to overturning moment (see section 5 for detail).

Blade's load around pitch axis can be regarded as disturbance in control design. Robust control includes disturbance in the model [50], so that the disturbance does not interfere with stability of the controller. Robust control seeks the "best" control which stabilizes the perturbation with limited effort and seeks the "maximally malevolent" disturbance [53].

E. Elisante et al. [51] proposed a robust controller with disturbances. A multivariable nonlinear system is considered in the study:

$$\dot{x} = f(x) + g(x)u + w(x)d$$
$$y = h(x)$$

Where x is the state variable, u is the manipulated input, d is the disturbance input and y is the output vector. The author distinguished the process depending on the measurability of the disturbance. If the disturbance is measured, the disturbance inputs are included in the control law. If none or not all disturbances are measurable, the disturbance inputs are used as a constant vector or treated as uncertainty.

A disturbance compensating model predictive control (DC-MPC) is proposed by Z. Li [52]. He applied the DC-MPC to ship heading control in the presence of wave disturbances. The disturbance compensation control Δu satisfies the following optimization problem:

$$\min_{\Delta u \in R^n} \left\| CB\Delta u + C\hat{\omega}(k-1) \right\|$$

Where $\hat{\omega}(k-1)$ is a disturbance of the previous time step *k-1*. Suppose the optimal solution of the previous equation is Δu^*. In case of $\hat{\omega}(k-1)=0$, $\Delta u^* = 0$, which leads to the standard MPC.

Input to the system is the sum of the input of the standard MPC and the input of the disturbance compensation as:

$$u(k) = u^*(k \mid k) + \Delta u^*$$

Coulomb and sliding friction

The effect of Coulomb friction can be alleviated by means of a feed-forward friction compensator (see Figure 2-14) [40]. A friction torque out of the friction compensator is added to the input torque as an offset to the input signal for the motor. In ideal case, this offset is the same as Coulomb friction. However, real Coulomb friction is compensated partly in practice in order to avoid instabilities. The additional feed-back element provides a compensation for viscous friction.

F. Altpeter [41] suggested the feed-forward friction compensator with an adaptation process. The adaptation process is used to reduce the risk of instability (see Figure 2-15). Y. Zhu et. al. [43] also added static friction compensator in an adaptive controller as:

$$\tau = \hat{M}(q)\ddot{q}_r + \hat{C}(q,\dot{q})\dot{q}_r + \hat{g}(q) + \hat{F}_v\dot{q}_r + \hat{F}_c\,\mathrm{sgn}(\dot{q}_r) - \Lambda_v e_v$$

Where τ is the vector of generalized input forces, q is the generalized position vector, $\hat{F}_v$ and $\hat{F}_c$ are the estimates of viscous and Coulomb friction forces, $\hat{M}, \hat{C}(q,\dot{q}), \hat{g}(q)$ are the estimates of mass matrix, centrifugal matrix and gravity vector. $\dot{q}_r = \dot{q}_d - \Lambda_p e$, $e_v = \dot{q} - \dot{q}_r$, $e = q - q_d$, Λ_v, Λ_p are positive definite gain matrices. $\hat{F}_c\,\mathrm{sgn}(\dot{q}_r)$ term shows the Coulomb friction is estimated and feedbacked in the controller.

Friction compensation by means of a friction observer is also presented by C. Canudas de Wit [42] (see Figure 2-16). More friction compensation methods are found in robotics such as [44], [45].

Studies on control or compensation of sliding friction are not found.
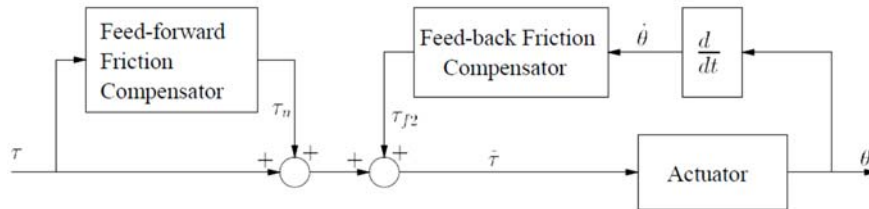
Figure 2-14: Feed-forward and feed-back friction compensators [40]
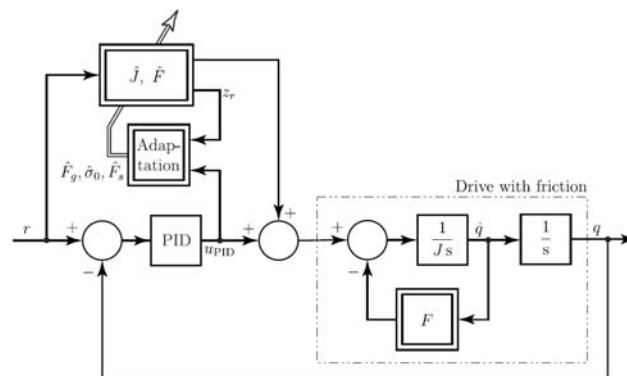
Figure 2-15: Feed-forward friction compensator with adaptation [41]
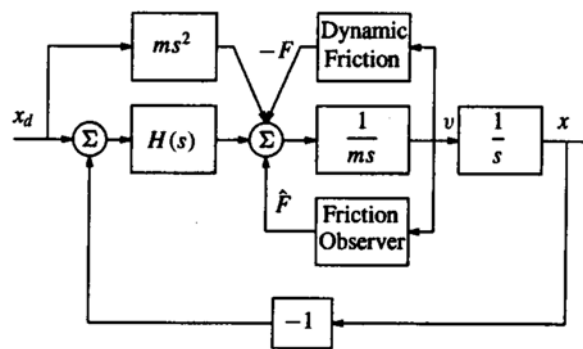
Figure 2-16: Friction compensation using a friction observer [42]

Viscous friction coefficient change

Ji-Ho Park et. al. [46] proposed an adaptive control for time-varying parameters. Stiffness and damping coefficients are changed due to aging effect of the machine. Adaptive control divides parameters into nominal and time-varying coefficients such as:

$$k(t) = \hat{k} + \Delta k(t)$$
$$b(t) = \hat{b} + \Delta b(t)$$

Where $\hat{k}$ and $\hat{b}$ are nominal stiffness and damping coefficients and $\Delta k(t)$ and $\Delta b(t)$ are time-varying parameters in the range of:

$$\Delta k(t) \in [\Delta k_{min}, \Delta k_{max}]$$
$$\Delta b(t) \in [\Delta b_{min}, \Delta b_{max}]$$

A state space equation is represented with a nominal state matrix A^* and a time-varying matrix $\Delta A(t)$ as:

$$\dot{x}(t) = (A^* + \Delta A(t))x(t) + Bu(t)$$

Such a nominal model reference control method is employed as:

$$\dot{\zeta}(t) = F\zeta(t) + Gr(t)$$

with a nominal state variable ζ , r a nominal input , F a nominal state matrix and G a input matrix. F must be stable, thus all the eigenvalues have negative real values. The nominal reference control method reduces the error which is defined as:

$$e(t) = \zeta(t) - x(t)$$

A Lyapunov stability theory is used to determine the controller. The Lyapunov function is defined as:

$$V(t) = e^T(t)Pe(t)$$

The matrix P must be positive definite in order to make $V(t)$ positive. The error has to converge, so the derivative of the Lyapunov function must be negative as:

$$\dot{V}(t) = \dot{e}^T(t)Pe(t) + e^T(t)P\dot{e}(t) < 0$$

The adaptation process estimates the time-varying coefficients because of aging effect enough fast. However viscous friction change due to temperature increase happens much faster than aging effect. The question of if an adaptive controller changes parameters quickly enough for exact modeling is still open.

A robust controller which considers a viscous friction change is not found, but a robust controller for general time-varying parameters is suggested by C. Pirie [47]. This research deals with a trajectory tracking of a linear time-varying (LTV) model which arises from linearization of a nonlinear model. A linear time-invariant (LTI) model is obtained with linearization of a nonlinear model around an equilibrium point. Variations of the parameters are regarded as uncertainties, which are contained in the structured uncertainty matrix $\overline{\Delta}$. The structured uncertainty matrix is found in Figure 2-17 in the form of:

$$\bar{\Delta} = \begin{bmatrix} \Delta^1 & \Delta^2 \\ \Delta^3 & 0 \end{bmatrix}$$
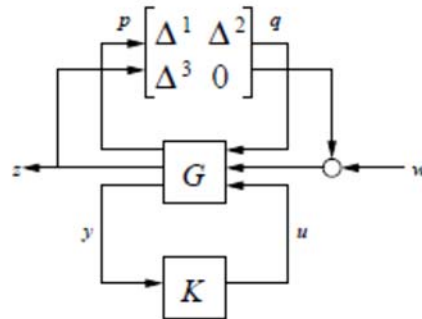
Figure 2-17: Structured uncertainty matrix for a robust control design [47]

2.2.3. Suggested solution in this research

A new controller has to handle the four problems – sinusoidal reference value, blade's load around pitch axis, nonlinearities of the pitch actuation system, and viscous friction coefficient change. A robust controller shows good performance and stability in the presence of disturbances and uncertainties.

The four problems are dealt in the robust control design as:

- Blade's load around pitch axis – disturbance weighting function (*Wd*)
- Nonlinearities of the pitch actuation system – disturbance weighting function (*Wd*)
- Viscous friction change – uncertainty block
- Sinusoidal reference value – reference model and the weighting functions (*Wp*, *Wu*)

Magnitudes and frequencies of the disturbances are included in *Wd*-block (see a red triangle block in Figure 2-18). The range of parameter uncertainty such as viscous friction change is defined in the uncertainty-block (see a sky-blue rectangular block in Figure 2-18). By introducing a reference model in the controller design, the closed-loop system behaves similar to the reference model. Designing of the weighting functions and the reference model is explained in section 6.3.3.

Several kinds of robust controllers are listed in section 6.3. H$_\infty$ and μ–synthesis are chosen in this research. The two robust controllers are supported by the Robust Control Toolbox of Matlab.

Cascade control is also robust against disturbance and relatively easy to design because it is based on simple PD-control. . A PD-controller is tested as a baseline.

As a test rig is built in section 4 for the two-motor-pitch-system, the load simulation for the test rig is written in section 5. The pitch angle controllers are suggested and compared in section 6 by means of the test rig and the load simulation.
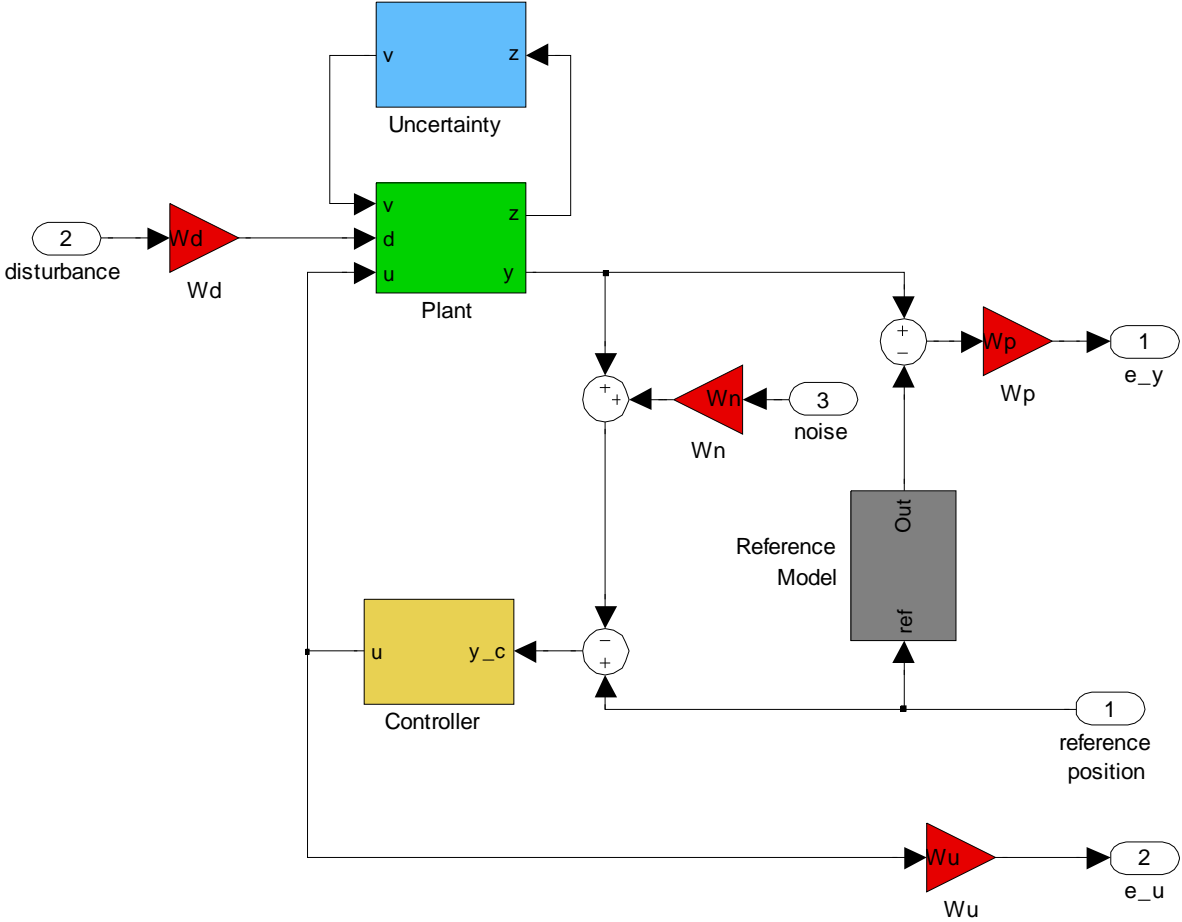
Figure 2-18: Structure of robust **H**∞ controller

3. Two-Motor-Pitch-System

In this research, two motors are equipped in each blade to compensate for gear play and eliminate torque peaks. Depending on directions and amplitudes of torques, the operation can be divided into four modes. The four modes are explained in section 3.1. In section 3.2, several methods are suggested and compared to distribute reference torque to the two motors.

3.1. Operating modes

Stop mode

If pitch angle stays, the pitch motor has to be braked. The brake moment must be larger than external torque by gravity, aerodynamic force and centrifugal force. A mechanical brake is located on the end of the motor and fastens the motor spindle automatically when no electric current is transferred to the motor. This motor brake can be also used for a two-motor-system. Since the gearbox amplifies the torque, a small brake is enough for fixing a large blade.

However, if the brake is operated when the pitch motor stops just in a short time, it is difficult to apply rapid pitch actions. The problem can be solved by imposing the same amplitude and opposite-direction torques on the two motors (see Figure 3-1). Because of sliding friction (see section 4.3.1), the pitch angle stops despite of external torque. As the motor torque increases, the sliding friction increases, too. The friction has to be larger than the external torque. The amplitude of motor torque has to be chosen to resist the external torque.

Figure 3-1: Stop mode

Normal operating mode

In order to rotate a blade around the pitch axis, one motor applies more torque than the other motor (see Figure 3-2). The torque directions of the two motors are the opposite. One motor with larger torque leads the pitch action and the other motor gives a tension to compensate for the gear play. In the figure, the left motor gives a torque counterclockwise and the right motor applies a torque clockwise. If the torque of the left motor is larger than that of the right motor, the ring rotates counterclockwise. If the torque of the right motor is larger, then the direction is clockwise. The amplitudes of the torques change, but the direction of each torque stays unchanged.

The torque difference leads to pitch action. Because of sliding friction, the torque difference of the two motors has to be larger than torque out of the one-motor-system. In addition, moment of inertia of the motor is doubled with the two-motor-pitch-system. The tension moment is fed back, but the sliding friction and added moment of inertia requires more motor torque in the two-motor-pitch-system. Thus the proposed two-motor-pitch-system requires more electricity than the current one-motor-pitch-system. The disadvantage can be covered fully by extending life span of the pitch actuation system.

Figure 3-2: Normal operating mode

Emergency mode

In an emergency, pitch action should be applied quickly. Pitch rate with 10°/sec is triggered for the emergency shutdown [19]. Rapid pitch action requires a large pitch moment so that both motors drive moments in the same direction (see Figure 3-3). Gear play is not compensated for, but emergency cases do not happen frequently. Thus, this strategy is more economical than using large and expensive motors.

Figure 3-3: Emergency mode

One-motor mode

Current wind turbines with one pitch motor per each blade stop their operation if one motor is out of order. In offshore wind turbines, harsh weather conditions often prohibit technical experts from accessing the turbines and it leads to economical loss of the wind turbine operator. However if one motor is out of order in a two-motor-pitch-system-turbine, another motor can drive like a one-motor-pitch-system (see Figure 3-4). The wind turbine does not need to stop. Gear play is not compensated for in this case, but this is an extraordinary case which seldom happens.

Figure 3-4: One-motor mode

3.2. Torque distributor

3.2.1. Modes of torque distributor

In order to provide tension on the blade root bearing, two motors have to drive in the opposite direction. Different torque in two motors requires two pitch angle controllers as in the upper graph of Figure 3-5. *Torque1* and *Torque2* in the graph must have the opposite sign in the normal operating

mode. If the amount of *Torque1* is higher than the amount of *Torque2*, the pitch motor 1 'drives' the blade rotation and the pitch motor 2 'gives tension' on the blade root bearing. The two pitch controllers act differently depending on the situation. Whereas the pitch angle controller of the 'driving' pitch motor acts like the current pitch angle controller, the pitch angle controller of the 'tension' pitch motor may order a small torque. This method leads to more variable control operations, but the two controllers can interact with each other and it makes control design difficult.

One pitch controller with a torque distributor can replace two pitch angle controllers (see lower graph in Figure 3-5). Pitch angle controllers can be built like current one-motor-pitch-systems. The torque distributor determines the reference torques of the two motors. The sum of *Torque1* and *Torque2* is the same as the input of the torque distributor. In a normal condition, the outputs of the torque distributor have the opposite sign. Although this method requires an additional torque distributor, the pitch angle controller can be designed as the existing ways. Thus this method is chosen in this research.

Torque distributors have the following 3 modes:

- Both motors active
- One motor out of order
- Both motors out of order

The mode *both motors active* corresponds to stop mode, normal operating mode and emergency mode in section 3.1. The mode *one motor out of order* is the same as the one-motor-system. If both motors are out of order, stopping the turbine is the only option.
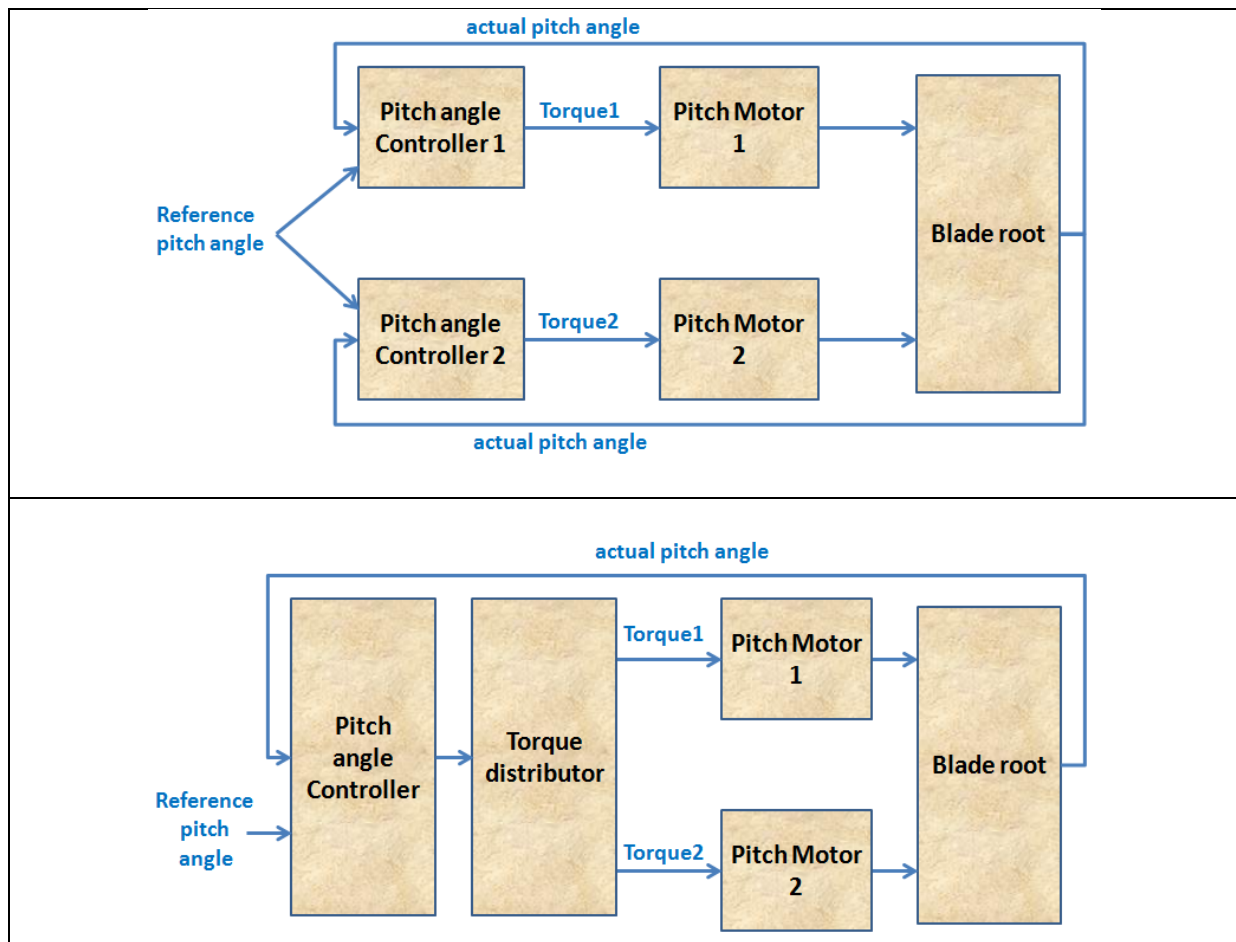
Figure 3-5: Pitch actuation system without and with torque distributor

3.2.2. Maximum torque and stationary torque

The maximum torque of a torque distributor is chosen based on the motor and gearbox. The smaller value between maximum torque of the motor and gearbox is selected as the maximum torque of a torque distributor.

Figure 3-6 shows rated torque out of the motor is 34.3Nm. Rated torque of the gearbox is written in Figure 3-7. In the figure, I can choose the lowest time span because our experiment does not take much time. Torque on the motor side is obtained by dividing output torque into gear ratio, 63.2. The maximum output torque is 1.2 times the rated torque [20] and gearbox efficiency is assumed to be 90%. 1.25 is recommended as the safety factor of a power transmission [21].

The allowed input torque of the gearbox is:

$$T_{gearbbox} = \frac{2000 \cdot 1.2}{63.2 \cdot 1.25 \cdot 0.9} \approx 34 \qquad \text{(3-1)}$$

which is slightly less than rated torque of the motor. Thus the maximum torque of a torque distributor is decided to be 34Nm.

Figure 3-6: rated torque out of the motor

Figure 3-7: rated torque of the gearbox [20]

Stationary torque is the torque of a motor which gives torque in the opposite direction of the rotation. In stop mode of section 3.1, amplitude of the torque out of each motor is the stationary torque. Figure 3-8 shows an example where the stationary torque is 5Nm.

Stationary torque increases sliding friction which helps to withstands external loads. Higher stationary torque resists more external loads but requires more electricity consumption. The amplitude of the stationary torque has to be chosen based on turbulent wind conditions.
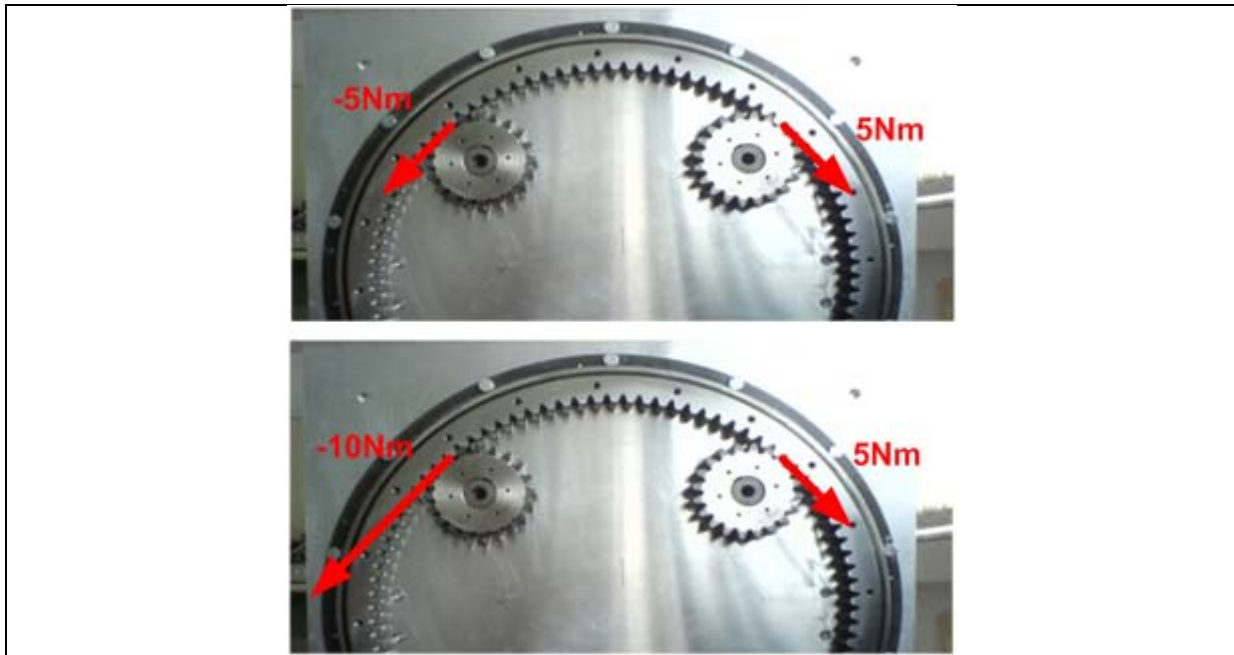
Figure 3-8: stationary torque = 5Nm

3.2.3. Art of torque distributors

As seen in the lower graph of Figure 3-5, reference torque is divided to torque-1 and torque-2 in the torque distributor. The main purpose of the torque distributor is that the two output torques must work in the opposite direction in case of the normal mode in section 3.1.

Three kinds of torque distributors are suggested in Figure 3-9, Figure 3-10 and Figure 3-11. Torque distributor-1 and 2 were presented by M. Hackl [13]. Stationary torque is chosen to be 5Nm for the test.

Maximum torque of each motor is limited to 34Nm (see (3-1)) in the torque distributors. In order to compare the effect of torque distributors, a torque distributor-base is also suggested (see Figure 3-12). Torque out of motor-1 is the same as motor-2 with a torque distributor-base. Gear play is not compensated for in this case.

The horizontal axes in the Figure 3-9 - Figure 3-12 are input torque of the torque distributor. The input torque is the same as the sum of the torques out of motor-1 and 2. The vertical axes are torque of motor-1 and 2. For example in Figure 3-12, total torque of 20Nm is distributed equally to the two motors, thus each motor receives 10Nm. Since the torques of the both motors have the same sign, no tension is applied in this case. On the other hand, outputs of the torque distributor-1 are 25Nm and -5Nm, which act in the opposite direction each other and compensate with gear play.

All the torque distributors pass points where torque of a motor is zero (see red circles in Figure 3-9 - Figure 3-11). On the points, one motor does not give torque, thus gear play is not compensated for. The point has to be as far as possible from the zero point.
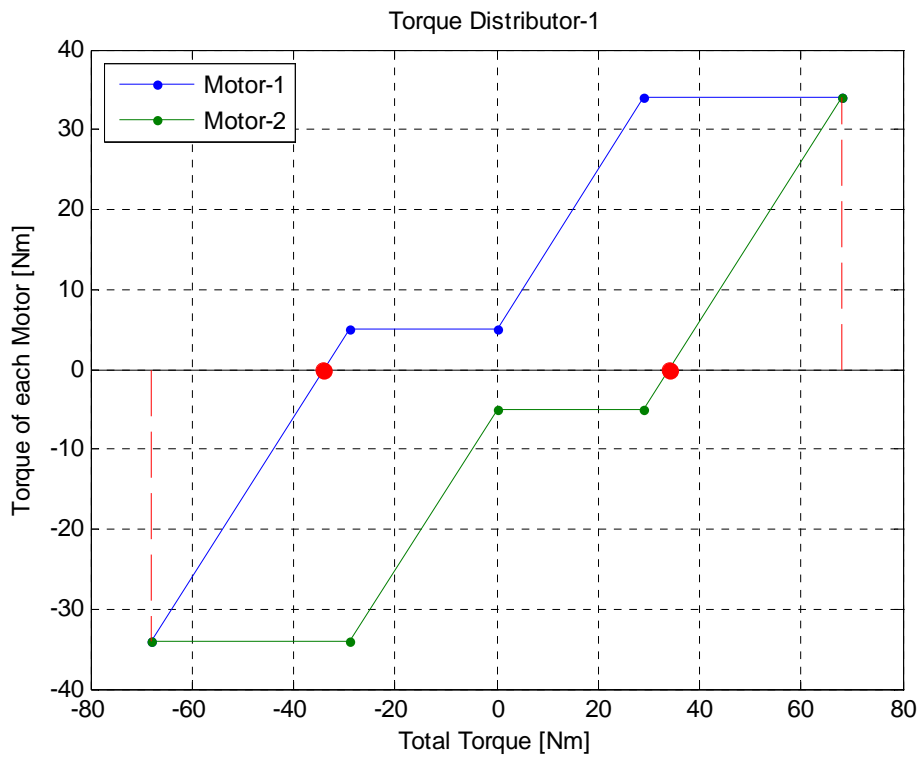
Figure 3-9: Torque distributor-1
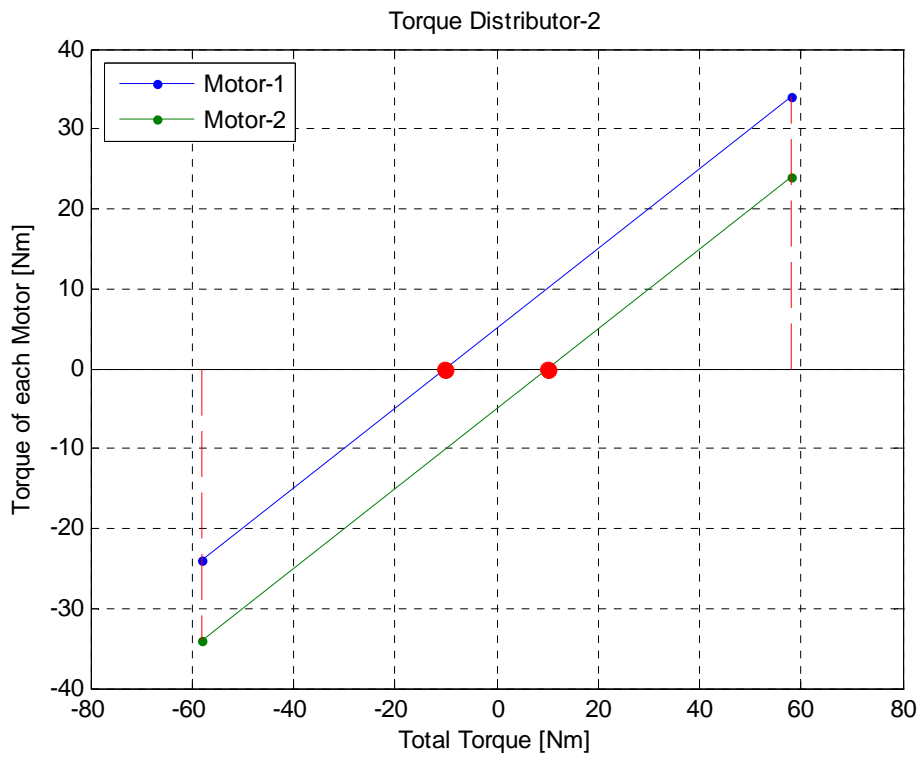
Figure 3-10: Torque distributor-2
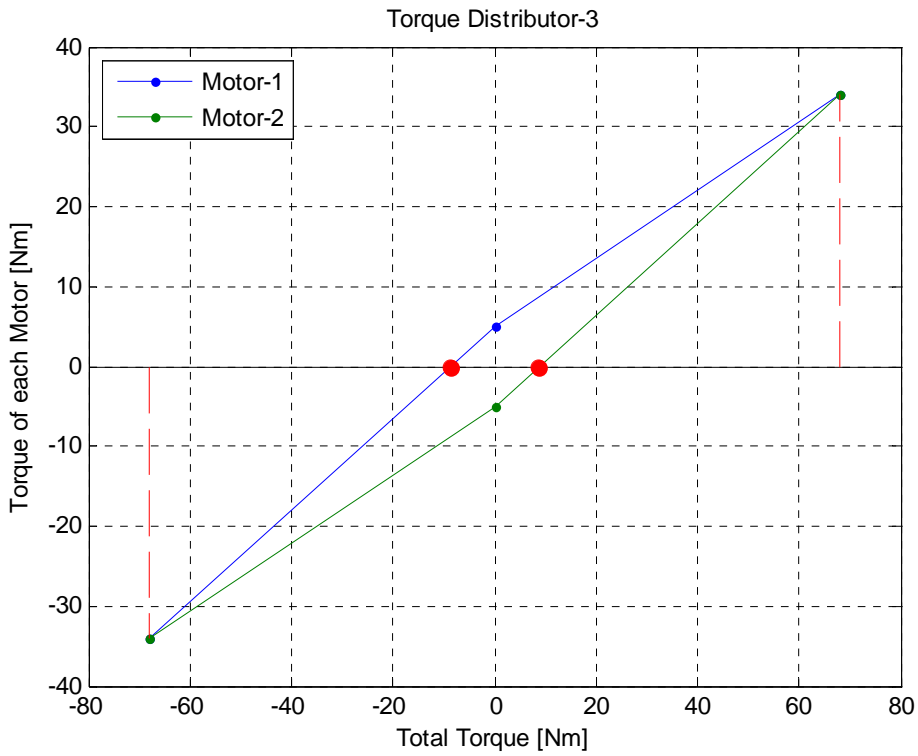
Figure 3-11: Torque distributor-3
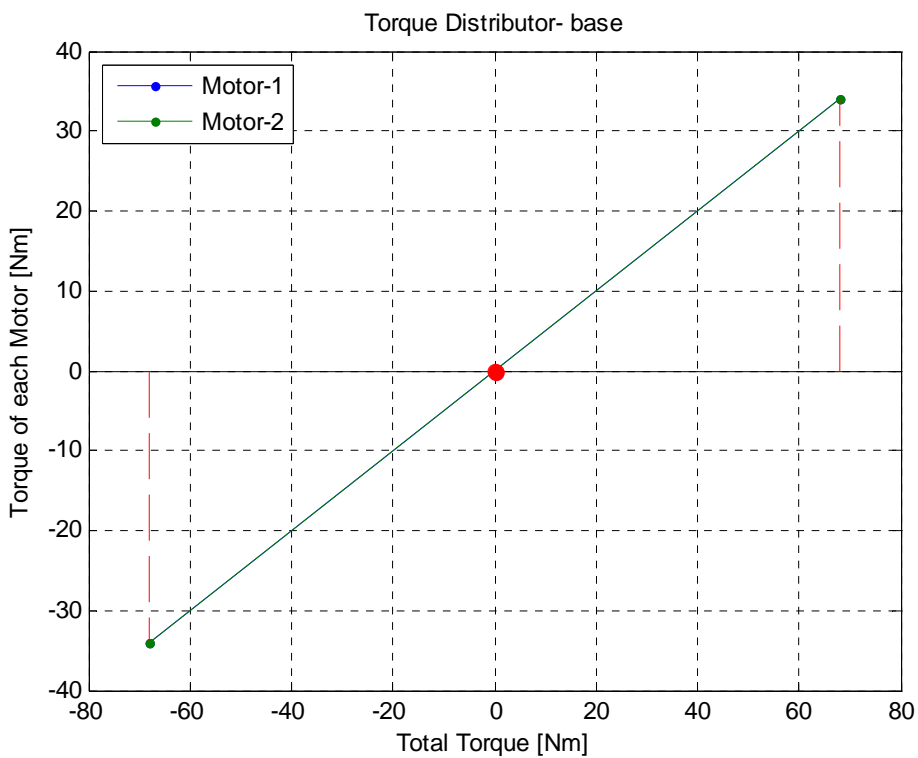
Figure 3-12: Torque distributor-base

Maximum torque is achieved if two motors give torques in the same direction. Larger maximum torque ensures better performance in emergency cases.

Total torque if a motor gives no torque and the maximum total torque with four torque distributors are written in Table 3-1. Torque distributor-1 wins the maximum values in both cases.

	Total torque if a motor gives no torque	Maximum total torque
Torque distributor-1	34 Nm	68 Nm
Torque distributor-2	10 Nm	58 Nm
Torque distributor-3	8.7 Nm	68 Nm
Torque distributor-base	0 Nm	68 Nm

Table 3-1: total torque if a motor gives no torque, maximum total torque

3.2.4. Comparison of torque distributors

As shown in Table 3-1, torque distributor-1 can hold more tension than other distributors. If total torque is bigger than 10Nm and smaller than 34Nm, only torque distributor-1 can avoid gear play. It is tested in the test rig. The second and third graphs in Figure 3-13 show that only torque distributor-1 does not have vibrations. Other torque distributors have torque peaks after the torque graphs pass 0 Nm. For example, torque distributor-base (TD-base) passes a point of zero torque at 0.7 second and vibration occurs at 0.8 second. Torque is measured with a torque sensor between the motor and gearbox (see the golden cylinder in Figure 3-14). The surface, where gear teeth meet, is changed as the sign of torque is changed.

The reference torque of torque distributor-1 is the biggest and torque distributor-base is the smallest in the lowest graph of Figure 3-13. Large tension between two motors increases sliding friction so that total torque is increased also. Sliding friction, which is explained in section 4.3.1, is a torque-dependent friction.

Simulations and experiments in the later sections are done with torque distributor-1. Reference torque is limited to 29Nm in normal operating mode to ensure tension. In the case, one motor has 34Nm and the other has -5Nm. In emergency mode, the torque limit is increased to 68Nm.
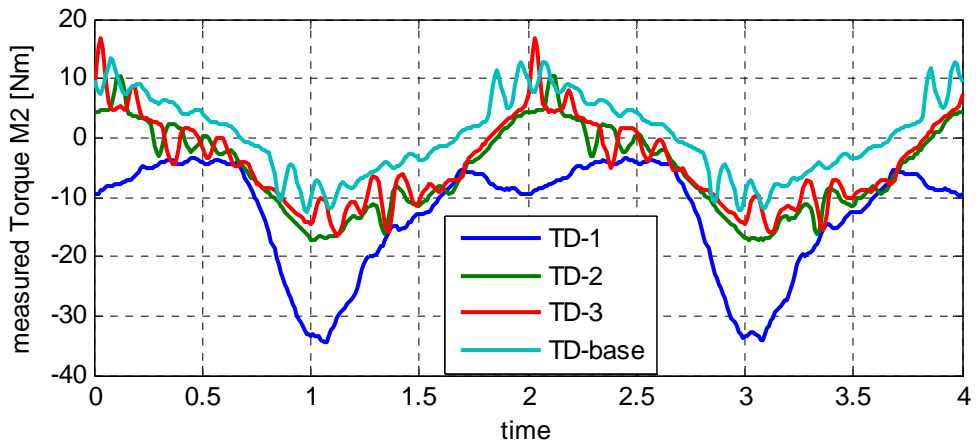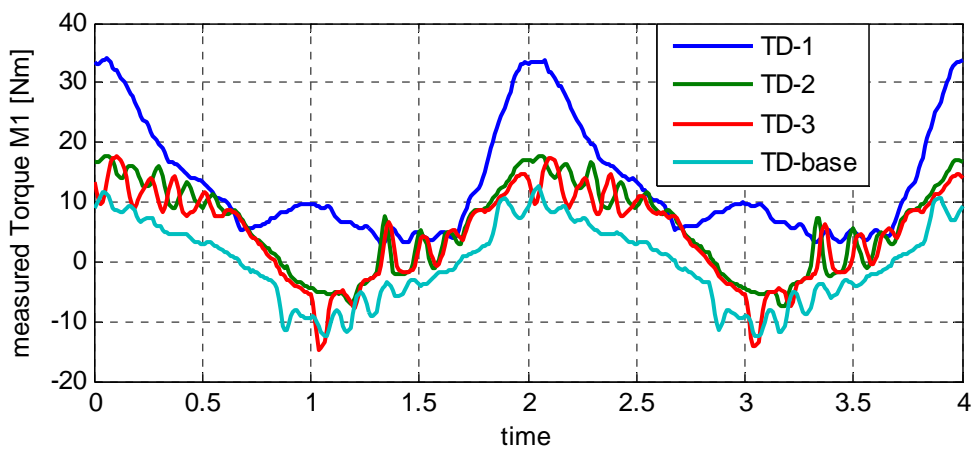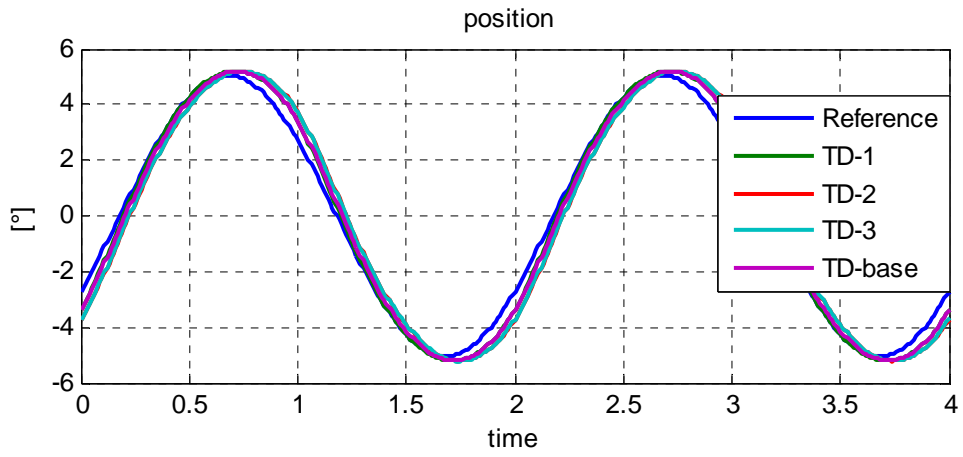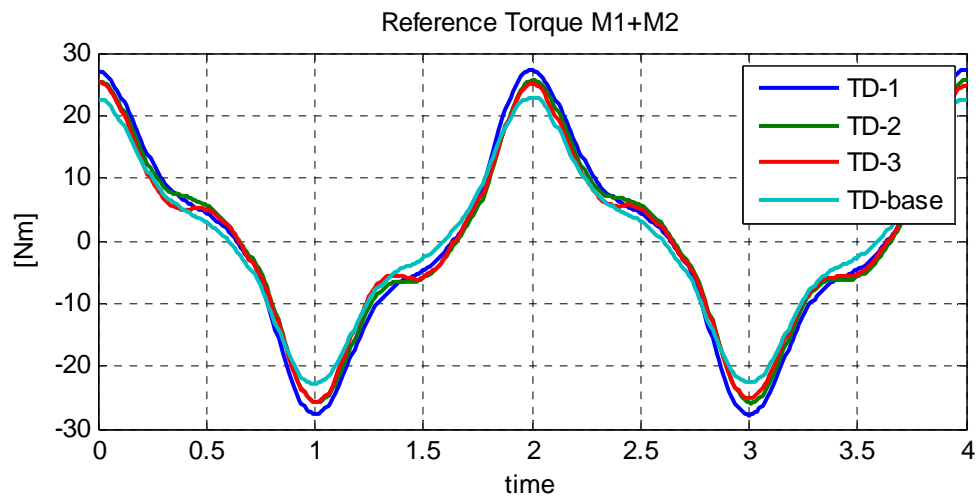
Figure 3-13: Torque distributor comparison, test rig

Figure 3-14: Torque sensor

4. Test rig

4.1. Composition of test rig

The pitch actuation system consists of several components. Characteristics of each component have to be determined for modeling of the system. The main characteristics are moment of inertia, spring, and damper. The characteristics primarily influence speed and torques of the system. The three elements determine the natural frequencies of the system.

Motor
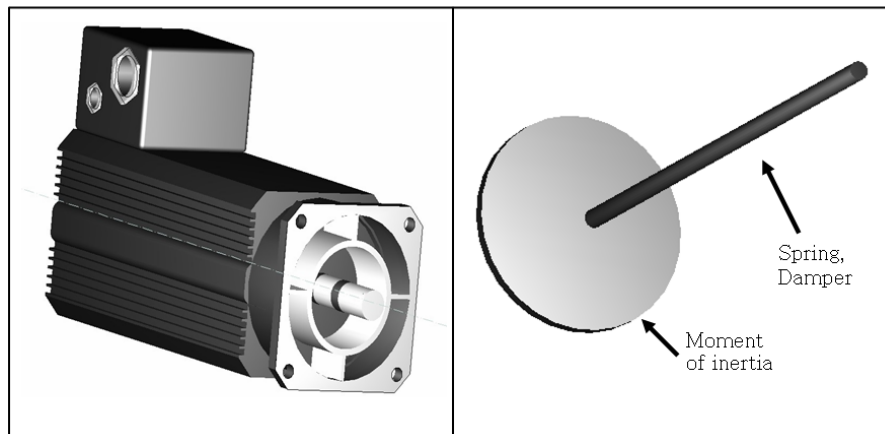
Figure 4-1: Motor model

The servo motor, used in the test rig, is composed of a rotor, stator, power electronics, and torque controller. Electrical parts are not necessary to be modeled because input of the motor is not current but torque. An inverter is connected between the motor and the pitch angle controller. The inverter converts the reference torque to current. As long as the current limits of the inverter are not reached, the electrical model is not required since the process runs much faster than the mechanical movement.

Mechanical characteristics, e.g. moment of inertia, spring, and damper, are needed for the modeling (see Figure 4-1). Moment of inertia causes the system to act slowly. The model with moment of inertia is shown in Figure 4-2. The spring and damper are related to differences of position or speed (See Figure 4-3).
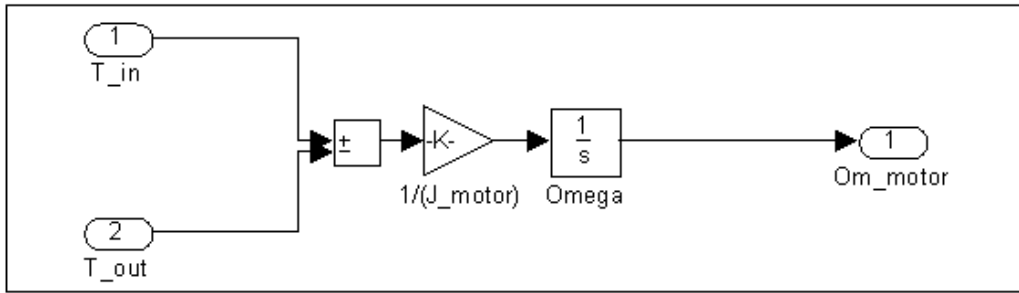
Figure 4-2: model with motor moment of inertia
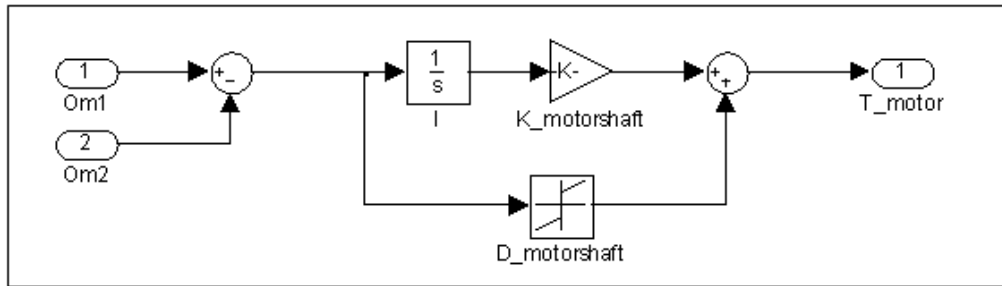
Figure 4-3: model with spring and damper

Clutch and shaft

The maximum torque is limited by the pitch angle controller and load simulator. However, mistakes can happen while designing the controller or simulator. In the test rig, we set up clutches (see Figure 4-4) only to the motors connected to the pitch angle controller because the pitch angle controller usually gives more torque than the load simulator. The clutches are attached to the motor in order to protect the gears, the weakest component in the test rig. The maximum torques are limited as software by the pitch angle controller and as hardware by the clutch. The maximum torque out of the pitch angle controller is set to be lower than that of clutch in order to avoid clutch release.

If the torque exceeds the limit, balls in the clutch leave the form and power stops being transmitted. When the torque is reduced, balls go back to the ball bed again after they slip for a short time around the ball bed. The power train is reconnected (see Figure 4-5).

S-R flipflop is used in the model to decide whether the clutch is connected or not. S-R means Set-Reset. Figure 4-6 shows the connection, departing, and reconnecting processes. $!Q = 1$! means that the clutch is connected and $!Q = 0$ is disconnected.

Figure 4-4: Clutch
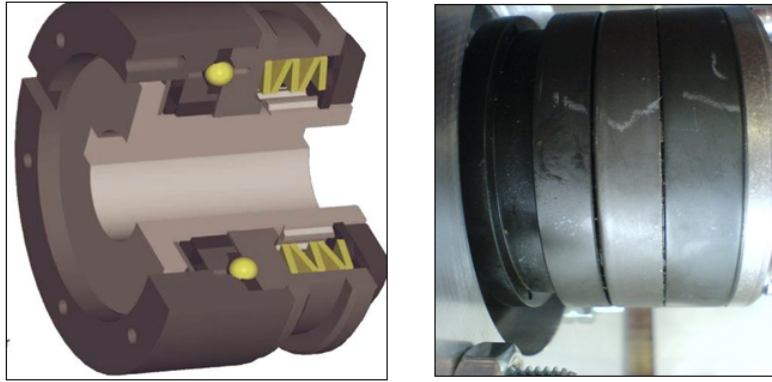
Usual case		Overloaded case	
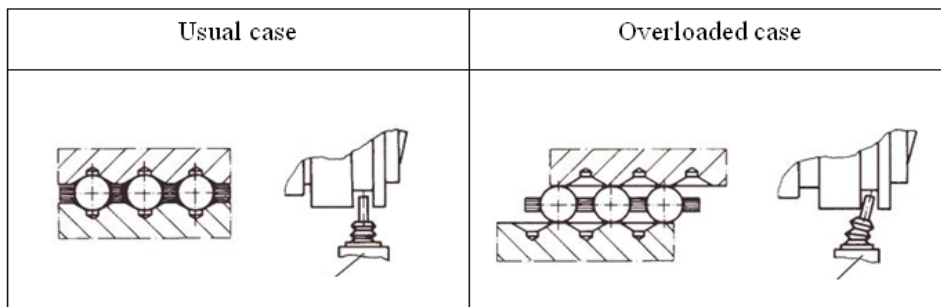
Figure 4-5: Behavior of clutch in usual and overloaded case [23]

	T>Tmax ↓	T=Trest ↓		Θ>Θslip ↓
S	0	1	0	0
R	1	0	0	1
!Q	1	0	0	1

Figure 4-6: Process of S-R flipflop and output [23]

The shaft is the component where most of the deformation occurs. Especially the shaft on the pitch actuation system has a rubber (see red part in Figure 4-10), the shaft on the pitch actuation system bends more than that on the load simulator. The spring and damping effect of the whole system is mainly affected by the shaft.

Gearbox

A simple gear system is shown in Figure 4-7. Gear play and torsion stiffness are ignored for simplicity.
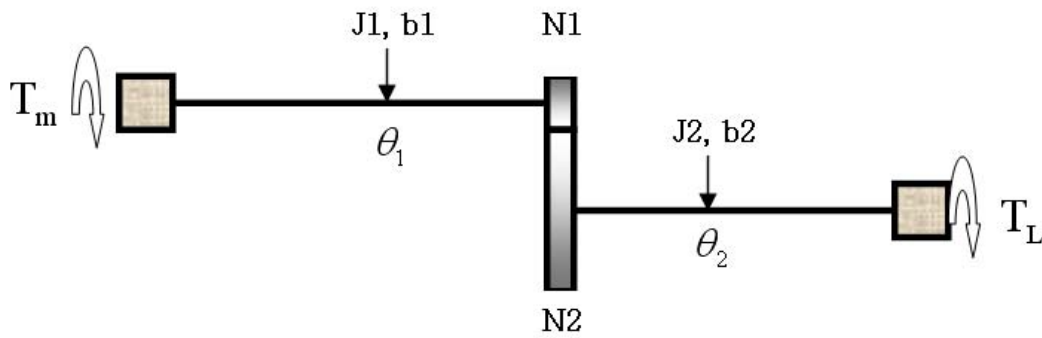
Figure 4-7: Simple gear model

The differential equation on the left axis is

$$J_1\ddot{\vartheta}_1 + b_1\dot{\vartheta}_1 + T_1 = T_m \tag{4-1}$$

where T_m is the generated torque of a motor and T_1 is torque transmitted to the right axis.

The right axis has a similar equation.

$$T_2 = J_2\ddot{\vartheta}_2 + b_2\dot{\vartheta}_2 + T_L \tag{4-2}$$

where T_L is an output torque.

Work transferred from left to right axis is the same. Thus

$$T_1\vartheta_1 = T_2\vartheta_2 \quad \text{or} \quad T_2 = iT_1 \quad \text{or} \quad \vartheta_2 = \frac{1}{i}\vartheta_1$$

where $i = \dfrac{N_2}{N_1}$

Equation (4-1)and (4-2) can be combined as follows.

$$J_{eq}\ddot{\vartheta}_1 + b_{eq}\dot{\vartheta}_1 = T_m - \frac{1}{i}T_L \tag{4-3}$$

With

$$J_{eq} = J_1 + \frac{1}{i^2}J_2 \quad , \quad b_{eq} = b_1 + \frac{1}{i^2}b_2$$

A gear needs a gap to place lubricating oil. The gap is called gear play, clearance, or backlash. Tolerance during production is also a reason for gear play. Gear play of the gearbox in the test rig is about 60° on the fast side. In the simulation using Matlab/Simulink, gear play is not modeled with *backlash* but with *lookup-table* because the input value has to be a position difference.

Pinion

A pinion (see Figure 4-8) itself has only moment of inertia. The gear mesh between the pinion and ring has friction and gear play. Gear play between pinion and ring is very small, but it is enlarged to around 30° at the motor position due to gear ratio.
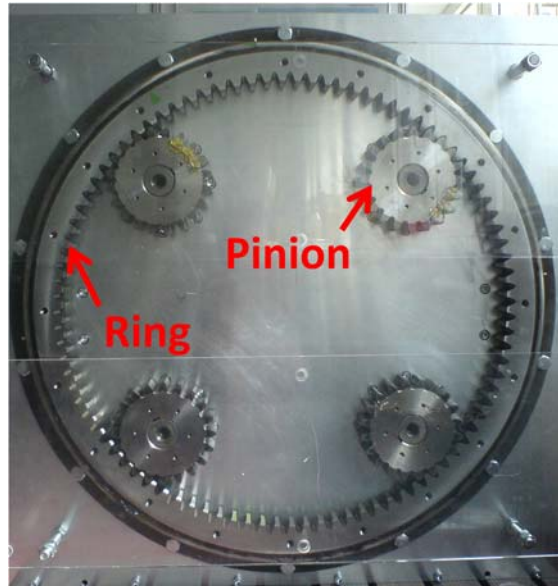
Figure 4-8: Pinion and ring

Ring

Mechanical characteristics of the gear mesh between the pinion and ring are contained in the pinion model. The ring (see Figure 4-8) has only moment of inertia and friction. Moment of inertia of the ring is divided by a square of the gear ratio to compare the value in the motor side. Thus the parameters of the ring have a small influence in spite of its large diameter and heavy mass.

4.2. Pitch actuation system modeling

Six kinds of models

A controller has to be errorless and designed to run the test rig in a stable manner. The controller is made based on a model of the test rig. We predict the behavior of a real system and prevent errors by the use of simulation, which also requires a model.

A model is a simplification of a system. Mass, spring, and damper are typical elements of mechanical system models. Friction is also added in this study.

Motor, clutch, gear, pinion, and ring are essential parts for modeling of the test rig. The model can be simplified by combining two or more parts together. Detailed models, e.g. complete model or intermediate model of Figure 4-9, represent the real system precisely. On the other hand, a simple model helps designing controllers and reduces difficulties in obtaining parameters.

Two things are to be considered as a model is chosen. The first thing is if the model represents enough well dynamic characteristics of the real test rig. It means the output of the model acts the same as the real test rig if the input is the same. In this research, motor torque is the input and ring position is the output.

The second thing to consider is if the model parameters can be obtained with small uncertainties. Mechanical parameters such as moment of inertia, friction and stiffness are not offered except motor. Numerical estimation is also difficult because of complex shape of the components. The gearbox is enclosed by a case and its detail drawing is not available. Pinion and ring have gear teeth whose moment of inertia is difficult to be estimated. Thus experiment is the only way to estimate parameters. Motor has to be connected in order to get the dynamic characteristics. Because of the shape, it is difficult to connect each part directly to a motor. Uncertainty of the each component is accumulated as parameters of a part are measured if the part is not connected to motor directly. For example, if complete model is chosen, uncertainty of the parameters in ring part is influenced by uncertainties of motor, clutch, gearbox and pinion.

The second thing is the reason why a simple model is chosen in this research. The first thing is confirmed in section 4.4.

Three simple models are presented in Figure 4-9. The main part of stiffness is an interface between the clutch and gearbox because the part is composed of rubber. The red component in Figure 4-10 is rubber, thus simple model-3 is chosen.

A clutch is not equipped in M3 and M4. Instead, a hollow shaft is the main part of stiffness. Models of M1&M2 and M3&M4 should be built differently. The exact model becomes Figure 4-11.

Complete Model

| Motor | | Clutch | | Gearbox | | Pinion | | Ring |

Intermediate Model

| Motor + Clutch | | Gearbox | | Pinion | | Ring |

Plain Model

| Motor + Clutch + Gearbox | | Pinion | | Ring |

Simple Model - 1

| Motor + Clutch + Gearbox | | Pinion + Ring |

Simple Model - 2

| Motor + Clutch + Gearbox + Pinion | | Ring |

Simple Model - 3

| Motor + Clutch | | Gearbox + Pinion + Ring |
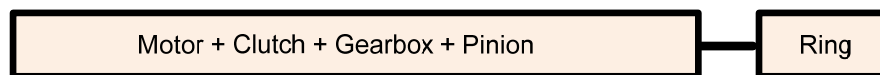
Figure 4-9: six kinds of models (partly from [23])

Figure 4-10: Two kinds of shaft
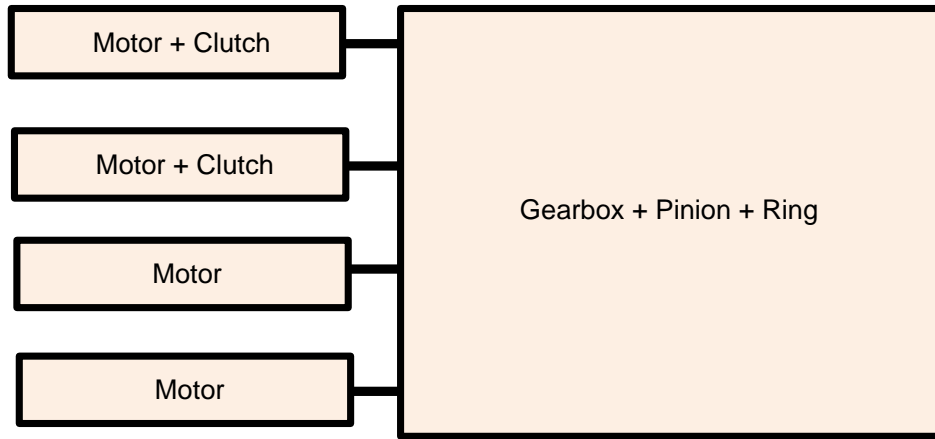
Figure 4-11: precise model of simple model-3

Linear model

Although nonlinear controllers have been developed in the last decades, linear controllers are still the main stream of the controller design. The suggested controllers in this research are also linear controllers, thus a linear model has to be designed first.

The simple model-3 can be written in a linear state equation like (4-4). The linear model is a basic to build a nonlinear model in Simulink. The controllers in this research are also designed based on the linear model.

$$\dot{x} = Ax + Bu$$
$$y = Cx + Du$$

(4-4)

with

$$x = \left[\theta_1, \theta_2, \theta_3, \theta_4, \theta_r, \dot{\theta}_1, \dot{\theta}_2, \dot{\theta}_3, \dot{\theta}_4, \dot{\theta}_r\right]^T$$

$$A = \begin{bmatrix}
0 & 0 & 0 & 0 & 0 & 1 & 0 & 0 & 0 & 0 \\
0 & 0 & 0 & 0 & 0 & 0 & 1 & 0 & 0 & 0 \\
0 & 0 & 0 & 0 & 0 & 0 & 0 & 1 & 0 & 0 \\
0 & 0 & 0 & 0 & 0 & 0 & 0 & 0 & 1 & 0 \\
0 & 0 & 0 & 0 & 0 & 0 & 0 & 0 & 0 & 1 \\
-\dfrac{k_1}{I_1} & 0 & 0 & 0 & \dfrac{k_1}{I_1} & -\dfrac{d_1}{I_1} & 0 & 0 & 0 & \dfrac{d_1}{I_1} \\
0 & -\dfrac{k_2}{I_2} & 0 & 0 & \dfrac{k_2}{I_2} & 0 & -\dfrac{d_2}{I_2} & 0 & 0 & \dfrac{d_2}{I_2} \\
0 & 0 & -\dfrac{k_3}{I_3} & 0 & \dfrac{k_3}{I_3} & 0 & 0 & -\dfrac{d_3}{I_3} & 0 & \dfrac{d_3}{I_3} \\
0 & 0 & 0 & -\dfrac{k_4}{I_4} & \dfrac{k_4}{I_4} & 0 & 0 & 0 & -\dfrac{d_4}{I_4} & \dfrac{d_4}{I_4} \\
\dfrac{k_1}{I_r} & \dfrac{k_2}{I_r} & \dfrac{k_3}{I_r} & \dfrac{k_4}{I_r} & -\dfrac{\sum_{i=1}^{4}k_i}{I_r} & \dfrac{d_1}{I_r} & \dfrac{d_2}{I_r} & \dfrac{d_3}{I_r} & \dfrac{d_4}{I_r} & -\dfrac{r+\sum_{i=1}^{4}d_i}{I_r}
\end{bmatrix}$$

$$B = \left[0,0,0,0,0,\frac{1}{I_1},0,0,0,0 \right]^T$$

$$C = \left[0,0,0,0,\frac{1}{\ddot{u}},0,0,0,0,0 \right]$$

$$D = 0$$

where k_i, d_i, I_i are *i-th* stiffness, damping and moment of inertia. *r* is viscous friction added on the ring. Viscous friction varies depending on temperature in the gearbox, so a mean value is used for viscous friction parameter in the modeling. *ü* is the total gear ratio of the gearbox and pinion. $\vartheta_i, \dot{\vartheta}_i$ are the angle and speed of *i-th* motor and ring.

Two motors operate as pitch actuators, but one reference value is originally given and transferred to two motors via torque distributors. The controller has to be designed as if only one motor is active, thus matrix *B* has only one column.

Nonlinear model in Simulink

Figure 4-12, Figure 4-13 and Figure 4-14 show a model of the test rig. The model is built in Matlab/Simulink. Nonlinearities such as Coulomb friction or gear play are contained in the model. The controllers are designed based on the linear model, but they are tested in the nonlinear model to validate their performances.
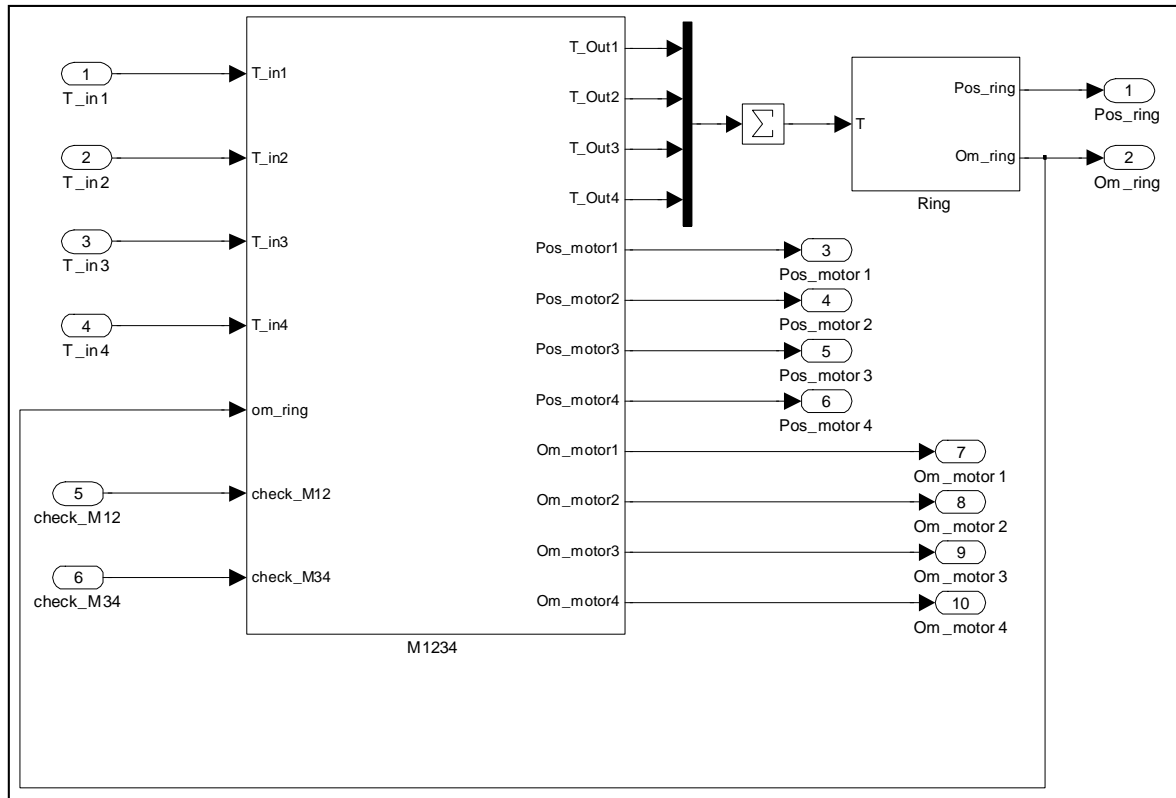
Figure 4-12: model of the test rig
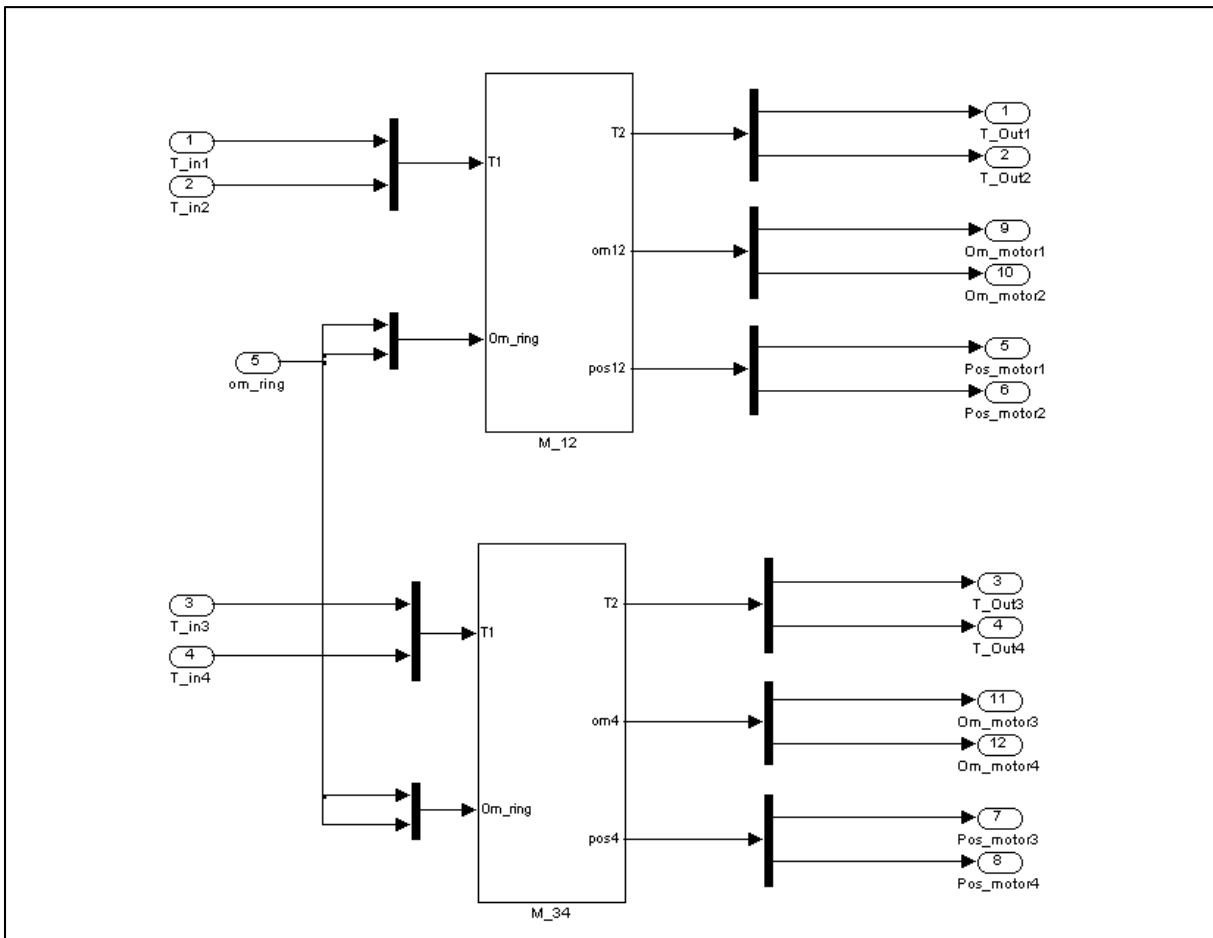
Figure 4-13: M1234 of Figure 4-12
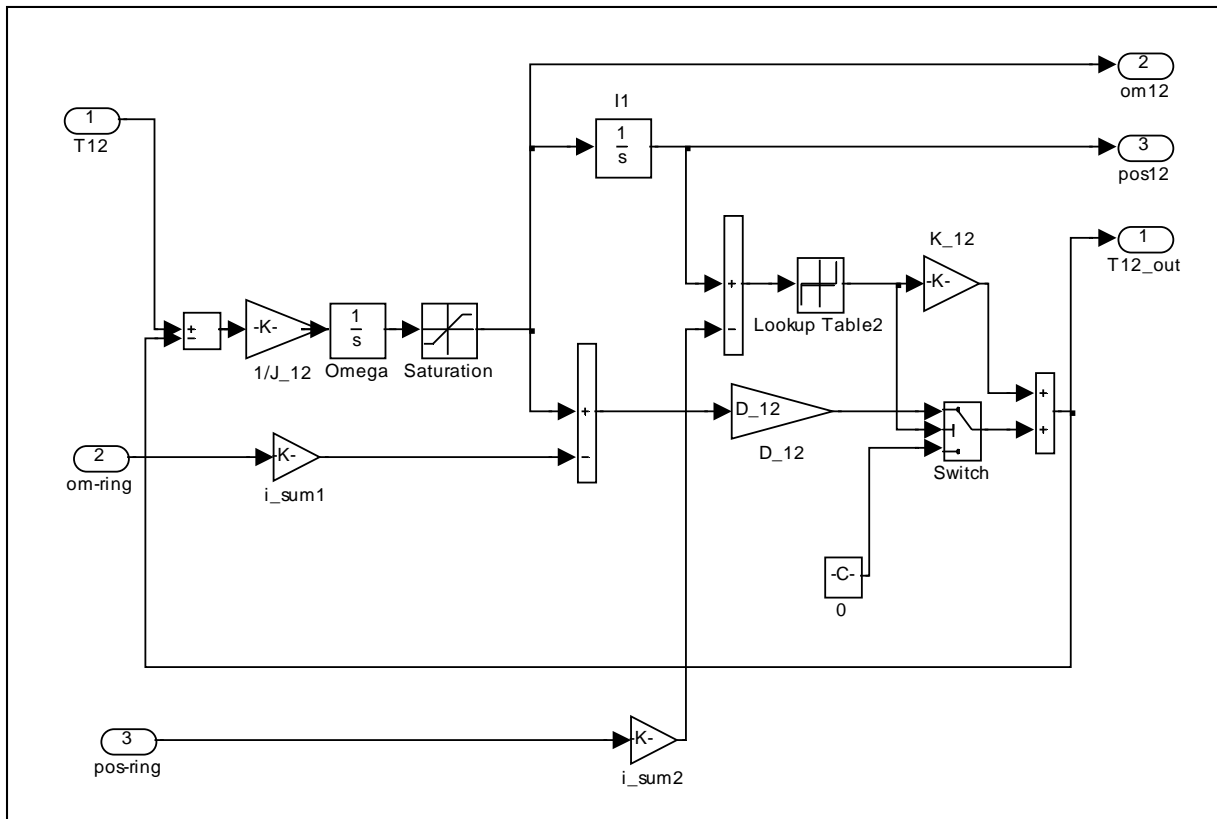
Figure 4-14: M-12 of Figure 4-13

4.3.Parameter estimation

The mechanical characteristics, e.g. friction, moment of inertia, stiffness and damper, are required not only to simulate the test rig similarly but also to build a suitable controller. Both friction and damper are the same regarding that both dissipate kinetic energy and are functions of rotational speeds in the system. The difference in the system is that friction is a function of absolute speed of each element and damper is a function of relative speed of the connecting point.

The importance of parameter estimation is not damaged though a robust controller is designed. Precise parameters enhance the stability and performance of the controller by reducing parameter uncertainties.

4.3.1. Friction

Friction is representative characteristics in a moving system. It causes tracking error and undesired motion. Coulomb friction occurs between two surfaces and is also called "dry friction". Whereas Coulomb friction is indifferent from speed, viscous friction is proportional to speed. The two frictions are enough for describing most frictions in a mechanical system. However, load-dependent sliding

friction is important as well in this research because all the four motors drive separately and create different loads on gear teeth. There are several more friction models such as Stribeck, Dahl's and LuGre model, but they are not dealt with in this research because the models focus on the very low speed.

Coulomb and viscous friction

Coulomb friction is constant and acts in the opposite direction of velocity. Viscous friction increases linearly as velocity increases. Due to linearity, viscous friction can be easily used for designing a controller. In very high speeds, viscous friction increases with a power of 2, but such an exponential increment is not seen in the test rig since maximum speed in the motor is limited to 3000 rpm. Friction equation with Coulomb (F_C) and viscous (F_v) friction coefficients is defined as:

$$F = F_C \cdot sign(\omega) + F_v \cdot \omega$$

ω is a rotational speed. The friction equation is also illustrated in Figure 4-15.
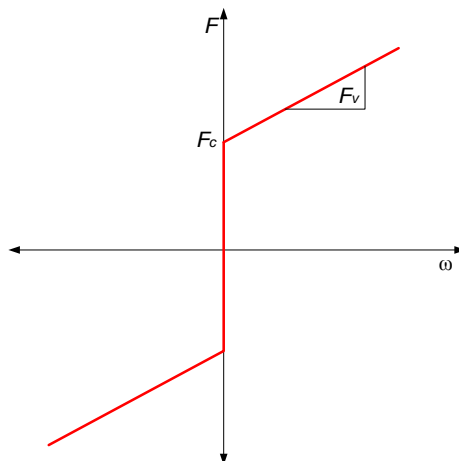
Figure 4-15: Coulomb and viscous friction

A problem with viscous friction is that the viscosity of the fluid in the gearbox is largely influenced by temperature. Figure 4-16 shows that the speed increases in spite of the constant torque. Viscous friction decreases as the temperature increases. A sensor is not equipped in the gearbox, thus the average viscous friction coefficient is used for building models and controllers. Minimum and maximum viscous friction coefficients are added in designing robust control.
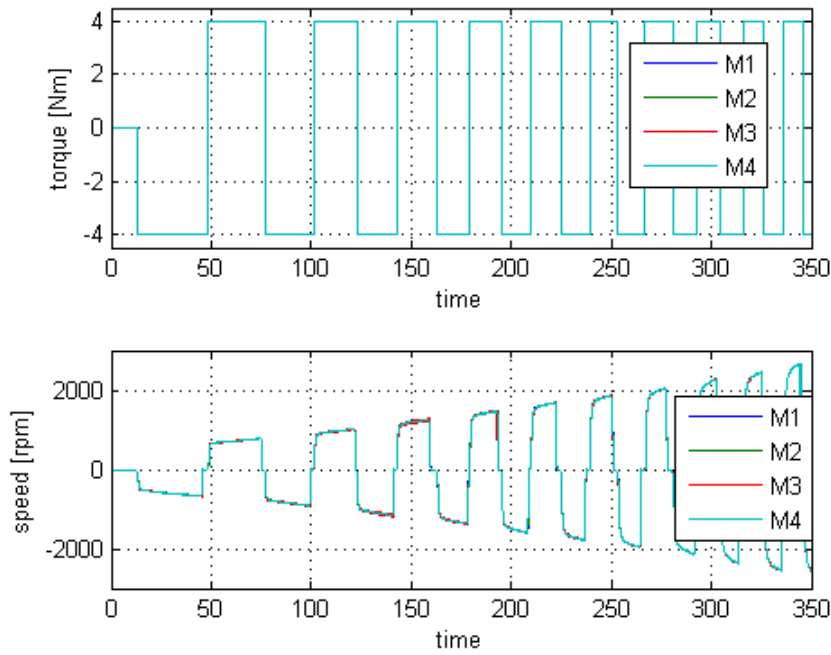
Figure 4-16: Speed increment with the same torque

Sliding friction

Sliding friction is caused by slippage between gear teeth. Minimizing the sliding friction is one of the main considerations of tooth profile design. Kuria et al. showed sliding friction occupies 98% of power loss for gear trains at low speeds (less than 2000 rpm) [24]. Sliding friction is referred to by different names, e.g. tooth friction loss [25], mechanical power loss [26] and gear friction loss [27].

The equation for power loss due to sliding friction is written by Martins et al. [27]:

$$P_{fr} = k_1 \cdot P_{in} \cdot \mu_m$$

where k_1 is a constant, P_{in} is input power and μ_m is the sliding friction coefficient. By dividing the equation with velocity:

$$M_{sliding} = k_1 \cdot M_{in} \cdot \mu_m$$

where $M_{sliding}$ is sliding friction, M_{in} is input torque. If ester oil is used as a lubricant in the gearbox, sliding friction coefficient μ_m is defined as [27]:

$$\mu_m = 0.048 \cdot k_2 \cdot \left(\frac{F_{bt}}{v} \right)^{0.0945}$$

where k_2 is a constant, F_{bt} is tooth normal force and v is entraining speed.

As tooth normal force is proportional to input torque and entraining speed can be replaced by rotational speed, sliding friction can be expressed as:

$$M_{sliding} = k \left(\frac{M_{in}}{\omega} \right)^{0.0945} \cdot M_{in}$$

where k is a constant number and ω is rotational speed.

Since four motors with gears are used, the total sliding friction is:

$$M_{sliding} = k \cdot \sum_{i=1}^{4} \left(\frac{M_{in,i}}{\omega} \right)^{0.0945} \cdot M_{in,i} \tag{4-5}$$

Figure 4-17 shows sliding friction decreases as motor speed increases and high torque induces high sliding friction. The rotational speed and torque are measured by experiment in the test rig. The sliding friction is determined according to (4-5). The coefficient k is not known, thus an arbitrary constant is given. The relationship between torque and sliding friction with constant rotational speed is also expressed in Figure 4-18. If rotational speed is constant, large torque induces large sliding friction.
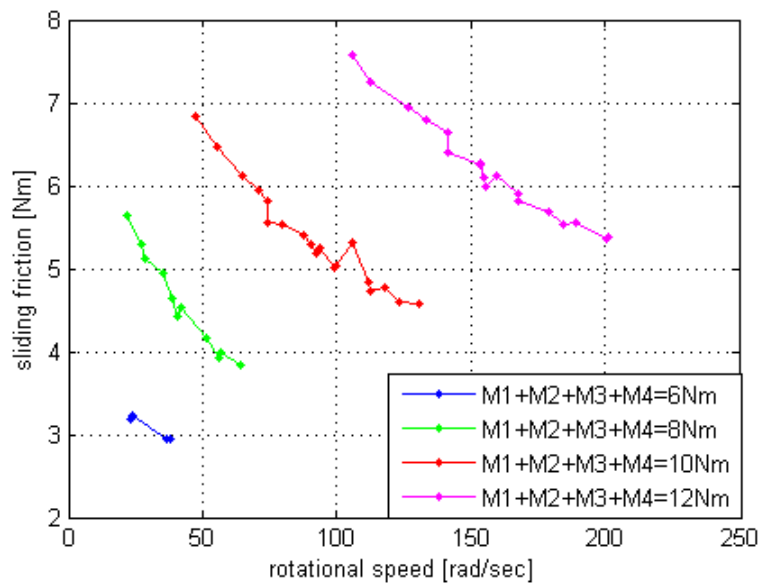
Figure 4-17: rotational speed vs. sliding friction
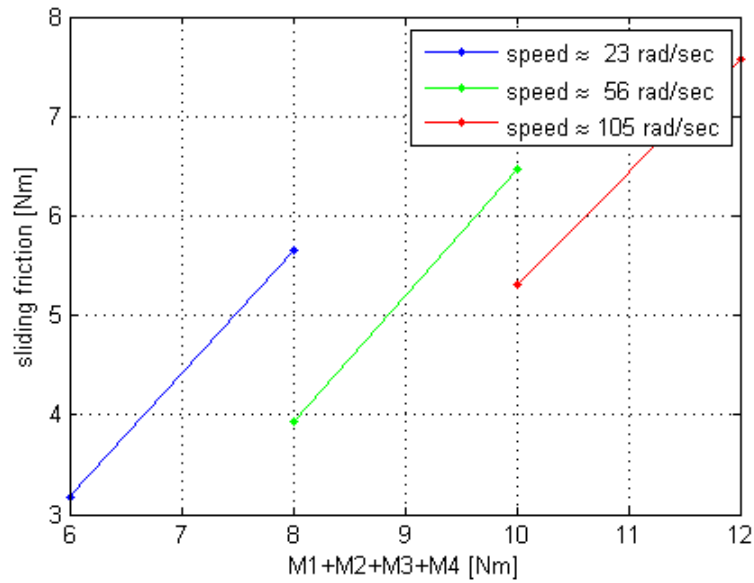
Figure 4-18: : total torque vs. sliding friction

Friction equation

The friction equation is expressed as:

$$Friction = Coulomb\,friction + viscous\,friction + sliding\,friction$$

$$= coulomb \cdot \frac{velocity}{|velocity|} + f_{viscous}(temperature) \cdot velocity + f_{sliding}(torque, velocity) \tag{4-6}$$

The parameters are gained with the least-square-method. In case the sum of torque is fixed, sliding friction comprises a larger percentage if each torque varies greatly like the left bar in Figure 4-19. This means less deviation of each torque induces low sliding friction and hence, high speed. The viscous friction coefficient is regarded to be fixed. Coefficient *k* in sliding friction is not known, thus sliding friction in the figure is not directly calculated. Sliding friction is regarded as the remaining torque after viscous and Coulomb frictions are subtracted from total torque.
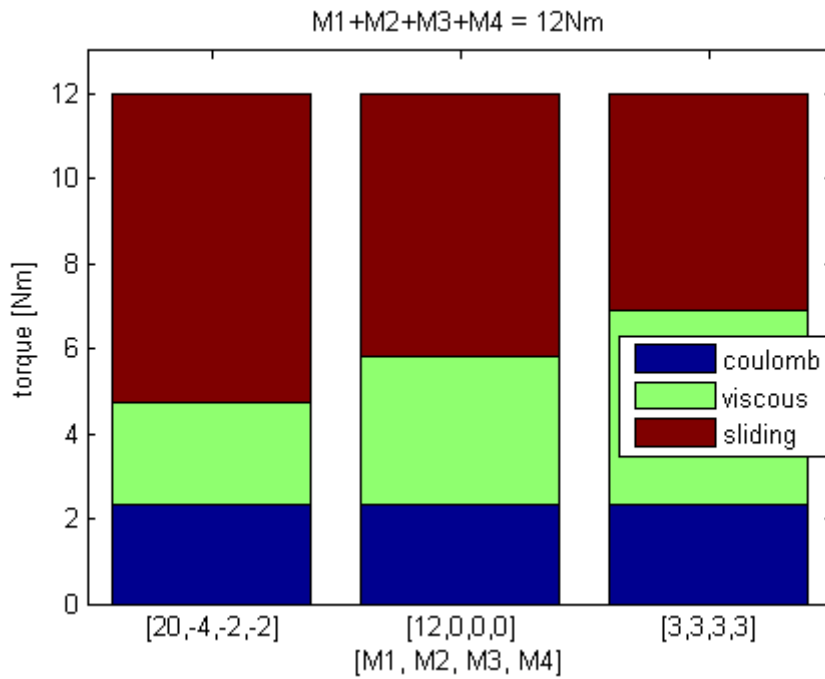
Figure 4-19: Components of friction – coulomb, viscous and sliding friction, total torque=12Nm

Alternative to the sliding friction

Figure 4-20 shows three cases where torque direction differs. The torque sum indicates friction. The friction graphs of the three cases are roughly parallel. The difference is sliding friction and it is constant if the tension between two motors is fixed. The constant sliding friction can be regarded as an added coulomb friction.

Thus the new friction equation is:

$$Friction = \sum_{i=1}^{2}\left(f_{coulomb}(tension_i)\cdot \frac{velocity}{|velocity|} \right) + f_{viscous}(temperature)\cdot velocity \qquad \text{(4-7)}$$

with

$$tension_1 = -\min(|M_1|,|M_2|)\cdot sign(\min(|M_1|,|M_2|))$$
$$tension_2 = -\min(|M_3|,|M_4|)\cdot sign(\min(|M_3|,|M_4|))$$

where M_i is torque out of motor-i.

In case $M_3 = 5Nm$, $M_4 = -5Nm$ and either $M_1 = -5Nm, |M_1| \leq |M_2|$ or $M_2 = -5Nm, |M_1| \geq |M_2|$, then both tension$_1$ and tension$_2$ are 5Nm. Figure 4-21 shows speed and torque in this case. The sum of Coulomb and sliding friction is determined as the graph is extended to the zero velocity. The slope is the viscous friction coefficient. The minimum and maximum coefficients are:

Friction coefficient	value
Minimum viscous friction coefficient [$Nm\cdot sec/\,rad$]	0.0628
Maximum viscous friction coefficient [$Nm\cdot sec/\,rad$]	0.2990

Minimum sum of Coulomb and sliding friction [Nm]	7.837
Maximum sum of Coulomb and sliding friction [Nm]	8.6099

Table 4-1: Viscous friction coefficient and sum of Coulomb and sliding friction
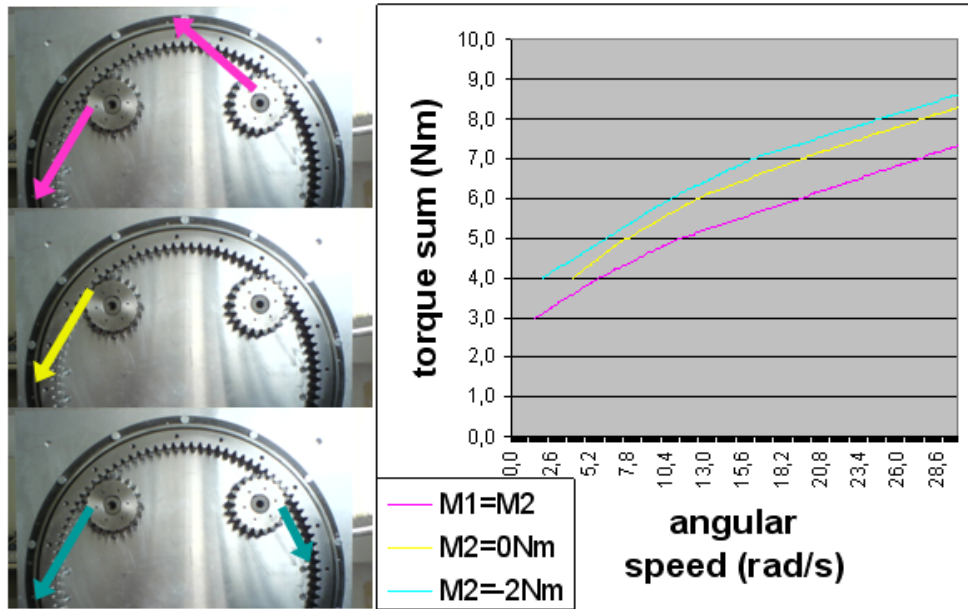
Figure 4-20: Friction at different motor setting
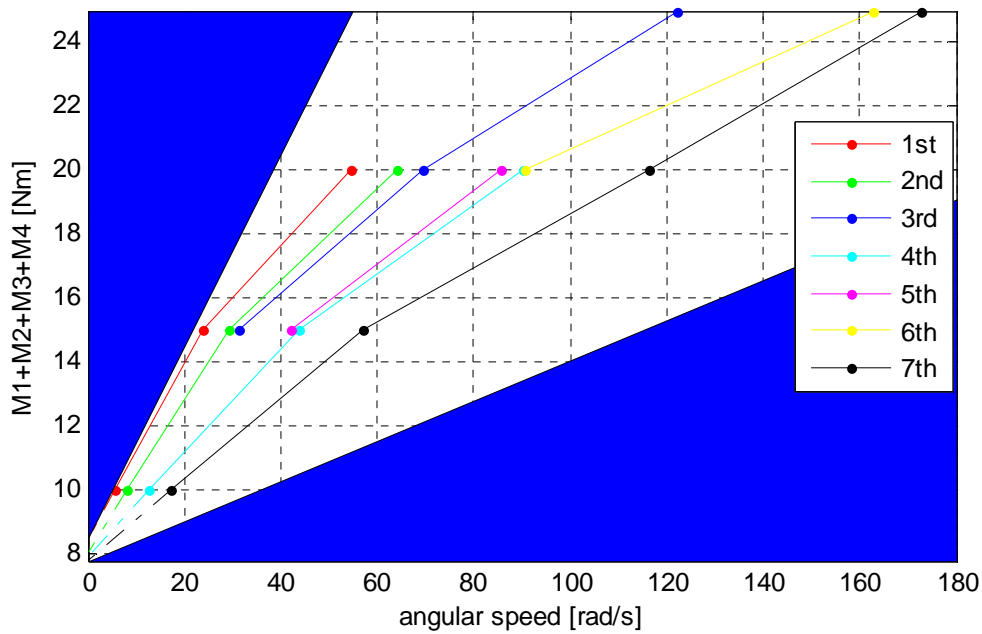
Figure 4-21: Friction graph

4.3.2. Moment of inertia of the whole test rig

Moment of inertia is the most important parameter in servo systems. The numerical way is not suitable because the structure of the gearbox is unknown and the shape of gear teeth in the pinion and ring is too complex to calculate. Thus, the moment of inertia of the test rig has to be calculated by means of measurement.

The main obstacle in measuring the moment of inertia is friction. As mentioned in section 4.3.1, the viscous friction changes according to the gearbox temperature. I must design a method which determines the moment of inertia even though friction is unknown. In this section, four kinds of methods are suggested to determine the moment of inertia of the whole test rig. ±1Nm is given for tension in the system (see Table 4-2). If all the motors work in the same direction, only the parts near the motors are measured. That is not expected in this experiment.

Title	12Nm		15Nm		18Nm	
	before	after	before	after	before	after
M1=M3	7	1	8.5	1	10	1
M2=M4	-1	-7	-1	-8.5	-1	-10

Table 4-2: Given torques for estimation of the moment of inertia

The moment of inertia of each motor set is not measured directly but estimated by means of the stiffness coefficient and the natural frequency. The natural frequency of the test rig is important for controller making so that moment of inertia of each motor set should be gained with natural frequency. The moment of inertia of the ring can be determined by subtracting the moment of inertia from four motor sets from that of the whole test rig.

Current method

Acceleration in each step and friction subtracted from input torque are used to draw moment of inertia in a conventional way (see Figure 4-22).

$$T = I \cdot \alpha + f(\omega)$$

where T is driving torque, I is moment of inertia, α is acceleration, and $f(\omega)$ friction.

Due to the vibrations in Figure 4-23, large deviation of the moment of inertia is seen (see Table 4-3).
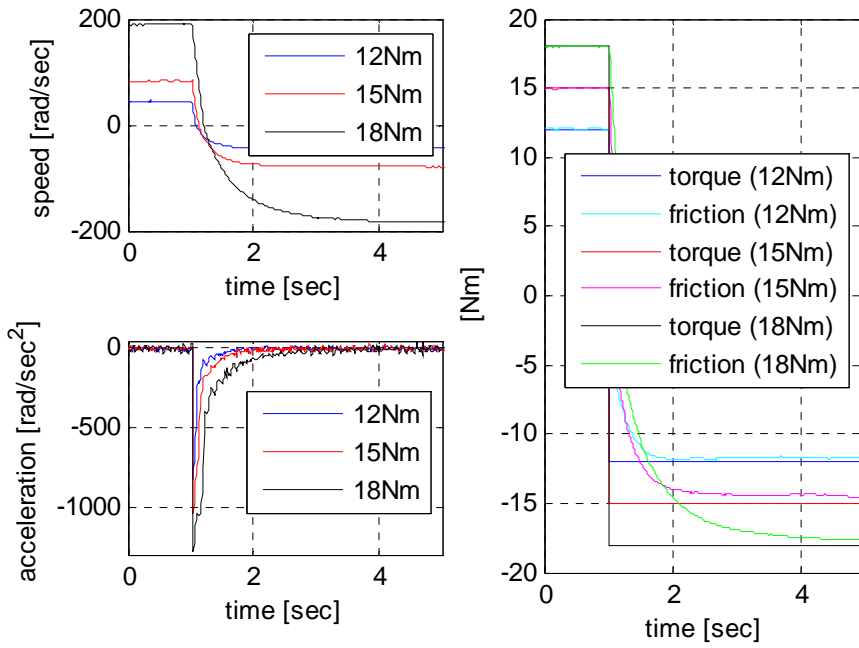
Figure 4-22: Lines for moment of inertia calculation
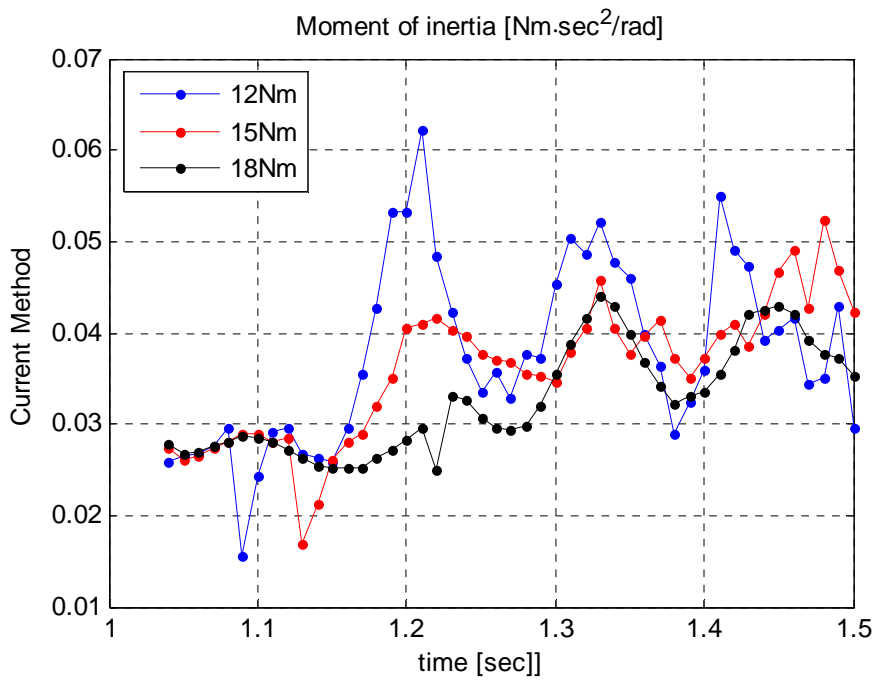
Figure 4-23: Moment of inertia over time

[Nmsec2/rad]	mean	min	Max
Total test rig	0.0355	0.0156 (-55.9%)	0.0622 (+75.3%)

Table 4-3: Moment of inertia with the current method without friction estimation (difference from mean)

Proposed method-1

Friction is compensated for on the two points where the speed sign is opposite and the magnitude is the same. The slope of the line which connects the two points is the acceleration. From the acceleration and torque, moment of inertia can be gained as:

$$I = \frac{t_2 - t_1}{\Omega(t_2) - \Omega(t_1)} \cdot \left(T(\Omega(t_2)) - T(\Omega(t_1)) \right) \quad , \quad \Omega(t_2) = -\Omega(t_1)$$
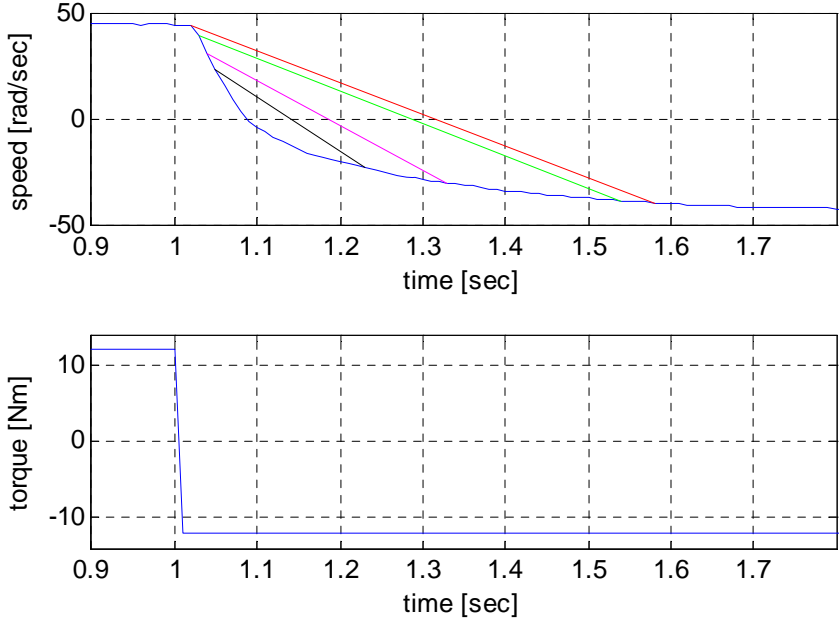
Figure 4-24: Lines for the moment of inertia calculation

Figure 4-24 shows the speed characteristic curve where the total torque changes from 12Nm to - 12Nm. The slopes of the lines decrease as the magnitude of the points increases. The slope indicates acceleration and is inversely proportional to the moment of inertia. Thus the moment of inertia increases as the pair of points move farther from the point with zero velocity (See Figure 4-25).
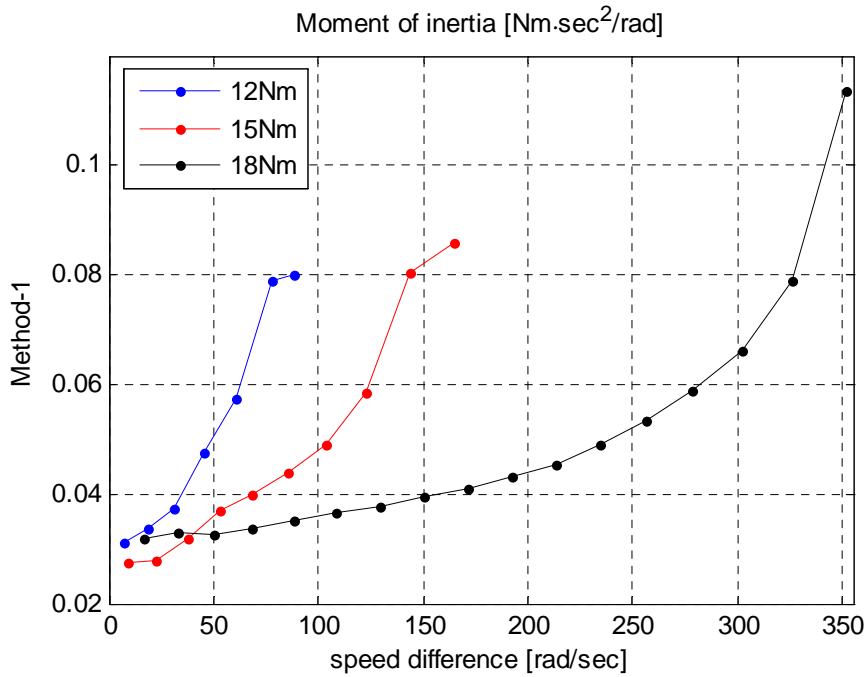
Figure 4-25: Moment of inertia over speed difference

The moment of inertia is obtained with several experiments and summarized in Table 4-4.

[Nmsec2/rad]	mean	min	Max
Total test rig	0.0493	0.0275 (-44.2%)	0.1135 (+130.1%)

Table 4-4: Moment of inertia with method-1 without friction estimation (difference from mean)

Proposed method-2

In Figure 4-24, the magnitude of the velocity decreases quickly to zero but increases slowly to a constant value. The reason is that friction helps velocity decrease and obstructs velocity increment. Choosing two points which are an equal distance apart from a time of zero velocity can be a good alternative to the previous method. The equation of moment of inertia is:

$$I = \frac{t_2 - t_1}{\Omega(t_2) - \Omega(t_1)} \cdot (T(\Omega(t_2)) - T(\Omega(t_1))) \quad , \quad \frac{t_1 + t_2}{2} = t_0$$

The speed graph passes zero at 1.09 seconds in Figure 4-26. The black line in the figure connects the point at 1.09-0.04 seconds and 1.09+0.04 seconds. The moment of inertia with this method is listed in Table 4-5. The deviation of moment of inertia with this method is much smaller than with method-1 (see Figure 4-27).
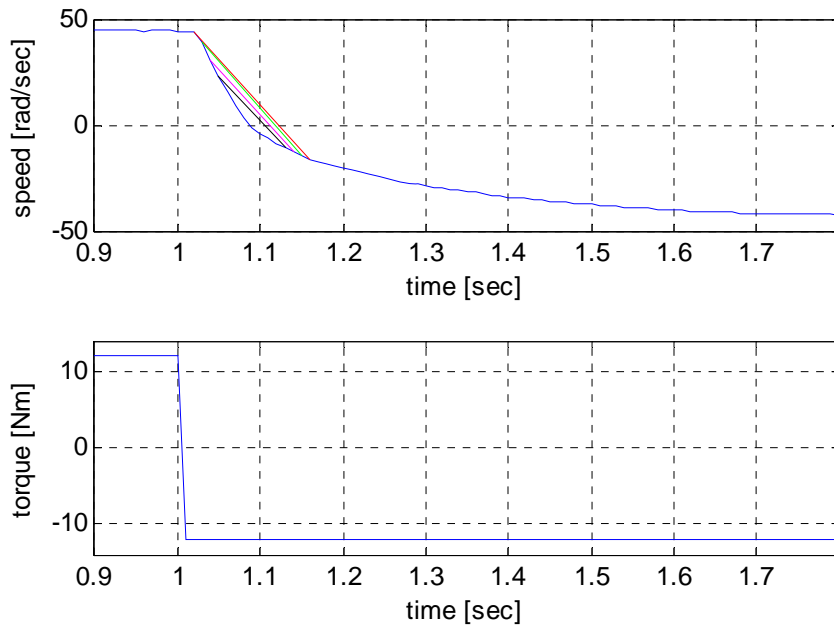
Figure 4-26: Lines for moment of inertia calculation

Moment of inertia [Nm·sec²/rad]
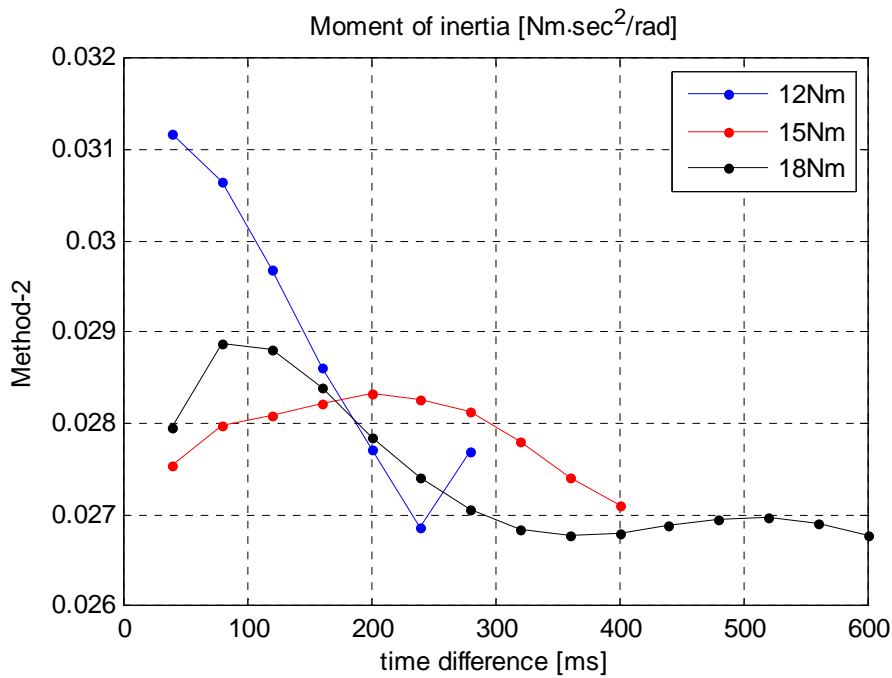
Figure 4-27: Moment of inertia over speed difference

[Nmsec2/rad]	mean	min	Max
Total test rig	0.0278	0.0263 (-5.4%)	0.0312 (+12.1%)

Table 4-5: Moment of inertia with method-2 without friction estimation (difference from mean)

Proposed method-3

In a constant speed, the speed is only dependent on friction. However, if a machine is in motion and its speed is changing, the current speed is not decided by the current friction but the friction accumulation from zero speed. The two points are chosen where areas of speed over time are the same (See Figure 4-28). The moment of inertia is determined as:

$$I = \frac{t_2 - t_1}{\Omega(t_2) - \Omega(t_1)} \cdot \left(T(\Omega(t_2)) - T(\Omega(t_1)) \right) \quad , \quad \int_{t_1}^{t_0} \Omega(t)dt = -\int_{t_0}^{t_2} \Omega(t)dt$$

The moment of inertia is drawn and written in Figure 4-29 and Table 4-6.
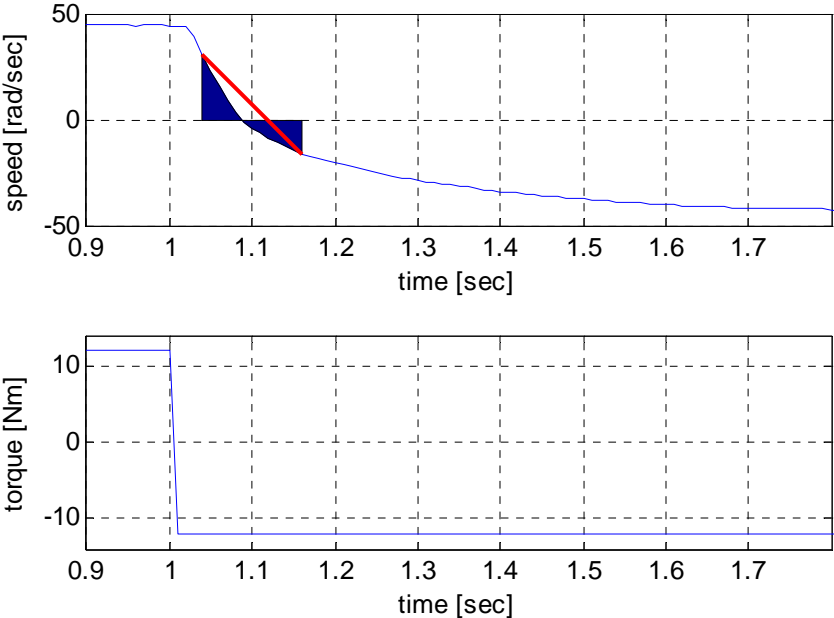
Figure 4-28: Lines for moment of inertia calculation
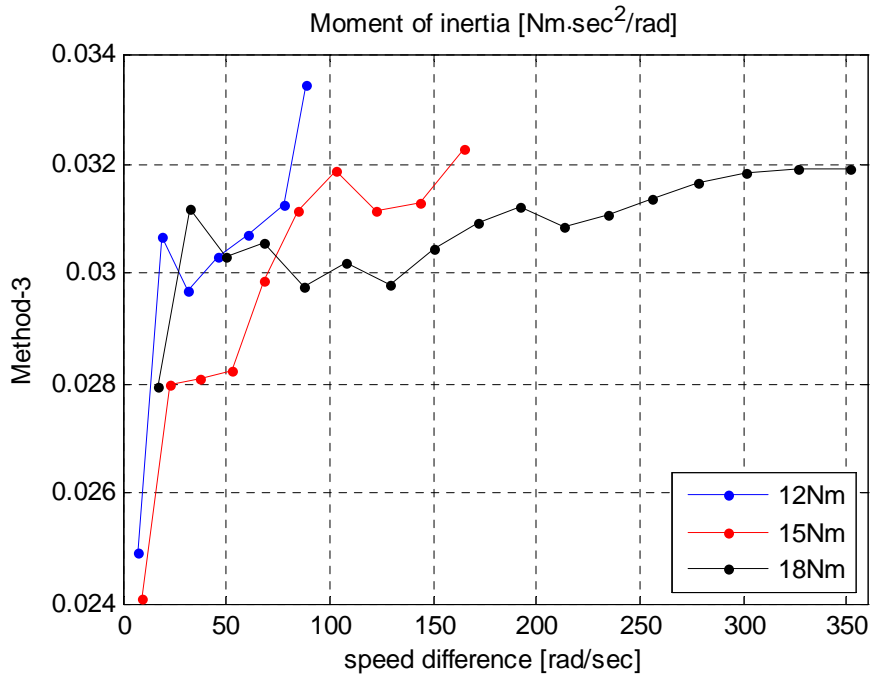
Figure 4-29: Moment of inertia over speed difference

[Nmsec2/rad]	mean	min	Max
Total test rig	0.0303	0.0241 (-20.5%)	0.0334 (+10.4%)

Table 4-6: Moment of inertia with method-3 without friction estimation (difference from mean)

Proposed method-4

As the friction changes at different temperatures in the gearbox but the temperature is hard to measure, moment of inertia varies at different temperatures. If the torque changes when the speed is constant, the difference between current and former torque is used for acceleration. At the instant of torque change, magnitude of the acceleration soars and is reduced to zero (see Figure 4-30).

The moment of inertia with this method is:

$$J = \frac{T_2 - T_1}{\alpha_{peak}}$$

where J is moment of inertia, T_2 is current torque, T_1 is former torque, and α_{peak} is acceleration on the peak.
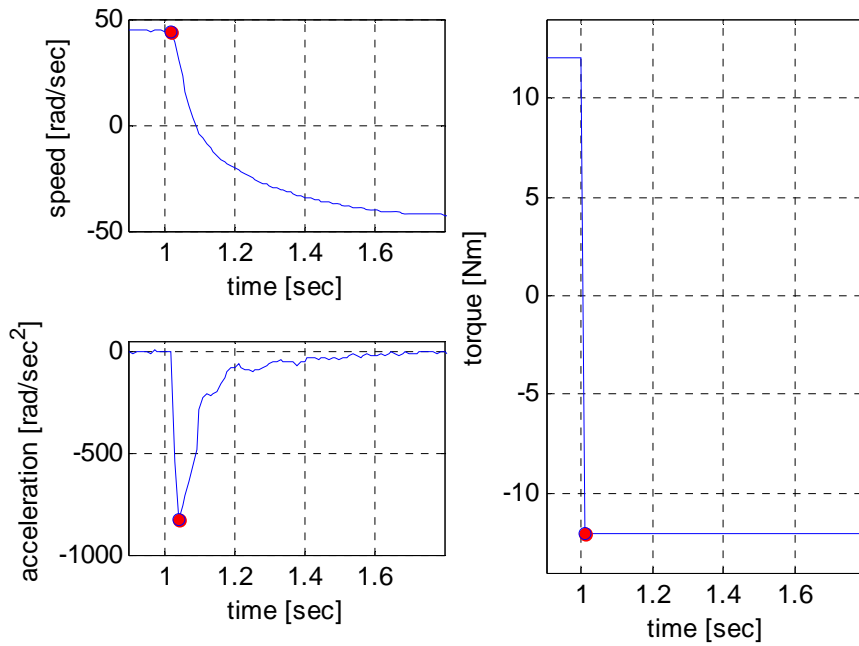
Figure 4-30: Lines for moment of inertia calculation

[Nmsec2/rad]	mean	min	Max
Total test rig	0.0286	0.0281 (-1.5%)	0.0288 (+0.9%)

Table 4-7: Moment of inertia with method-4 without friction estimation (difference from mean)

Comparison of the five methods by means of simulations in Simulink

Five methods (one current method and four proposed methods) are presented to measure moment of inertia. The best method to determine moment of inertia can be decided by simulations. Three kinds of simulations are performed to determine moment of inertia:

- Moment of inertia and viscous friction are modeled.
- Moment of inertia, viscous and Coulomb friction are modeled.
- Moment of inertia, viscous and Coulomb friction and viscous friction change are modeled.

The Simulink model for the comparison is shown in Figure 4-31. Since viscous friction change is difficult to measure in the test rig, the scope is designed to observe only Coulomb and viscous friction. Figure 4-32 shows torque, speed and friction graphs where Coulomb and viscous friction and viscous friction change are considered. The moment of inertia in the simulation is 1.
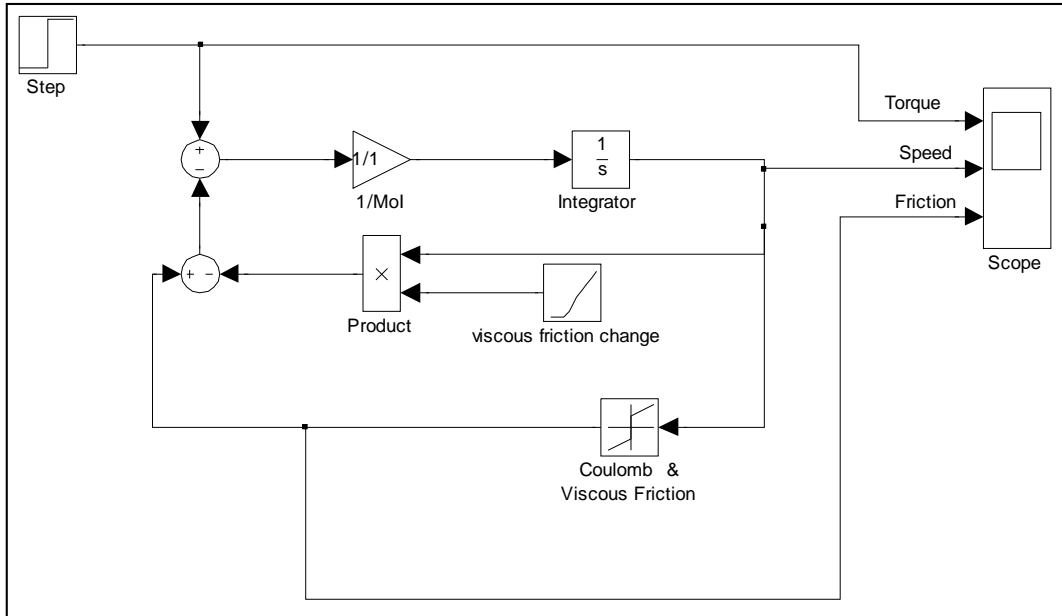
Figure 4-31: Simulink-model to determine moment of inertia
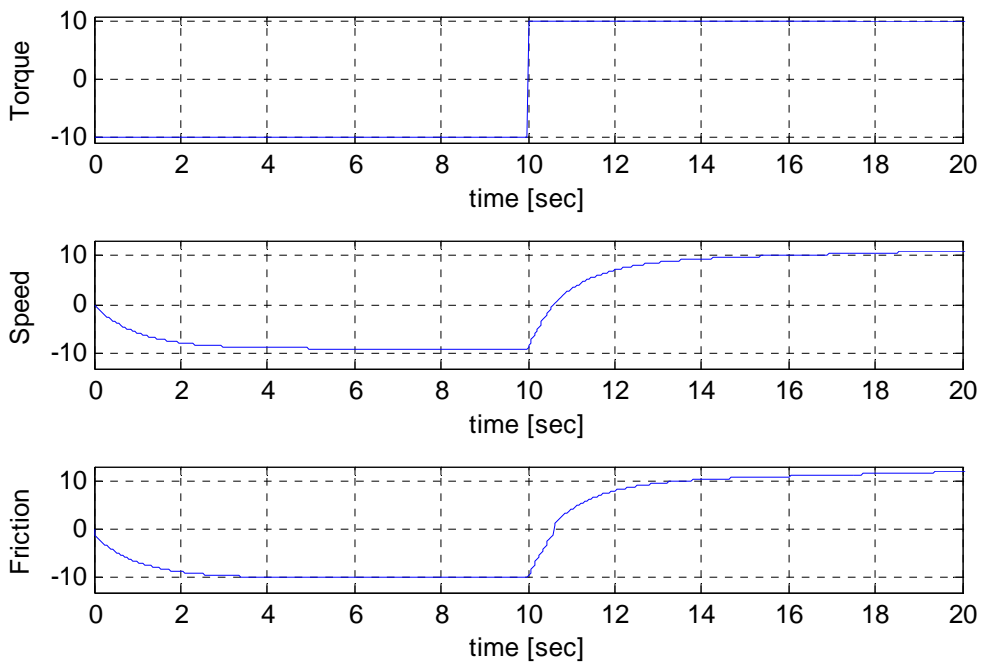
Figure 4-32: Torque, speed and friction in the simulation to determine moment of inertia

Figure 4-33, Figure 4-34 and Figure 4-35 show moment of inertia out of the three simulations. In the event that only viscous friction is modeled, current method, method-3, and method-4 draw satisfactory value. As Coulomb friction is added, values by current method and method-3 scatter. Viscous friction change causes current method to no longer be valid. The value for current method goes to negative. Method-4 in all cases possesses a very close value to the given moment of inertia. Its maximum tolerance of moment of inertia is 0.5%.

Moment of inertia [Nm*sec^2/rad]
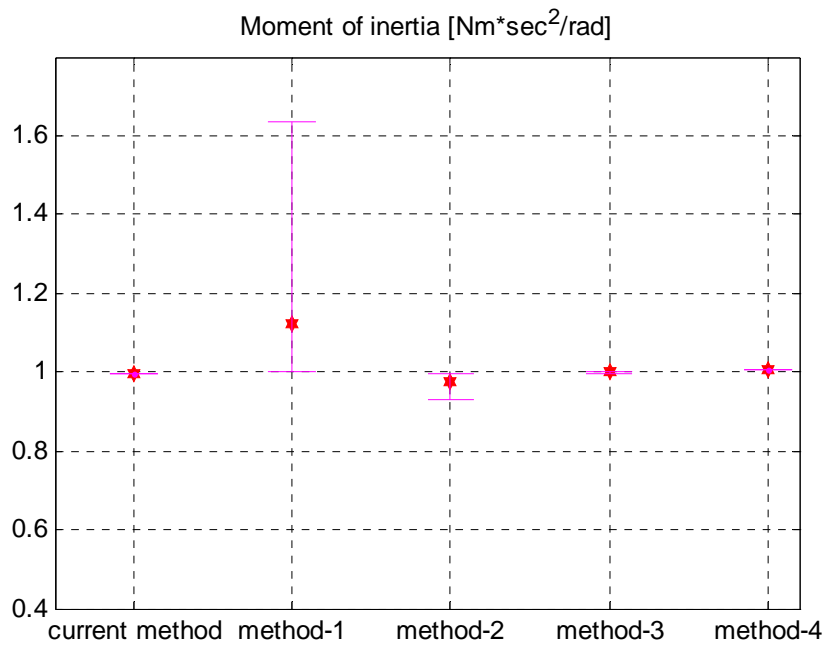
Figure 4-33: moment of inertia from simulation with viscous friction

Moment of inertia [Nm*sec^2/rad]
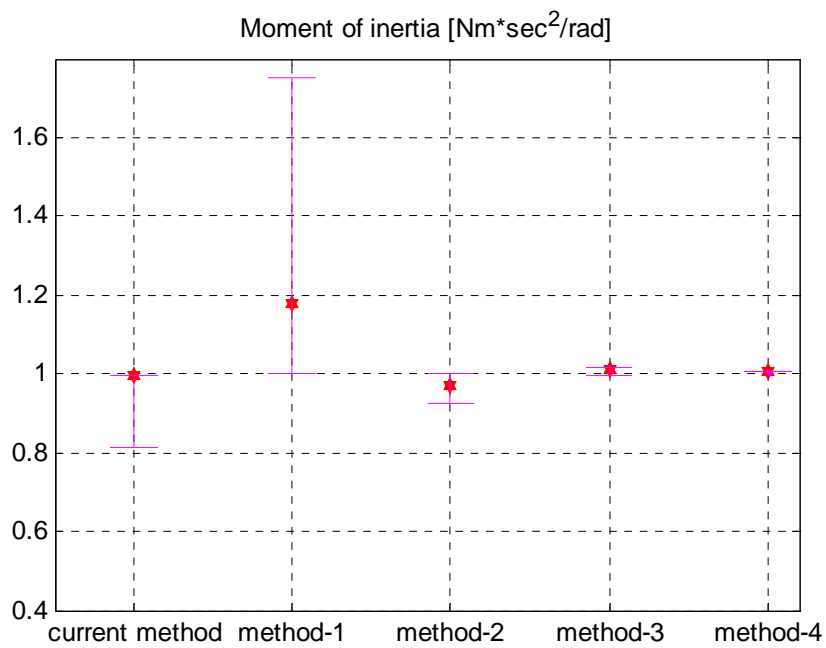
Figure 4-34: moment of inertia from simulation with viscous and Coulomb friction
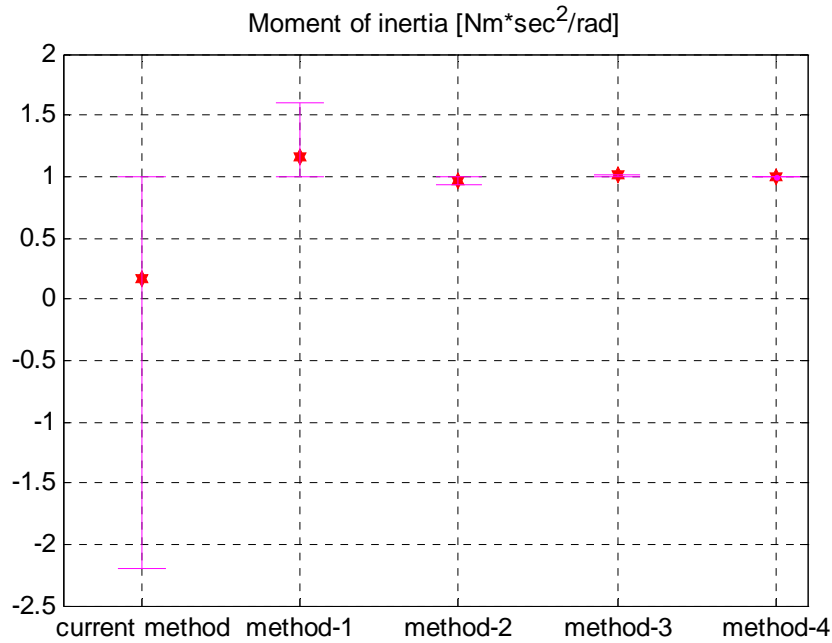
Figure 4-35: moment of inertia from simulation with viscous, Coulomb friction and viscous friction change

Despite method-4 inducing the most correct value, other methods are not useless and can be used as references. Figure 4-36 shows the moment of inertia with current and three methods. If the speed difference is small, moment of inertia with method-1 is close to the given value. The moment of inertia with method-2 at a small time difference is near 1. Similar to method-1, method-3 has the correct value at a low speed difference. The moment of inertia by current method can be used only near the point where torque changes.
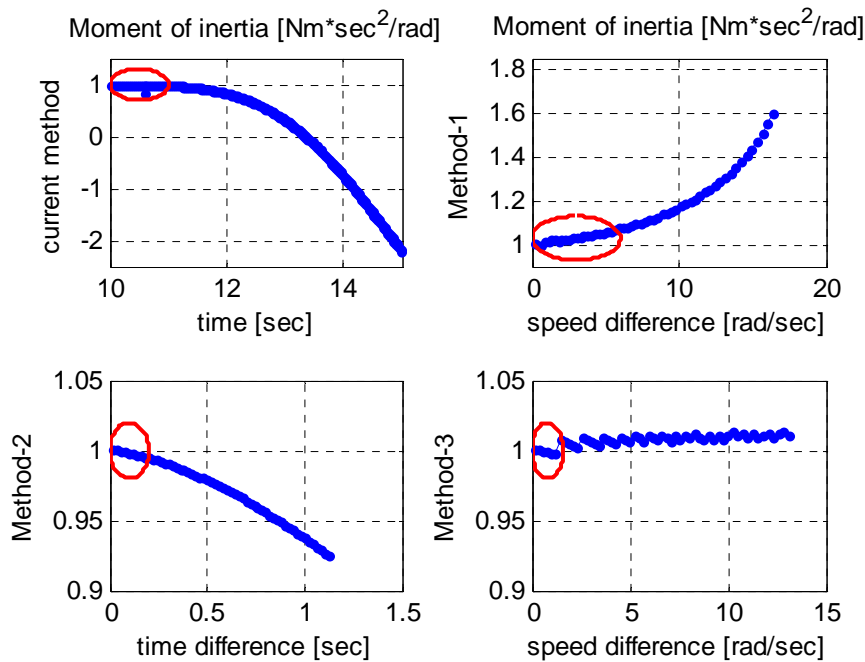
Figure 4-36: moment of inertia

Summary – moment of inertia

Current method induces a large deviation, making it unreliable. Method-1 and 2 are relatively easy to use. Method-3 is physically more precise than the first two methods. Method-4 is the best way to determine moment of inertia because it minimizes the effect of friction on determining moment of inertia. The moment of inertia with the six methods is listed together in Figure 4-37. In the figure, method-4 has the least deviation.

Moment of inertia [Nm*sec^2/rad]
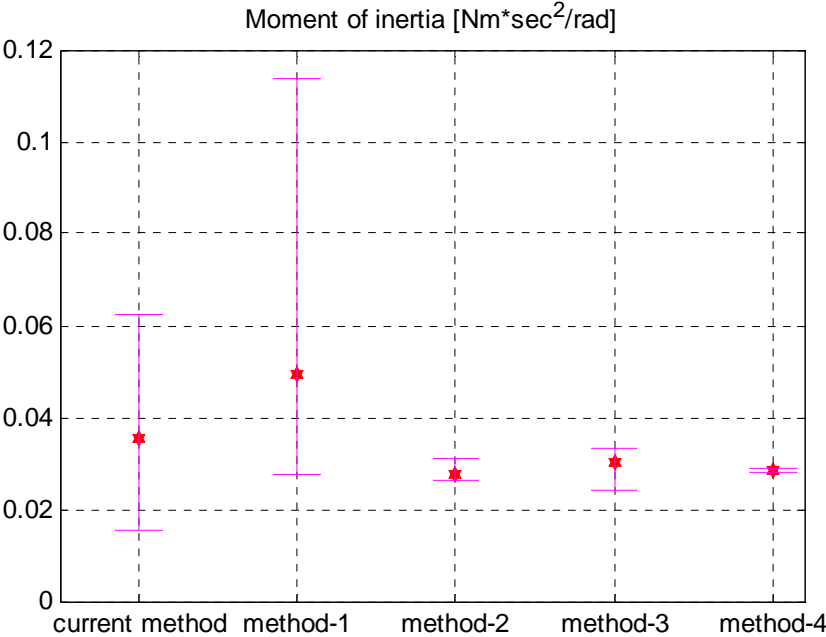
Figure 4-37: summary – moment of inertia

4.3.3. Parameters of each motor set

Stiffness coefficient, damping coefficient and moment of inertia are the essential mechanical parameters in each motor set. In designing a controller, the most important factor is the natural frequency, which is decided by the three parameters.

There are two ways to obtain the parameters. In both methods, natural frequency remains the same.

The first way is:

1. Stiffness (K)determination by measurement
2. Logarithmic decrement (δ) and damping ratio (ζ) from position and torque
3. Damped natural frequency (f_d) from position and torque measurement

4. Undamped natural frequency (f_n) by means of damped natural frequency (f_d) and damping ratio (ζ)
5. Moment of inertia (J) from stiffness coefficient (K) and undamped natural frequency (f_n)
6. Damping coefficient (c) from damping ratio (ζ), undamped natural frequency (f_n) and moment of inertia (J)

The other way is:

1. Moment of inertia (J)determination by measurement
2. Logarithmic decrement (δ) and damping ratio (ζ) from position and torque
3. Damped natural frequency (f_d) from position and torque measurement
4. Undamped natural frequency (f_n) by means of damped natural frequency (f_d) and damping ratio (ζ)
5. Damping coefficient (c) from damping ratio (ζ), undamped natural frequency (f_n) and moment of inertia (J)
6. Stiffness (K) from moment of inertia (J) and undamped natural frequency (f_n)

With the first method, stiffness is obtained directly from measurement. However, friction interferes with movement in a stiffness test. In particular, sliding friction hinders measurement because it increases as the counter tension increases. Ways to compensate for friction in the stiffness test have not been developed. Thus, stiffness cannot be measured correctly.

The second method is chosen to get the parameters. In the previous section, several methods are suggested to compensate for friction while the moment of inertia is determined.

Moment of inertia

In the second method, the moment of inertia of the motor and clutch is measured because the connecting point of the clutch and shaft is the main part of stiffness. The material of the connecting point is rubber, thus it deflects much more than other parts. The next important part of stiffness is the shaft. Whereas M1 and M2 equip clutches, M3 and M4 connect motors directly to shafts (see Figure 4-10). The moment of inertia written on the motor is used for M3 and M4 (see Figure 4-39).

In section 4.3.2, method-4 is chosen as the best and other methods are correct in a restricted region. Unlike the acceleration graph of the whole test rig in Figure 4-22, the acceleration with a motor and clutch vibrates greatly (see Figure 4-38). Thus, method-4 is not appropriate in this case. The next best methods are method-2 as seen in Figure 4-37. Method-2 is used to determine the moment of inertia of a motor and clutch which is listed in Table 4-8. Since clutches are equipped in M1 and M2, the moment of inertia of M1&M2 is bigger than that of M3&M4.
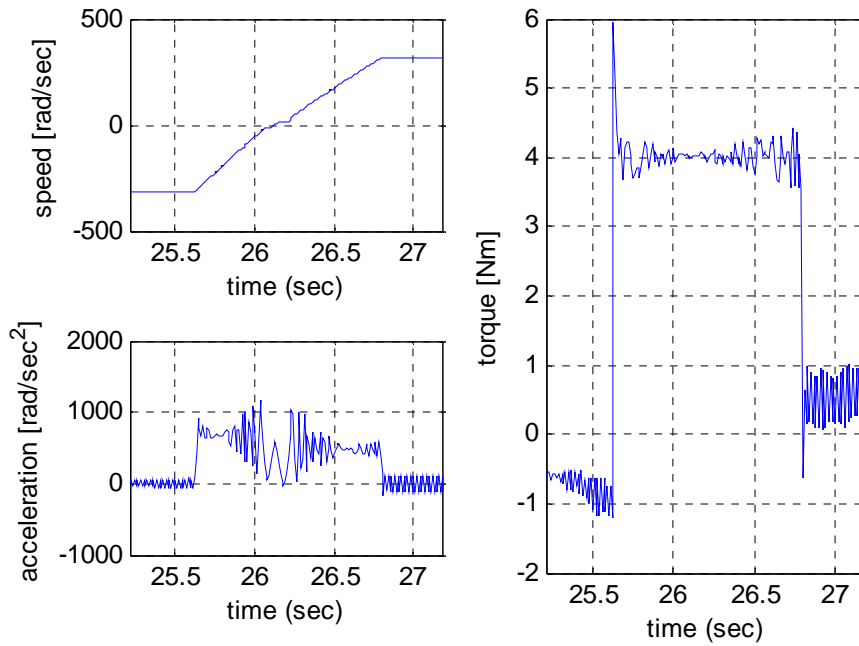
Figure 4-38: Speed, acceleration and torque of M2
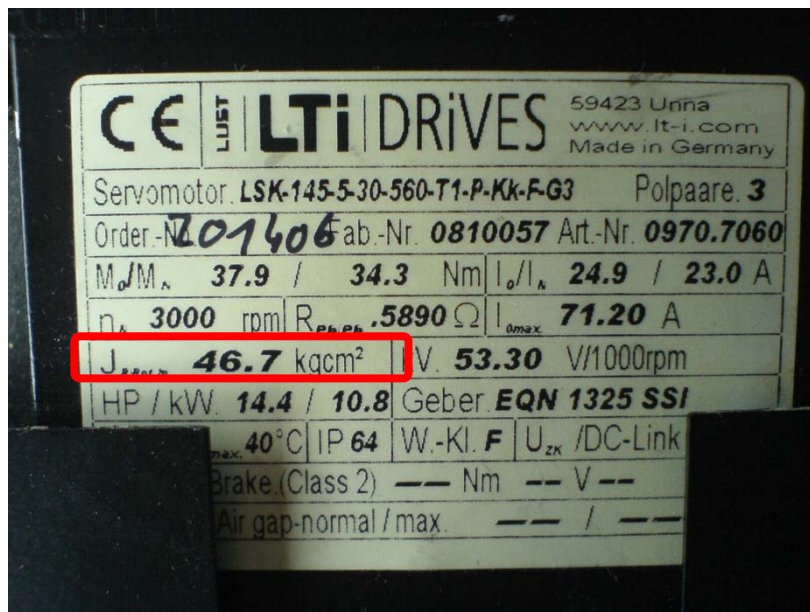
Figure 4-39: Moment of inertia of a motor

Motor set	Moment of inertia (J) [Nm·sec^2/rad]		
	mean	min	max
M1 & M2	0.00649	0.00593	0.00715
M3 & M4	0.00467	0.00467	0.00467

Table 4-8: Moment of inertia of M1&M2 and M3&M4

The moment of inertia of the ring part is calculated by using Table 4-7 and Table 4-8. Moment of inertia of the ring contains only the uncertainty of the whole test rig.

	Moment of inertia (J_{ring}) [Nm·sec²/rad]		
	mean	min	max
Ring	0.0063	0.0058	0.0065

Table 4-9: Moment of inertia of ring

Natural frequency

Logarithmic decrement and damping ratio are gained from the magnitude of peaks in the position graph. (See Figure 4-40)
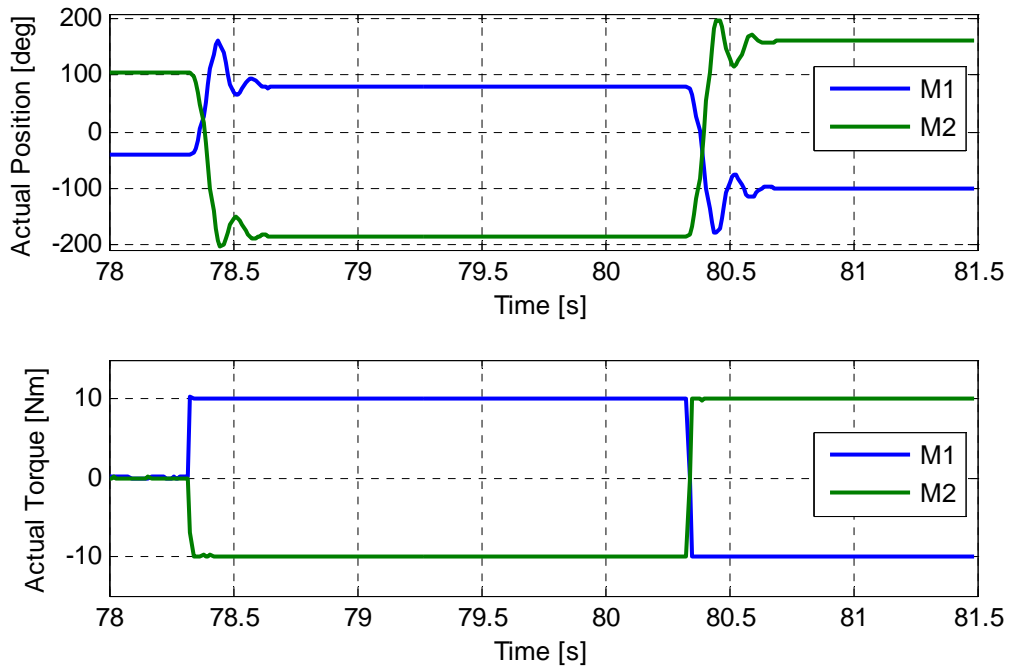
Figure 4-40: position and torque for damping measurement

The logarithmic decrement is defined:

$$\delta = \ln\left(\frac{x_1}{x_2}\right)$$

where x_1 and x_2 are the magnitudes of the 1st and 2nd peaks.

Damping ratio, ζ , is gained from the logarithmic decrement as:

$$\zeta = \frac{\delta}{\sqrt{4\pi^2 + \delta^2}}$$

The damping ratio in Table 4-10 is less than 1, thus the system is underdamped. It can be noticed also in Figure 4-40.

Damped natural frequency is found from the duration between the first and second peaks. The values are listed in Table 4-11.

Motor set	Damping ratio (ζ) [.]		
	mean	min	max
M1 & M2	0.25	0.23	0.33
M3 & M4	0.24	0.22	0.31

Table 4-10: damping ratio of M1&M2 and M3&M4

Motor set	Damped natural frequency (f_d) [Hz]		
	mean	min	max
M1 & M2	8.03	7.14	10.10
M3 & M4	10.39	9.55	11.11

Table 4-11: damped natural frequency of M1&M2 and M3&M4

Undamped natural frequency (f_n) is calculated with the help of the damping ratio (ζ):

$$f_n = \frac{f_d}{\sqrt{1 - \zeta^2}}$$

where f_d is the damped natural frequency in Hz.

Motor set	Undamped natural frequency (f_n) [Hz]		
	mean	min	max
M1 & M2	8.31	7.39	10.45
M3 & M4	10.71	9.84	11.45

Table 4-12: undamped natural frequency of M1&M2 and M3&M4

Damping coefficient

The critical damping coefficient, c_{cr}, is defined as:

$$c_{cr} = 2 \cdot J \cdot \omega_n = 2 \cdot J \cdot f_n \cdot 2\pi$$

where J is the moment of inertia of M1&M2 and M3&M4. ω_n and f_n are the undamped natural frequency in radian and Hz.

The damping coefficient is calculated by means of the critical damping coefficient (c_{cr}) and damping ratio (ζ):

$$c = c_{cr} \cdot \zeta$$

The damping coefficient is listed in Table 4-13. Because M1&M2 have rubber in the connecting point of the clutch and shaft, the damping coefficients of M1&M2 are bigger than that of M3&M4. M. Abdulhadi [28] presented damping force of rubber has linear relation with the rate of displacement.

Motor set	Damping coefficient (c) [Nm·sec/rad]		
	mean	min	max
M1 & M2	0.17	0.15	0.22
M3 & M4	0.15	0.14	0.19

Table 4-13: damping coefficient of M1&M2 and M3&M4

Stiffness coefficient

Since harmonic vibration occurs due to stiffness and moment of inertia, the stiffness, K, is obtained as:

$$K_i = J_i \cdot (2\pi \cdot f_n)^2 \text{ , i=1, 2, 3, 4}$$

The stiffness coefficient is seen in Table 4-14. The rubber in M1&M2 is soft, thus M1&M2 have a smaller stiffness coefficient than that of M3&M4.

Motor set	Stiffness coefficient (K) [Nm/rad]		
	mean	min	max
M1 & M2	17.69	13.98	27.95
M3 & M4	21.13	17.85	27.95

Table 4-14: stiffness coefficient of M1&M2 and M3&M4

4.4. Simulation vs. Experiment

A simulation must fully represent the dynamics of the real system. Figure 4-41 and Figure 4-42 show the motor position and speed of the step response in experiment and simulation. The brief shapes of both tests are the same, but vibration does not disappear in the experiment speed graph. The

difference is not based on the damping coefficient. If the damping coefficient was incorrect, the vibration would have had to vanish after 536 seconds in the figure. However, the vibration amplitudes are not diminished in a steady state. The vibration in the steady state occurs due to differing friction. Rough surfaces, differing distribution of lubricating oil and small errors in the design of gear teeth may cause differing friction. Such differing friction stimulates vibration in a steady state. A small amount of vibration in the speed graph can be disregarded because it has little effect on the position graph. Positions and speeds in the figures are the absolute values.
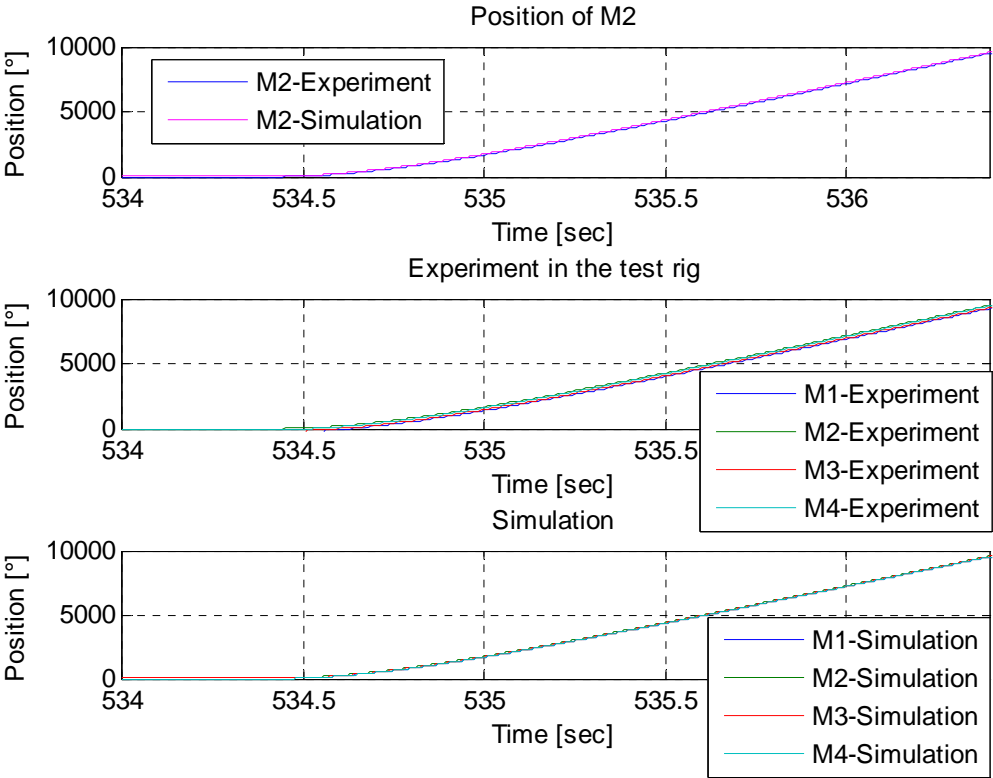
Figure 4-41: Position of four motors in experiment and simulation without controller
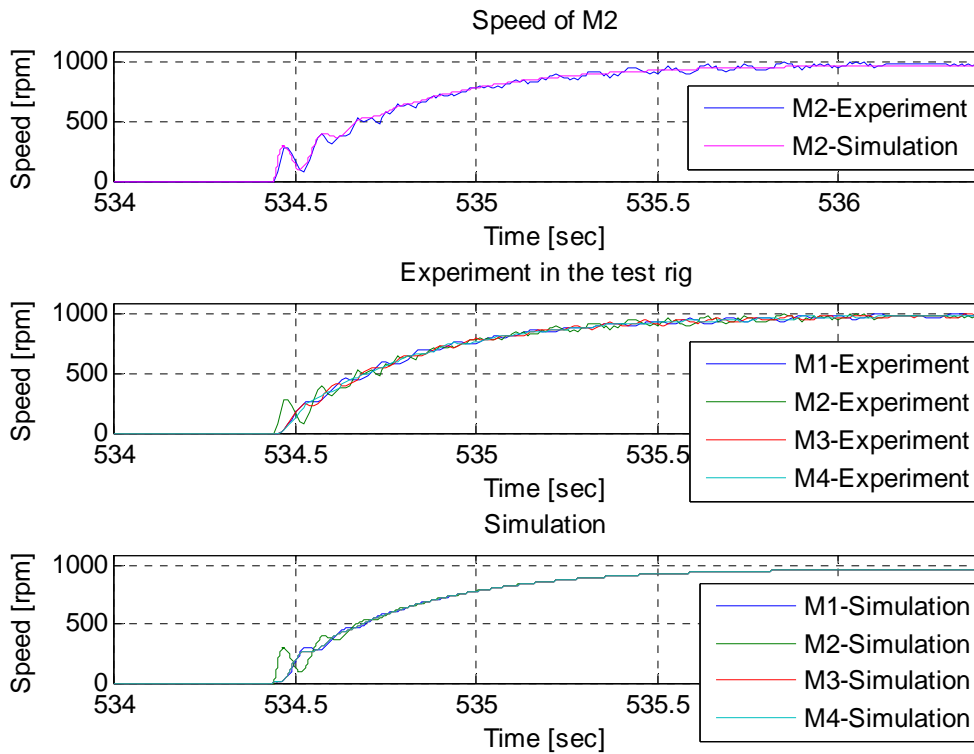
Figure 4-42: Speed of four motors in experiment and simulation without controller

As the input is sinusoidal-shaped, the position (Figure 4-43) and speed (Figure 4-44) in the simulation are nearly the same as in the experiment. The position graph is sinusoidal-shaped, but the speed graph is no longer smooth when speed passes zero. Such a non-differentiable point occurs due to the nonlinearity of Coulomb friction. Without Coulomb friction, the shape of the speed graph would be a cosine curve.
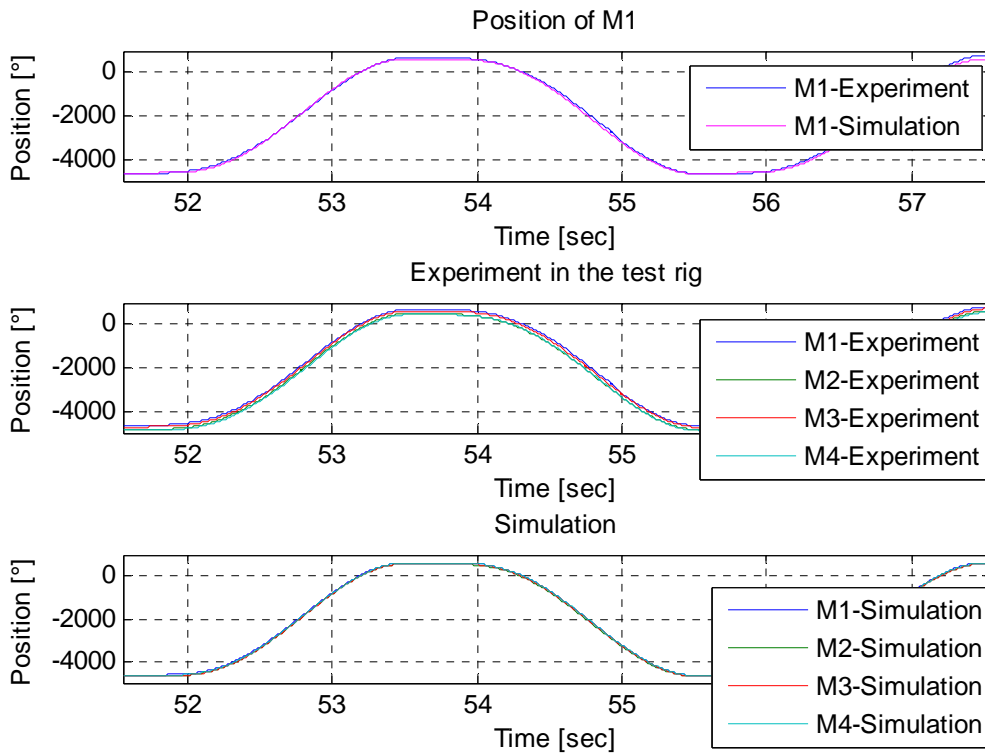
Figure 4-43: Position of four motors in experiment and simulation without controller
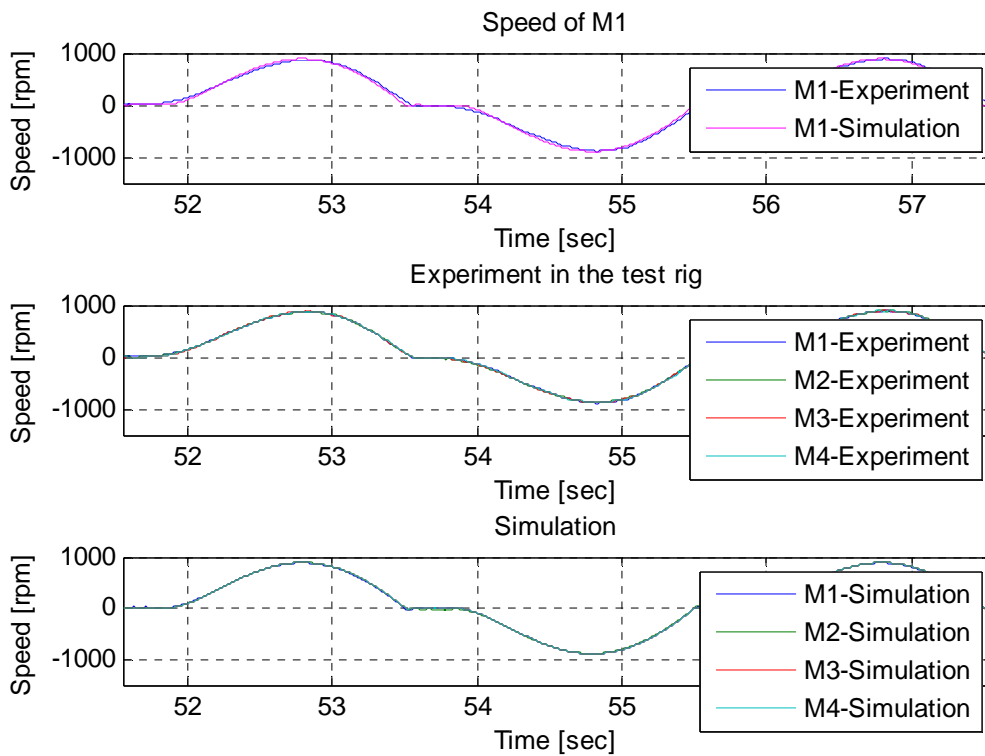
Figure 4-44: Speed of four motors in experiment and simulation without controller

Whereas the motors are driven directly in the figures above, Figure 4-45 - Figure 4-48 show the graphs where the test rig follows the reference positions. A PD controller in the section 6.1 is used for the following figures. The step response is seen in Figure 4-45. In the transient state, a small difference is found which is affordable as the model represents the test rig.
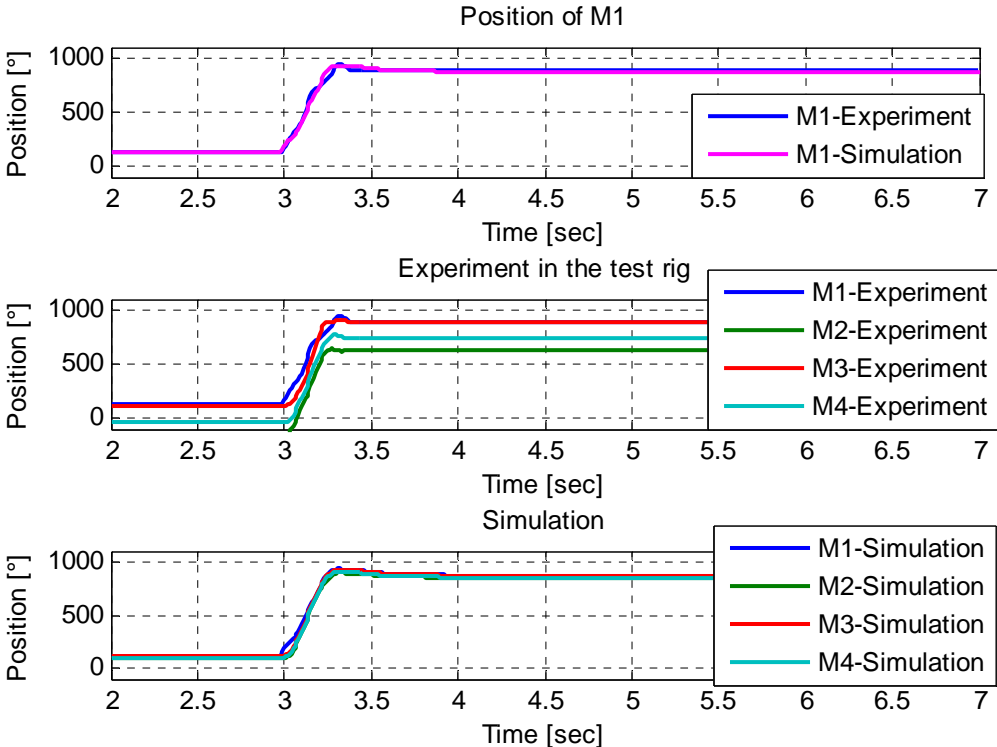
Figure 4-45: Position of four motors in experiment and simulation with controller

In case the reference position is sinusoidal form, the position and speed are compared in Figure 4-46 and Figure 4-47. Unlike the speed graph without controller in Figure 4-44, the speed graph in Figure 4-47 is complicated. The model represents the test rig enough well.
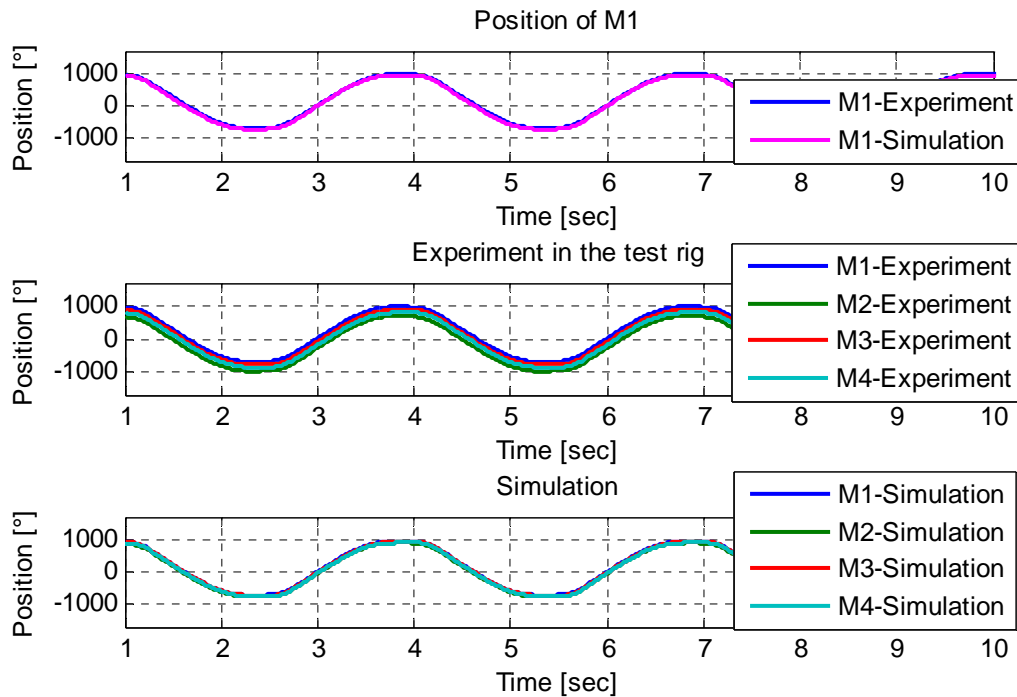
Figure 4-46: Position of four motors in experiment and simulation with controller
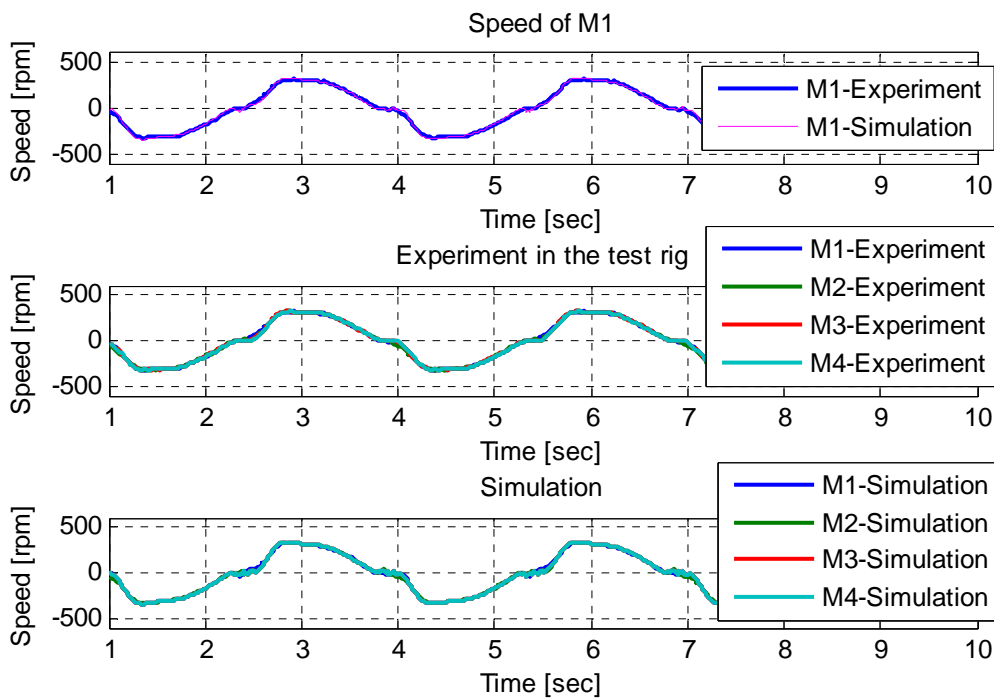
Figure 4-47: Speed of four motors in experiment and simulation with controller

A reference pitch angle is set as an individual pitch controller is used in a turbulent wind condition. Like the upper figures, experiment and simulation graphs are very similar (see Figure 4-48).
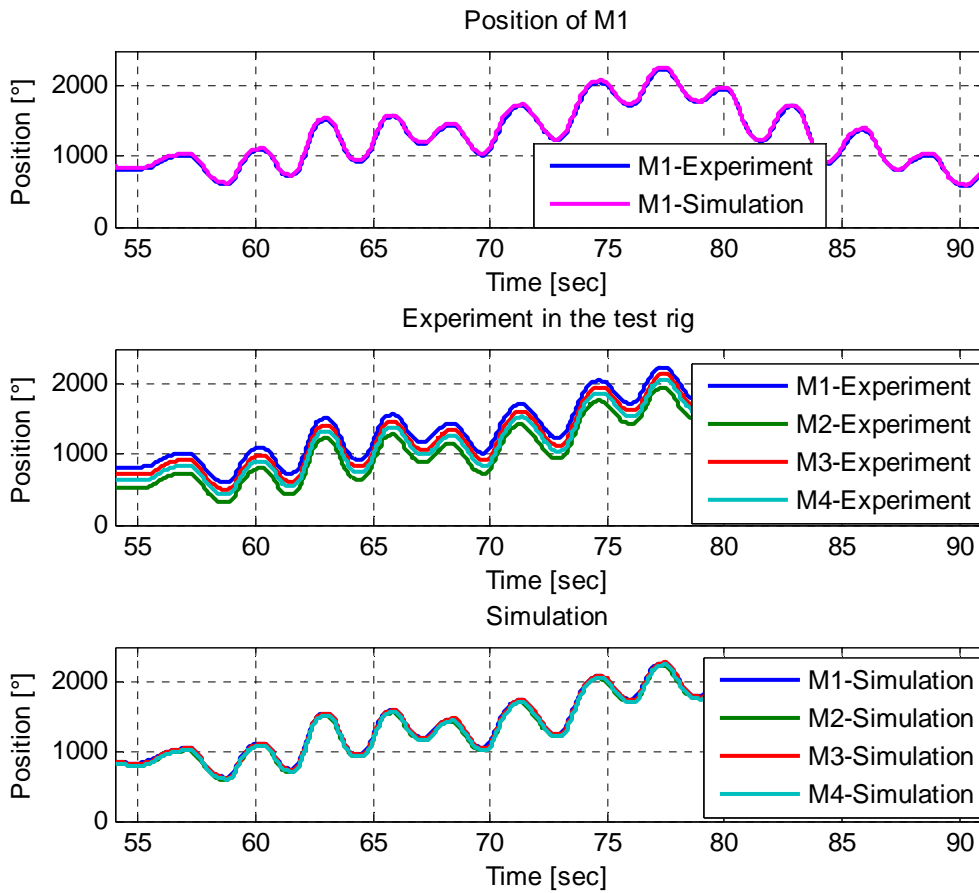
Figure 4-48: Position of four motors in experiment and simulation with reference input

4.5.Position calculator

In wind turbines, a position sensor is located on each blade root (see left graph in Figure 4-49). Pitch angle is measured by the position sensor and is fed back to the pitch angle controller. However, the test rig does not equip such a sensor on the ring (see right graph in Figure 4-49). The ring position has to be estimated by using the four motor positions.
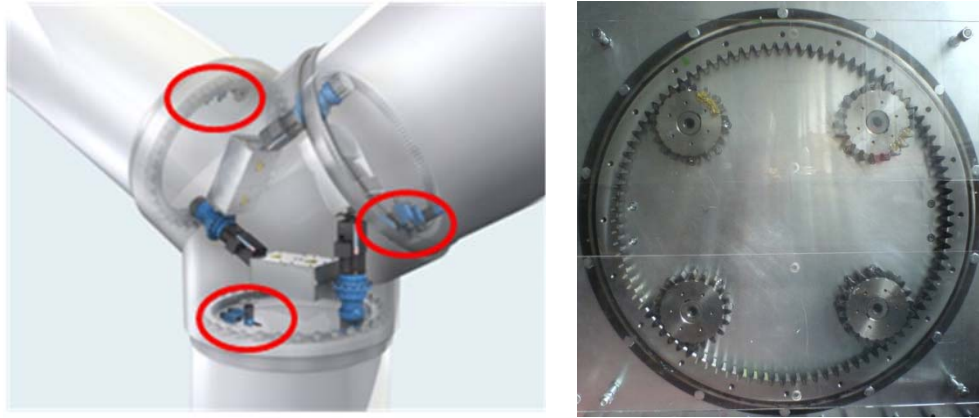
Figure 4-49: position sensor in a wind turbine and test rig

A simple way to guess the ring position is using the average value of either two pitch motor positions or four motor positions.

A better way is to estimate the ring position with an observer. The observer compensates for errors of ring position by means of motor positions, speeds and inputs. When gear play is not compensated for, gear teeth are not attached when rotational direction changes. The ring is not connected on the moment, thus both the moment of inertia and especially stiffness are reduced in a short time. The error of ring position can become very large and it is hard for the observer to correct the error. Therefore, the observer can only be used when gear play is compensated for.

As seen in (4-4) of section 4.2, the test rig is modeled as:

$$\dot{x} = Ax + Bu$$
$$y = Cx + Du$$

with

$$x = \left[\theta_1, \theta_2, \theta_3, \theta_4, \theta_r, \dot{\theta}_1, \dot{\theta}_2, \dot{\theta}_3, \dot{\theta}_4, \dot{\theta}_r\right]^T$$

$$A = \begin{bmatrix}
0 & 0 & 0 & 0 & 0 & 1 & 0 & 0 & 0 & 0 \\
0 & 0 & 0 & 0 & 0 & 0 & 1 & 0 & 0 & 0 \\
0 & 0 & 0 & 0 & 0 & 0 & 0 & 1 & 0 & 0 \\
0 & 0 & 0 & 0 & 0 & 0 & 0 & 0 & 1 & 0 \\
0 & 0 & 0 & 0 & 0 & 0 & 0 & 0 & 0 & 1 \\
-\dfrac{k_1}{I_1} & 0 & 0 & 0 & \dfrac{k_1}{I_1} & -\dfrac{d_1}{I_1} & 0 & 0 & 0 & \dfrac{d_1}{I_1} \\
0 & -\dfrac{k_2}{I_2} & 0 & 0 & \dfrac{k_2}{I_2} & 0 & -\dfrac{d_2}{I_2} & 0 & 0 & \dfrac{d_2}{I_2} \\
0 & 0 & -\dfrac{k_3}{I_3} & 0 & \dfrac{k_3}{I_3} & 0 & 0 & -\dfrac{d_3}{I_3} & 0 & \dfrac{d_3}{I_3} \\
0 & 0 & 0 & -\dfrac{k_4}{I_4} & \dfrac{k_4}{I_4} & 0 & 0 & 0 & -\dfrac{d_4}{I_4} & \dfrac{d_4}{I_4} \\
\dfrac{k_1}{I_r} & \dfrac{k_2}{I_r} & \dfrac{k_3}{I_r} & \dfrac{k_4}{I_r} & -\dfrac{\sum\limits_{i=1}^{4} k_i}{I_r} & \dfrac{d_1}{I_r} & \dfrac{d_2}{I_r} & \dfrac{d_3}{I_r} & \dfrac{d_4}{I_r} & -\dfrac{r + \sum\limits_{i=1}^{4} d_i}{I_r}
\end{bmatrix}$$

(4-8)

$$B = \left[0,0,0,0,\frac{1}{I_1},0,0,0,0\right]^T$$

$$C = \left[0,0,0,0,\frac{1}{\ddot{u}},0,0,0,0\right]$$

$$D = 0$$

where k_i, d_i, I_i are stiffness, damping and moment of inertia of the *i-th* motor set. r is viscous friction. $\ddot{u}$ is the total gear ratio of the gearbox and pinion. $\vartheta_i, \dot{\vartheta}_i$ are the position and angular speed of the *i-th* motor sets and the ring.

The output y is ring position. The controller aims to locate ring position the same as reference position. An observer contains estimation error terms to compensate. The mathematical model of the Luenberger observer is defined as:

$$\dot{\tilde{x}} = A\tilde{x} + B_{obs}u + K_e\left(C_{obs}\tilde{x} - y\right)$$

$$B_{obs} = B$$

$$C_{obs} = C$$

where $\tilde{x}$ is the estimated state and K_e is a weighting matrix to compensate for estimation error.

However, the output y is the ring position to be observed. It is a paradox to observe ring position by means of ring position. The problem can be solved by changing matrix C_{obs}. The matrix C_{obs} is changed to:

$$\dot{\tilde{x}} = A\tilde{x} + B_{obs}u + K_e\left(C_{obs}\tilde{x} - y\right)$$

$$B_{obs} = B$$

$$C_{obs} = \begin{bmatrix} 1 & 0 & 0 & 0 & 0 & 0 & 0 & 0 & 0 & 0 \\ 0 & 1 & 0 & 0 & 0 & 0 & 0 & 0 & 0 & 0 \\ 0 & 0 & 1 & 0 & 0 & 0 & 0 & 0 & 0 & 0 \\ 0 & 0 & 0 & 1 & 0 & 0 & 0 & 0 & 0 & 0 \\ 0 & 0 & 0 & 0 & 0 & 1 & 0 & 0 & 0 & 0 \\ 0 & 0 & 0 & 0 & 0 & 0 & 1 & 0 & 0 & 0 \\ 0 & 0 & 0 & 0 & 0 & 0 & 0 & 1 & 0 & 0 \\ 0 & 0 & 0 & 0 & 0 & 0 & 0 & 0 & 1 & 0 \end{bmatrix}$$

(4-9)

The outputs of the observer become the positions and speeds of the 4 motors as follows:

$$y = \begin{bmatrix} \theta_1 & \theta_2 & \theta_3 & \theta_4 & \dot{\theta}_1 & \dot{\theta}_2 & \dot{\theta}_3 & \dot{\theta}_4 \end{bmatrix}^T$$

Note that the matrix C_{obs} in (4-9) is used only for making an observer. For the design of linear controllers, the original matrix C is used. The Simulink model of the observer is illustrated in Figure 4-50.
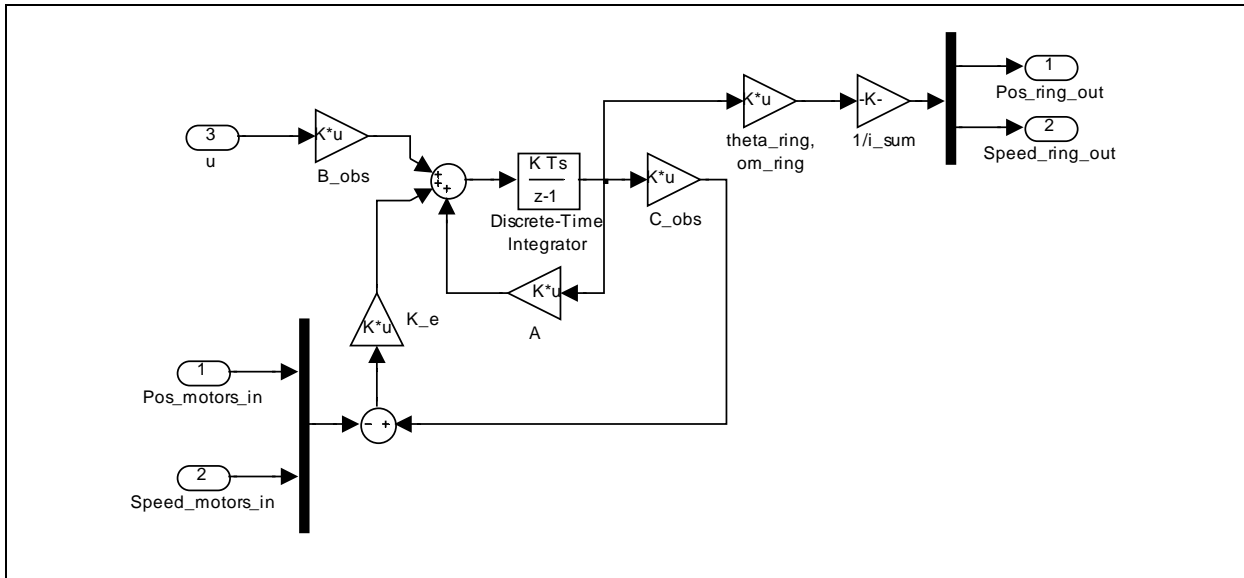
Figure 4-50: Simulink model of the observer

As the system is $\dot{x} = Ax + Bu$ and the observer is $\dot{\tilde{x}} = A\tilde{x} + B_{obs}u + K_e(C_{obs}\tilde{x} - y)$, the difference between the real state and observed state is:

$$e(t) = x(t) - \tilde{x}(t)$$

and observer error is:

$$\dot{e} = A \cdot (x - \tilde{x}) - K_e \cdot (C_{obs} \cdot \tilde{x} - C_{obs} \cdot x)$$
$$= (A + K_e \cdot C_{obs}) \cdot e$$

The matrix K_e must be chosen to make the matrix $A + K_e \cdot C_{obs}$ stable.

The observation matrix K_e is chosen as:

$$K_e = -100 \cdot \begin{bmatrix} 1 & 0 & 0 & 0 & 0 & 0 & 0 & 0 \\ 0 & 1 & 0 & 0 & 0 & 0 & 0 & 0 \\ 0 & 0 & 1 & 0 & 0 & 0 & 0 & 0 \\ 0 & 0 & 0 & 1 & 0 & 0 & 0 & 0 \\ 0 & 0 & 0 & 0 & 0 & 0 & 0 & 0 \\ 0 & 0 & 0 & 0 & 1 & 0 & 0 & 0 \\ 0 & 0 & 0 & 0 & 0 & 1 & 0 & 0 \\ 0 & 0 & 0 & 0 & 0 & 0 & 1 & 0 \\ 0 & 0 & 0 & 0 & 0 & 0 & 0 & 1 \\ 0 & 0 & 0 & 0 & 0 & 0 & 0 & 0 \end{bmatrix}$$

Eigenvalues of $A + K_e \cdot C_{obs}$ are:

$$-57.02 \pm 54.46i$$

$$-113.98 \pm 81.99i$$

$$-113.1 \pm 50.54i$$

$$-114.33 \pm 54.73i$$

$$-116.06 \pm 65.32i$$

Since all the real components of the eigenvalues are less than zero, the matrix $A + K_e \cdot C_{obs}$ is stable.

The system has only one input in (4-9). Therefore, matrix B_{obs} has 10 times 1 matrix. The test rig actually has four inputs, but two are not controllable and the other two are connected via a torque distributor. The controller can give only one reference torque. However, all four inputs can be considered in designing an observer. The B_{obs} matrices of the two observers are listed in Table 4-15. The T$_{pitch}$ in observer-1 is the same as T$_1$+T$_2$ in observer-2 because T$_{pitch}$ is divided into T$_1$ and T$_2$ via the torque distributor.

Observer-1	Observer-2
$\dot{\tilde{x}} = A\tilde{x} + B_{obs}u + K_e(C_{obs}\tilde{x} - y)$	
$B_{obs} = \begin{bmatrix} 0 \\ 0 \\ 0 \\ 0 \\ 0 \\ 1/I_1 \\ 0 \\ 0 \\ 0 \\ 0 \end{bmatrix}$, input=T$_{pitch}$	$B_{obs} = \begin{bmatrix} 0 & 0 & 0 & 0 \\ 0 & 0 & 0 & 0 \\ 0 & 0 & 0 & 0 \\ 0 & 0 & 0 & 0 \\ 0 & 0 & 0 & 0 \\ 1/I_1 & 0 & 0 & 0 \\ 0 & 1/I_2 & 0 & 0 \\ 0 & 0 & 1/I_3 & 0 \\ 0 & 0 & 0 & 1/I_4 \\ 0 & 0 & 0 & 0 \end{bmatrix}$, input=$\begin{bmatrix} T_1 \\ T_2 \\ T_3 \\ T_4 \end{bmatrix}$

$$A = \begin{bmatrix}
0 & 0 & 0 & 0 & 0 & 1 & 0 & 0 & 0 & 0 \\
0 & 0 & 0 & 0 & 0 & 0 & 1 & 0 & 0 & 0 \\
0 & 0 & 0 & 0 & 0 & 0 & 0 & 1 & 0 & 0 \\
0 & 0 & 0 & 0 & 0 & 0 & 0 & 0 & 1 & 0 \\
0 & 0 & 0 & 0 & 0 & 0 & 0 & 0 & 0 & 1 \\
-\dfrac{k_1}{I_1} & 0 & 0 & 0 & \dfrac{k_1}{I_1} & -\dfrac{d_1}{I_1} & 0 & 0 & 0 & \dfrac{d_1}{I_1} \\
0 & -\dfrac{k_2}{I_2} & 0 & 0 & \dfrac{k_2}{I_2} & 0 & -\dfrac{d_2}{I_2} & 0 & 0 & \dfrac{d_2}{I_2} \\
0 & 0 & -\dfrac{k_3}{I_3} & 0 & \dfrac{k_3}{I_3} & 0 & 0 & -\dfrac{d_3}{I_3} & 0 & \dfrac{d_3}{I_3} \\
0 & 0 & 0 & -\dfrac{k_4}{I_4} & \dfrac{k_4}{I_4} & 0 & 0 & 0 & -\dfrac{d_4}{I_4} & \dfrac{d_4}{I_4} \\
\dfrac{k_1}{I_r} & \dfrac{k_2}{I_r} & \dfrac{k_3}{I_r} & \dfrac{k_4}{I_r} & -\dfrac{\sum\limits_{i=1}^{4} k_i}{I_r} & \dfrac{d_1}{I_r} & \dfrac{d_2}{I_r} & \dfrac{d_3}{I_r} & \dfrac{d_4}{I_r} & -\dfrac{r+\sum\limits_{i=1}^{4} d_i}{I_r}
\end{bmatrix}$$

$$C_{obs} = \begin{bmatrix}
1 & 0 & 0 & 0 & 0 & 0 & 0 & 0 & 0 & 0 \\
0 & 1 & 0 & 0 & 0 & 0 & 0 & 0 & 0 & 0 \\
0 & 0 & 1 & 0 & 0 & 0 & 0 & 0 & 0 & 0 \\
0 & 0 & 0 & 1 & 0 & 0 & 0 & 0 & 0 & 0 \\
0 & 0 & 0 & 0 & 0 & 1 & 0 & 0 & 0 & 0 \\
0 & 0 & 0 & 0 & 0 & 0 & 1 & 0 & 0 & 0 \\
0 & 0 & 0 & 0 & 0 & 0 & 0 & 1 & 0 & 0 \\
0 & 0 & 0 & 0 & 0 & 0 & 0 & 0 & 1 & 0
\end{bmatrix}$$

$$K_e = -100 \cdot \begin{bmatrix}
1 & 0 & 0 & 0 & 0 & 0 & 0 & 0 \\
0 & 1 & 0 & 0 & 0 & 0 & 0 & 0 \\
0 & 0 & 1 & 0 & 0 & 0 & 0 & 0 \\
0 & 0 & 0 & 1 & 0 & 0 & 0 & 0 \\
0 & 0 & 0 & 0 & 0 & 0 & 0 & 0 \\
0 & 0 & 0 & 0 & 1 & 0 & 0 & 0 \\
0 & 0 & 0 & 0 & 0 & 1 & 0 & 0 \\
0 & 0 & 0 & 0 & 0 & 0 & 1 & 0 \\
0 & 0 & 0 & 0 & 0 & 0 & 0 & 1 \\
0 & 0 & 0 & 0 & 0 & 0 & 0 & 0
\end{bmatrix}$$

Table 4-15: Two kinds of observers

Actual ring position cannot be measured in the test rig because a position sensor is not equipped on the ring, thus performance of the position calculator has to be estimated in simulation. In the previous section, it is shown that the simulation with Simulink represents the dynamics of the test rig well. Figure 4-51 and Figure 4-52 show ring position in simulation. Ring position is estimated with an average of two pitch motors (simple), observer of one input (observer-1) and observer of four inputs (observer-2). Estimation errors of the three methods are less than 0.1°. The observers calculate the

position more accurately than average (simple). Observer-2 is a little closer to the actual position than observer-1. The estimation error of observer-2 is 0.05°.

Real wind turbines equip position sensors on the blade roots, thus position calculation is required only in the test rig. Both 0.05° and 0.1° estimation errors may be acceptable since they are not a crucial part of this research.
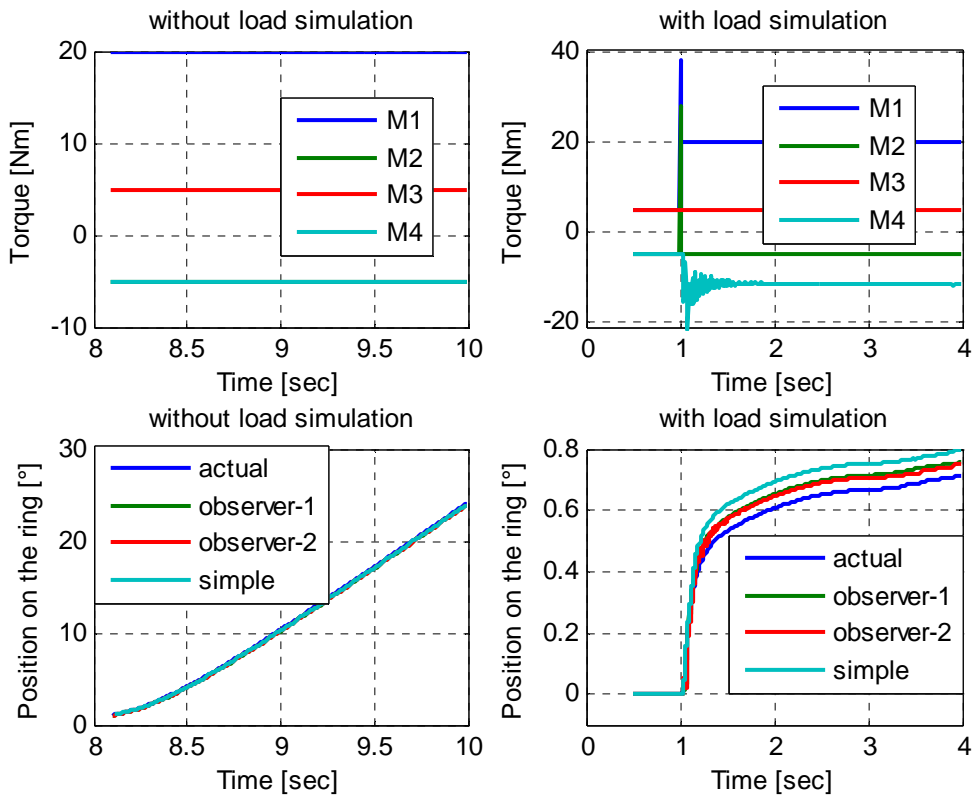
Figure 4-51: Ring position without/with observer in simulation of step input
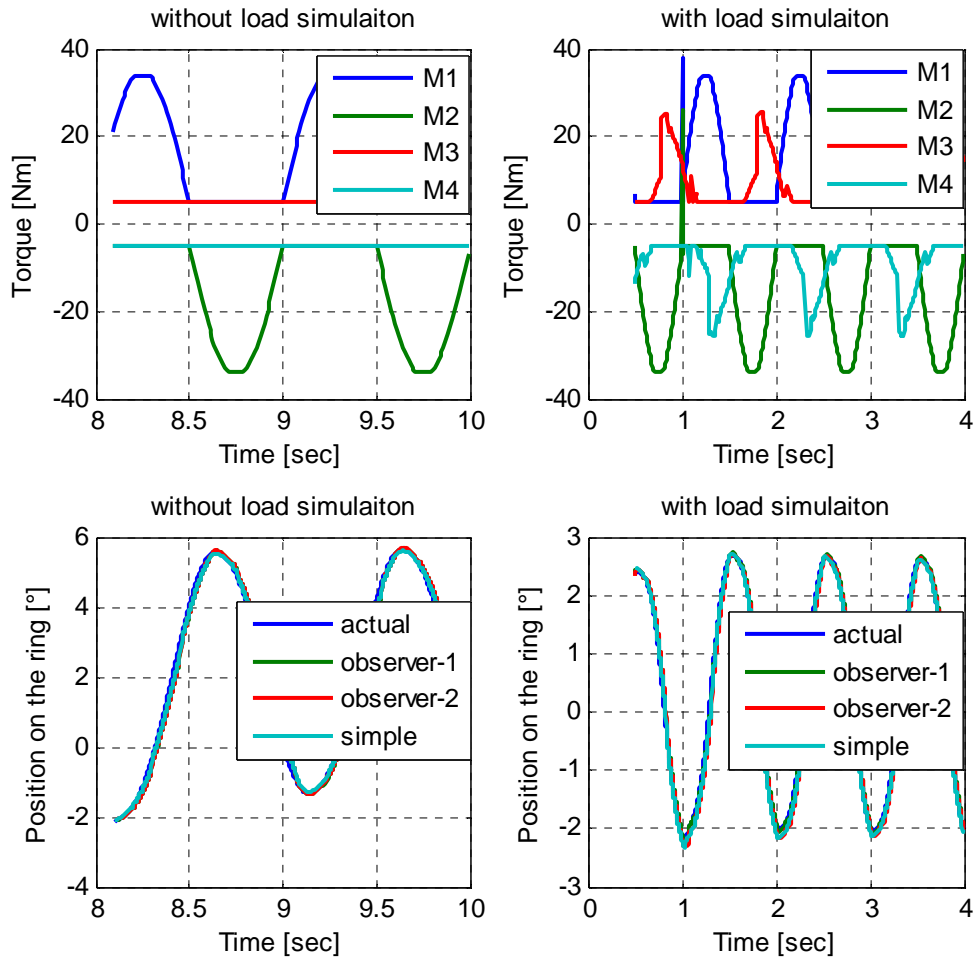
Figure 4-52: Ring position without/with observer in simulation of sine input

5. Load simulation

Gravity, centrifugal force, rotational and thrust force are the main sources of load on pitch bearings of a wind turbine. These forces affect pitching action by increasing:

- Torque about the pitch axis
- Friction of the pitch bearing
- Moment of inertia of the blade about the pitch axis

The load around the pitch axis can be written in an equation:

$$Load = Torque(F_g, F_r, F_t, F_c) + Friction(F_g, F_r, F_t, F_c) \cdot sign(\dot{\theta}) + MomentOfInertia(F_g, F_r, F_t, F_c) \cdot \ddot{\theta}$$

where F_g, F_r, F_t, F_c are gravity, rotational force, thrust force and centrifugal force. $\dot{\vartheta}$, $\ddot{\vartheta}$ are speed and acceleration of pitch angle in radian. The Matlab/Simulink model of the load simulation is illustrated in Figure 5-1. Friction changes according to the sign of the pitch rate. Torque about pitch axis is a function of the pitch angle and the rotor position. Inertia force is a multiplication of blade's moment of inertia and pitch acceleration. Since the load disturbs the pitch action, -1 is multiplied at the end of the figure.

Load on the pitch bearing changes according to the pitch angle (see Figure 5-2). Friction due to overturning moment and gravity are the main source of load. Torque about the pitch axis is composed of gravity, aerodynamic force and centrifugal loading. Aerodynamic force and centrifugal loading are neglected because they are small and parameters to calculate the forces are insufficient.

Friction, which is one of the biggest parts of load, is validated with measured data in a previous research [33]. Details are explained in the section 5.2.

Pitch actions in case of load simulation are tested in section 6.4. The rotational speed is determined under assumption that tip speed ratio (tsr) is 7, wind speed (V_{wind}) is 12m, hub length (h) is 2m, blade length (L) is 40m. Thus the rotational speed is:

$$\omega = \frac{tsr \cdot V_{wind}}{L + \dfrac{h}{2}} \cdot \frac{1}{2\pi} = \frac{7 \cdot 12}{40 + \dfrac{2}{2}} \cdot \frac{1}{2\pi} = 0.33 Hz$$

Figure 5-1: Simulink block of load simulation
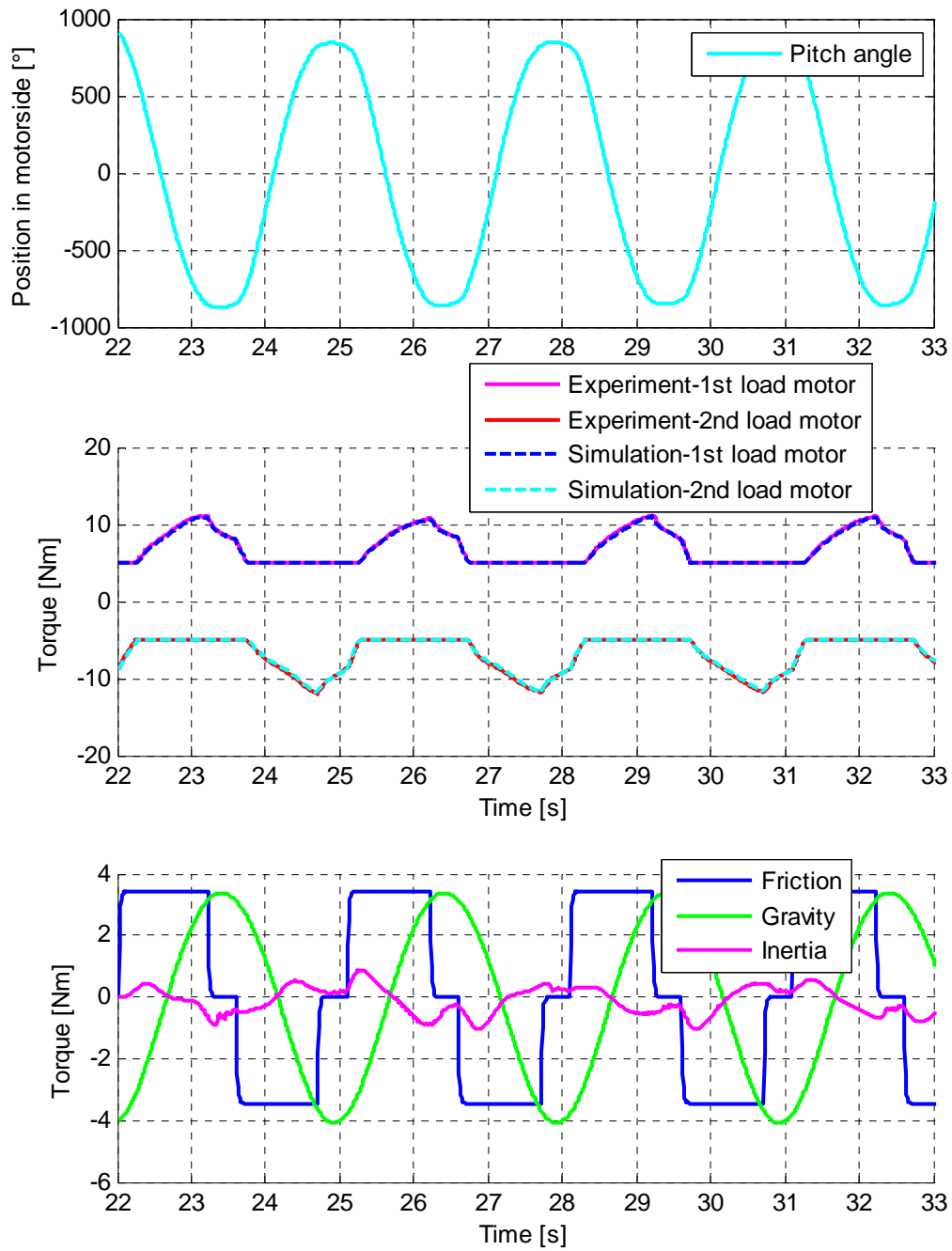
Figure 5-2: Pitch angle and load around pitch axis

5.1. Torque about the pitch axis

5.1.1. Gravity

Blade self-weight causes not only edgewise/flapwise bending moment but also torsional moment about the pitch axis. The frequency of the gravity loading corresponds to the rotation θ of the blade as indicated in Figure 5-3. Torque due to gravity is canceled if the pitch axis is designed to be the same as the center of gravity.

Assuming that the center of gravity is located on the chord, the torque about the pitch axis is:

$$T_g = \sum_{i=1}^{n} m_i \cdot d_i \cdot g \cdot \sin(\alpha + \beta_i)\sin\theta \qquad \text{(5-1)}$$

where

- m_i : mass of the element i
- d_i : distance between center of gravity and pitch axis in the element i
- α : pitch angle
- β_i : twist angle of the element i
- θ : azimuth angle of the blade from the top
- n : number of sections in a blade
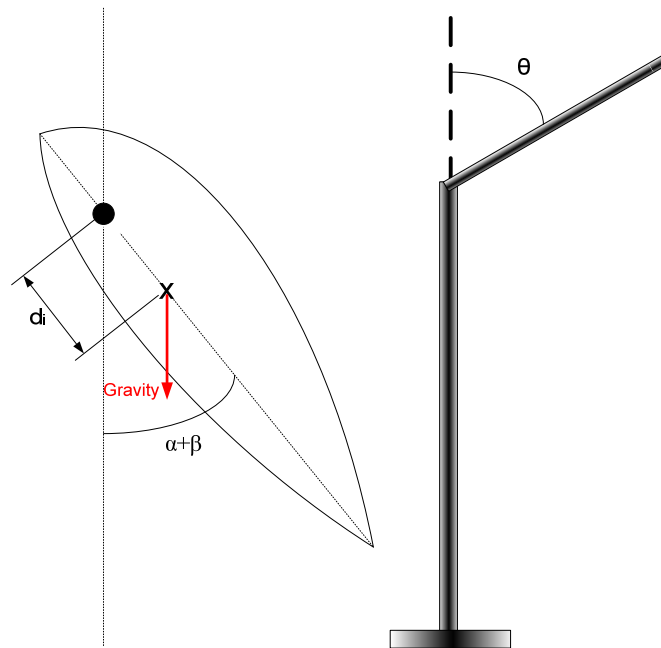
Figure 5-3: Torque due to gravity

The blade data gained from Risø [28] specifies that the center of gravity is located on the same point with pitch axis. Therefore, d_i is zero and the torque due to gravity is also zero. In order to add gravity, the distance between pitch axis and center of gravity is shifted in the load simulation. The amplitude of gravity is almost the same as that of friction in the measurement of a real wind turbine [33]. Thus gravity in this research is set to be the same as the friction. As seen in Figure 5-4, torque due to gravity has maximum value if the azimuth angle, θ, is around 90° or 270° and zero at θ = around 0°

or 180°. Because of twist angles, β_i, the azimuth angles for maximum or zero are shifted. Gravity increases as the pitch angle increases as expected in Figure 5-3.
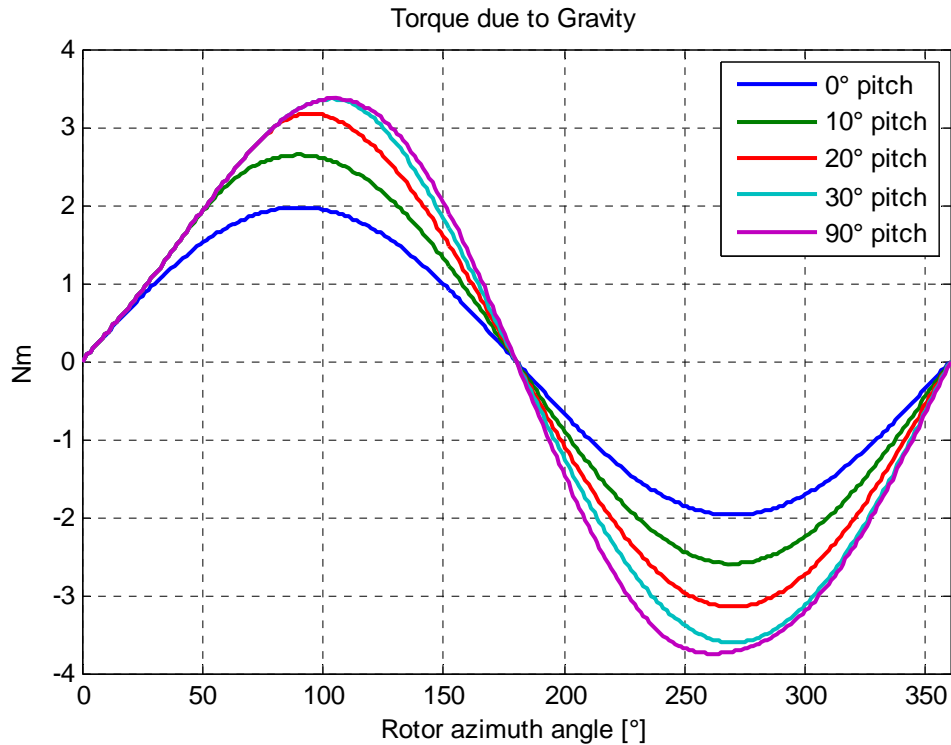
Figure 5-4: torque due to gravity

5.1.2. Aerodynamic force – rotational and thrust forces

Forces on a blade can be calculated with the sum of forces on aerofoil sections. The two forces on a two-dimensional aerofoil section are lift and drag forces (see left graph of Figure 5-5). Aerodynamic force is the vector sum of lift and drag forces and it can be divided as rotational and thrust forces as in Figure 5-5. Rotational force acts parallel to the plane of rotation and thrust force faces downwind (see Figure 5-6).

Aerodynamic force is distributed on the surface of aerofoil sections. Regarding a point where no torsional force is applied, the point is usually not the same as the pitch axis. Torque around the pitch axis due to aerodynamic force is:

$$T_a = \sum_{i=1}^{n} F_A \cdot x \cdot \cos\varphi = \sum_{i=1}^{n} \{L \cdot \cos(\varphi + \delta) + D \cdot \sin(\varphi + \delta)\} \cdot x$$

where

- F_A: aerodynamic force

- L : lift force
- D : drag force
- $\delta = \operatorname{atan}\left(\dfrac{D}{L}\right)$
- n : number of sections in a blade
- x : distance between pitch axis and a point where torsional moment due to aerodynamic forces is compensated
- φ : angle of aerodynamic force
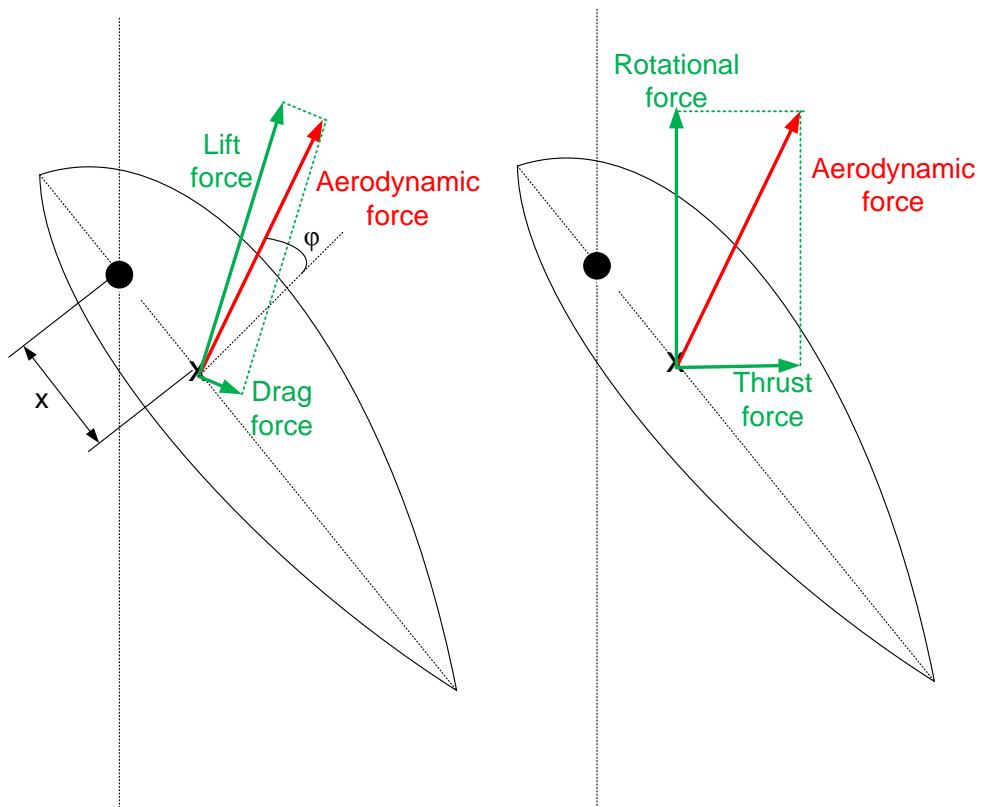
Figure 5-5: aerodynamic force on an aerofoil section
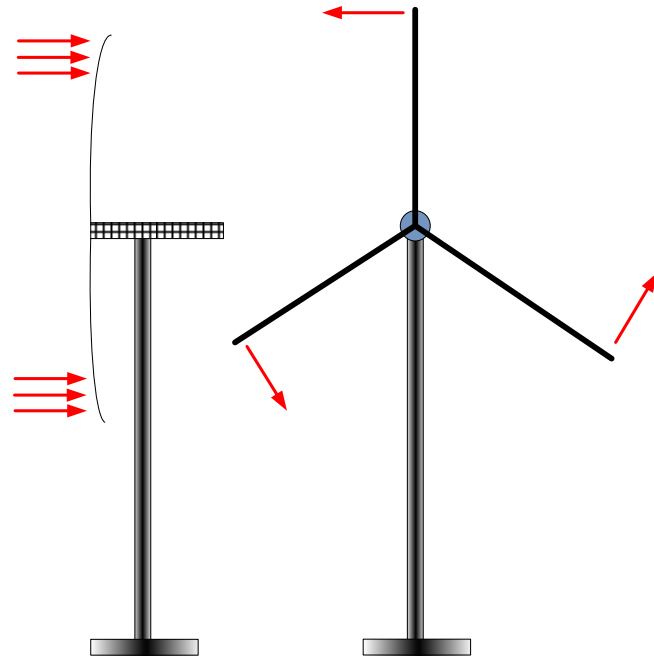
Figure 5-6: thrust (left) and rotational forces (right)

Bossanyi et al. [30] assert that the aerodynamic pitching moment is difficult to predict as aerodynamic data may be incomplete over the range of incidence of interest. M. Geyler [33] did not consider the aerodynamic moment based on measurement. Torque due to aerodynamic force is simulated to be relatively small in comparison with friction due to the overturning moment in section 5.2. The distance between the pitch axis and the center of torsional moment due to aerodynamic forces, x, could not be obtained in the blade data. Aerodynamic moment is not considered in this research.

5.1.3. Centrifugal loading

A rotating blade experiences an outward force away from the center of rotation as shown in Figure 5-7. The outward force, referred to as centrifugal force, causes blades to deflect upwind whereas thrust force results in the blade bending downwind. Thus, centrifugal force alleviates flapwise bending moment caused by thrust force. It is known as centrifugal relief. Bossanyi et al. [30] mentioned that centrifugal loading is small.

Torque due to centrifugal loading is:

$$T_c = \sum_{i=1}^{n} C \cdot a \cdot \cos\beta = \sum_{i=1}^{n} \{\omega^2 r_i m_i \delta r\} \cdot a \cdot \cos\beta \qquad (5\text{-}2)$$

where

- C : centrifugal force

- a : distance between pitch axis and a point where torsional moment due to centrifugal force is canceled
- ω : rotational speed in radian
- r_i : distance of aerofoil from blade root
- m_i : mass of section i
- δr : thickness of an aerofoil section
- β : 90° - pitch angle

The value a is not known in the blade data and centrifugal loading influences torque about pitch axis small in comparison to friction due to overturning moment. Centrifugal loading is not contained in the load simulation.
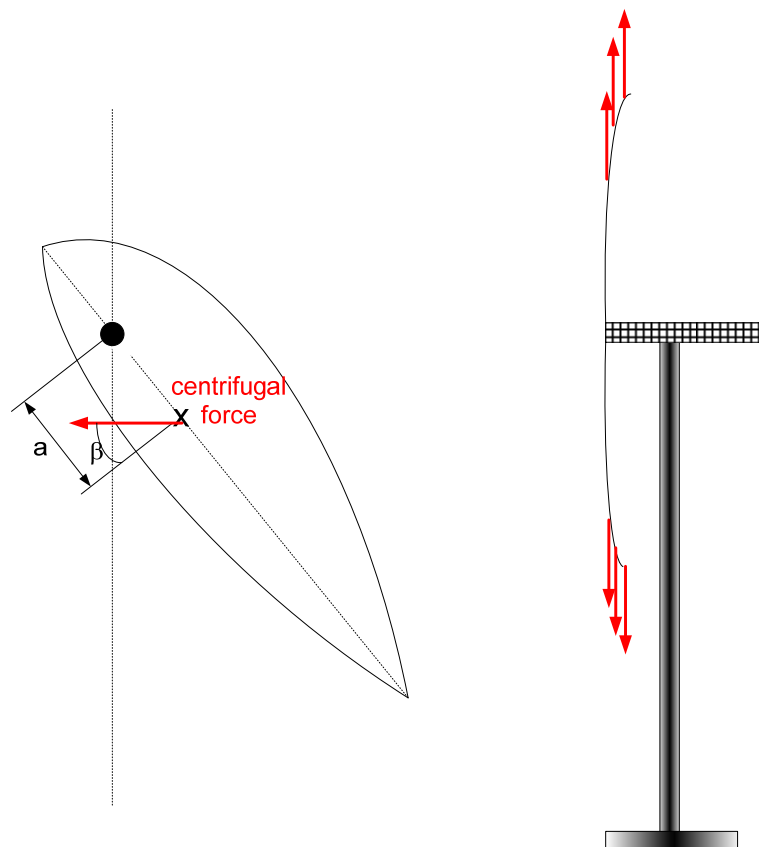
Figure 5-7: centrifugal force

5.2. Friction due to overturning moment

Gravity, aerodynamic and centrifugal loads influence the overturning moment on the blade root. The overturning moment in Figure 5-8 affects friction of the bearing, which obstructs pitching action. The

vector sum of *Mx* and *My* in Figure 5-9 also corresponds to the overturning moment. Bossanyi et al. [30] mentioned that friction torque is extremely significant and has a dominant influence on actuator demand.
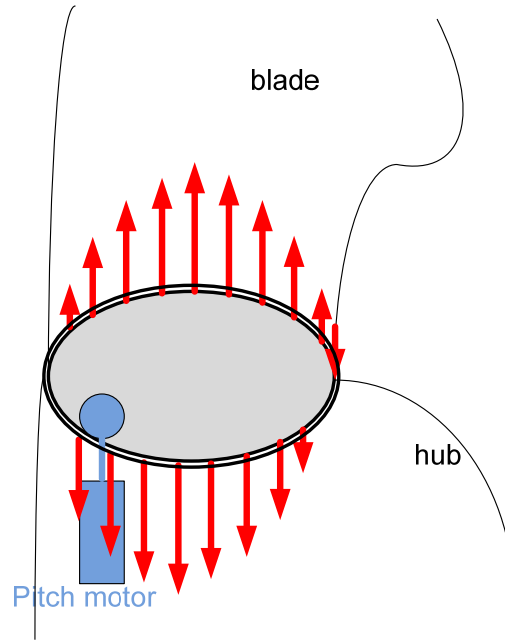
Figure 5-8: overturning moment

The overturning moment, M_{xyB}, is a vector sum of the edgewise bending moment, G_{1E}, and flapwise bending moment, G_{1F}. Thus:

$$M_{xyB} = \sqrt{G_{1E}^{\;2} + G_{1F}^{\;2}}$$

Friction around the pitch axis is calculated with the Hoesch-Rothe-Erde-Formula [32].

$$M_{friction} = \frac{\mu}{2}\left(4.4 \cdot M_{xyB} + \left|F_{zB}\right| \cdot D_L + 2.2 \cdot F_{xyB} \cdot D_L \cdot 1.73\right) + M_{fric,0} \qquad (5\text{-}3)$$

μ and $M_{fric,0}$ is given by the manufacturer. F_{zB} and F_{xyB} are forces in the z and xy-direction of the blade's local coordinate as seen in Figure 5-9. F_{zB} and F_{xyB} are negligibly small compared to the overturning moment, so these terms may be ignored [33].

M. Geyler [33] proposed an easier and more precise way of calculating friction on the bearing around the pitch axis:

$$M_{friction} = \text{constant} \qquad (5\text{-}4)$$

Through several measurements with wind turbines by M. Geyler [33], this new friction equation was determined to be more precise than the Hoesch-Rothe-Erde-Formula. He tested collective pitch control in a few above rated wind speeds and individual pitch control in a few below rated wind speeds. The constant friction value is found through least-square-approximation.
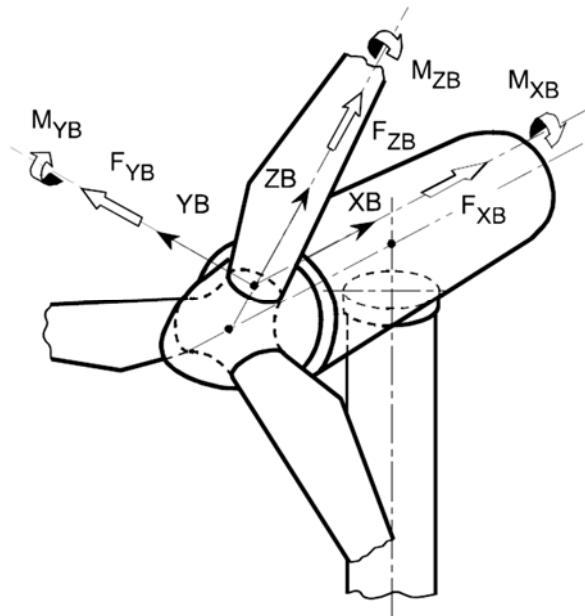
Figure 5-9: coordinate for blade load [34]

5.3. Blade's moment of inertia around pitch axis

Gravity, aerodynamic force and centrifugal force cause blades to bend in flapwise and edgewise directions. Bossanyi et al. [30] found that a blade's moment of inertia around the pitch axis is increased by 44% due to deflection. Blade inertia may be 1/10 of pitch motor inertia because inertia is proportional to the square of the gear ratio [30].

Blade's moment of inertia around pitch axis is determined with flapwise/edgewise/torsional deflections. Modeling a blade with dozens of sections is challenging for a personal computer. A multibody model is a good option to represent blade properties and reduce complexity. Moment of inertia with a multibody model is formulated in (5-25) and (5-26) in section 5.3.3.

Blade data is obtained from the data sheet of a test HAWC in Risø [29]. The information consists of 24 sets of mass, radius, modulus of elasticity, second moment of inertia, etc. By the use of modal analysis, the blade is modeled with a 2-mass-spring-damper-system.

Blade's natural frequencies are determined in section 5.3.1. The natural frequencies are used to get the mechanical parameters of the multibody model. This process is written in section 5.3.2. By means of the mechanical parameters, moment of inertia around pitch axis is calculated in section 5.3.3.

5.3.1. Blade's natural frequencies and mode shapes

Natural frequencies in flapwise, edgewise and torsional directions are required to model a multibody system. Natural frequencies and mode shapes are computed using the finite element method. A multibody system is designed to have the most similar mode shape at the first natural frequency.

Blade-bending vibrations occur in flapwise and edgewise directions. The directions are also called weak and strong principal axes. The weak principal axis is usually regarded to be in the plane of rotation; however, this is not the case with a twist-coupled blade. Twist-coupled blades make the flexure about the two principal axes interact together and change natural frequencies in both directions.

Torsional vibration is generally ignored because of high torsional stiffness. However, increasing the turbine size requires light and soft blades, so torsional natural frequencies are not so large any more as to be neglected. In addition, the project mainly deals with processes during fast pitching. Torsional natural frequencies are to be considered to build a safe and precise controller.

Finite element method

The finite element method is a useful numerical technique for the calculation of natural frequencies and mode shapes. Several commercial finite element codes, e.g. ANSYS or ABAQUS, are available. However, a simple example such as a bar can be solved with programming languages such as MATLAB or C. The finite element method consists of two distinct ways; discretization and *connection*. A model is first divided into small parts which are called *finite elements*. The endpoints of each element are called *nodes*. The partial differential equation for each finite element is solved and assembled together, resulting in mass and stiffness matrices which describe the vibration of the structure as a whole.

The mass matrix for the blade element is [34]:

$$M_i = \begin{pmatrix} M_T & 0 & 0 \\ 0 & M_{By} & 0 \\ 0 & 0 & M_{Bz} \end{pmatrix}$$

where

$$M_T = \frac{\mu_{mx}l}{6}\begin{pmatrix} 2 & 1 \\ 1 & 2 \end{pmatrix}$$

$$M_{By} = M_{Bz} = \frac{\mu l}{420}\begin{pmatrix} 156 & -22l & 54 & 13l \\ -22l & 4l^2 & -13l & -3l^2 \\ 54 & -13l & 156 & 22l \\ 13l & -3l^2 & 22l & 4l^2 \end{pmatrix}$$

In the equations, μ is a mass per unit length and μ_{mx} is a moment of inertia about the torsional axis. l represents for a length of each finite element.

The global stiffness matrix is

$$K_i = \begin{pmatrix} K_T & 0 & 0 \\ 0 & K_{By} & 0 \\ 0 & 0 & K_{Bz} \end{pmatrix}$$

where

$$K_T = \frac{B_x}{l}\begin{pmatrix} 1 & -1 \\ -1 & 1 \end{pmatrix}$$

$$K_{By} = \frac{B_y}{l^3}\begin{pmatrix} 12 & -6l & -12 & -6l \\ -6l & 4l^2 & 6l & 2l^2 \\ -12 & 6l & 12 & 6l \\ -6l & 2l^2 & 6l & 4l^2 \end{pmatrix}$$

$$K_{Bz} = \frac{B_z}{l^3}\begin{pmatrix} 12 & -6l & -12 & -6l \\ -6l & 4l^2 & 6l & 2l^2 \\ -12 & 6l & 12 & 6l \\ -6l & 2l^2 & 6l & 4l^2 \end{pmatrix}$$

The stiffness values written in the matrices are:

- Bending stiffness in the plane of rotation $B_y = EI_y$, $I_y = \int_A z^2 dA$

- Bending stiffness perpendicular to the plane of rotation $B_z = EI_z$, $I_z = \int_A y^2 dA$

- Torsional stiffness $B_x = GI_p$, I_p is a polar moment of inertia about the pitch axis.

The matrices are used for the differential equation

$$M_i \ddot{x} + K_i x = p \qquad\qquad\qquad (5\text{-}5)$$

with loads on the system p.

Each element is bent in a different amount about the principal axis. With the transformation matrix T, the equation (5-5) is changed as:

$$T^T M_i T\ddot{\hat{x}} + T^T K_i T\hat{x} = T^T p \qquad (5\text{-}6)$$

where $\hat{x}$ is a variable based on the principal axis, whereas x is a local coordinate starting from the bent axis.

Elements share variables with their neighborhoods. Equation (5-6) of each element is coupled by means of the index table written in Table 5-1. The numbers in the table are named according to Figure 5-10. The global equation of the entire beam is then:

$$M_g \ddot{\overline{x}} + K_g \overline{x} = \overline{p} \qquad (5\text{-}7)$$

	$W_{0,i}$	$B_{0,i}$	$W_{1,i}$	$B_{1,i}$
Element 1	0	0	1	2
Element 2	1	2	3	4
Element 3	3	4	5	6
Element 4	5	6	7	8
…	…	…	…	…

Table 5-1: Index table for coupling elements
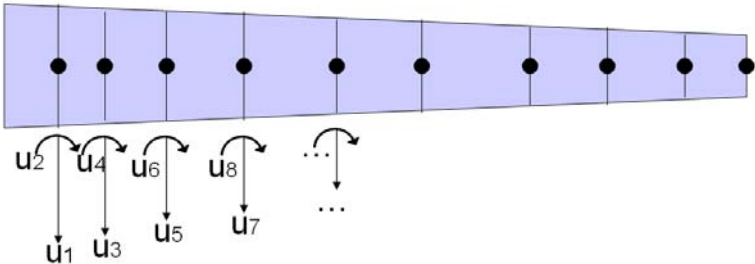
Figure 5-10: variable numbers for the index table

The blade data is gained from a 2 MW test HAWC in Risø [28]. The first and second natural frequencies have to be computed to model a 2-mass-spring-damper-system. The determined static natural frequencies and mode shapes are shown in Table 5-2 and Figure 5-11. Since the blade is flexible in flapwise and stiff in edgewise, the natural frequencies in flapwise are lower than those in edgewise.

	1st natural frequency	2nd natural frequency
flapwise	1.12Hz	3.04 Hz
edgewise	1.71 Hz	5.62 Hz
Torsion	34.76 Hz	60.11 Hz

Table 5-2: determined static natural frequencies from FEM
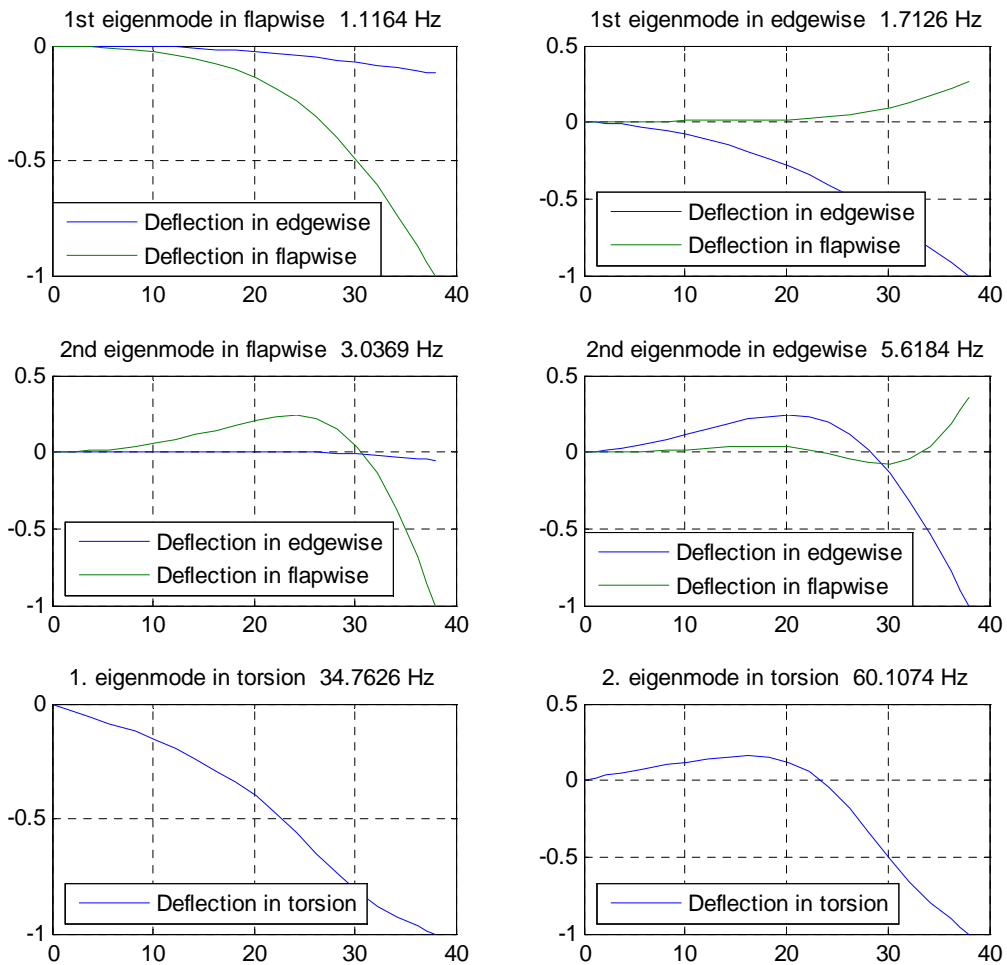
Figure 5-11: Mode shapes

Stodola method

Static natural frequencies determined with FEM can be confirmed by using the Stodola method. The method observes mode shapes caused by arbitrary inertia loads. After repetition, the mode shape converges and the first natural frequency is found from the formula [37]:

$$w_1 = \sqrt{\frac{\text{Tip deflection input to the last iteration}}{\text{Tip deflection output from the last iteration}}}$$

The second natural frequency is calculated in the same manner, but the orthogonality condition has to be added. Without the condition, the mode converges to the first eigenmode. Details of the method can be found in Clough and Penzien (1993) [36] and in section 5.3.2 which is derived from Hansen (2000) [37].

The static natural frequencies computed by the Stodola method are presented in Table 5-3. 2nd natural frequency in edgewise direction is not listed since the value becomes a complex number after

6th iteration. The natural frequencies by means of FEM and Stodola method are close as seen in the table. Therefore, the natural frequencies obtained by the Stodola can guarantee the values with FEM.

	1st natural frequency		2nd natural frequency	
	FEM	Stodola	FEM	Stodola
flapwise	1.12Hz	1.11Hz	3.04 Hz	3.14 Hz
edgewise	1.71 Hz	1.73 Hz	5.62 Hz	-
Torsion	34.76 Hz	31.53 Hz	60.11 Hz	60.35 Hz

Table 5-3: determined static natural frequencies by FEM and Stodola method

Natural frequencies during operation

The natural frequencies are checked in sections 5.3.1 when a wind turbine is at a standstill. However, most of the control problems occur during operation and the natural frequencies during operation are different from those at a standstill.

When a wind turbine rotates, the blades deflect in flapwise and edgewise directions due to the thrust and lift forces. Simultaneously, centrifugal force on the blade conducts energy in the opposite direction. The centrifugal force makes the blade stiff and thereby increases natural frequencies [1] . The effect is called centrifugal stiffening.

In contrast to the increment of the natural frequencies in flapwise and edgewise directions, natural frequencies in the torsional direction decrease during operation. One reason is blade deflection which increases the moment of inertia in the torsional direction. A more important reason is that a blade root in a torsional direction is not fastened during pitch actions. A blade root is connected to a bearing which is fixed in all degrees of freedom except the torsional direction. The bearing is also coupled to a gearbox and a motor. The natural frequencies in the torsional direction during operation are determined by the mechanical characteristics of the blade, bearing, gearbox, and motor. Limited mass and stiffness of the bearing, gearbox, and motor cause the natural frequencies during operation to be smaller than those at a standstill.

However, the difference of natural frequencies in standstill and during operation is relatively small. Thus it is not worth to modify parameters of the blade model in every rotor speed or load condition. Thus the natural frequencies in static condition are used for the blade modeling.

5.3.2. Modeling the blade with multibody system and comparison to FEM

Multibody model

Calculated eigenmodes in section 5.3.1 are used for constructing a multibody system. While a large number of bodies allows the multibody system to be similar to the real system, a small number of bodies helps the developer to build a controller with less complexity. A compromise should be found in-between: a system with two multibodies is selected in the research.

A bending point of the multibody system is determined where the deviation area between the mode shape of the finite element model and multibody model is minimized [39]. Deflections at the root, bending point, and tip are identical as seen in Figure 5-12. Note that the bars for calculating a bending point are shorter than the length of the multibody system which will be used for simulation, but the difference is negligible. Whereas the bending point in flapwise direction is 12th point, the point in edgewise is 11th point where the deviation area is the smallest. Since flapwise deflection is larger than edgewise bending, flapwise bending effect is more important in the load simulation. Thus the multibody blade model has a joint at the 12th point.

Moment of inertia is determined by the blade information and the bending point. Eigenfrequencies are used to calculate stiffness and damping coefficients.
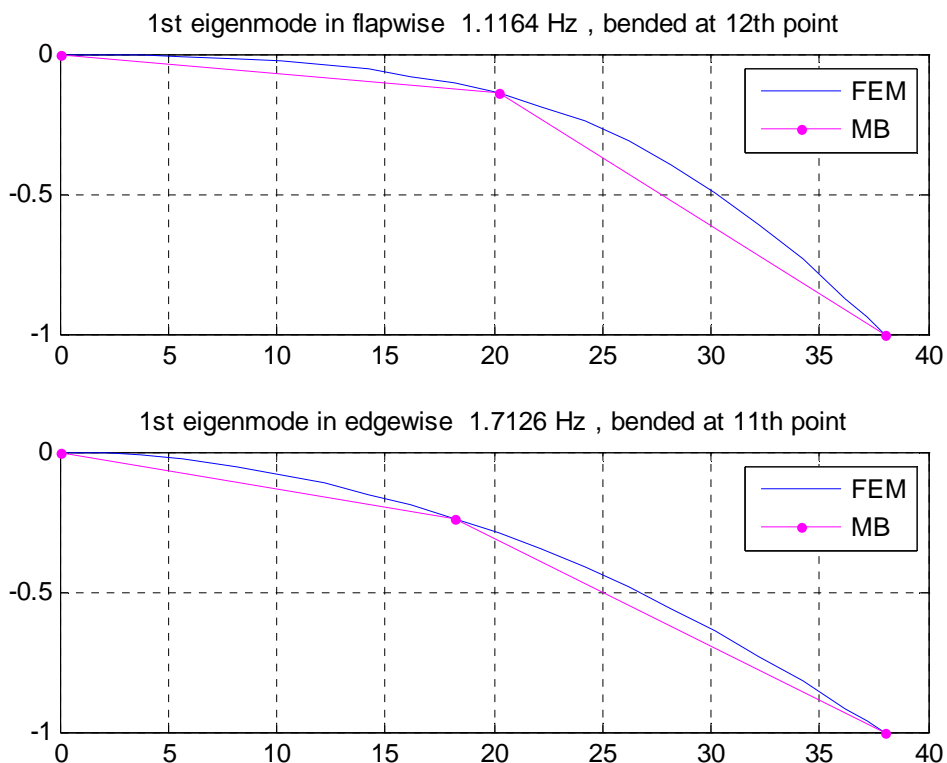
Figure 5-12: Mode shape of the multibody (MB) model and finite elements model (FEM) at the first eigenmode in flapwise and edgewise
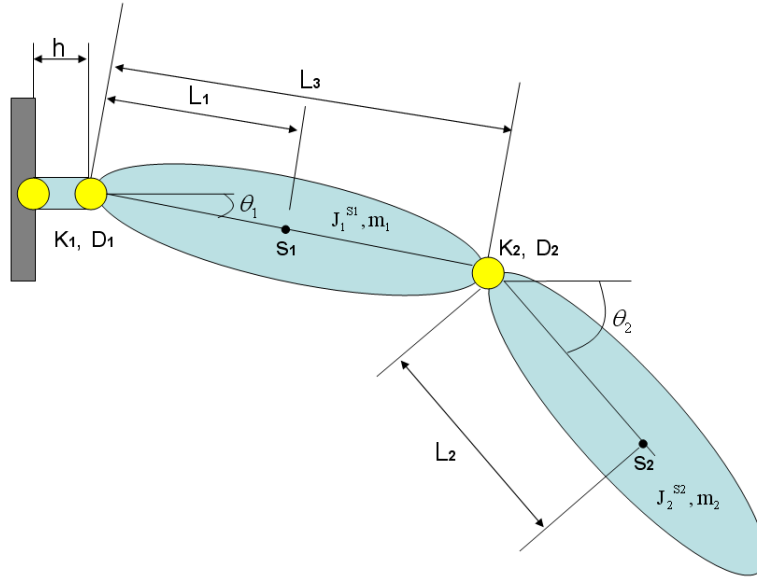
Figure 5-13: Multibody model of the blade

The multibody system of Figure 5-13 can be designed with the Lagrange equation of the second kind:

$$\frac{d}{dt}\left(\frac{\partial L}{\partial \dot{q}_i}\right) - \frac{\partial L}{\partial q_i} = \frac{\delta W}{\delta q_i}$$

(5-8)

The virtual work, denoted δW, is the work done in causing the virtual displacement. Lagrangian, L, is the difference between the kinetic and the potential energies.

From the kinetic energy,

$$\begin{aligned}
T &= \frac{1}{2}J_1^{S_1}\dot{\theta}_1^2 + \frac{1}{2}m_1L_1^2\dot{\theta}_1^2 + \frac{1}{2}J_2^{S_2}\dot{\theta}_2^2 + \frac{1}{2}m_2\left(L_3\dot{\theta}_1\sin\theta_1 + L_2\dot{\theta}_2\sin\theta_2\right)^2 + \frac{1}{2}m_2\left(L_3\dot{\theta}_1\cos\theta_1 + L_2\dot{\theta}_2\cos\theta_2\right)^2 \\
&= \frac{1}{2}\left(J_1^{S_1} + m_1L_1^2 + m_2L_3^2\right)\dot{\theta}_1^2 + \frac{1}{2}\left(J_2^{S_2} + m_2L_2^2\right)\dot{\theta}_2^2 + m_2L_2L_3\dot{\theta}_1\dot{\theta}_2\left(\cos\theta_1\cos\theta_2 + \sin\theta_1\sin\theta_2\right) \\
&= \frac{1}{2}J_1\dot{\theta}_1^2 + \frac{1}{2}J_2\dot{\theta}_2^2 + J_{12}\dot{\theta}_1\dot{\theta}_2\cos(\theta_1 - \theta_2)
\end{aligned}$$

the potential energy,

$$U = \frac{1}{2}K_1\theta_1^2 + \frac{1}{2}K_2(\theta_2 - \theta_1)^2$$

The Lagrange function is

$$\begin{aligned}
L &= T - U \\
&= \frac{1}{2}J_1\dot{\theta}_1^2 + \frac{1}{2}J_2\dot{\theta}_2^2 + J_{12}\dot{\theta}_1\dot{\theta}_2\cos(\theta_1 - \theta_2) - \frac{1}{2}K_1\theta_1^2 - \frac{1}{2}K_2(\theta_2 - \theta_1)^2
\end{aligned}$$

Partial derivative of the Lagrange function is

$$\frac{d}{dt}\left(\frac{\partial L}{\partial \dot\theta_1}\right) = J_1\ddot\theta_1 + J_{12}\ddot\theta_2 \cos(\theta_1 - \theta_2) - J_{12}\dot\theta_2\left(\dot\theta_1 - \dot\theta_2\right)\sin(\theta_1 - \theta_2)$$

$$\frac{d}{dt}\left(\frac{\partial L}{\partial \dot\theta_2}\right) = J_2\ddot\theta_2 + J_{12}\ddot\theta_1 \cos(\theta_1 - \theta_2) - J_{12}\dot\theta_1\left(\dot\theta_1 - \dot\theta_2\right)\sin(\theta_1 - \theta_2)$$

$$\frac{\partial L}{\partial \theta_1} = -K_1\theta_1 + K_2(\theta_2 - \theta_1)$$

$$\frac{\partial L}{\partial \theta_1} = -K_2(\theta_2 - \theta_1)$$

The virtual work and its derivatives are

$$\delta W = -D_1\dot\theta_1\delta\theta_1 - D_2\left(\dot\theta_2 - \dot\theta_1\right)\left(\delta\theta_2 - \delta\theta_1\right)$$

$$\frac{\delta W}{\delta\theta_1} = -D_1\dot\theta_1 + D_2\left(\dot\theta_2 - \dot\theta_1\right)$$

$$\frac{\delta W}{\delta\theta_2} = -D_2\left(\dot\theta_2 - \dot\theta_1\right)$$

By assuming θ_1 and θ_2 are small, such terms are simplified like:

$$\sin(\theta_1 - \theta_2) = \theta_1 - \theta_2$$
$$\cos(\theta_1 - \theta_2) = 1$$
$$\dot\theta_1\theta_1 = \dot\theta_1\theta_2 = \dot\theta_2\theta_1 = \dot\theta_2\theta_2 = 0$$

Thus, the equation (5-8) is linearised as follows:

$$\begin{bmatrix} J_1 & J_{12} \\ J_{12} & J_2 \end{bmatrix}\begin{bmatrix} \ddot\theta_1 \\ \ddot\theta_2 \end{bmatrix} + \begin{bmatrix} D_1 + D_2 & -D_2 \\ -D_2 & D_2 \end{bmatrix}\begin{bmatrix} \dot\theta_1 \\ \dot\theta_2 \end{bmatrix} + \begin{bmatrix} K_1 + K_2 & -K_2 \\ -K_2 & K_2 \end{bmatrix}\begin{bmatrix} \theta_1 \\ \theta_2 \end{bmatrix} = \begin{bmatrix} 0 \\ 0 \end{bmatrix} \qquad \text{(5-9)}$$

where

- $J_1 = J_1^{s_1} + m_1 L_1^2 + m_2 L_3^2$
- $J_2 = J_2^{s_2} + m_2 L_2^2$
- $J_{12} = m_2 L_2 L_3$

$J_1^{s_1}$ is the moment of inertia of the part on the root side about the center of gravity, s_1, and $J_2^{s_2}$ is that on the tip side about the s_2. $L_3 = 0$ leads to $J_{12} = 0$ in the torsional direction.

Let the matrix $M = \begin{bmatrix} J_1 & J_{12} \\ J_{12} & J_2 \end{bmatrix}$, $D = \begin{bmatrix} D_1 + D_2 & -D_2 \\ -D_2 & D_2 \end{bmatrix}$, $K = \begin{bmatrix} K_1 + K_2 & -K_2 \\ -K_2 & K_2 \end{bmatrix}$ and $x = \begin{bmatrix} \theta_1 \\ \theta_2 \end{bmatrix}$,

so that stiffness parameters in K can be found from the undamped natural frequency in section 5.3.1. To compute stiffness parameters, let the vector x in equation (5-9) be replaced with:

$$x = M^{-\frac{1}{2}}q$$

and multiplying the resulting equation by $M^{-\frac{1}{2}}$. This yields:

$$I\ddot{q} + \tilde{D}\dot{q} + \tilde{K}q = 0 \qquad\qquad \text{(5-10)}$$

where I is a unit matrix, $\tilde{D} = M^{-\frac{1}{2}}DM^{-\frac{1}{2}}$, $\tilde{K} = M^{-\frac{1}{2}}KM^{-\frac{1}{2}}$.

Since undamped static natural frequencies from FEM are applied, consider $D = 0$ first. The solution q can be assumed with $q(t) = ve^{jwt}$ where v is a vector of constants. This substitution yields from equation (5-10):

$$\tilde{K}v = \omega^2 v = \lambda v \qquad\qquad \text{(5-11)}$$

as assuming the eigenvalues $\lambda = \omega^2$ and eigenvectors $v \neq 0$.

Since $M = M^T$, $M^{-\frac{1}{2}}$ can be described like:

$$M^{-\frac{1}{2}} = \left(M^{-\frac{1}{2}}\right)^T = \begin{bmatrix} a & b \\ b & c \end{bmatrix}$$

Then,

$$\tilde{K} = M^{-\frac{1}{2}}KM^{-\frac{1}{2}}$$
$$= \begin{bmatrix} a & b \\ b & c \end{bmatrix}\begin{bmatrix} K_1 + K_2 & -K_2 \\ -K_2 & K_2 \end{bmatrix}\begin{bmatrix} a & b \\ b & c \end{bmatrix}$$
$$= \begin{bmatrix} a^2 K_1 + a^2 K_2 - 2abK_2 + b^2 K_2 & abK_1 + abK_2 - b^2 K_2 - acK_2 + bcK_2 \\ abK_1 + abK_2 - b^2 K_2 - acK_2 + bcK_2 & b^2 K_1 + b^2 K_2 - 2bcK_2 + c^2 K_2 \end{bmatrix}$$

From equation (5-11), the determinant is:

$$\det\left(\lambda I - \tilde{K}\right)$$
$$= \lambda^2 - \left[\left(a^2 + b^2\right)K_1 + \left\{(a-b)^2 + (b-c)^2\right\}K_2\right]\lambda + \left\{abK_1 + (a-b)(b-c)K_2\right\}^2 + \left\{a^2 K_1 + (a-b)^2 K_2\right\}\left\{b^2 K_1 + (b-c)^2 K_2\right\}$$

Let the first two static natural frequencies in radian ω_1 and ω_2, then,

$$\left(a^2 + b^2\right)K_1 + \left\{(a-b)^2 + (b-c)^2\right\}K_2 = \omega_1 + \omega_2$$
$$\left\{abK_1 + (a-b)(b-c)K_2\right\}^2 + \left\{a^2 K_1 + (a-b)^2 K_2\right\}\left\{b^2 K_1 + (b-c)^2 K_2\right\} = \omega_1\omega_2$$

Stiffness parameters K_1 and K_2 are determined by the following two equations.

$$\frac{(a-b)^2+(b-c)^2}{a^2+b^2}K_2{}^2-\frac{\omega_1+\omega_2}{a^2+b^2}K_2+\frac{\omega_1\omega_2}{a^2c^2+b^4-2ab^2c}=0$$

$$K_1=-\frac{(a-b)^2+(b-c)^2}{a^2+b^2}K_2+\frac{\omega_1+\omega_2}{a^2+b^2}$$

A damping matrix D is computed from a decoupled modal equation:

$$I\ddot{r}+P^T\tilde{D}P\dot{r}+P^T\tilde{K}Pr=0 \tag{5-12}$$

where P is the matrix composed of eigenvector v in equation (5-11). As the $P^T\tilde{D}P$ becomes $\begin{pmatrix}\hat{D}_1 & 0 \\ 0 & \hat{D}_2\end{pmatrix}$, $\hat{D}_1$ and $\hat{D}_2$ are the same as $2\zeta_1\omega_1$ and $2\zeta_2\omega_2$, where ζ represents the modal damping ratio.

As the user defines a modal damping ratio, e.g. 0.05 in the research, D_1 and D_2 are found after some steps. In fact, the modal damping ratio is dependent on the natural frequencies such as the following expression. However, the modal damping ratios are often regarded as constant for easy calculation.

$$\zeta_i=\frac{\alpha}{2\omega_i}+\frac{\beta\omega_i}{2} \text{ with } \alpha,\ \beta \text{ : constant}$$

The damped static natural frequencies are written in Table 5-4 and compared with undamped static natural frequencies. The resulting parameters for damping and stiffness matrices follow in Table 5-5.

	1st undamped natural frequency	1st damped natural frequency	2nd undamped natural frequency	2nd damped natural frequency
flapwise	1.12 Hz	1.12 Hz	3.04 Hz	3.03 Hz
edgewise	1.71 Hz	1.71 Hz	5.62 Hz	5.61 Hz
torsion	34.76 Hz	34.72 Hz	60.11 Hz	60.03 Hz

Table 5-4: undamped and damped static natural frequencies

	J_1 [kg·m]	J_2 [kg·m]	D_1 [N·s]	D_2 [N·s]	K_1 [N]	K_2 [N]
flapwise	$1.64\cdot10^6$	$1.30\cdot10^5$	$9.71\cdot10^5$	$8.56\cdot10^4$	$1.63\cdot10^8$	$1.48\cdot10^7$
edgewise	$1.64\cdot10^6$	$1.30\cdot10^5$	$1.94\cdot10^6$	$2.39\cdot10^5$	$3.19\cdot10^8$	$6.09\cdot10^7$
torsion	$1.32\cdot10^4$	$1.53\cdot10^2$	$4.94\cdot10^5$	$3.36\cdot10^3$	$1.87\cdot10^9$	$7.37\cdot10^6$

Table 5-5: Parameters of the multibody system

Comparison of multibody model to FEM

Parameters of the multibody system are calculated from the blade's natural frequencies gained from FEM. One way to find whether a 2-body-model represents FEM sufficiently or not is to check static deflection. External loads and reactions are distributed gravity in this case. Forces and moments acting within the member are gained from equation (5-13) and (5-14). The blade is assumed to be located parallel to the horizontal surface.

$$\frac{dT_y}{dz} = g(z) \tag{5-13}$$

$$\frac{dM_x}{dz} = T_y \tag{5-14}$$
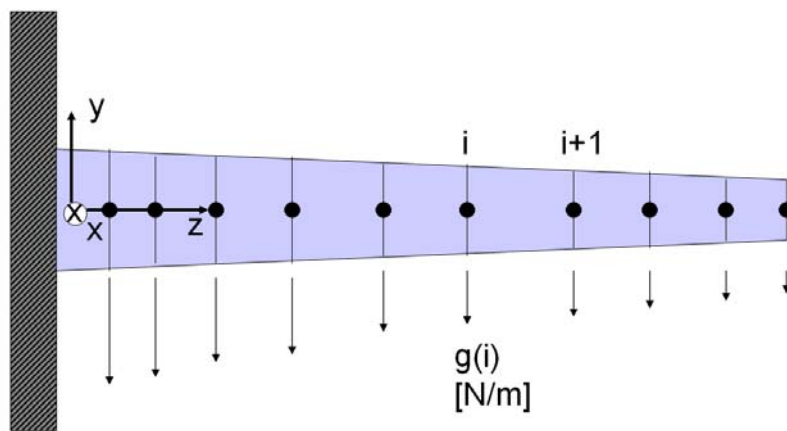
Figure 5-14: a discrete blade model
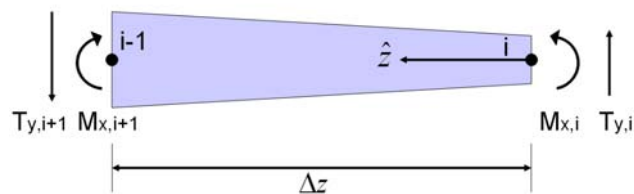
Figure 5-15: Force and moment of the blade element

Shear force T_y is computed by integrating gravity g(z) and used to calculate the bending moment M_x .

Gravity in Figure 5-14 between two points is assumed to vary linearly as:

$$g(\hat{z}) = \frac{g_{i-1} - g_i}{\Delta z} \hat{z} + g_i \tag{5-15}$$

where $\hat{z}$ is the distance from point i and Δz is the distance between points i and $i-1$ as sketched in Figure 5-15.

T_y is computed from the tip (N) to the root (1) since $T_{y,N}$ is zero.

The shear force T_y due to the distributed load is:

$$T_y(\hat{z}) = T_{y,i} + \frac{g_{i-1} - g_i}{2\Delta z}\hat{z}^2 + g_i\hat{z}$$

(5-16)

$T_{y,i-1}$ is computed by inserting $\hat{z} = \Delta z$ as:

$$T_{y,i-1} = T_{y,i} + \frac{g_{i-1} - g_i}{2}\Delta z$$

(5-17)

Since the bending moment at $M_{x,N} = 0$, M_x is also calculated from N to 1.

Integration of equation (5-14) yields:

$$M_x(\hat{z}) = M_{x,i} + T_{y,i}\hat{z} + \frac{g_{i-1} - g_i}{6\Delta z}\hat{z}^3 + \frac{1}{2}g_i\hat{z}^2$$

(5-18)

$\hat{z} = \Delta z$ in equation (5-18) yields:

$$M_{x,i-1} = M_{x,i} + T_{y,i}\Delta z + \left(\frac{1}{6}g_{i-1} + \frac{1}{3}g_i\right)(\Delta z)^2$$

(5-19)

The angular deformation ϑ_x and deflection w_y are expressed in equation (5-20) and (5-21) regarding each blade element as a beam.

$$\frac{d\vartheta_x(z)}{dz} = \frac{M_x}{EI_x}$$

(5-20)

$$\frac{dw_y(z)}{dz} = \vartheta_x(z)$$

(5-21)

where **E** is Young's modulus and I_x is the moment of inertia of the cross-sectional area with respect to the x axis. ϑ_x and w_y are calculated from 1 to N since $\vartheta_{x,1} = w_{y,1} = 0$.

Integrating equation (5-20) and inserting $\hat{z} = \Delta z$ yields:

$$\vartheta_{i+1} = \vartheta_i + \frac{1}{2}\left(\frac{M_{x,i+1}}{E_{i+1}I_{x,i+1}} + \frac{M_{x,i}}{E_i I_{x,i}}\right)\Delta z$$

(5-22)

In the same way, w_y is computed by using equation (5-21) and (5-22):

$$w_{i+1} = w_i + \vartheta_i \Delta z + \left(\frac{1}{6} \frac{M_{x,i+1}}{E_{i+1}I_{x,i+1}} + \frac{1}{3} \frac{M_{x,i}}{E_i I_{x,i}} \right)(\Delta z)^2 \tag{5-23}$$

State-space representation of the multibody system is written by adding gravity in the Lagrange equation of the second kind in section 5.3.2.

$$\begin{bmatrix} J_1 & J_{12} \\ J_{12} & J_2 \end{bmatrix} \begin{bmatrix} \ddot{\vartheta}_1 \\ \ddot{\vartheta}_2 \end{bmatrix} + \begin{bmatrix} D_1 + D_2 & -D_2 \\ -D_2 & D_2 \end{bmatrix} \begin{bmatrix} \dot{\vartheta}_1 \\ \dot{\vartheta}_2 \end{bmatrix} + \begin{bmatrix} K_1 + K_2 & -K_2 \\ -K_2 & K_2 \end{bmatrix} \begin{bmatrix} \vartheta_1 \\ \vartheta_2 \end{bmatrix} = \begin{bmatrix} (m_1 L_1 + m_2 L_3)g \\ m_2 L_2 g \end{bmatrix} \tag{5-24}$$

Parameters of the multibody model are validated in case of a static deflection. Figure 5-16 shows the static deflection of FEM and a multibody system while gravity forces are distributed on the blade. Since the joint of multibody model is chosen considering the flapwise eigenmode, the multibody model shows more similar behavior to the FEM model in flapwise deflection than in edgewise bending. Edgewise bending is illustrated with a negative sign in order to avoid overlapping with the flapwise graphs. Thus signs of the deflection in the graph have no meaning.
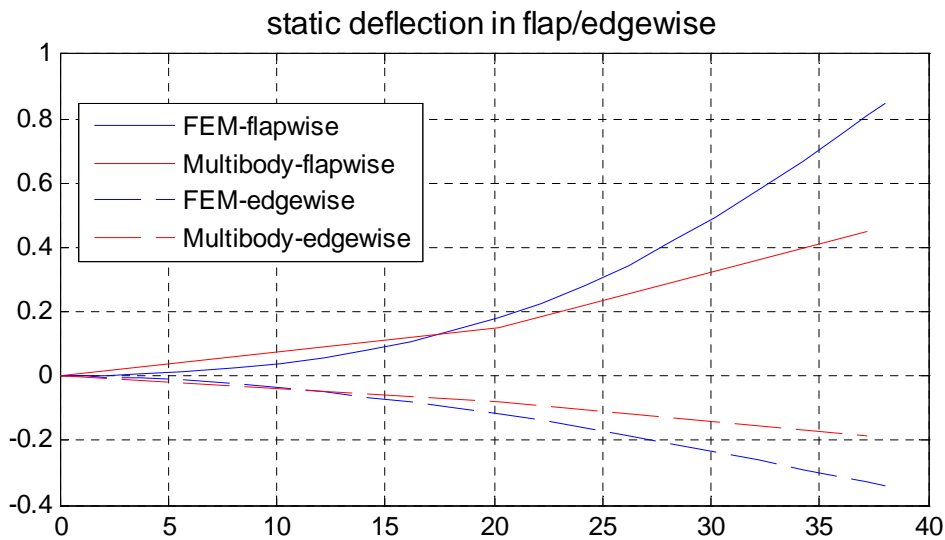
Figure 5-16: static deflection of FEM and multibody system

5.3.3. Calculation of moment of inertia around pitch axis

A blade's moment of inertia around the pitch axis is affected by edgewise/flapwise/torsional moment of inertia, so that:

$$J_{pitch} = J_E + J_F + \left(J_{1T} + J_{2T} \right) \tag{5-25}$$

where J_{1T} and J_{2T} are J_1 and J_2 in torsional direction in Table 5-5 in section 5.3.2. Test HAWC in Risø [29] is used for blade data.

Moments of inertia due to edgewise and flapwise deflections about the pitch axis are:

$$J_E = m_1 \left(L_1 \sin\vartheta_{1E} \right)^2 + m_2 \left(L_3 \sin\vartheta_{1E} + L_2 \sin\vartheta_{2E} \right)^2$$
$$J_F = m_1 \left(L_1 \sin\vartheta_{1F} \right)^2 + m_2 \left(L_3 \sin\vartheta_{1F} + L_2 \sin\vartheta_{2F} \right)^2$$

(5-26)

E and F indicate edgewise and flapwise directions. ϑ_{1E} and ϑ_{2E} are found by equation (5-28) and ϑ_{1F} and ϑ_{2F} are obtained by equation (5-31).

Edgewise deflection angles due to gravity and rotational force

Gravity is responsible for edgewise bending moment. It causes tensile and compressive stresses on the bearing of the blade root. Aerodynamic force is divided into rotational and thrust force. Rotational force also induces edgewise bending moment.

The blade is not a uniform bar but a sum of complete aerofoil shapes. The finite element method is generally used to investigate blade characteristics. However, dozens of parts in a blade are hard to simulate, so a blade is divided into two sections. The way to divide parts is discussed in section 5.3.2.

Each part of a blade has mass, spring and damping characteristics. In the edgewise direction, gravity and rotational force are implied as shown in Figure 5-17.
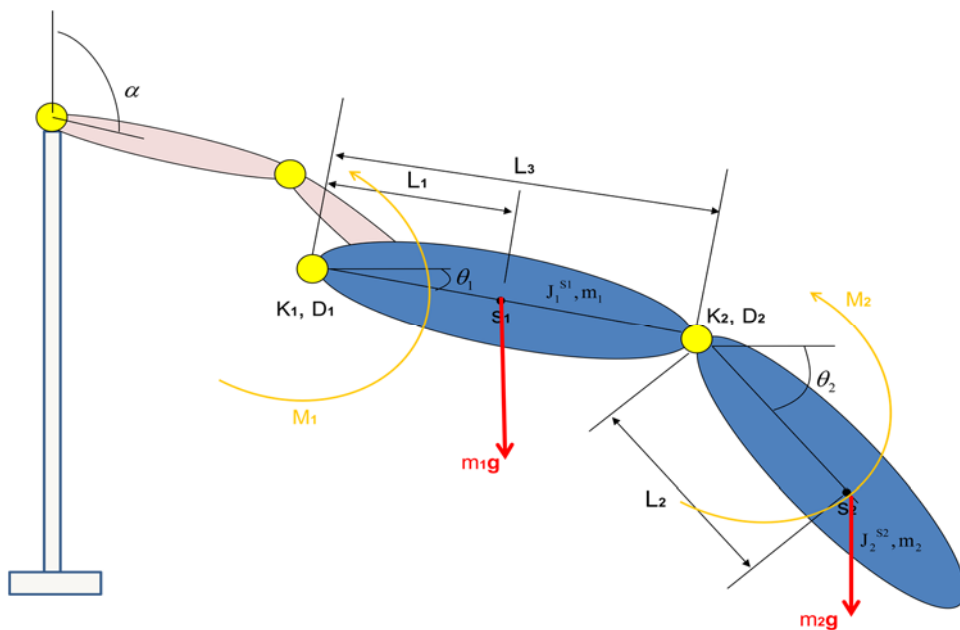
Figure 5-17: Edgewise deflection angles due to gravity and rotational moment

A Lagrange equation of the second kind is used to determine load on the blade root in an edgewise direction:

$$\frac{d}{dt}\left(\frac{\partial L}{\partial \dot{q}_i}\right) - \frac{\partial L}{\partial q_i} = \frac{\delta W}{\delta q_i} \qquad \text{(5-27)}$$

where

$$L = T - U$$

with kinetic energy T and potential energy U.

The kinetic energy is calculated as:

$$T = \frac{1}{2}J_1\dot{\theta}_1^2 + \frac{1}{2}J_2\dot{\theta}_2^2 + J_{12}\dot{\theta}_1\dot{\theta}_2\cos(\theta_1 - \theta_2)$$

The potential energy is:

$$U = \frac{1}{2}K_1\vartheta_1^2 + \frac{1}{2}K_2(\vartheta_2 - \vartheta_1)^2 - m_1 g\sin(\alpha)L_1\sin(\vartheta_1) - m_2 g\sin(\alpha)\{L_3\sin(\vartheta_1) + L_2\sin(\vartheta_2)\}$$

Dissipation and implied force or moment are included in virtual work,

$$\delta W = -D_1\dot{\vartheta}_1\delta\vartheta_1 - D_2(\dot{\vartheta}_2 - \dot{\vartheta}_1)(\delta\vartheta_2 - \delta\vartheta_1) + M_1\delta\vartheta_1 + M_2(\delta\vartheta_2 - \delta\vartheta_1)$$

and by assuming ϑ_1 and ϑ_2 are small, such a linear equation is derived:

$$\begin{bmatrix} J_1 & J_{12} \\ J_{12} & J_2 \end{bmatrix}\begin{bmatrix} \ddot{\vartheta}_1 \\ \ddot{\vartheta}_2 \end{bmatrix} + \begin{bmatrix} D_1 + D_2 & -D_2 \\ -D_2 & D_2 \end{bmatrix}\begin{bmatrix} \dot{\vartheta}_1 \\ \dot{\vartheta}_2 \end{bmatrix} + \begin{bmatrix} K_1 + K_2 & -K_2 \\ -K_2 & K_2 \end{bmatrix}\begin{bmatrix} \vartheta_1 \\ \vartheta_2 \end{bmatrix}$$
$$= \begin{bmatrix} M_1 - M_2 - (m_1 L_1 - m_2 L_3)g\sin(\alpha)\cos(\vartheta_1) \\ M_2 - m_2 g\sin(\alpha)L_2\cos(\vartheta_2) \end{bmatrix} \qquad \text{(5-28)}$$

where

- $J_1 = J_1^{s_1} + m_1 L_1^2 + m_2 L_3^2$
- $J_2 = J_2^{s_2} + m_2 L_2^2$
- $J_{12} = m_2 L_2 L_3$

$J_1^{s_1}$ is the moment of inertia of the part on the root side about the center of gravity, s_1, and $J_2^{s_2}$ is that on the tip side about the s_2. Section 5.3.2 explains more in detail how J_1, J_2, J_{12} are calculated. The parameters are listed also in Table 5-5 of section 5.3.2.

The edgewise angles, ϑ_1 and ϑ_2, in (5-28) are used for ϑ_{1E} and ϑ_{2E} in (5-26).

Flapwise deflection angles due to gravity, thrust and centrifugal forces

Depending on blade position, gravity applies not only to the edgewise bending moment but also the flapwise bending moment. If the azimuth angle is zero or 180°, the edgewise bending moment is canceled, but the flapwise bending moment is affected by gravity (see Figure 5-18 and Figure 5-19). Likewise, if the azimuth angle is 90° or 270°, the flapwise bending moment is not influenced by gravity. The thrust force of aerodynamic force and centrifugal force also have an impact on the flapwise bending moment.
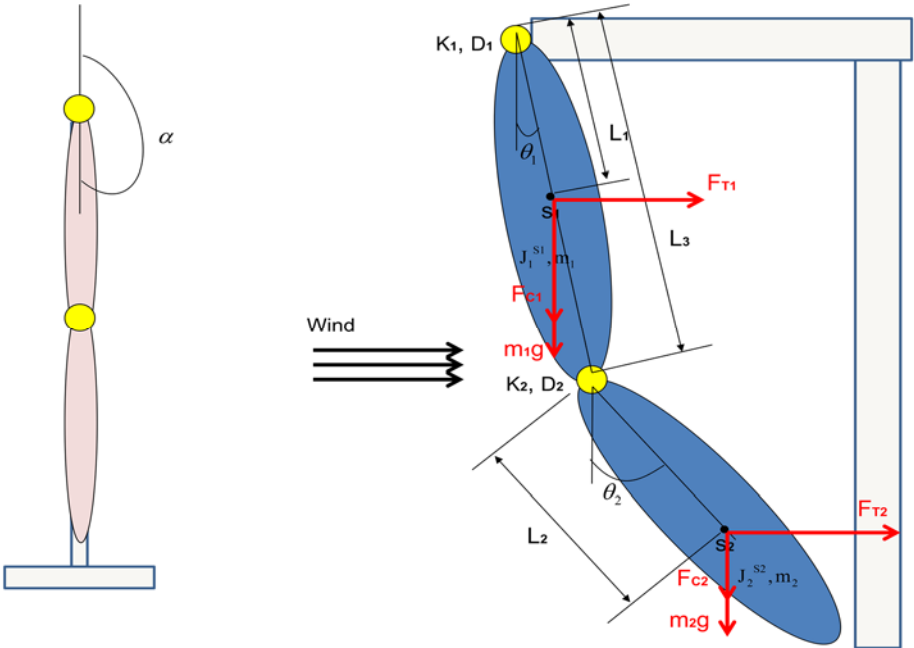
Figure 5-18: Flapwise deflection angles due to thrust and centrifugal forces with 180° azimuth angle (view from side)
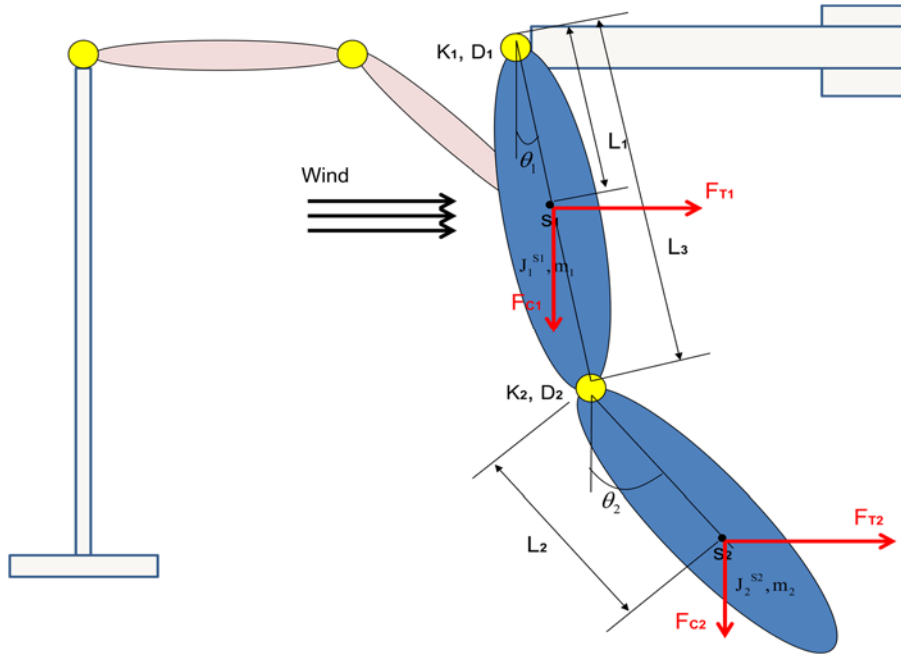
Figure 5-19: Flapwise deflection angles due to thrust and centrifugal forces with 90° azimuth angle (view from top)

As in the previous section, to determine edgewise bending moment, flapwise bending moment is calculated with a Lagrange equation of the second kind.

Given that the azimuth angle= α , the effect of gravity on flapwise bending moment is influenced by $-m_i g \cdot \cos(\alpha), i = 1,2$

A Lagrange equation of the second kind is used also for flapwise direction:

$$\frac{d}{dt}\left(\frac{\partial L}{\partial \dot{q}_i}\right) - \frac{\partial L}{\partial q_i} = \frac{\delta W}{\delta q_i} \tag{5-29}$$

where

$$L = T - U$$

with kinetic energy T and potential energy U .

The kinetic energy is calculated as:

$$T = \frac{1}{2}J_1\dot{\theta}_1^{\,2} + \frac{1}{2}J_2\dot{\theta}_2^{\,2} + J_{12}\dot{\theta}_1\dot{\theta}_2\cos(\theta_1 - \theta_2)$$

And the potential energy is:

$$U = \frac{1}{2}K_1\vartheta_1^{\,2} + \frac{1}{2}K_2(\vartheta_2 - \vartheta_1)^2 - m_1 g \cos(\alpha)L_1 \sin(\vartheta_1) - m_2 g \cos(\alpha)\{L_3 \sin(\vartheta_1) + L_2 \sin(\vartheta_2)\}$$

Dissipation and implied force are included in virtual work,

$$\delta W = -D_1 \dot{\theta}_1 \delta\theta_1 - D_2 \left(\dot{\theta}_2 - \dot{\theta}_1\right)\left(\delta\theta_2 - \delta\theta_1\right) + F_{T1}L_1 \cos(\theta_1)\cdot\delta\theta_1$$
$$+ F_{T2}L_2 \cos\left(\theta_2 - \theta_1\right)\left(\delta\theta_2 - \delta\theta_1\right) - F_{c1}L_1 \sin(\theta_1)\cdot\delta\theta_1 - F_{c2}L_2 \sin\left(\theta_2 - \theta_1\right)\left(\delta\theta_2 - \delta\theta_1\right)$$

and by assuming ϑ_1 and ϑ_2 are small, such a linear equation is derived:

$$\begin{bmatrix} J_1 & J_{12} \\ J_{12} & J_2 \end{bmatrix}\begin{bmatrix} \ddot{\theta}_1 \\ \ddot{\theta}_2 \end{bmatrix} + \begin{bmatrix} D_1 + D_2 & -D_2 \\ -D_2 & D_2 \end{bmatrix}\begin{bmatrix} \dot{\theta}_1 \\ \dot{\theta}_2 \end{bmatrix} + \begin{bmatrix} K_1 + K_2 & -K_2 \\ -K_2 & K_2 \end{bmatrix}\begin{bmatrix} \theta_1 \\ \theta_2 \end{bmatrix}$$
$$= \begin{bmatrix} \left\{F_{T1}L_1 \cos(\theta_1) - F_{T2}L_2 \cos\left(\theta_2 - \theta_1\right) - F_{c1}L_1 \sin(\theta_1) + F_{c2}L_2 \sin\left(\theta_2 - \theta_1\right)\right\} \\ -\left(m_1 L_1 - m_2 L_3\right)g \cos(\alpha)\cos(\theta_1)\} \\ \cdot\left\{F_{T2}L_2 \cos\left(\theta_2 - \theta_1\right) - F_{c2}L_2 \sin\left(\theta_2 - \theta_1\right) - m_2 g \cos(\alpha)L_2 \cos(\theta_2)\right\} \end{bmatrix}$$

(5-30)

where

- $J_1 = J_1^{s_1} + m_1 L_1{}^2 + m_2 L_3{}^2$

- $J_2 = J_2^{s_2} + m_2 L_2{}^2$

- $J_{12} = m_2 L_2 L_3$

$J_1^{s_1}$ is the moment of inertia of the part on the root side about the center of gravity, s_1, and $J_2^{s_2}$ is that on the tip side about the s_2. Derivation of the equations is explained in section 5.3.2 in detail. The parameters are listed in Table 5-5 of section 5.3.2.

Unlike the edgewise bending, flapwise bending behavior is largely influenced by an aerodynamic damping. The aerodynamic damping is illustrated in Figure 5-20. In the second figure, tower top moves toward the wind direction. Then the relative wind speed on the blade is reduced and the angle of attack is also decreased. A smaller angle of attack leads to lower lift force and drag force. The thrust force is reduced by $d\Delta$ in the figure. Since the tower top moves downwind, reduction of the thrust force means the movement of the wind turbine is disturbed. Likewise the movement of a nacelle upwind increases the angle of attack and the thrust force (see the fourth figure). Thus the nacelle is forced to decelerate. Such phenomena are called aerodynamic damping.
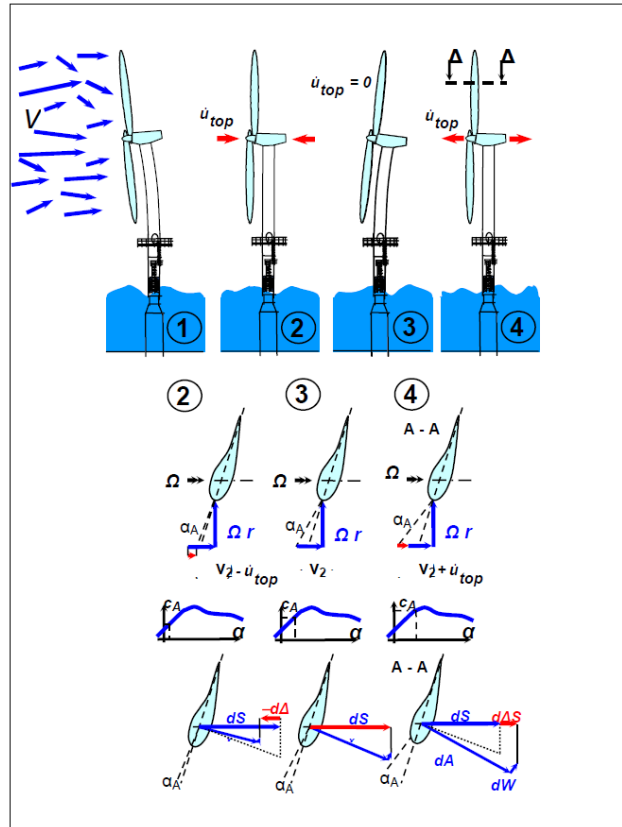
Figure 5-20: aerodynamic damping [31]

As $\dot{\theta}_1 = \dot{\theta}_2 = \ddot{\theta}_1 = \ddot{\theta}_2 = 0$, the equation (5-30) can be simple forms such as:

$$\begin{bmatrix} \theta_1 \\ \theta_2 \end{bmatrix} = \begin{bmatrix} K_1 + K_2 & -K_2 \\ -K_2 & K_2 \end{bmatrix}^{-1} \begin{bmatrix} \{F_{T1}L_1\cos(\theta_1) - F_{T2}L_2\cos(\theta_2 - \theta_1) - F_{c1}L_1\sin(\theta_1) \\ + F_{c2}L_2\sin(\theta_2 - \theta_1) - (m_1L_1 - m_2L_3)g\cos(\alpha)\cos(\theta_1)\} \\ \{F_{T2}L_2\cos(\theta_2 - \theta_1) - F_{c2}L_2\sin(\theta_2 - \theta_1) - m_2g\cos(\alpha)L_2\cos(\theta_2)\} \end{bmatrix} \qquad (5\text{-}31)$$

The flapwise deflection angles, ϑ_1 and ϑ_2, in (5-29) are used for ϑ_{1F} and ϑ_{2F} in (5-26).

6. Pitch angle controller

Pitch controller adjusts pitch angles according to the states of a wind turbine. Limiting generator speed and power is the basic function of the pitch controller. It also reduces load on the components such as blade and tower. The output of the pitch controller is transferred to the pitch angle controller. The pitch angle controller receives a reference pitch angle from the pitch controller and an actual pitch angle from the wind turbine (see Figure 6-1). The pitch angle controller determines the pitch motor torque and sends it to the pitch motors in the wind turbine. The aim of the pitch angle controller is precise tracking of the reference pitch angle by controlling pitch motor moment.

The currently used pitch angle controller is a profile generator. However, a profile generator is not suitable for individual pitch control or tower damping control because of phase delay. The alternative for the profile generator has to be found and it should consider the four effects: sinusoidal reference value, blade's load around pitch axis, Coulomb and sliding friction, and viscous friction coefficient change. These are mentioned in section 2.2.1.

The first problem is sinusoidal reference value which is typical in individual pitch control or tower damping control. Large phase delay in tracking sinusoidal reference value may cause unexpected effect such as instability. Blade's load around pitch axis, the second problem, obstructs pitch angle tracking. The main sources of blade's load are friction due to overturning moment and gravity of a blade. The third problem is Coulomb and sliding friction of the pitch actuation system. The nonlinear frictions are hard to be controlled with a linear controller. The last problem is viscous friction coefficient change. Temperature in the gearbox varies during wind turbine operations and it affects viscosity of lubricant oil in the gearbox. Thus the viscous friction coefficient is not constant.

Various methods are suggested in section 2.2.2 to handle each of the four problems. All the four problems can be solved all together by means of a robust controller. Robust controller can regard blade's load and Coulomb/sliding frictions as disturbance and viscous friction coefficient change as uncertainty. Tracking sinusoidal reference pitch angle is dealt with by means of a reference model and a weighting function.

To compare effects of the robust controller, a classical controller (PD-controller) is suggested as a baseline. A cascade controller is also proposed because it can be easily designed and is known to be robust against disturbances. Whereas a robust controller considers disturbance and uncertainties in the designing step, the classical controllers have to use time domain simulation to validate their robustness.
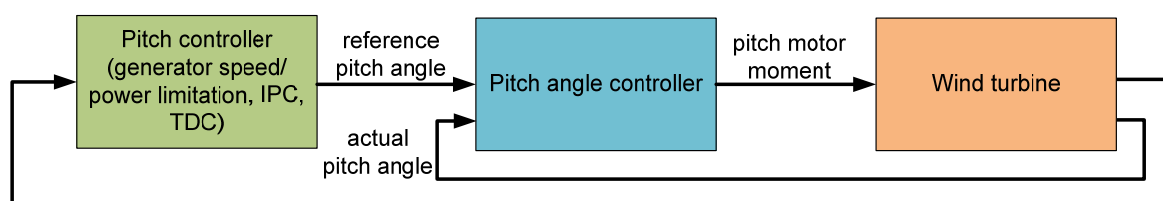
Figure 6-1: Pitch angle controller

6.1. PD controller as a baseline

A PD controller is tested as a baseline. In order to design a PD controller, a linear model of the test rig is required (see (4-4) in section 4.2).

Controller parameters are determined by means of a bode diagram (see Figure 6-2). The phase margin is chosen to be larger than 45° in order to prevent large overshoot. The best parameters are chosen after fine-tuning in the test rig. The integral coefficient can be zero and the PD-controller is designed. The parameters of the PD-controller are:

$$K_p = 2000, K_d = 200$$
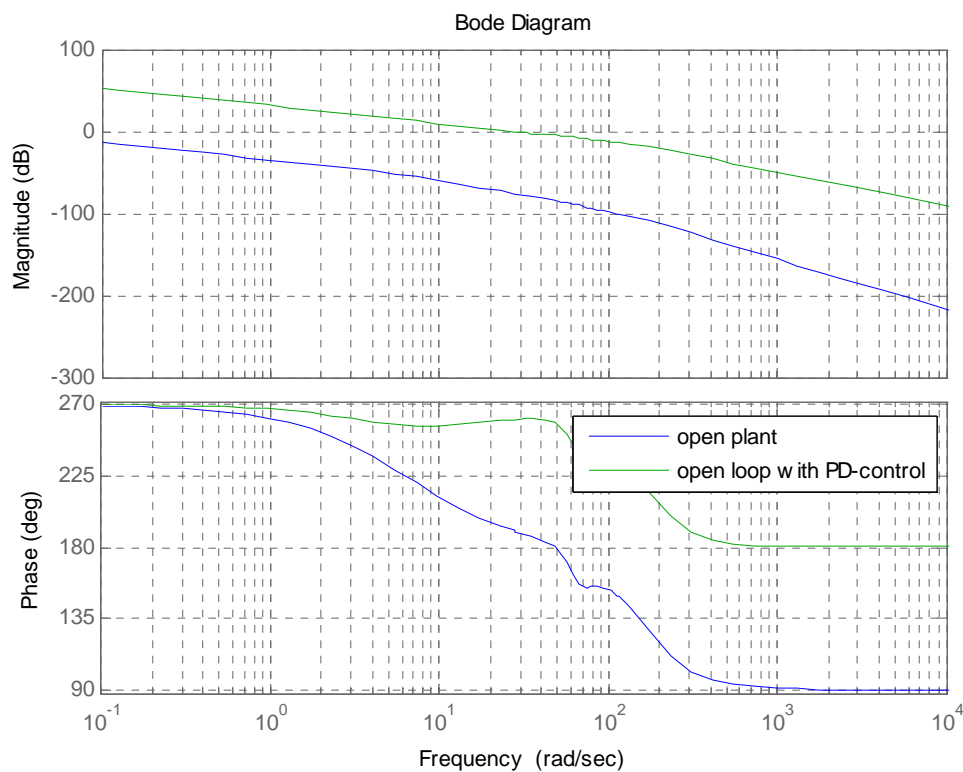
Figure 6-2: Bode diagram with PD controller

Step response in the test rig is seen in Figure 6-3. The stationary error found in the graph is explained as follows.

The linear state space model in section 4.2 is converted to a transfer function with:

$$P(s) = \frac{b_9 s_9 + b_8 s_8 \cdots + b_1 s_1 + b_0}{s_{10} + a_9 s_9 \cdots + a_1 s_1 + a_0}$$

The plant has a numerator with 9th order and a denominator with 10th order. The parameters $b_9, b_8, \cdots b_0, a_{10}, a_9, \cdots a_0$ are real numbers. As the PD controller is connected to the plant like Figure 6-4, the connected transfer function of the controller and the plant is:

$$G(s) = \left(K_p + K_d s\right) P(s) = K_0 \frac{(T_1 s + 1)(T_2 s + 1) \cdots (T_{10} s + 1)}{(P_1 s + 1)(P_2 s + 1) \cdots (P_{10} s + 1)}$$

where $K_0, T_1 \cdots T_{10}, P_1 \cdots P_{10}$ are positive numbers. With the PD control, the numerator and the denominator of the transfer function have the same order.

Steady state error is found like:

$$e_{ss} = \lim_{t \to \infty} e(t) = \lim_{s \to 0} s \cdot E(s) = \lim_{s \to 0} \frac{s}{1 + G(s)} R(s)$$

Since the Laplace function of step input is $1/s$,

$$e_{ss} = \lim_{s \to 0} \frac{s}{1 + G(s)} R(s) = \lim_{s \to 0} \frac{s}{1 + G(s)} \frac{1}{s} = \frac{1}{1 + G(0)} = \frac{1}{1 + K_0}$$

The constant K_0 can be increased by increasing K_p of the PD controller. Thus, increasing K_p of the PD controller reduces the steady state error in the system.
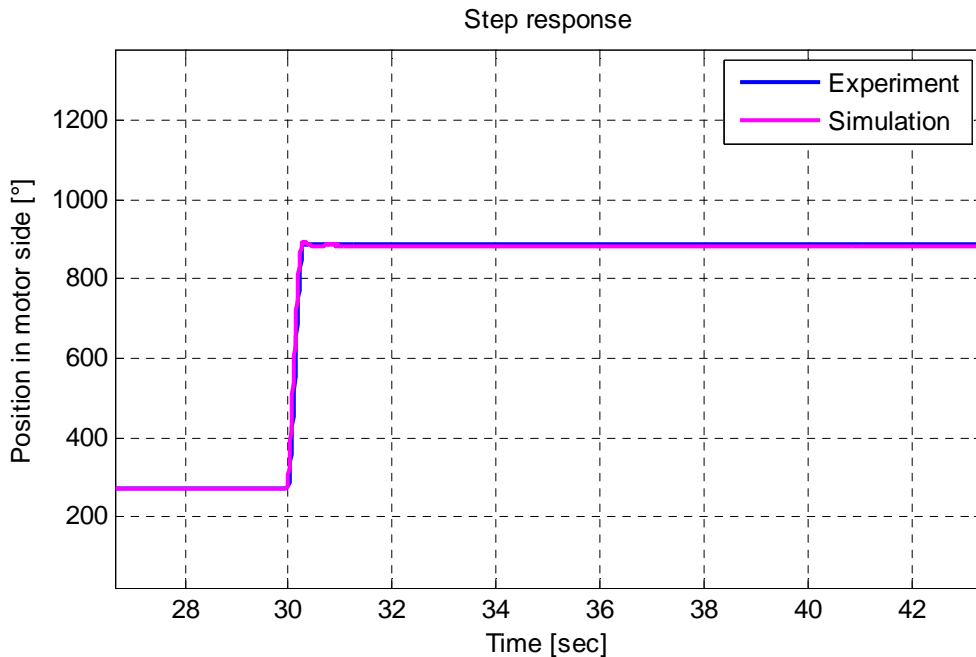
Figure 6-3: Step response with PD controller (experiment)
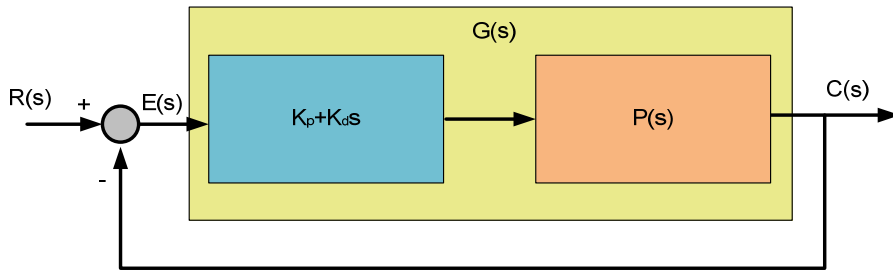
Figure 6-4: Block diagram with PD-controller

6.2. Cascade controller

A cascade controller is a combination of two PID controllers. An outer loop controller controls pitch position while an inner loop controller handles pitch speed (see Figure 6-5). The biggest advantage of a cascade controller is robustness against disturbance. However, a cascade controller acts generally slower than a single PID controller. Parameters of the controller are determined by use of a Bode diagram in Figure 6-6 so that the PD- and PI-controller are chosen as the outer and inner controller. The parameters of the controller are:

control place	Parameter
outer ring – position control	$K_P = 300, \ K_d = 30$
inner ring – velocity control	$K_P = 3, \ K_i = 5$

Table 6-1: Parameters of cascade controller

Step response is seen in Figure 6-7. The actual position reaches to the reference later than PD control, but the steady state error is reduced.

125
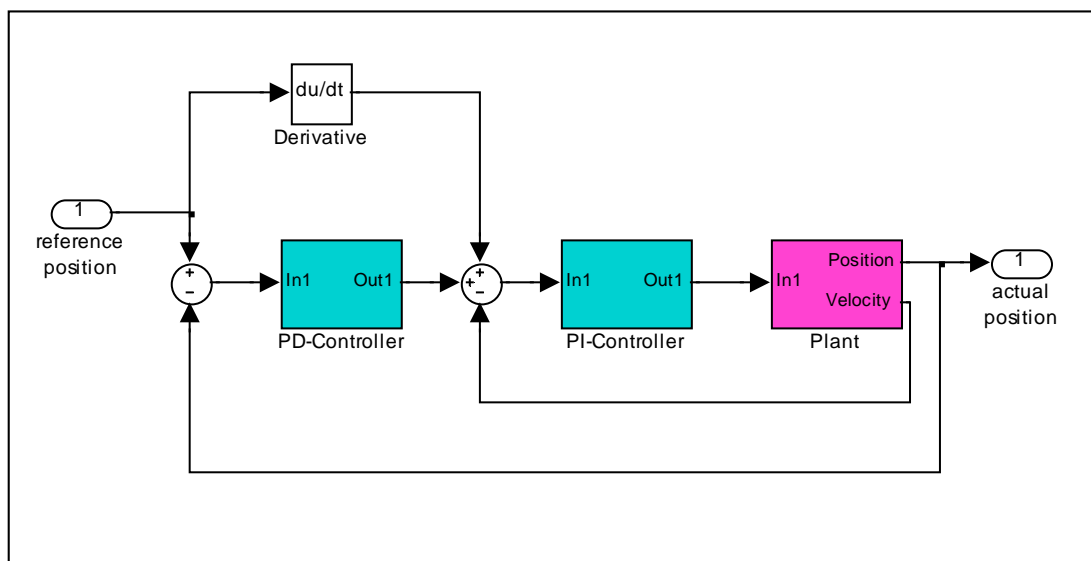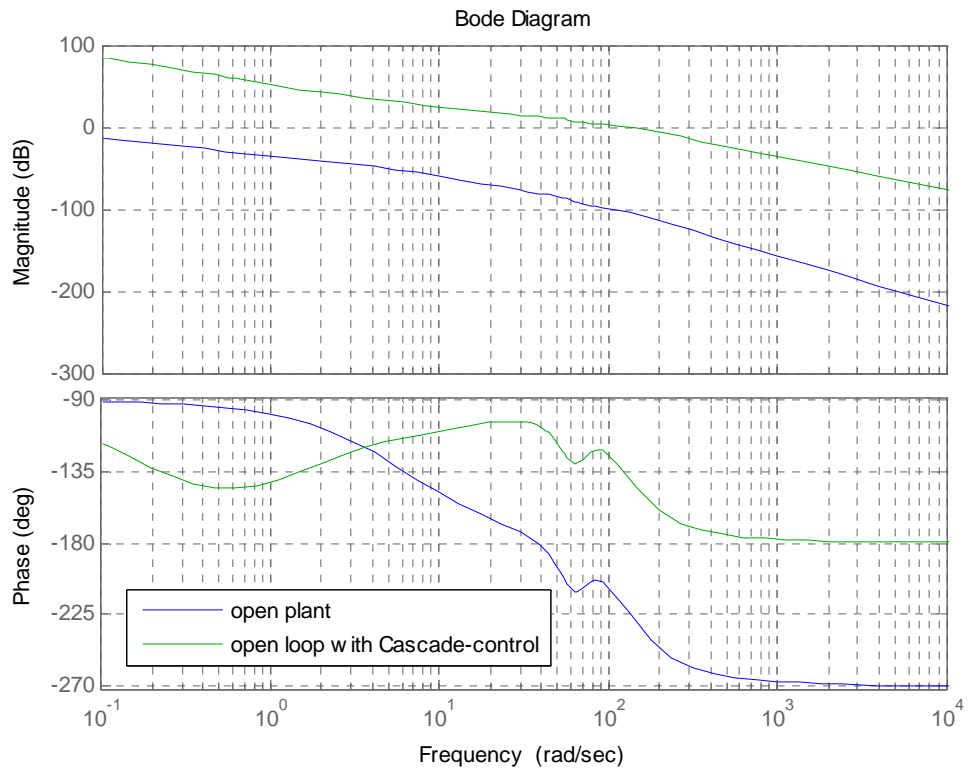
Bode Diagram

Figure 6-6: Bode diagram with cascade controller
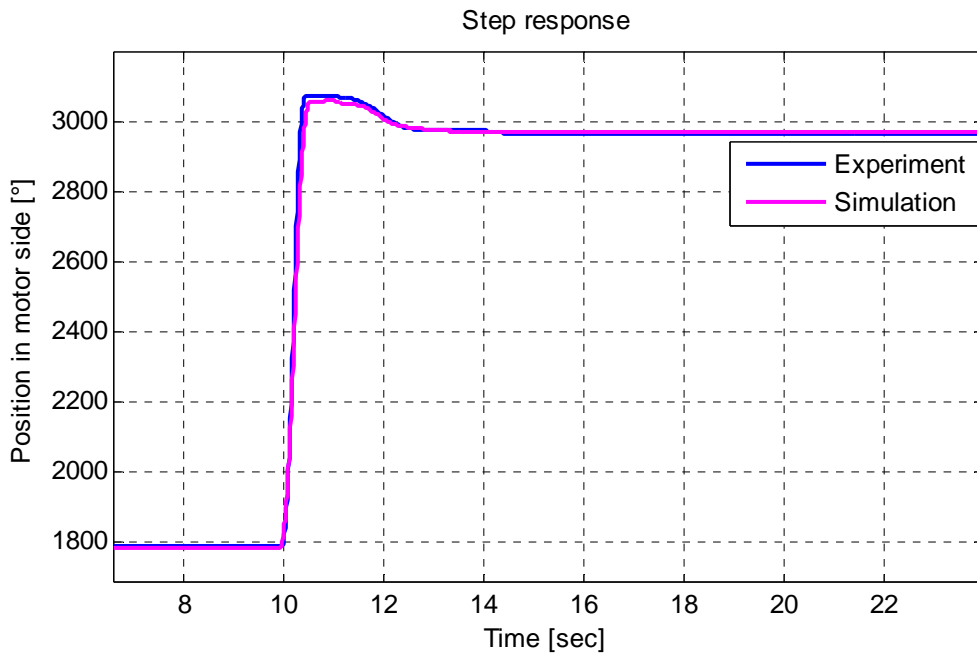
Step response

Figure 6-7: Step response with cascade controller (experiment)

Since an inner loop controller is composed of a PI-controller and the maximum motor moment is limited, anti-windup must be added as in Figure 6-8. Let the anti-windup L_{AW}, the derivative of u_I is like:

$$\dot{u}_I = K_I \cdot e + L_{AW} \cdot (u - u_G) = K_I \cdot e + L_{AW} \cdot (u - u_I - K_P \cdot e) = -L_{AW} \cdot u_I + (K_I - L_{AW} K_P) e + L_{AW} \cdot u$$

In order to make u_I independent from the input e, anti-windup is designed like:

$$L_{AW} = \frac{K_I}{K_P}$$

Then the error term is exclueded from the differential equation like:

$$\dot{u}_I = -L_{AW} \cdot u_I + L_{AW} \cdot u$$
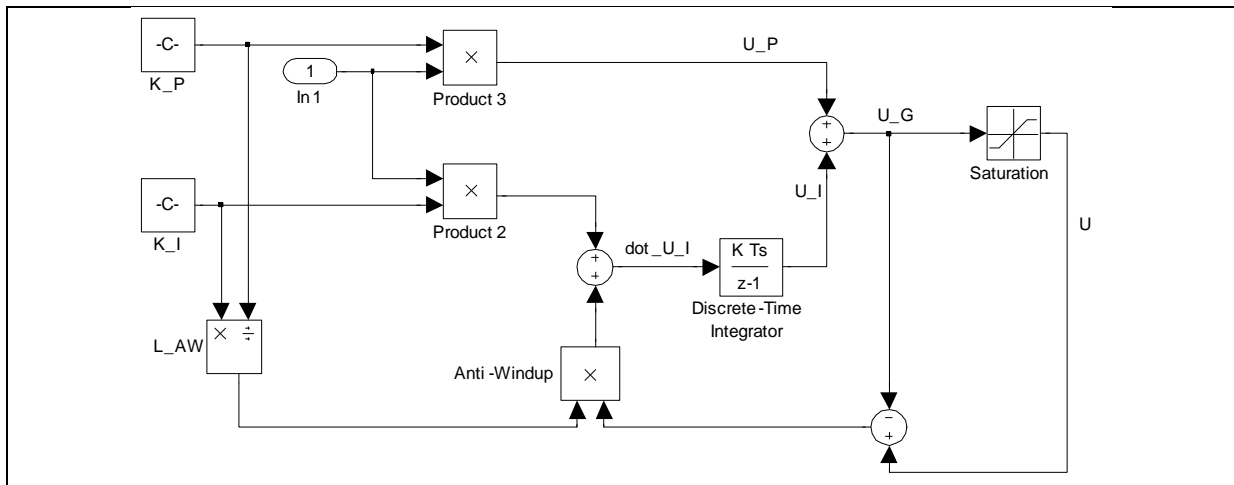
Figure 6-8: PI-controller with Anti-Windup

6.3. Robust controller

6.3.1. Introduction of robust controller

Robust control is a method to ensure stability and performance even though the system implies parameter uncertainties or experiences an outer impulse such as disturbance or noise. Parameter uncertainties and outer impulses are bounded to design a robust controller. Whereas adaptive control is dynamic, robust control is static because system variations are not adapted. Instead, robust control is designed in assumption that certain variables are unknown but bounded.

Robust control includes the five considerations [54]:

- Tracking performance
- Disturbance rejection
- Sensitivity to modeling errors
- Stability margin
- Sensitivity to sensor noise

H_∞ control and μ–synthesis are studied in this research. These are most well-known robust controllers and are implied in the Robust Control Toolbox of Matlab. Thus users have only to designate weighting factors and a reference model. Users do not need to program complex iteration process to build a robust controller.

H_∞ - Loop shaping is also widely used and can be performed with the Robust Control Toolbox. H_∞ - Loop shaping can solve the restrictions on the number of right-half plane poles and is free from pole-zero cancellation between the model and controller [50]. However the controller requires a precompensator and/or a postcompensator (see K_1 in Figure 6-9) in addition to a feedback controller (see K_2 in Figure 6-9). The compensators may enhance performance and stability, but choosing parameters for the compensators in a relative complex system is challenging.
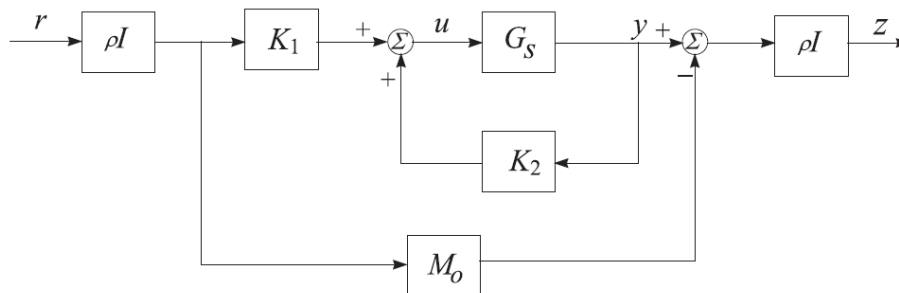
Figure 6-9: H∞ - Loop shaping configuration [50]

An emerging area of robust control is sliding mode control (see Figure 6-10). Sliding mode control is a particular class of variable structure control. It is useful for a wide class of systems including nonlinear, uncertain and time-delayed systems [56]. However, sliding mode control is not contained in the Robust Control Toolbox. Learning and programming sliding mode control might require much time and effort. Thus the controller is not dealt with in this research.
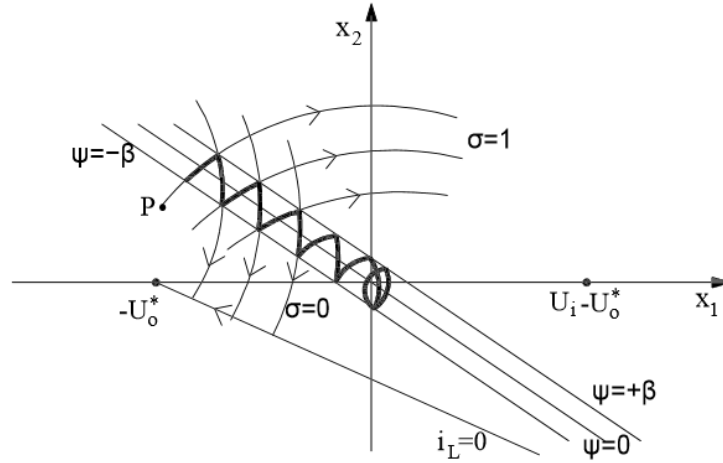
Figure 6-10: sliding mode control [59]

H∞ control

H∞ control was introduced in the late 1970s and early 1980s. The name H∞ control comes from H∞ and H∞ norm. H∞ is the space of functions in the right-half of the complex plane. H∞ norm is the maximum singular value of the function over that space and is the maximum gain in any direction and at any frequency. H∞ control searches for a controller to reduce H∞ norm of transfer functions from reference, disturbance and noise to imaginary outputs (e_y and e_u in Figure 6-14). The singular values must be less than 1. There are two methods for H∞ controller: One is based on Riccati equations and the other uses linear matrix inequalities [55]. H∞ control achieves robust stability against unstructured perturbation and nominal performance. Robust performance can be obtained by means of weighting functions [50].

Good tracking and energy limitation are considered for an example with the following mixed sensitivity function:

$$\min_{K} \left\| \begin{array}{c} \left(I + GK\right)^{-1} \\ K\left(I + GK\right)^{-1} \end{array} \right\|_{\infty} \tag{6-1}$$

The reference tracking is depicted as h_1 and control signal energy is shown as h_2 in Figure 6-11. Then the matrix in (6-1) can be written as:

$$\min_{K} \left\| \begin{array}{c} F_{er} \\ F_{ur} \end{array} \right\|_{\infty} = \min_{K} \left\| \begin{array}{c} F_{h_1 r} \\ F_{h_2 r} \end{array} \right\|_{\infty}$$

F_{er} and F_{ur} mean the closed-loop function from reference (r) to error (e) and control signal (u).
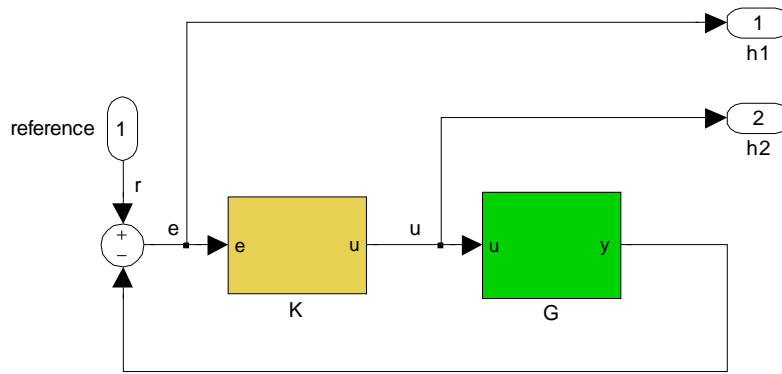
Figure 6-11: Addition of two outputs for a mixed sensitivity consideration

The block diagram in Figure 6-11 can be recast into a standard configuration like Figure 6-12. All the signals are grouped into sets of two inputs and two outputs. Two inputs are external input and control signal. Two outputs are output to the controller and the rest output. The rest output, h, denotes the output signals to be minimized as equation (6-1). The objective is to find a controller, K, to minimize the output, h. Since $w=r$ and $h = (h_1, h_2)$, it is equivalent to minimize the H$_\infty$ norm of the transfer function from w to h.
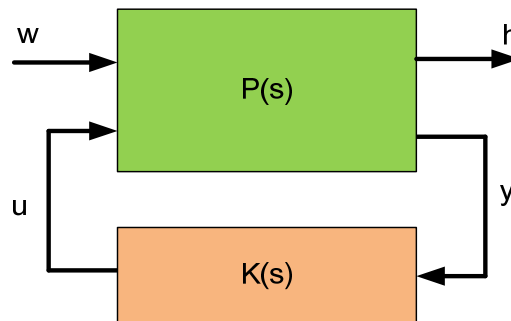
Figure 6-12: standard H$_\infty$ configuration for Figure 6-11

Since the generalized plant, P, has two inputs (w,u) and two outputs (h,y), it can be modeled with 2x2 matrix as:

$$P(s) = \begin{bmatrix} P_{11}(s) & P_{12}(s) \\ P_{21}(s) & P_{22}(s) \end{bmatrix}$$

The transfer function from w to h is expressed as:

$$h = \left[P_{11} + P_{12}K(I - P_{22}K)^{-1}P_{21} \right]w$$
$$= F_L(P,K)w$$

where $F_L(P,K)$ is the lower linear fractional transformation of P and K. The design objective in equation (6-1) can be written as:

$$\min_K \left\| F_L(P, K) \right\|_\infty$$

Inputs and outputs in Figure 6-11 and Figure 6-12 are linked as:

$$w = r, h = \begin{bmatrix} h_1 \\ h_2 \end{bmatrix} = \begin{bmatrix} e \\ u \end{bmatrix}, y = e, u = u$$

Since the error e is difference between the reference and the actual value, the output y and the error e are:

$$y = e = w - G \cdot u$$

Therefore, the generalized plant, P, has:

$$P_{11} = \begin{bmatrix} I \\ 0 \end{bmatrix}, P_{12} = \begin{bmatrix} -G \\ I \end{bmatrix}, P_{21} = I, P_{22} = -G$$

The generalized plant P becomes:

$$P = \begin{bmatrix} I & -G \\ 0 & I \\ I & -G \end{bmatrix}$$

In practical design, weighting function is included for H$_\infty$ control. As the weighting functions (W_1, W_2) are added to the outputs as seen in Figure 6-13, the mixed sensitivity matrix is made as:

$$\min_K \left\| \begin{matrix} W_1(I + GK)^{-1} \\ W_2K(I + GK)^{-1} \end{matrix} \right\|_\infty \tag{6-2}$$

The generalized plant P has new outputs as:

$$h_1 = W_1 \cdot e = W_1 \cdot w - W_1 G \cdot u$$

$$h_2 = W_2 \cdot u$$

$$y = e = w - G \cdot u$$

Therefore, the generalized plant P implies the weighting functions as:

$$P = \begin{bmatrix} W_1 & -W_1 G \\ 0 & W_2 \\ I & -G \end{bmatrix}$$
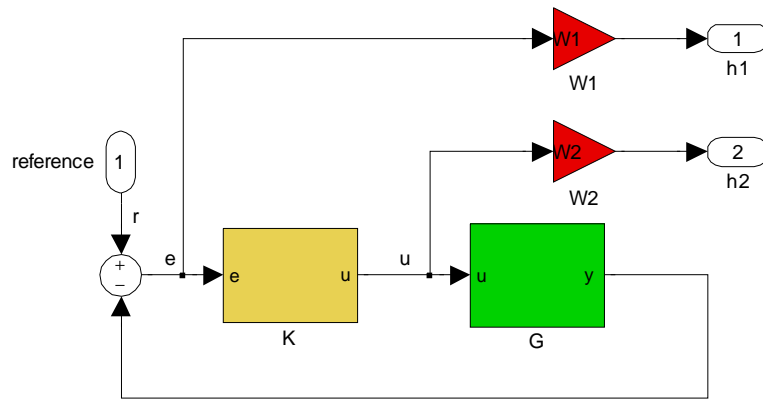
Figure 6-13: block diagram with weighting functions

The current research considers also disturbance and noise. Thus the standard H$_\infty$ configuration for this research has a complex structure as seen in Figure 6-14.
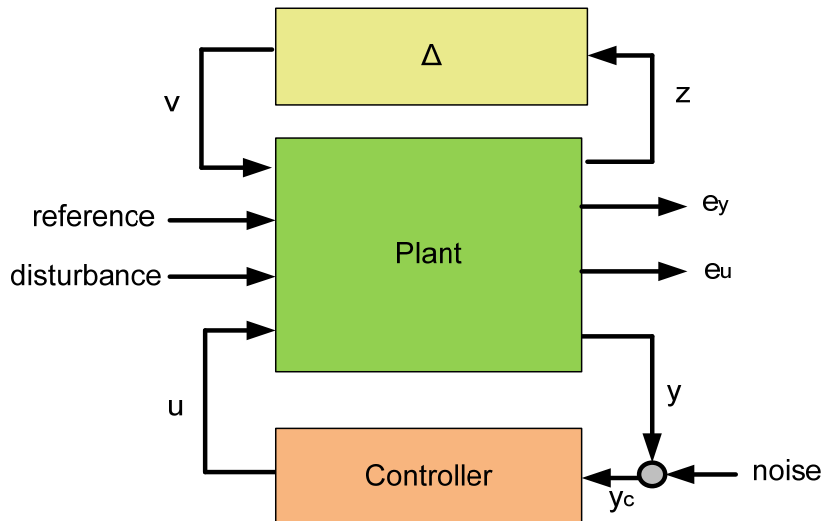
Figure 6-14: standard H$_\infty$ configuration for the current research

μ –synthesis (dk-iteration)

The feedback controller is usually designed based on a nominal plant model. In case perturbation is found in the plant, the performance of the closed-loop system can be unsatisfactory. Robust performance is the criterion to determine performance of a system in the presence of perturbation. In Figure 6-15, uncertainty is contained in the system. *z* and *v* are the input and output signals of the uncertainty block. *w* denotes the exogenous input including reference signal, disturbance, noise. *h* designates the output consisting of tracking error and actuator signal. System performance is decided by transfer function from *w* to *h*. Let *Q* be partitioned as:

$$Q = \begin{bmatrix} Q_{11} & Q_{12} \\ Q_{21} & Q_{22} \end{bmatrix}$$

The closed-loop system is defined with the input w and the output h as:

$$h = [Q_{22} + Q_{21}K(I - Q_{11}K)^{-1}Q_{12}]w$$

$$= F_u(Q, \Delta)w$$

Robust stability means stability of the system with respect to the perturbation Δ. Robust stability is set as:

$$\left\| F_U(Q, \Delta) \right\|_\infty < 1$$

Robust performance is a performance in the presence of the perturbation Δ. Robust performance is defined as:

$$\left\| Q \right\|_\mu < 1$$

where μ is a structured singular value of the system. Thus the maximum magnitude of Q has to be less than 1.
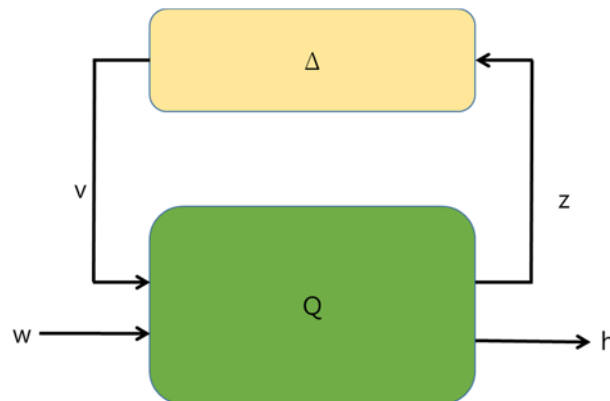
Figure 6-15: standard Q-Δ configuration for robust performance

For controller design, the transfer function Q is divided into a plant (P) and the controller (K) (see Figure 6-16). The plant P is connected to three inputs (v, w, u) and three outputs (z, h, y). The plant P may be partitioned as:

$$P = \begin{bmatrix} P_{11} & P_{12} & P_{13} \\ P_{21} & P_{22} & P_{23} \\ P_{31} & P_{32} & P_{33} \end{bmatrix}$$

The transfer function Q is:

$$Q(P, K) = F_L(P, K) = \begin{bmatrix} P_{11} & P_{12} \\ P_{21} & P_{22} \end{bmatrix} + \begin{bmatrix} P_{13} \\ P_{23} \end{bmatrix} K(I - P_{33}K)^{-1} [P_{31} \quad P_{32}]$$

For robust stability and robust performance, the following equation has to be satisfied with a controller, K:

$$\sup_{\omega \in R}\left(F_L\left(P,K\right)\right) \leq 1$$
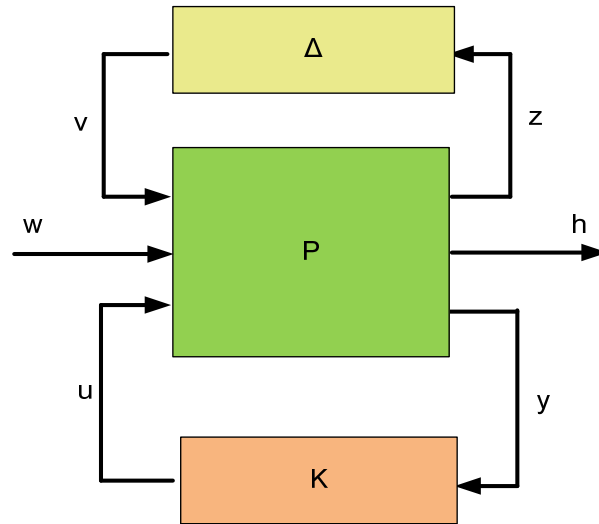
Figure 6-16: standard Q-Δ configuration where Q is divided into a plant and a controller

DK-iteration is used to enhance the performance of μ -synthesis. A controller must satisfy:

$$\sup_{\omega \in R}\left(D_L \cdot F_L\left(P,K\right) \cdot D_R\right) < 1 \qquad \text{(6-3)}$$

where D_L and D_R are the scaling matrix on the left and right side (see Figure 6-17).

As the scaling matrix, D, corresponds to D_L and D_R in Figure 6-17, the DK-iteration is performed in several steps.

Step 1: D is given first. Usually $D=I$.

Step 2: Fix D and calculate K with H$_\infty$ control

Step 3: Fix K and solve D at each frequency, where $\sup_{\omega \in R}\left(D_L \cdot F_L\left(P,K\right) \cdot D_R\right)$ is minimized

Step 4: Curve fit D to get a stable and minimum-phase D.

Step 2-4 are repeated until a pre-specified convergence tolerance or equation (6-3) is achieved.

DK-iteration's convergence is not proven yet. However, the method needs only a few steps to find an optimal controller in practical applications [55].
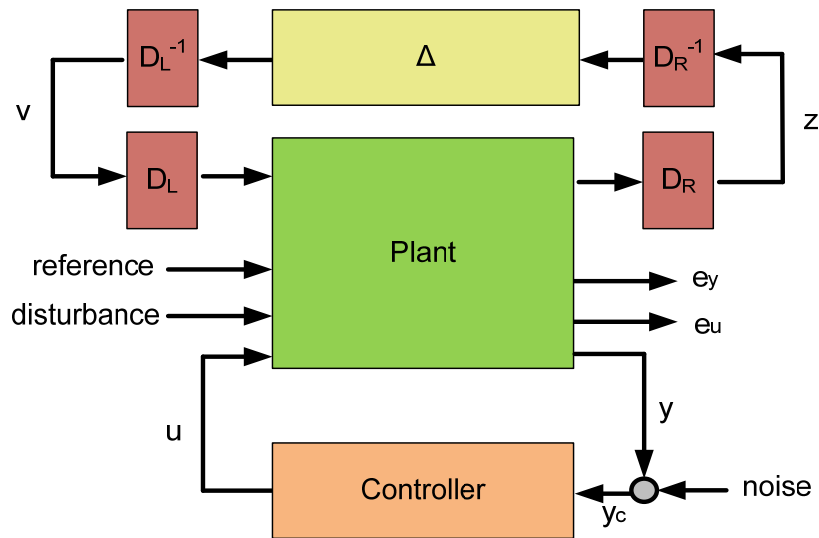
Figure 6-17: standard of μ-synthesis configuration for the current research

H$_\infty$ procedure achieves robust stability and nominal performance [50]. Robust performance is not handled in H$_\infty$ procedure, but user can obtain robust performance by applying appropriate weighting functions. On the contrary, μ –synthesis achieves robust performance in the designing step [50]. μ –synthesis takes structured uncertainty into account in order to reduce conservativeness of H$_\infty$ procedure [57]. μ –synthesis is robust to a more realistic class of perturbation, thus μ –synthesis is less conservative and has more flexibility for control performance [58].

However, μ –synthesis requires a detailed control plant with structured uncertainty knowledge [58]. Since μ –synthesis generates a high-order controller, the order has to be reduced if a low performance computer is used. The controller finding process requires iterative cycles, thus it takes longer time to get the optimum solution in comparison to H$_\infty$ procedure.

6.3.2. Modeling of the test rig for robust controller

State space with unstructured uncertainty

The test rig is modeled with the moment of inertia, J, damping of the shaft, d, stiffness of the shaft, k, viscous friction, f_r, and disturbance, τ. The subscript, *1-4*, is the number of the motor sets and *r* is ring. A single input torque is divided into two torques in the torque distributor, so the input torque, u, is linked only to the first motor set even if two motors act as pitch motors. The differential equation of the test rig is written as:

$$J_1\ddot{\theta}_1 + d_1\left(\dot{\theta}_1 - \dot{\theta}_r\right) + k_1\left(\theta_1 - \theta_r\right) + \tau_1 = u$$

$$J_2\ddot{\theta}_2 + d_2\left(\dot{\theta}_2 - \dot{\theta}_r\right) + k_2\left(\theta_2 - \theta_r\right) + \tau_2 = 0$$

$$J_3\ddot{\theta}_3 + d_3\left(\dot{\theta}_3 - \dot{\theta}_r\right) + k_3\left(\theta_3 - \theta_r\right) + \tau_3 = 0$$

$$J_4\ddot{\theta}_4 + d_4\left(\dot{\theta}_4 - \dot{\theta}_r\right) + k_4\left(\theta_4 - \theta_r\right) + \tau_4 = 0$$

$$J_r\ddot{\theta}_r + \sum_{i=1}^{4}\left\{d_i\left(\dot{\theta}_r - \dot{\theta}_i\right) + k_i\left(\theta_r - \theta_i\right)\right\} + f_r\cdot\dot{\theta}_r + \tau_r = 0$$

$$\Leftrightarrow
\begin{bmatrix}
J_1 & 0 & 0 & 0 & 0 \\
0 & J_2 & 0 & 0 & 0 \\
0 & 0 & J_3 & 0 & 0 \\
0 & 0 & 0 & J_4 & 0 \\
0 & 0 & 0 & 0 & J_r
\end{bmatrix}
\begin{bmatrix}
\ddot{\theta}_1 \\ \ddot{\theta}_2 \\ \ddot{\theta}_3 \\ \ddot{\theta}_4 \\ \ddot{\theta}_r
\end{bmatrix}
+
\begin{bmatrix}
d_1 & 0 & 0 & 0 & -d_1 \\
0 & d_2 & 0 & 0 & -d_2 \\
0 & 0 & d_3 & 0 & -d_3 \\
0 & 0 & 0 & d_4 & -d_4 \\
-d_1 & -d_2 & -d_3 & -d_4 & \sum_{i=1}^{4}d_i + f_r
\end{bmatrix}
\begin{bmatrix}
\dot{\theta}_1 \\ \dot{\theta}_2 \\ \dot{\theta}_3 \\ \dot{\theta}_4 \\ \dot{\theta}_r
\end{bmatrix}
+$$

$$\begin{bmatrix}
k_1 & 0 & 0 & 0 & -k_1 \\
0 & k_2 & 0 & 0 & -k_2 \\
0 & 0 & k_3 & 0 & -k_3 \\
0 & 0 & 0 & k_4 & -k_4 \\
-k_1 & -k_2 & -k_3 & -k_4 & \sum_{i=1}^{4}k_i
\end{bmatrix}
\begin{bmatrix}
\theta_1 \\ \theta_2 \\ \theta_3 \\ \theta_4 \\ \theta_r
\end{bmatrix}
+
\begin{bmatrix}
-1 \\ 0 \\ 0 \\ 0 \\ 0
\end{bmatrix}
\cdot u
=
\begin{bmatrix}
-1 & 0 & 0 & 0 & 0 \\
0 & -1 & 0 & 0 & 0 \\
0 & 0 & -1 & 0 & 0 \\
0 & 0 & 0 & -1 & 0 \\
0 & 0 & 0 & 0 & -1
\end{bmatrix}
\begin{bmatrix}
\tau_1 \\ \tau_2 \\ \tau_3 \\ \tau_4 \\ \tau_r
\end{bmatrix}$$

$$\Leftrightarrow M\cdot\ddot{\Theta} + N\cdot\dot{\Theta} + P\cdot\Theta + G\cdot u = T\cdot d \tag{6-4}$$

with

$$\Theta =
\begin{bmatrix}
\theta_1 \\ \theta_2 \\ \theta_3 \\ \theta_4 \\ \theta_r
\end{bmatrix}
, M =
\begin{bmatrix}
J_1 & 0 & 0 & 0 & 0 \\
0 & J_2 & 0 & 0 & 0 \\
0 & 0 & J_3 & 0 & 0 \\
0 & 0 & 0 & J_4 & 0 \\
0 & 0 & 0 & 0 & J_r
\end{bmatrix}
, N =
\begin{bmatrix}
d_1 & 0 & 0 & 0 & -d_1 \\
0 & d_2 & 0 & 0 & -d_2 \\
0 & 0 & d_3 & 0 & -d_3 \\
0 & 0 & 0 & d_4 & -d_4 \\
-d_1 & -d_2 & -d_3 & -d_4 & \sum_{i=1}^{4}d_i + f_r
\end{bmatrix}
,$$

$$P =
\begin{bmatrix}
k_1 & 0 & 0 & 0 & -k_1 \\
0 & k_2 & 0 & 0 & -k_2 \\
0 & 0 & k_3 & 0 & -k_3 \\
0 & 0 & 0 & k_4 & -k_4 \\
-k_1 & -k_2 & -k_3 & -k_4 & \sum_{i=1}^{4}k_i
\end{bmatrix}
, G =
\begin{bmatrix}
-1 \\ 0 \\ 0 \\ 0 \\ 0
\end{bmatrix}
, T =
\begin{bmatrix}
-1 & 0 & 0 & 0 & 0 \\
0 & -1 & 0 & 0 & 0 \\
0 & 0 & -1 & 0 & 0 \\
0 & 0 & 0 & -1 & 0 \\
0 & 0 & 0 & 0 & -1
\end{bmatrix}
, d =
\begin{bmatrix}
\tau_1 \\ \tau_2 \\ \tau_3 \\ \tau_4 \\ \tau_r
\end{bmatrix}$$

Equation (6-4) can be expressed in a block diagram as Figure 6-18. Since the matrix, M, is invertible, the equation (6-4) can be changed as:

$$\ddot{\Theta} = -M^{-1}N\dot{\Theta} - M^{-1}P\Theta - M^{-1}Gu + M^{-1}Td$$
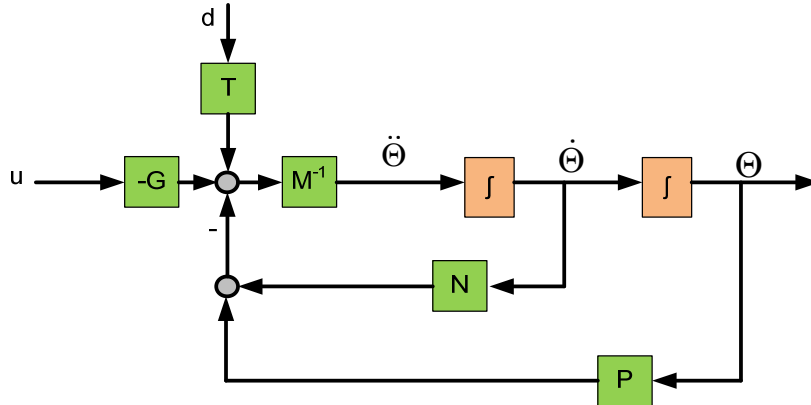
Figure 6-18: block diagram of the test rig model

Let $\begin{bmatrix} x_1 & x_2 & x_3 & x_4 & x_5 \end{bmatrix}^T = \Theta$ and $\begin{bmatrix} x_6 & x_7 & x_8 & x_9 & x_{10} \end{bmatrix}^T = \dot{\Theta}$, the following state space is made:

$$\begin{bmatrix} \dot{x}_1 \\ \vdots \\ \dot{x}_5 \\ \dot{x}_6 \\ \vdots \\ \dot{x}_{10} \end{bmatrix} = \begin{bmatrix} 0_{5\times5} & I_{5\times5} \\ -M^{-1}P & -M^{-1}N \end{bmatrix} \begin{bmatrix} x_1 \\ \vdots \\ x_5 \\ x_6 \\ \vdots \\ x_{10} \end{bmatrix} - \begin{bmatrix} 0_{5x1} \\ M^{-1}Gu \end{bmatrix} + \begin{bmatrix} 0_{5x1} \\ M^{-1}Td \end{bmatrix} \qquad (6\text{-}5)$$

Uncertainty block has to be separated for robust controller design as seen in Figure 6-14 and Figure 6-17. Moment of inertia is divided into normal parameter $\bar{J}_i$ and uncertainty δ_{J_i} as:

$$J_i = \bar{J}_i \cdot \left(1 + p_{J_i} \cdot \delta_{J_i}\right), i = 1,2,3,4,r$$

$$\left| \delta_{J_i} \right| \leq 1$$

The moment of inertia matrix M can be written as:

$$M = \begin{bmatrix} \bar{J}_1\left(1+p_{J_1}\delta_{J_1}\right) & 0 & 0 & 0 & 0 \\ 0 & \bar{J}_2\left(1+p_{J_2}\delta_{J_2}\right) & 0 & 0 & 0 \\ 0 & 0 & \bar{J}_3\left(1+p_{J_3}\delta_{J_3}\right) & 0 & 0 \\ 0 & 0 & 0 & \bar{J}_4\left(1+p_{J_4}\delta_{J_4}\right) & 0 \\ 0 & 0 & 0 & 0 & \bar{J}_r\left(1+p_{J_r}\delta_{J_r}\right) \end{bmatrix}$$

$$= \begin{bmatrix} \bar{J}_1 & 0 & 0 & 0 & 0 \\ 0 & \bar{J}_2 & 0 & 0 & 0 \\ 0 & 0 & \bar{J}_3 & 0 & 0 \\ 0 & 0 & 0 & \bar{J}_4 & 0 \\ 0 & 0 & 0 & 0 & \bar{J}_r \end{bmatrix} + \begin{bmatrix} \bar{J}_1 \cdot p_{J_1} & 0 & 0 & 0 & 0 \\ 0 & \bar{J}_2 \cdot p_{J_2} & 0 & 0 & 0 \\ 0 & 0 & \bar{J}_3 \cdot p_{J_3} & 0 & 0 \\ 0 & 0 & 0 & \bar{J}_4 \cdot p_{J_4} & 0 \\ 0 & 0 & 0 & 0 & \bar{J}_r \cdot p_{J_r} \end{bmatrix} \cdot \begin{bmatrix} \delta_{J_1} & 0 & 0 & 0 & 0 \\ 0 & \delta_{J_2} & 0 & 0 & 0 \\ 0 & 0 & \delta_{J_3} & 0 & 0 \\ 0 & 0 & 0 & \delta_{J_4} & 0 \\ 0 & 0 & 0 & 0 & \delta_{J_r} \end{bmatrix}$$ (6-6)

$$= \bar{M} + M_P \cdot \Delta_M$$

with the nominal matrix $\bar{M}$ and uncertainty matrix Δ_M. The matrix M_p limits range of the uncertainty. Since the magnitude of δ_{J_i}, is limited to be smaller than 1, the size of the uncertainty is decided by p_{J_i}. Uncertainties of moment of inertia coefficient are set based on Table 4-8 and Table 4-9. As the mean, minimum, and maximum moment of inertia are $J_{mean,i}$, $J_{min,i}$, $J_{max,i}$, the factor, p_{J_i}, is determined by:

$$p_{J_i} = \max\left(\frac{J_{max,i} - J_{mean,i}}{J_{mean,i}}, \frac{J_{mean,i} - J_{min,i}}{J_{mean,i}} \right)$$

And $J_{mean,i}$ is used as $\bar{J}_i$. Thus:

$$p_{J_1} = p_{J_2} = 0.1017$$
$$p_{J_3} = p_{J_4} = 0$$
$$p_{J_r} = 0.0794$$

Because the moments of inertia of the two load motors (J_3, J_4) are obtained from the technical specification of the motor (see Figure 4-39), p_{J_3} and p_{J_4} are zero.

In the same way, damping coefficient and friction matrix in (6-5) are also divided as:

$$N = \begin{bmatrix} \bar{d}_1\left(1+p_{d_1}\delta_{d_1}\right) & 0 & 0 & 0 & -\bar{d}_1\left(1+p_{d_1}\delta_{d_1}\right) \\ 0 & \bar{d}_2\left(1+p_{d_2}\delta_{d_2}\right) & 0 & 0 & -\bar{d}_2\left(1+p_{d_2}\delta_{d_2}\right) \\ 0 & 0 & \bar{d}_3\left(1+p_{d_3}\delta_{d_3}\right) & 0 & -\bar{d}_3\left(1+p_{d_3}\delta_{d_3}\right) \\ 0 & 0 & 0 & \bar{d}_4\left(1+p_{d_4}\delta_{d_4}\right) & -\bar{d}_4\left(1+p_{d_4}\delta_{d_4}\right) \\ -\bar{d}_1\left(1+p_{d_1}\delta_{d_1}\right) & -\bar{d}_2\left(1+p_{d_2}\delta_{d_2}\right) & -\bar{d}_3\left(1+p_{d_3}\delta_{d_3}\right) & -\bar{d}_4\left(1+p_{d_4}\delta_{d_4}\right) & \sum_{i=1}^{4}\bar{d}_i\left(1+p_{d_i}\delta_{d_i}\right)+\bar{f}_r\left(1+p_{fr}\delta_{fr}\right) \end{bmatrix}$$

$$= \begin{bmatrix} \overline{d}_1 & 0 & 0 & 0 & -\overline{d}_1 \\ 0 & \overline{d}_2 & 0 & 0 & -\overline{d}_2 \\ 0 & 0 & \overline{d}_3 & 0 & -\overline{d}_3 \\ 0 & 0 & 0 & \overline{d}_4 & -\overline{d}_4 \\ -\overline{d}_1 & -\overline{d}_2 & -\overline{d}_3 & -\overline{d}_4 & \sum_{i=1}^{4} \overline{d}_i + \overline{f}_r \end{bmatrix}$$

$$+ \begin{bmatrix} \overline{d}_1 \cdot p_{d_1} & 0 & 0 & 0 & 0 \\ 0 & \overline{d}_2 \cdot p_{d_2} & 0 & 0 & 0 \\ 0 & 0 & \overline{d}_3 \cdot p_{d_3} & 0 & 0 \\ 0 & 0 & 0 & \overline{d}_4 \cdot p_{d_4} & 0 \\ \overline{d}_1 \cdot p_{d_1} & \overline{d}_2 \cdot p_{d_2} & \overline{d}_3 \cdot p_{d_3} & \overline{d}_4 \cdot p_{d_4} & \overline{f}_r \cdot p_{f_r} \end{bmatrix} \cdot \begin{bmatrix} \delta_{d_1} & 0 & 0 & 0 & 0 \\ 0 & \delta_{d_2} & 0 & 0 & 0 \\ 0 & 0 & \delta_{d_3} & 0 & 0 \\ 0 & 0 & 0 & \delta_{d_4} & 0 \\ 0 & 0 & 0 & 0 & \delta_{f_r} \end{bmatrix} \cdot \begin{bmatrix} 1 & 0 & 0 & 0 & -1 \\ 0 & 1 & 0 & 0 & -1 \\ 0 & 0 & 1 & 0 & -1 \\ 0 & 0 & 0 & 1 & -1 \\ 0 & 0 & 0 & 0 & 1 \end{bmatrix}$$

$$= \overline{N} + N_1 \cdot \Delta_C \cdot N_2$$

with the nominal matrix $\overline{N}$ and uncertainty matrix Δ_C. The matrix N_1 and N_2 determine range of the uncertainty.

The stiffness matrix is also divided into nominal and uncertainty matrices as:

$$P = \begin{bmatrix} \overline{k}_1\left(1 + p_{k_1}\delta_{k_1}\right) & 0 & 0 & 0 & -\overline{k}_1\left(1 + p_{k_1}\delta_{k_1}\right) \\ 0 & \overline{k}_2\left(1 + p_{k_2}\delta_{k_2}\right) & 0 & 0 & -\overline{k}_2\left(1 + p_{k_2}\delta_{k_2}\right) \\ 0 & 0 & \overline{k}_3\left(1 + p_{k_3}\delta_{k_3}\right) & 0 & -\overline{k}_3\left(1 + p_{k_3}\delta_{k_3}\right) \\ 0 & 0 & 0 & \overline{k}_4\left(1 + p_{k_4}\delta_{k_4}\right) & -\overline{k}_4\left(1 + p_{k_4}\delta_{k_4}\right) \\ -\overline{k}_1\left(1 + p_{k_1}\delta_{k_1}\right) & -\overline{k}_2\left(1 + p_{k_2}\delta_{k_2}\right) & -\overline{k}_3\left(1 + p_{k_3}\delta_{k_3}\right) & -\overline{k}_4\left(1 + p_{k_4}\delta_{k_4}\right) & \sum_{i=1}^{4} \overline{k}_i\left(1 + p_{k_i}\delta_{k_i}\right) \end{bmatrix}$$

$$= \begin{bmatrix} \overline{k}_1 & 0 & 0 & 0 & -\overline{k}_1 \\ 0 & \overline{k}_2 & 0 & 0 & -\overline{k}_2 \\ 0 & 0 & \overline{k}_3 & 0 & -\overline{k}_3 \\ 0 & 0 & 0 & \overline{k}_4 & -\overline{k}_4 \\ -\overline{k}_1 & -\overline{k}_2 & -\overline{k}_3 & -\overline{k}_4 & \sum_{i=1}^{4} \overline{k}_i \end{bmatrix} +$$

$$\begin{bmatrix} \overline{k}_1 \cdot p_{k_1} & 0 & 0 & 0 \\ 0 & \overline{k}_2 \cdot p_{k_2} & 0 & 0 \\ 0 & 0 & \overline{k}_3 \cdot p_{k_3} & 0 \\ 0 & 0 & 0 & \overline{k}_4 \cdot p_{k_4} \\ -\overline{k}_1 \cdot p_{k_1} & -\overline{k}_2 \cdot p_{k_2} & -\overline{k}_3 \cdot p_{k_3} & -\overline{k}_4 \cdot p_{k_4} \end{bmatrix} \cdot \begin{bmatrix} \delta_{k_1} & 0 & 0 & 0 \\ 0 & \delta_{k_2} & 0 & 0 \\ 0 & 0 & \delta_{k_3} & 0 \\ 0 & 0 & 0 & \delta_{k_4} \end{bmatrix} \begin{bmatrix} 1 & 0 & 0 & 0 & -1 \\ 0 & 1 & 0 & 0 & -1 \\ 0 & 0 & 1 & 0 & -1 \\ 0 & 0 & 0 & 1 & -1 \end{bmatrix}$$

$$= \overline{P} + P_1 \cdot \Delta_P \cdot P_2$$

with the nominal matrix $\bar{P}$ and uncertainty matrix Δ_P. The matrix P_1 and P_2 determine range of the uncertainty.

The uncertainty range of damping coefficient and spring coefficient can be determined as:

$$p_{d_i} = \max\left(\frac{d_{max,i} - d_{mean,i}}{d_{mean,i}}, \frac{d_{mean,i} - d_{min,i}}{d_{mean,i}} \right), i = 1,2,3,4$$

$$p_{k_i} = \max\left(\frac{k_{max,i} - k_{mean,i}}{k_{mean,i}}, \frac{k_{mean,i} - k_{min,i}}{k_{mean,i}} \right), i = 1,2,3,4$$

The damping coefficient and spring coefficient have such uncertainties according to Table 4-13 and Table 4-14:

$$p_{d_1} = p_{d_2} = 0.2941$$
$$p_{d_3} = p_{d_4} = 0.2667$$
$$p_{k_1} = p_{k_2} = 0.5800$$
$$p_{k_3} = p_{k_4} = 0.3228$$

The nominal damping coefficient and spring coefficient are determined as:

$$\bar{d}_i = d_{mean,i}, i = 1,2,3,4$$
$$\bar{k}_i = k_{mean,i}, i = 1,2,3,4$$

Amplitude of the uncertainty elements, $\delta_{J_i}, \delta_{d_i}, \delta_{k_i}, \delta_{f_r}$, are smaller than 1. The viscous friction coefficient varies greatly depending on temperature as described in section 4.3.1, so nominal and range of the viscous friction is:

$$\bar{f}_r = \frac{f_{r,max} + f_{r,min}}{2} = 1.5961 \cdot 10^4, p_{f_r} = \frac{f_{r,max} - f_{r,min}}{f_{r,max} + f_{r,min}} = 0.6528$$

where $f_{r,max}, f_{r,min}$ are the maximum and minimum viscous friction coefficients in Table 4-1.

The equation (6-5) is described with uncertainties ($\Delta_M, \Delta_C, \Delta_P$) as:

$$\begin{bmatrix} \dot{x}_1 \\ \vdots \\ \dot{x}_5 \\ \dot{x}_6 \\ \vdots \\ \dot{x}_{10} \end{bmatrix} = \begin{bmatrix} 0_{5\times5} & I_{5\times5} \\ -\left(\bar{M} + M_P \cdot \Delta_M\right)^{-1}\left(\bar{P} + P_1 \cdot \Delta_P \cdot P_2\right) & -\left(\bar{M} + M_P \cdot \Delta_M\right)^{-1}\left(\bar{N} + N_1 \cdot \Delta_C \cdot N_2\right) \end{bmatrix} \begin{bmatrix} x_1 \\ \vdots \\ x_5 \\ x_6 \\ \vdots \\ x_{10} \end{bmatrix}$$

$$-\begin{bmatrix} 0_{5\times1} \\ \left(\bar{M} + M_P \cdot \Delta_M\right)^{-1} Gu \end{bmatrix} + \begin{bmatrix} 0_{5\times1} \\ \left(\bar{M} + M_P \cdot \Delta_M\right)^{-1} Td \end{bmatrix}$$

(6-7)

Block diagram in Figure 6-18 is modified with uncertainty as in Figure 6-19.
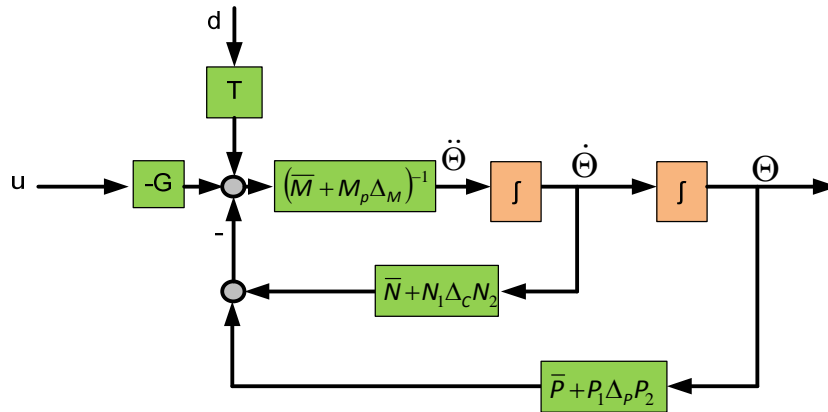
Figure 6-19: block diagram of the test rig model with unstructured uncertainty

State space with structured uncertainty

State space for the test rig is made with uncertainties (Δ_M, Δ_C, Δ_P) in equation (6-7). However, the uncertainties have to be isolated in order to design a robust controller like the uncertainty block Δ and plant block in Figure 6-14 and Figure 6-17.

Uncertainty in the inversed moment of inertia can be separated as seen in Figure 6-20. The output, $\ddot{\Theta}$, is expressed with a temporary input, x_{in}, as:

$$\ddot{\Theta} = \left(\overline{M} + M_P \Delta_M\right)^{-1} x_{in}$$

As the matrix, M_P, and the uncertainty, Δ_M, is feedbacked like the right diagram in Figure 6-20, the output, $\ddot{\Theta}$, is modified as:

$$
\begin{aligned}
\ddot{\Theta} &= \overline{M}^{-1}\left(x_{in} - M_P \Delta_M \ddot{\Theta}\right) \\
&= \overline{M}^{-1} x_{in} - \overline{M}^{-1} M_P \Delta_M \ddot{\Theta} \\
\Leftrightarrow \ddot{\Theta} &= \left(1 + \overline{M}^{-1} M_P \Delta_M\right)^{-1} \overline{M}^{-1} x_{in} \\
&= \left(\overline{M}\left(1 + \overline{M}^{-1} M_P \Delta_M\right)\right)^{-1} x_{in} \\
&= \left(\overline{M} + M_P \Delta_M\right)^{-1} x_{in}
\end{aligned}
$$
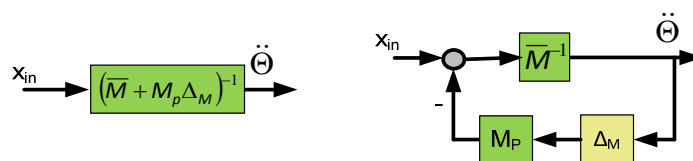
Figure 6-20: inversed moment of inertia block with unstructured uncertainty (left) and with structured uncertainty (right)

Uncertainties in the damping and stiffness blocks in Figure 6-19 can be separated in an easy way like Figure 6-21.

Let the outputs of the plant to the uncertainty z_J, z_C, z_K and the inputs of the plant from the uncertainty v_J, v_C, v_K, uncertainties (Δ_M, Δ_C, Δ_P) in Figure 6-19 are separated as seen in Figure 6-22.
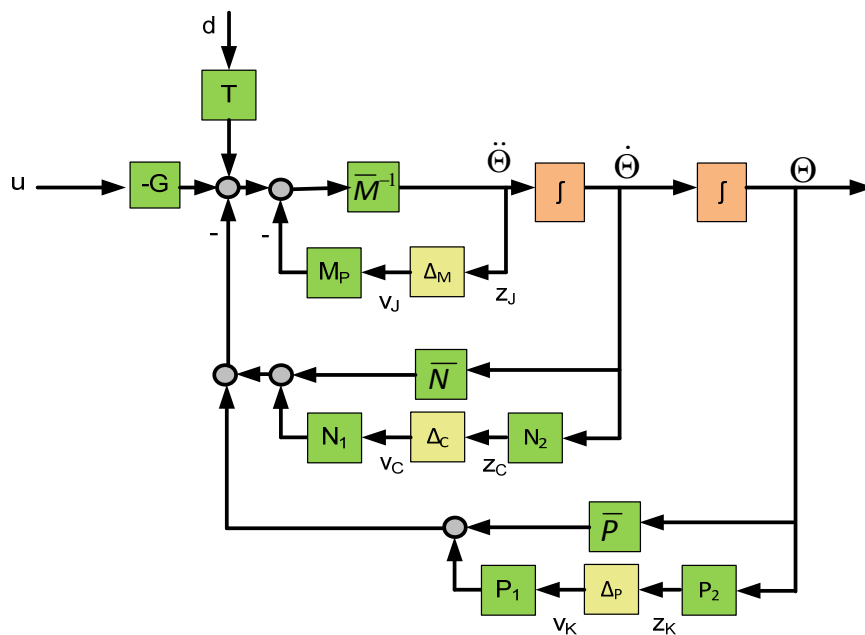
Figure 6-22: block diagram of the test rig model with structured uncertainty

From the block diagram in Figure 6-22, the following equations can be drawn:

$$\ddot{\Theta} = \overline{M}^{-1}\left(-M_P v_J - \overline{N}\dot{\Theta} - N_1 v_C - \overline{P}\Theta - P_1 v_K - Gt_m + Td\right)$$

$$= -\overline{M}^{-1}\overline{P}\Theta - \overline{M}^{-1}\overline{N}\dot{\Theta} - \overline{M}^{-1}M_P v_J - \overline{M}^{-1}N_1 v_C - \overline{M}^{-1}P_1 v_K - \overline{M}^{-1}Gu + \overline{M}^{-1}Td$$

$$z_J = \ddot{\Theta}$$

$$= -\overline{M}^{-1}\overline{P}\Theta - \overline{M}^{-1}\overline{N}\dot{\Theta} - \overline{M}^{-1}M_P v_J - \overline{M}^{-1}N_1 v_C - \overline{M}^{-1}P_1 v_K - \overline{M}^{-1}Gu + \overline{M}^{-1}Td$$

$$z_C = N_2 \dot{\Theta}$$

$$z_K = P_2 \Theta$$

(6-8)

Let the state space variables $\begin{bmatrix} x_1 & x_2 & x_3 & x_4 & x_5 \end{bmatrix}^T = \Theta$, $\begin{bmatrix} x_6 & x_7 & x_8 & x_9 & x_{10} \end{bmatrix}^T = \dot{\Theta}$, and the ring position defined as the output of the model as $y = \theta_r = x_5$, the equation (6-8) and y can be expressed with the state space variables as:

$$\begin{bmatrix} \dot{x}_1 \\ \dot{x}_2 \\ \dot{x}_3 \\ \dot{x}_4 \\ \dot{x}_5 \end{bmatrix} = \begin{bmatrix} x_6 \\ x_7 \\ x_8 \\ x_9 \\ x_{10} \end{bmatrix}$$

$$\begin{bmatrix} \dot{x}_6 \\ \dot{x}_7 \\ \dot{x}_8 \\ \dot{x}_9 \\ \dot{x}_{10} \end{bmatrix} = -\overline{M}^{-1}\overline{P}\begin{bmatrix} x_1 \\ x_2 \\ x_3 \\ x_4 \\ x_5 \end{bmatrix} - \overline{M}^{-1}\overline{N}\begin{bmatrix} x_6 \\ x_7 \\ x_8 \\ x_9 \\ x_{10} \end{bmatrix} - \overline{M}^{-1}M_P v_J - \overline{M}^{-1}N_1 v_C - \overline{M}^{-1}P_1 v_K + \overline{M}^{-1}Td - \overline{M}^{-1}Gu$$

$$z_J = -\overline{M}^{-1}\overline{P}\begin{bmatrix} x_1 \\ x_2 \\ x_3 \\ x_4 \\ x_5 \end{bmatrix} - \overline{M}^{-1}\overline{N}\begin{bmatrix} x_6 \\ x_7 \\ x_8 \\ x_9 \\ x_{10} \end{bmatrix} - \overline{M}^{-1}M_P v_J - \overline{M}^{-1}N_1 v_C - \overline{M}^{-1}P_1 v_K + \overline{M}^{-1}Td - \overline{M}^{-1}Gu$$

<div align="right">(6-9)</div>

$$z_C = N_2 \begin{bmatrix} x_6 \\ x_7 \\ x_8 \\ x_9 \\ x_{10} \end{bmatrix}$$

$$z_K = P_2 \begin{bmatrix} x_1 \\ x_2 \\ x_3 \\ x_4 \\ x_5 \end{bmatrix}$$

$$y = \begin{bmatrix} 0 & 0 & 0 & 0 & 1 \end{bmatrix} \begin{bmatrix} x_1 \\ x_2 \\ x_3 \\ x_4 \\ x_5 \end{bmatrix}$$

The equation (6-9) of the plant is described with a 30x25 matrix as follows.

$$
\begin{bmatrix} \dot{x}_1 \\ \vdots \\ \dot{x}_5 \\ \dot{x}_6 \\ \vdots \\ \dot{x}_{10} \\ - \\ z_J \\ z_c \\ z_k \\ - \\ y \end{bmatrix}
=
\left[\begin{array}{ccc|cccc|ccc}
0_{5\times5} & I_{5\times5} & | & & 0_{5\times14} & & | & & 0_{5\times6} & \\
-\overline{M}^{-1}\overline{P} & -\overline{M}^{-1}\overline{N} & | & -\overline{M}^{-1}M_P & -\overline{M}^{-1}N_1 & -\overline{M}^{-1}P_1 & | & -\overline{M}^{-1}T & & -\overline{M}^{-1}G \\
- & - & + & - & - & - & + & - & - & - \\
-\overline{M}^{-1}\overline{P} & -\overline{M}^{-1}\overline{N} & | & -\overline{M}^{-1}M_P & -\overline{M}^{-1}N_1 & -\overline{M}^{-1}P_1 & | & -\overline{M}^{-1}T & & -\overline{M}^{-1}G \\
0_{5\times5} & N_2 & | & & 0_{5\times14} & & | & & 0_{5\times6} & \\
P_2 & 0_{4\times5} & | & & 0_{4\times14} & & | & & 0_{4\times6} & \\
- & - & + & - & - & - & + & - & - & - \\
0,0,0,0,1 & 0_{1\times5} & | & & 0_{1\times14} & & | & & 0_{1\times6} &
\end{array}\right]
\cdot
\begin{bmatrix} x_1 \\ \vdots \\ x_5 \\ x_6 \\ \vdots \\ x_{10} \\ - \\ v_J \\ v_c \\ v_k \\ - \\ d \\ u \end{bmatrix}
\qquad \text{(6-10)}
$$

The state space of the plant in equation (6-10) and uncertainty block is expressed in Figure 6-23.
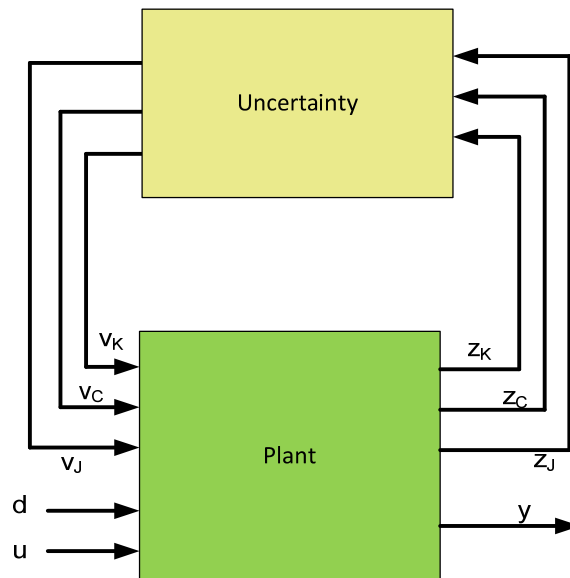
Figure 6-23: uncertainty and plant blocks for robust control design

6.3.3. Robust controller design

A control path must be modeled first to design a controller. Parameters of the control path model such as moment of inertia, stiffness and damping are measured, but the value is not always correct. In particular, viscous friction coefficient changes greatly according to temperature in the gearbox (see section 4.3.1 in detail), thus exact parameters cannot be obtained. A robust controller handles the parameter uncertainties in the Uncertainty-block of Figure 6-24. Coulomb and sliding friction as well as blade load are considered in the *Wd*-block. Noise is filtered through the *Wn*-block. Motor

torque is limited with the *Wu*-block. The *Wp*-block controls performance by comparing the reference model and actual outputs.

Figure 6-24: Structure of H∞ controller

Figure 6-25: Structure of μ–synthesis

By use of the weighting functions and a reference model, a closed-loop system of Figure 6-24 and Figure 6-25 can be written as:

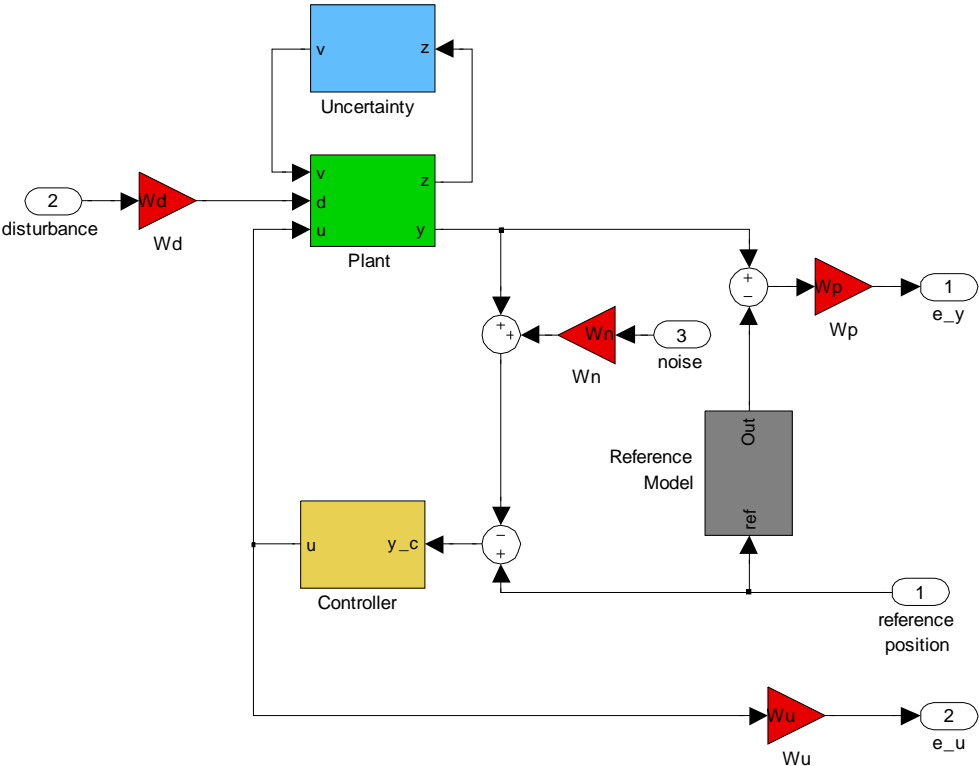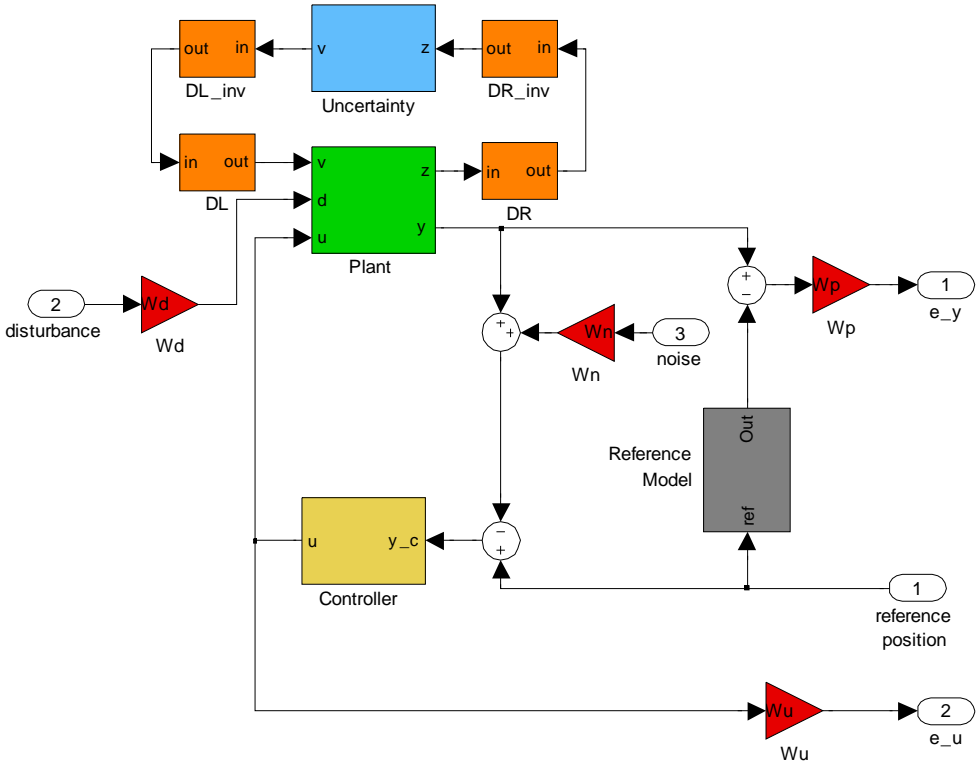$$\begin{bmatrix} e_y \\ e_u \end{bmatrix} = \begin{bmatrix} W_P\left(\dfrac{GK}{I+GK}-M\right) & W_P\dfrac{G}{I+GK}W_d & -W_P\dfrac{GK}{I+GK}W_n \\ W_u\dfrac{K}{I+GK} & -W_u\dfrac{KG}{I+GK}W_d & -W_u\dfrac{K}{I+GK}W_n \end{bmatrix} \cdot \begin{bmatrix} ref \\ dist \\ noise \end{bmatrix} \qquad (6\text{-}11)$$

The structures of H$_\infty$ control and μ–synthesis have three inputs – reference position, disturbance, noise – and two outputs - e_y and e_u . Their frequency area must be taken into account in making the reference model and four weighting functions -*Wp, Wu, Wd, Wn*. The four blocks – D$_L$, D$_R$, D$_L$$^{-1}$, D$_R$$^{-1}$- in μ–synthesis are determined automatically by Robust Control Toolbox in Matlab.

The first input is reference position. The shape of reference position is a combination of constant, ramp and harmonic form. The frequency of the harmonic signal can be 1P, 2P, 3P, …, but 1P and 3P are usually used for individual pitch control and tower damping control. P means periodic loading. 1P is calculated from rotational speed. The rotational speed is determined by means of tip speed ratio, blade length, hub radius and rated wind speed. Tip speed ratio is assumed to be 7 and the wind speed at rated generator speed is assumed to be 12m/s. 40m blade in Risø [29] is used in this research and hub radius is set to be 1m. The rotational speed, 1P, is determined as:

$$1P = \frac{7\cdot 12}{40+1}\cdot\frac{1}{2\pi} \approx 0.33Hz$$

3P is three times of 1P, thus around 1Hz. The frequency range is used to design the reference model, *M*.

The second input is disturbance. Disturbance contains nonlinear frictions and load simulation. The nonlinear friction is Coulomb and sliding frictions, which change if sign of pitch rate changes. Thus the frequency range for nonlinear friction is the same as that of actual pitch angles. Another part of disturbance is load simulation. As written in section 5, load simulation is composed of gravity, aerodynamic force, centrifugal loading, friction due to overturning moment and blade's moment of inertia. Gravity, aerodynamic force and centrifugal loading are influence by actual pitch angle. Pitch angle is found in the equations of gravity and centrifugal loading (see (5-1), (5-2)). Aerodynamic force is determined by lift and drag forces, which rely on pitch angle. Blade's moment of inertia is affected by gravity, aerodynamic force and centrifugal loading, thus it is also influenced by actual pitch angle. Friction due to overturning moment is changed when sign of the actual pitch rate changes. Assuming vibrations of the actual pitch angle are negligible in high frequency, the frequency range of the actual pitch angle is the same as that of the reference pitch angle. Thus the disturbance weighting function - *Wd* – can be designed with the frequency of the reference pitch angle. The amplitudes of nonlinear friction and load simulation are used to determine the gains of *Wd*.

The third input is sensor noise. Unlike the previous two inputs, sensor noise is not related to the reference pitch angle. The frequency and amplitude of sensor noise are obtained from measurements in the test rig.

The rest two weighting functions - *Wp, Wu* – are not related directly to the inputs. The two weighting functions are designed to increase tracking performance, make robust against noise and disturbance and limit the motor torque as long as the two outputs stay less than 1 in equation (6-11). Since the sensor noise has little influence on the outputs in the simulation, frequencies of *Wp* and *Wu* are also coupled with those of the two inputs- reference position and disturbance. The gains of *Wp* and *Wu* are determined only by means of closed loop functions such as sensitivity or complementary sensitivity.

User designates the reference model -*M*- and four weighting functions -*Wp, Wu, Wd, Wn*. Then the robust control toolbox in Matlab searches for the best controller with the weighting functions and the reference model. Robust control design must adequately attenuate noise and reduce disturbance effects in the presence of parameter uncertainties.

Sensor noise weighting function

Wn defines frequency and amplitude of sensor noise. As shown in Figure 6-24, sensor noise is added to output of the plant. Noise exists in high frequencies, so noise weighting function is determined to be a high-pass filter (see Figure 6-26). The signals of the test rig are transferred in every 0.01 second with the minimum resolution of position 0.001°. In case torque sum of the four motors are around zero, motors do not rotate and motor positions are constant. No vibration is found in the transferred data. Thus either frequency of the sensor noise is higher than 100Hz or magnitude of the noise is lower than 0.001°. Noise weighting function has a gain=0.001° and frequency in numerator = 100Hz. Since the noise weighting function is a high-pass filter, the frequency in denominator is larger than 100Hz. 1000Hz is chosen in this research. *i* is gear ratio.

$$W_n = 0.001 \cdot \frac{\pi}{180} \cdot \frac{1}{i} \cdot \frac{\dfrac{1}{2\pi \cdot 100}s+1}{\dfrac{1}{2\pi \cdot 1000}s+1}$$
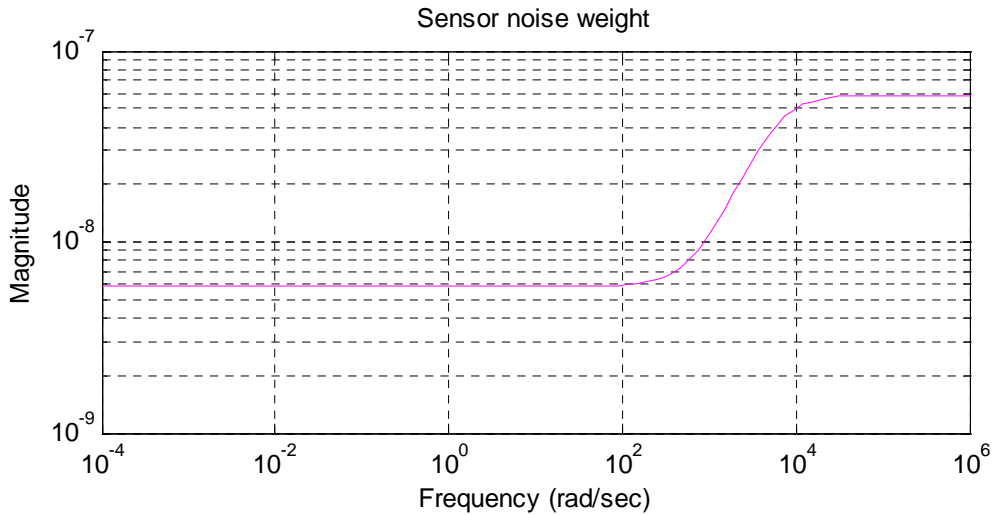
Figure 6-26: Noise weighting function

Reference model

The reference model is designed as a second order system like the equation.

$$M_0 = \frac{\omega_0{}^2}{s^2 + 2\zeta\omega_0 s + \omega_0{}^2}$$

The damping ratio, ζ, is assumed $1/\sqrt{2}$ for critical damping. The undamped natural frequency, ω_0, is chosen to be 4 Hz according to its settling time. Settling time is determined as:

$$T_{settle} = \frac{ln(0.02)}{\zeta \,\omega_0} = \frac{3.9}{\frac{1}{\sqrt{2}}(4 \cdot 2\pi)} \approx 0.22 sec$$

Modal frequency response of the reference model is expressed in Figure 6-27. Settling time is defined as the time required for the step response (see Figure 6-28) to reach within a range of certain percentage (usually 5% or 2%) of the final value. As the sine signal is given as an input, the actual value follows the reference value 0.02 seconds later, thus the phase angle is 0.02 sec/3 sec=2.4°.
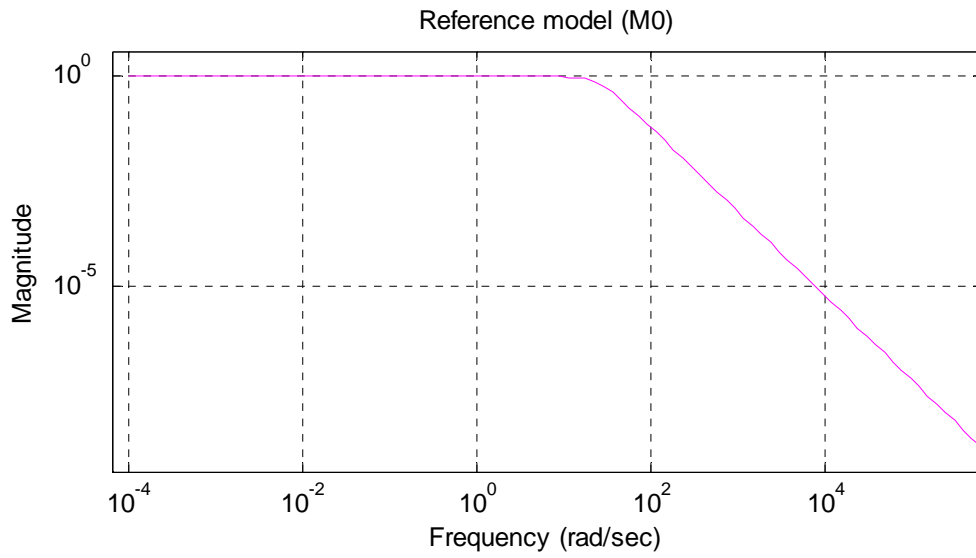
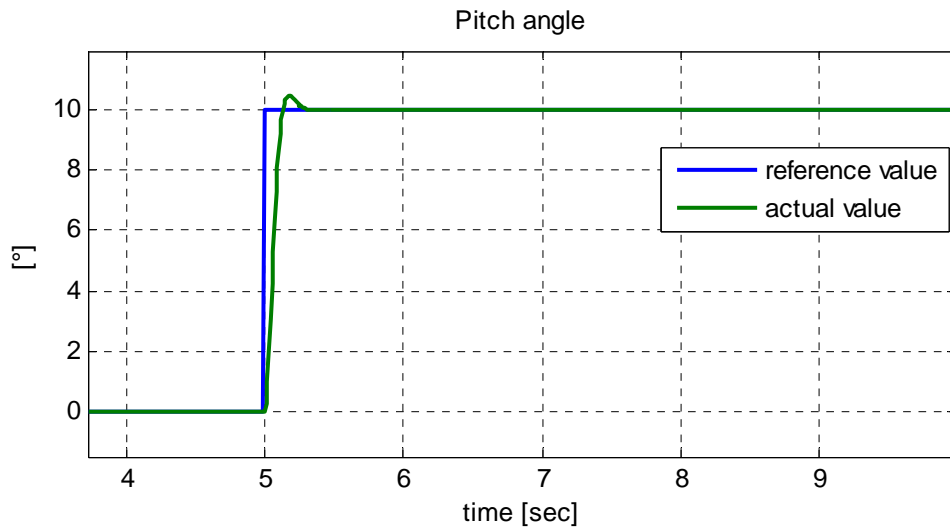**Figure 6-27: Modal frequency response of reference model**

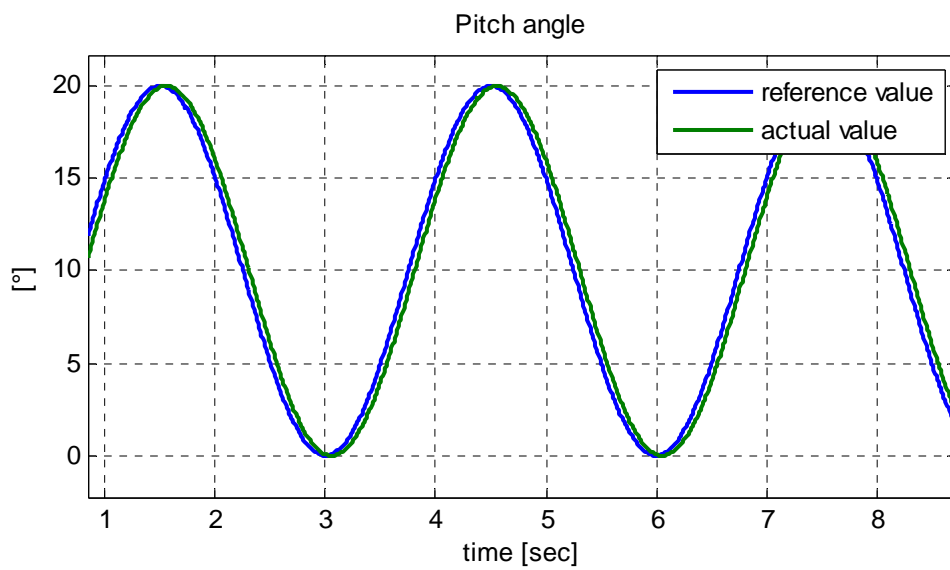**Figure 6-28: step response of reference model**

Figure 6-29: sinusoidal response of reference model

Disturbance weighting function

Friction is simulated in the blade ring. Whereas viscous friction is taken into account in uncertainty block, Coulomb and sliding frictions are nonlinear and are contained in the disturbance matrix. Simulated load on the blade is transferred to the load motors. The maximum sum of Coulomb and sliding friction is 8.6099Nm in section 4.3.1. 9Nm is applied in the disturbance weighting function.

The maximum load is 29Nm because the maximum torque of a motor is 34Nm and another load motor gives tension with 5Nm. This value is used as a gain of one of the load motors. Since the two load motors are coupled together, one value is enough for describing two torques of the load motors.

Gravity, aerodynamic force, centrifugal load and blade's moment of inertia are dependent on the pitch angle. Friction changes due to the sign of pitch rate. As the individual pitch control or tower damping control is used, loads on the pitch actuation system are dominated by 1P or 3P.

Disturbance due to load simulation exists in frequency less than 1P and 3P. In this research, 2Hz is chosen as the cutoff frequency, which is a little higher than 3P≈1Hz.

Unlike the sensor noise weighing function, disturbance weight has a square in the transfer function. This ensures steep drop around the cutoff frequency. The frictions and load act in low-frequency areas, thus the disturbance weight is also a low-pass filter as in Figure 6-30.

$$
W_d = \begin{bmatrix} 0 & 0 & 0 & 0 & 0 \\ 0 & 0 & 0 & 0 & 0 \\ 0 & 0 & 29 & 0 & 0 \\ 0 & 0 & 0 & 0 & 0 \\ 0 & 0 & 0 & 0 & 9 \end{bmatrix} \cdot \frac{\left(\dfrac{1}{2\pi \cdot 100} s + 1 \right)^2}{\left(\dfrac{1}{2\pi \cdot 2} s + 1 \right)^2}
$$
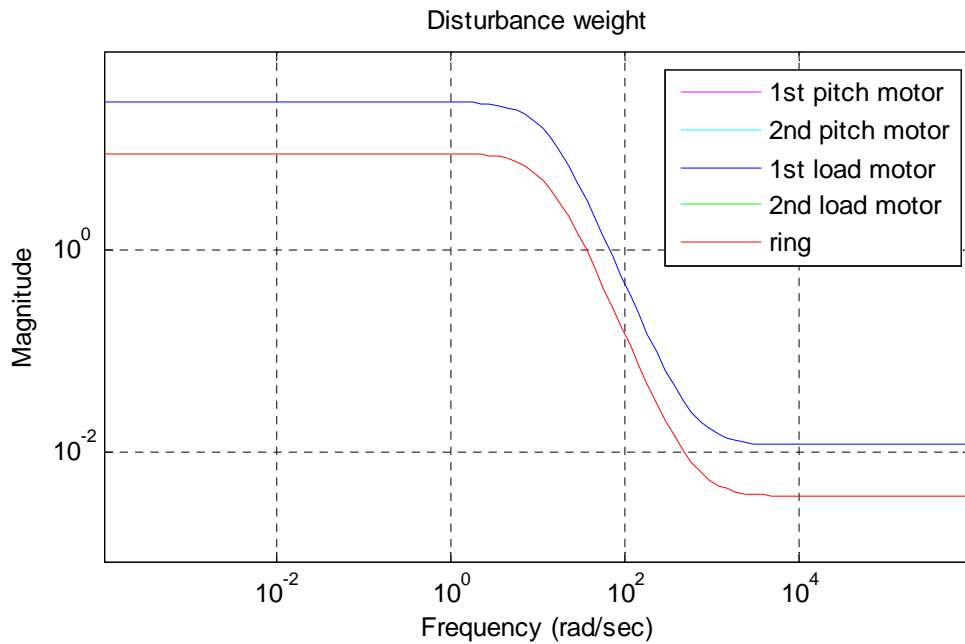
Figure 6-30: Disturbance weighting function
(Disturbances in 1st pitch motor, 2nd pitch motor and 2nd load motor are zero.)

Control weighting function

The control weighting function constrains motor torque. Different from disturbance and the noise weighting functions, the control weighting function is attached to the output node. Control output is limited to be lower than the inverse control weighting function, thus the control weighting function is a high-pass filter (see Figure 6-31). Since pitch angle change is less than 1P or 3P, the cutoff frequency is chosen to be 2Hz. Motor behavior is inactive above 100Hz. Gain of the control weighting function is determined to make the imaginary output, e_u , less than 1. At first the baseline PD controller or the cascade controller is used for K in equation (6-11) to determine the gain of Wu. After several tries and errors, 10^{-4} is chosen for the gain.

$$W_u = 10^{-4} \cdot \frac{\frac{1}{2\pi \cdot 2}s + 1}{\frac{1}{2\pi \cdot 100}s + 1}$$
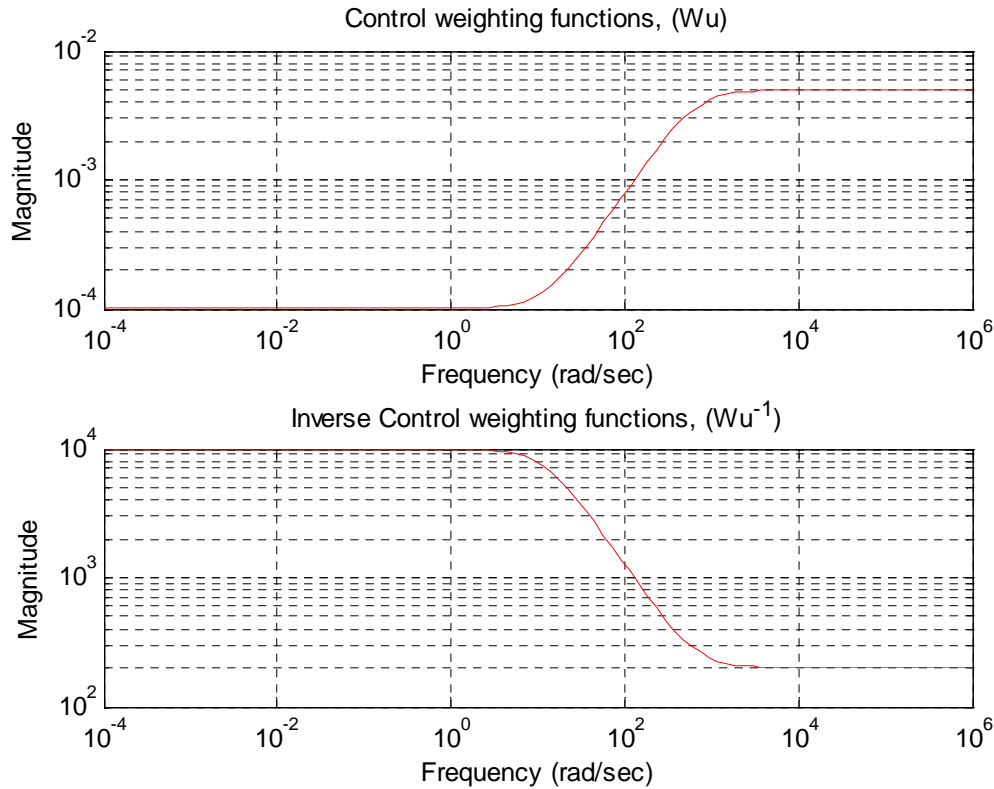
Figure 6-31: Control weighting function and its inverse

Performance weighting function

The performance weighting function restrains the difference between the reference model and the test rig in low-frequency areas, thus the inverse performance weighting function has to be a high-pass filter. Like the disturbance and control weighting functions, 2Hz is chosen for the cutoff frequency. In the frequency less than 2Hz, the complementary sensitivity is similar to the reference model and the system is robust against disturbance and noise.

Gain of the performance weighting function of μ-synthesis is adjusted to make the singular value of the three criteria less than 1 - nominal performance, robust stability and robust performance. As shown in (6-11), large gain in W_p means that the closed loop behaves similar to the reference model and is robust against disturbance and noise. Since gain in μ-synthesis is 100 times larger than H$_\infty$, an improved performance is expected with μ-synthesis.

$$\text{H}_\infty : \qquad W_p = 1.125 \cdot 10^{-3} \cdot \frac{\left(\dfrac{1}{2\pi \cdot 100} s + 1\right)^2}{\left(\dfrac{1}{2\pi \cdot 2} s + 1\right)^2}$$

µ-synthesis :

$$W_p = 1.125 \cdot 10^{-1} \cdot \frac{\left(\dfrac{1}{2\pi \cdot 100}s+1\right)^2}{\left(\dfrac{1}{2\pi \cdot 2}s+1\right)^2}$$
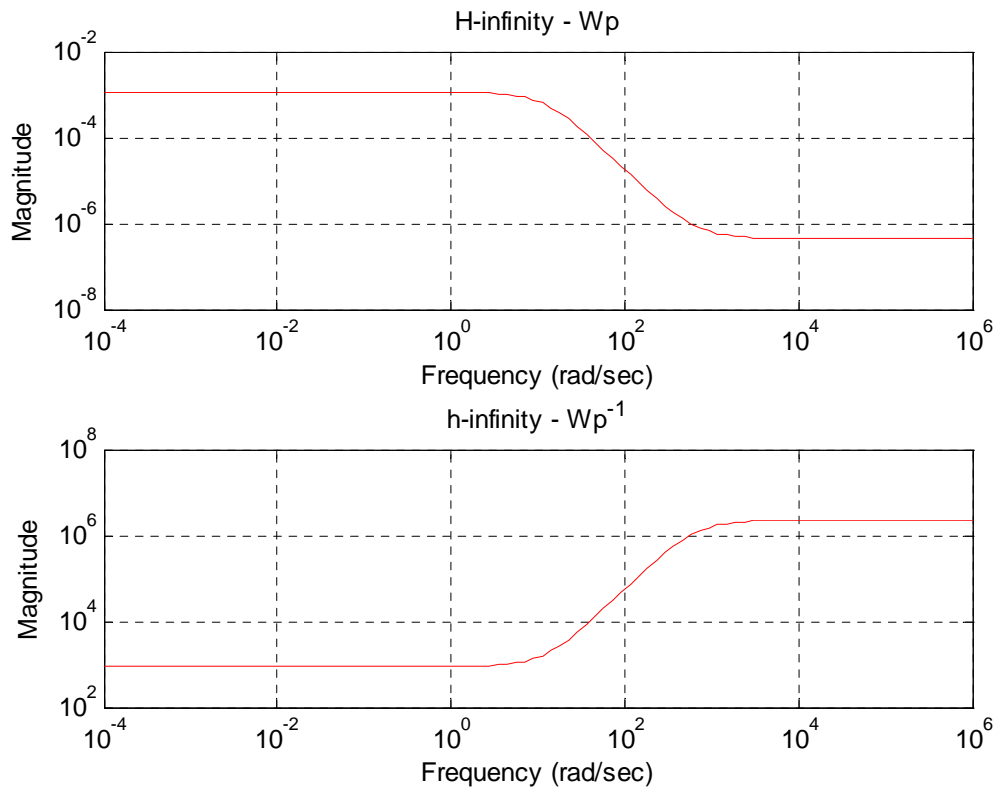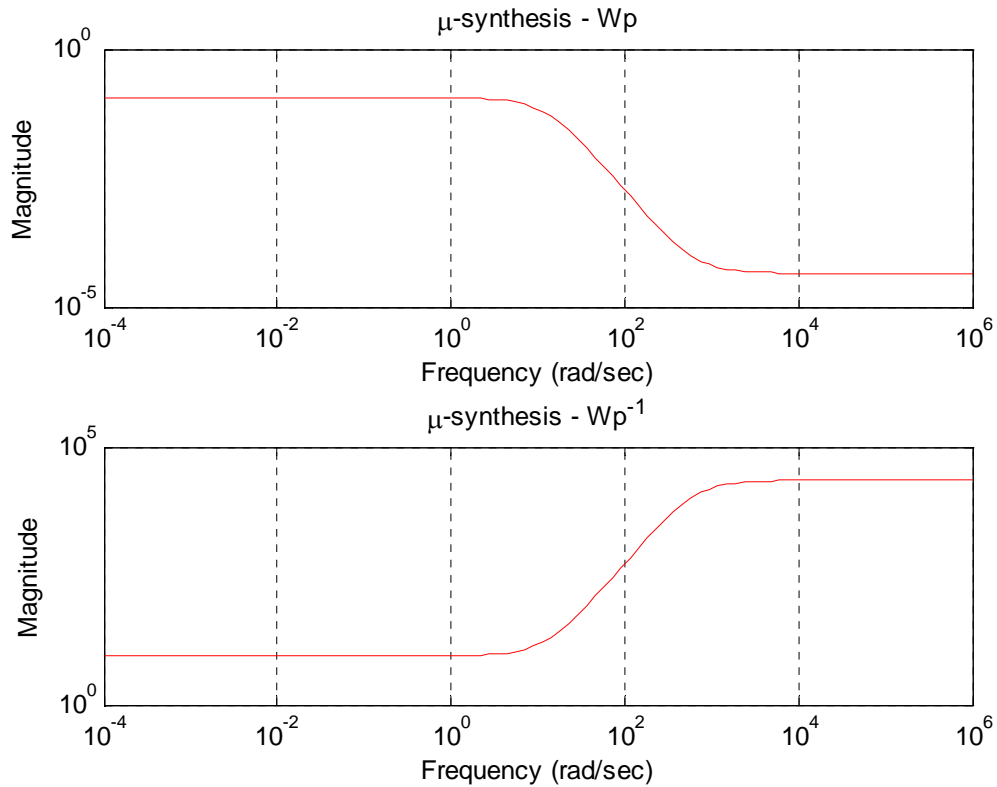
Figure 6-32: Performance weighting function and its inverse

6.3.4. Performance of the robust controller

A robust controller must satisfy the following three criteria – nominal performance, robust stability and robust performance. "Nominal performance" determines if all the singular values of the nominal transfer functions are less than 1. Uncertainty is not considered in this step. "Robust stability" distinguishes stability of the plant with uncertainty. "Robust performance" is the harshest of the three criteria. The singular values of all the transfer functions with uncertainty must be less than 1.

Nominal performance

Regard a closed-loop system with a controller (K), a plant (G_{nom}), a weighting function (W_1). The plant does not imply uncertainties.
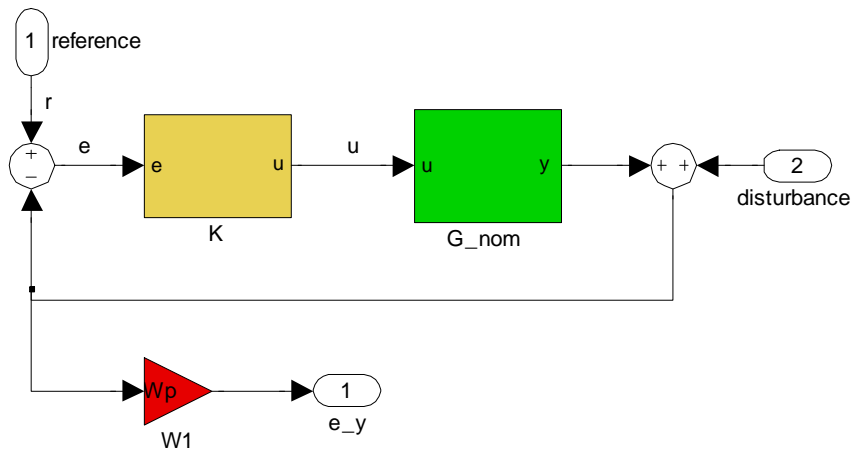
Figure 6-33: An example block diagram with a weighting function, W_1

Nominal performance is defined as:

$$\left\| W_1 \frac{I}{I + G_{nom}K} \right\|_\infty < 1 \qquad \text{(6-12)}$$

$(I + G_{nom}K)^{-1}$ is the output sensitivity function, which indicates the effect of disturbance to the error. It also denotes the transfer function from reference to error. The equation (6-12)(6-11) can be written as:

$$\left\| I + G_{nom}K \right\|_\infty > \left\| W_1 \right\|_\infty$$

This equation is illustrated graphically in Figure 6-34. The Nyquist plot of $G_{nom}(i\omega)K(i\omega)$ has to avoid a circle with center -1 and radius $W_1(i\omega)$.
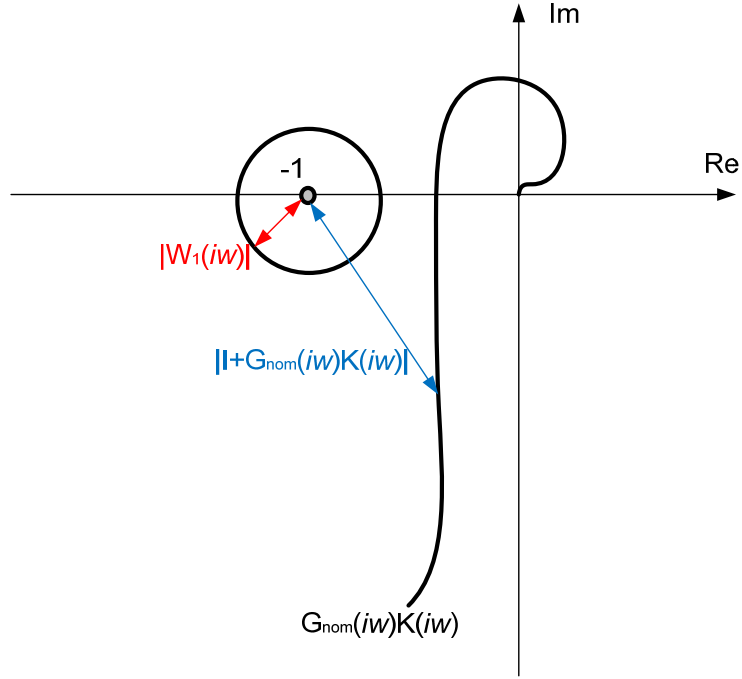
Figure 6-34: Nyquist plot for describing nominal performance

The model in this research has three inputs and two outputs as seen in equation (6-11). Thus 3x2 matrix is used for nominal performance determination. The singular value of the nominal plant model, G_{nom} , has to be less than 1. The weighting functions and a reference model must be designed to satisfy the following criterion.

$$\left\|\begin{bmatrix} W_P\left(\dfrac{G_{nom}K}{I+G_{nom}K}-M\right) & W_P\dfrac{G_{nom}}{I+G_{nom}K}W_d & -W_P\dfrac{G_{nom}K}{I+G_{nom}K}W_n \\ W_u\dfrac{K}{I+G_{nom}K} & -W_u\dfrac{KG_{nom}}{I+G_{nom}K}W_d & -W_u\dfrac{K}{I+G_{nom}K}W_n \end{bmatrix}\right\|_{\infty} < 1 \qquad \text{(6-13)}$$

Robust stability

Robust stability means a system is not only stable for the nominal plat but also for the real plant, whose parameters are somewhat different from the nominal plant. As the magnitude of uncertainty (Δ) is limited to $W_2(\omega)$, then $\|\Delta(i\omega)\|_{\infty} < W_2(\omega)$. The radius of a circle at the frequency ω in Figure 6-35 is $W_2(\omega)\|G_{nom}(i\omega)K(i\omega)\|_{\infty}$.

For the stability of a system with uncertainties, the distance between -1 and the nominal system has to be farther than the radius of a circle on the nominal system. This is written as:

$$\|I + G_{nom}(i\omega)K(i\omega)\|_{\infty} > W_2(\omega)\|G_{nom}(i\omega)K(i\omega)\|_{\infty} \qquad \text{(6-14)}$$
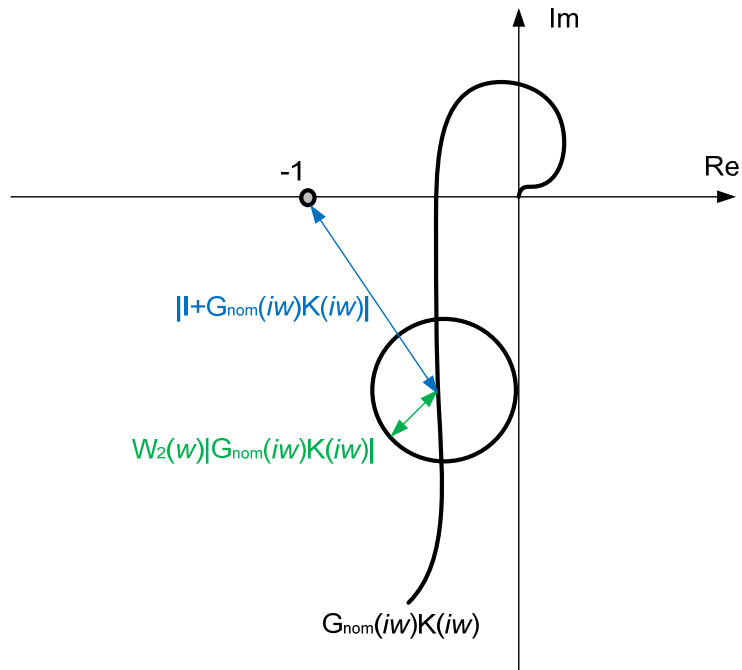
Figure 6-35: Nyquist plot for describing robust stability

Robust performance

Robust performance is a performance of a perturbed feedback loop. Based on the nominal system in Figure 6-33, an uncertainty block is added in Figure 6-36.
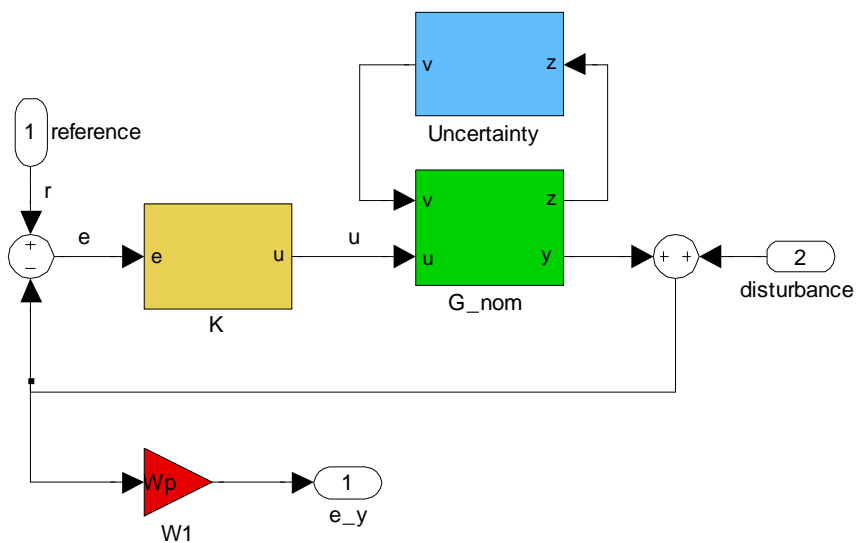
Figure 6-36: An example block diagram with uncertainty and a weighting function

A necessary and sufficient condition for robust performance is [55]:

$$\left\| \left| W_1 S_1 \right| + \left| W_2 S_2 \right| \right\|_\infty < 1 \qquad \text{(6-15)}$$

Where S_1 is a sensitivity function and S_2 is a complementary sensitivity function as:

$$S_1 = \frac{I}{I + G_{nom}K}, S_2 = \frac{G_{nom}K}{I + G_{nom}K}$$

Equation (6-15) can be written as:

$$\left\| \left| W_1 \frac{I}{I + G_{nom}K} \right| + \left| W_2 \frac{G_{nom}K}{I + G_{nom}K} \right| \right\|_\infty < 1 \qquad \text{(6-16)}$$

$$\Leftrightarrow \left\| \left| W_1 \right| + \left| W_2 G_{nom}K \right| \right\|_\infty < \left\| I + G_{nom}K \right\|_\infty$$

The left side of the equation (6-16) is the sum of radius of the two circles in Figure 6-37 and the right side is the distance between -1 and the nominal system. Thus the two circles do not cross if robust performance is satisfied.
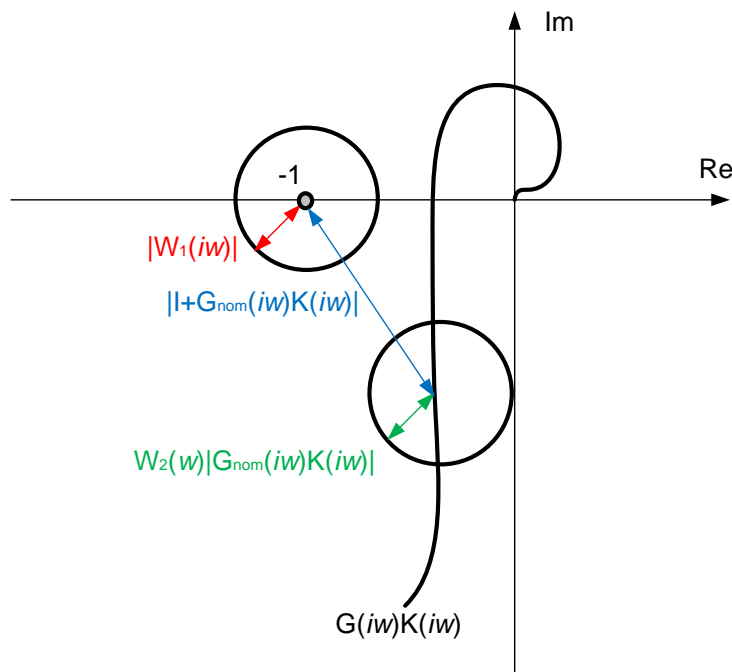
Figure 6-37: Nyquist plot for describing robust performance

Like the nominal performance, robust performance must satisfy the 3x2 matrix criterion. The model contains uncertainty, therefore $G = F_U(G_{nom,}\Delta)$. Robust performance of the perturbed system in this research is:

$$\left\| \begin{bmatrix} W_P\left(\dfrac{GK}{I+GK}-M\right) & W_P\dfrac{G}{I+GK}W_d & -W_P\dfrac{GK}{I+GK}W_n \\ W_u\dfrac{K}{I+GK} & -W_u\dfrac{KG}{I+GK}W_d & -W_u\dfrac{K}{I+GK}W_n \end{bmatrix} \right\|_\infty < 1 \qquad \text{(6-17)}$$

Performance of H∞ controller and µ-synthesis

Singular values of the three criteria are:

	H∞	µ-synthesis
Nominal performance	0.005	0.822
Robust stability	0.695	0.795
Robust performance	0.699	0.826

Table 6-2: singular values of nominal performance, robust stability and robust performance

All the three criteria of H∞ robust controller and µ-synthesis is smaller than 1. Figure 6-38 shows the magnitude of each term in the nominal performance matrix in (6-13). of µ-synthesis reaches its maximum in low frequency in the upper middle figure. It means robustness against disturbance is challenging. Nominal performance of H∞ robust controller is very small in comparison to µ-synthesis.

Nominal performance, robust stability and robust performance in frequency domain are seen in Figure 6-39, Figure 6-40 and Figure 6-41. The nominal performance of the µ-synthesis declines between 2 and 30 rad/s. The robust stability graphs of both controllers soar around at 20 rad/s. Robust performance is a mixture of nominal performance and robust stability. The robust performance graphs with the two controllers are similar to the combination of the upper two graphs.
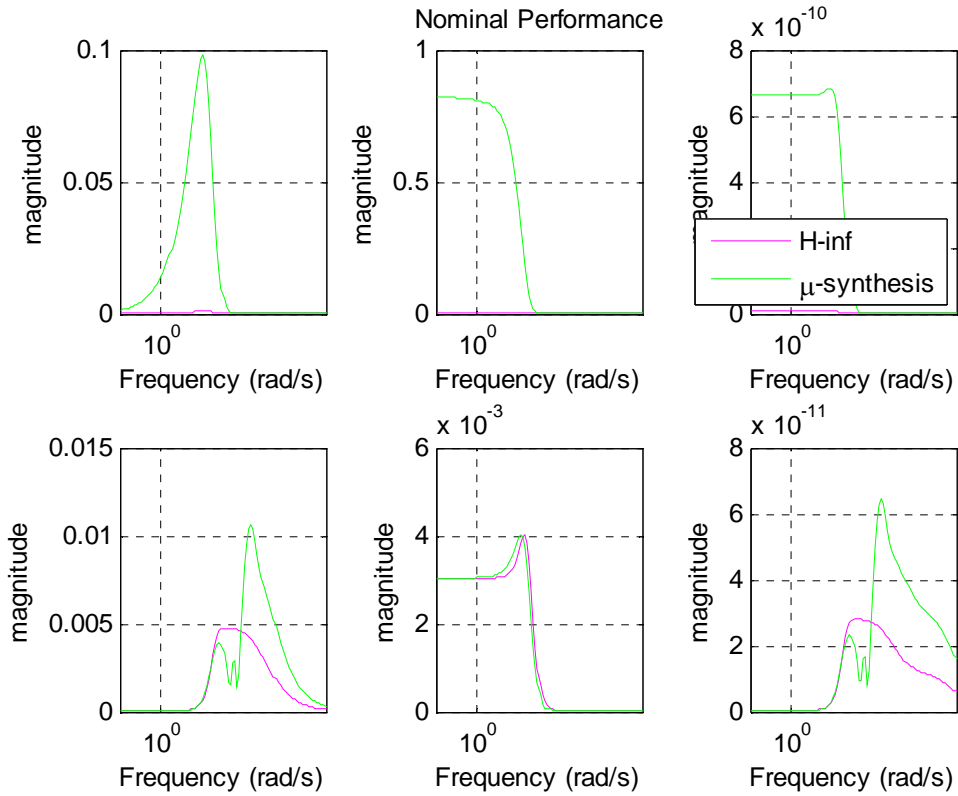
Figure 6-38: Magnitude of each part in the nominal performance matrix of (6-13)
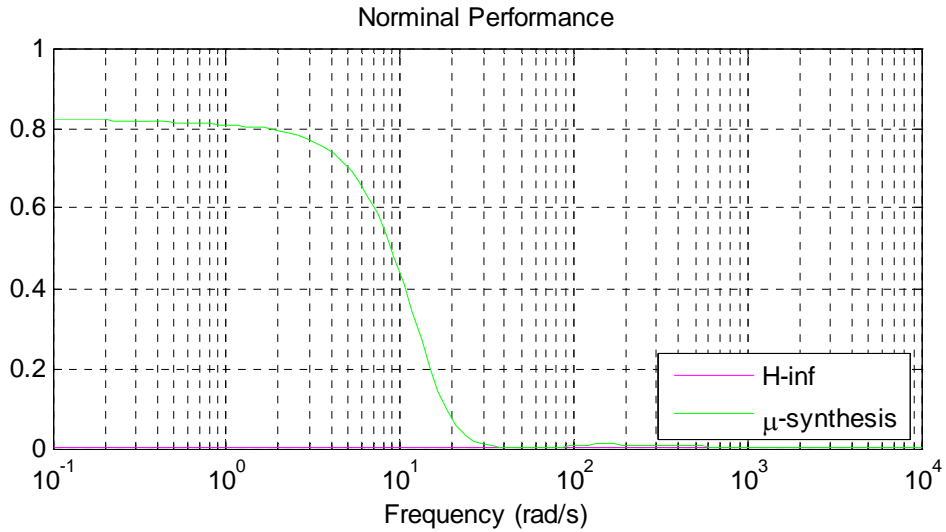
Figure 6-39: Singular values of the nominal performance over frequency
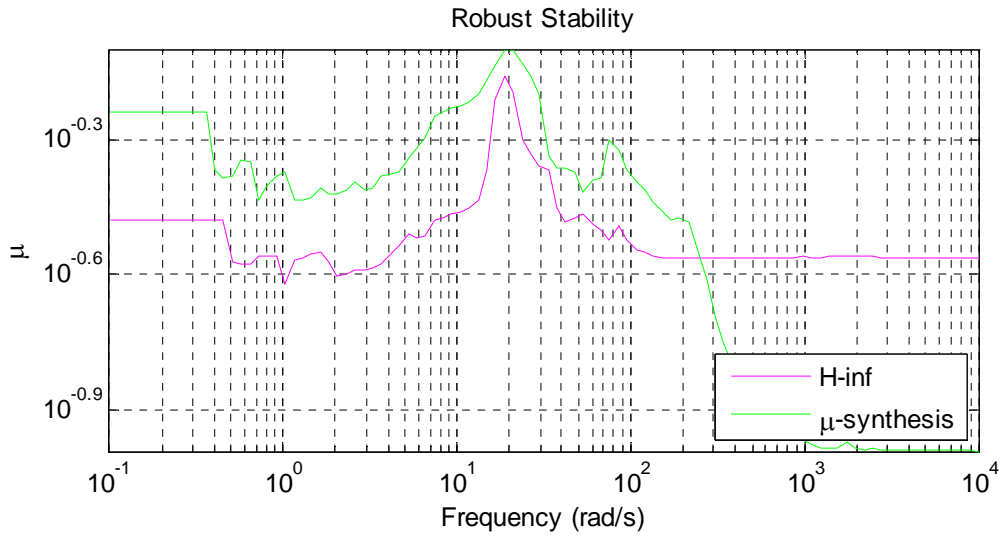
Figure 6-40: Singular values of the robust stability over frequency
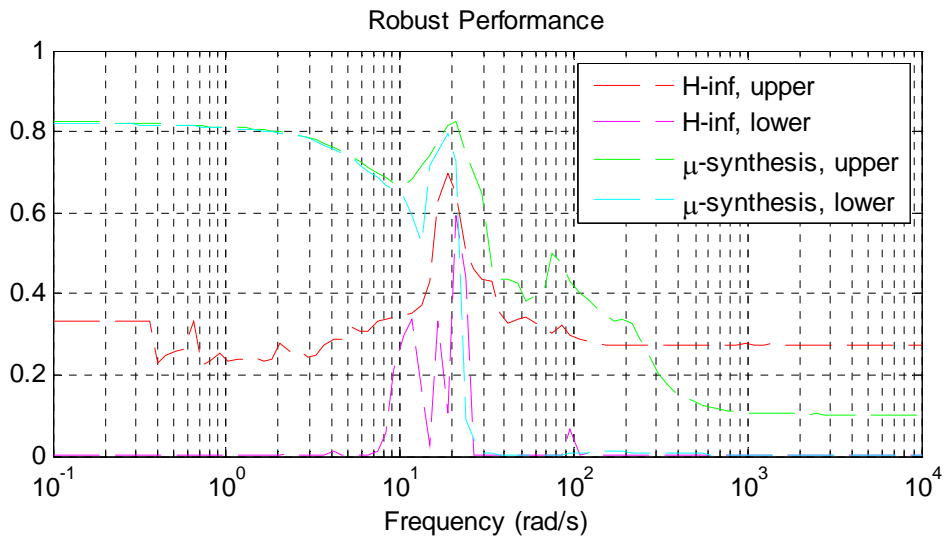
Figure 6-41: Singular values of the robust performance over frequency

Figure 6-42 and Figure 6-43 show the closed-loop transient response in simulation and experiment. μ-synthesis reacts faster than H$_\infty$ controller.
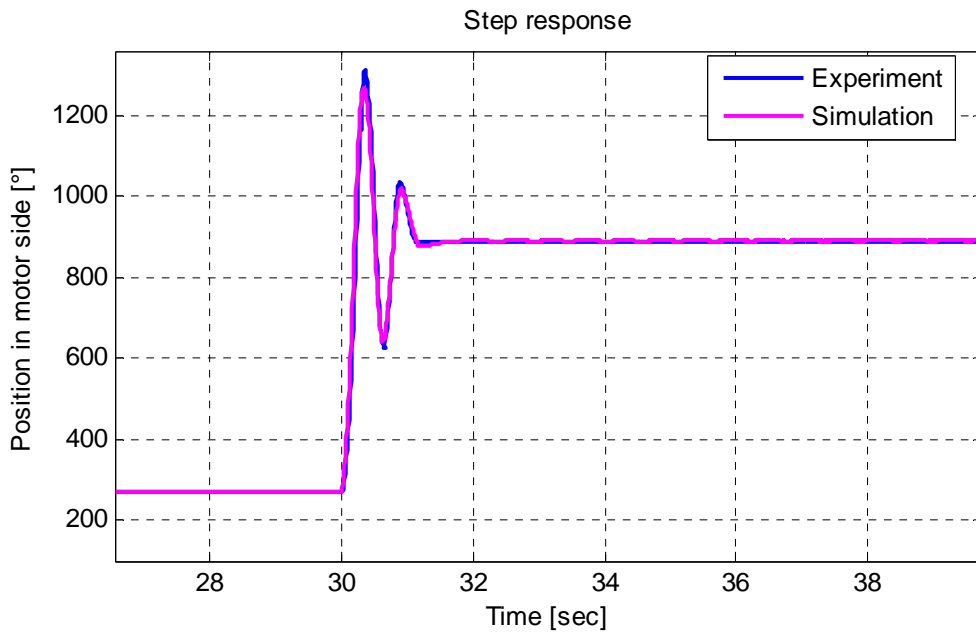
Figure 6-42: closed-loop transient response, H∞ robust controller
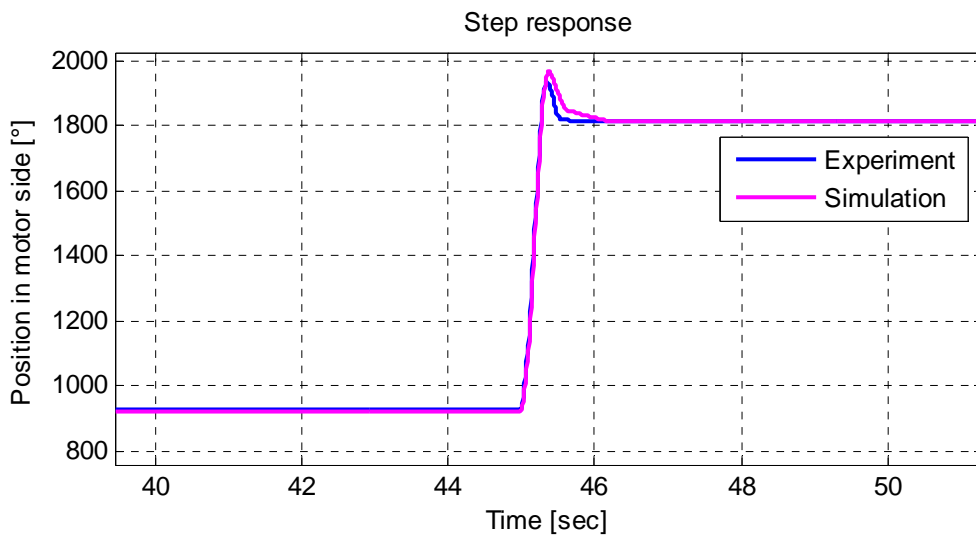
Figure 6-43: closed-loop transient response, μ-synthesis

6.4. Comparison of the four pitch angle controllers

Experimental setup

Four pitch angle controllers (PD-base, cascade, H∞ controller and μ-synthesis) were proposed in the section 6.1, 6.2 and 6.3. The suggested pitch angle controllers are compared in the test rig with the following pitch controllers as:

- Collective pitch control

- Individual pitch control
- Tower damping control

Collective pitch control is currently used control whereas individual pitch control and tower damping control represent for new developing control for load reduction (see section 1.2 for more in detail).

The criterion to compare the four pitch angle controllers is tracking performance. It is tested how good the pitch angle controllers track the reference signal in the presence of the following hindrances: sinusoidal reference value, blade's load around pitch axis, nonlinearities of the pitch actuation system, and viscous friction coefficient change. The tracking performance is determined by calculating root-mean-square ($error_{RMS}$) of the errors between the reference pitch angles ($\vartheta_{ref,i}$) and the actual pitch angles ($\vartheta_{act,i}$) as:

$$error_{RMS} = \sqrt{\frac{\sum_{i=1}^{n_{signals}} \left(\vartheta_{ref,i} - \vartheta_{act,i}\right)^2}{n_{signals}}}$$

where $n_{signals}$ is the number of signals. Root-mean-square of the errors is one of the most widely used assessment of misfit/fit [60]. Because its approximate distributional properties are known, it is possible to obrain parametric confidence intervals [60]. Root-mean-square (RMS) of the errors is preferred to mean-square of the errors as it is on the same scale as the data. Mean-square (MS) of the errors is written as:

$$error_{MS} = \frac{\sum_{i=1}^{n_{signals}} \left(\vartheta_{ref,i} - \vartheta_{act,i}\right)^2}{n_{signals}}$$

Mean-absolute (MA) of the errors is another accuracy measure as:

$$error_{MA} = \frac{\sum_{i=1}^{n_{signals}} \left|\vartheta_{ref,i} - \vartheta_{act,i}\right|}{n_{signals}}$$

RMS is more sensitive to outliers than mean-absolute [61]. For example, pitch angles travel as Figure 6-44. Whereas the actual-A is departed from reference pitch angles by 2 degrees, distances between the actual-B and the references vary in 1 and 3 degrees. Whereas mean-absolute values of the errors of both cases are the same, root-mean-square of errors of actual-B is larger than that of actual-A (see Table 6-3). Since large deviation is weighted more with root-mean-square than with mean-absolute, root-mean-square deals with worst cases better than mean-absolute.
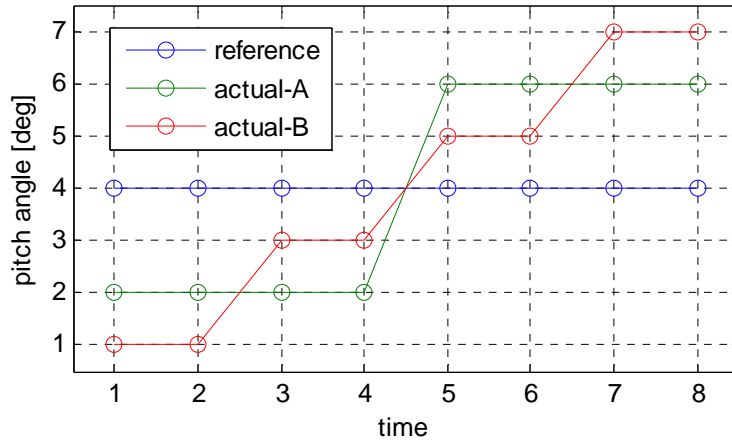
Figure 6-44: example to compare mean-absolute and root-mean-square of errors

	Mean-absolute	Root-mean-square
actual-A	2	2
actual-B	2	2.24

Table 6-3: Mean-absolute and root-mean-square of the errors between reference and actual signals

For the study, a turbulence wind with 12m/s average speed is simulated. Pitch angles corresponding to the wind speed are obtained from the Bladed simulation with a 5MW wind turbine. Bladed is the most well-known software program for wind turbine simulation. Its simulation results are used for certification. Whereas the rotational frequency of the 5MW turbine rotor in rated wind is 0.25Hz, the frequency of the used Risø [28] blade is 0.33Hz. The rotational frequency, which is also called 1P, is also the frequency of the cycles with individual pitch control. The frequency of the cycle with tower damping control is 3 times larger than individual pitch control with a three-blade-turbine. The frequency is called 3P. The two robust controllers are designed in consideration of 1P and 3P. Gravity in the load simulation is changed in 1P cycle. Thus the pitch angles from Bladed software are compressed to 0.25/0.33 times of the time axis. While the pitch angles are adjusted to the cycles in individual pitch control and tower damping control, the pitch angles in collective pitch control are also compressed. Thus the compressed pitch angles are the same as the case with 12m/s wind speed and higher turbulence than the original Bladed simulation.

Tracking performances of the pitch angle controllers

Root-mean-square (RMS) of the errors between the reference signals and the actual signals are listed in Table 6-4 and Figure 6-45. The pitch angles with collective pitch control are found in Figure 6-46. As the RMS of the PD-controller is set to be 100%, the values of the cascade, the H_∞ controller and the μ-synthesis are 71.6%, 70.2% and 51.0%. Thus the μ-synthesis shows the best tracking performance. The cascade and the H_∞ controller tracks the reference signals of the collective pitch control more precisely than the PD-controller.

Pitch angles of the individual pitch control are seen in Figure 6-47. RMS of the PD-controller is 0.2937 which is 64.3% larger than the PD-controller with collective pitch control. RMS of the other three pitch angle controllers are also larger with individual pitch control than collective pitch control. Individual pitch control requires frequent change of pitch angles. As the sign of pitch rate changes, the friction on the blade root is changed. Friction change is simulated and given to the test rig via the load motors and it prohibits pitch angle controllers to track the reference signal. Frequent change of pitch angles leads to frequent change of the nonlinear friction in the pitch actuation system. In addition, the reference signal of individual pitch control is composed of signals of collective pitch control and a sinusoidal signal. Since the H_∞ controller and μ-synthesis imply consideration of sinusoidal reference signal, blade's load around pitch axis, and nonlinearities of the pitch actuation system, increase of errors of the two robust controllers is less than the two classical controllers. The increases are 0.1150 with the PD-controller, 0.2519 with the cascade controller, 0.0458 with the H_∞ controller and 0.0134 with μ-synthesis. Therefore, the tracking performances of the robust controllers are proved more obviously in the experiments with individual pitch control. RMS of the H_∞ controller and μ-synthesis are 58.3% and 35.6% in comparison to the PD-controller with individual pitch control.

Cascade controller shows a worse tracking performance than PD-controller in the experiment with individual pitch controller. The pitch angles of the individual pitch control change in 1P cycle and the 1P is 0.33Hz (=2.1 rad/s) in this research. The phase angle of the PD-controller in 1P is around -100° and that of the cascade controller is around -130° (see Figure 6-2 and Figure 6-6). Since the phase angle of the cascade controller in 1P is nearer to -180°, it is concluded that the cascade controller performs worse than PD-controller with individual pitch control.

Figure 6-48 shows the pitch angles with tower damping control. RMS of the PD-controller with tower damping control is 5.8% more than that with collective pitch control. The pitch angles of tower damping control do not vary so much as individual pitch control, thus the error with tower damping control is less than the error with individual pitch control. RMS of the two robust controllers are 71.7% and 51.5% of the RMS of the PD-controller with tower damping control. The percentages of the two robust controllers are similar to the cases with collective pitch control.

	PD-controller	Cascade	H_∞ controller	μ-synthesis
Collective pitch control	0.1787 (100%)	0.1280 (71.6%)	0.1255 (70.2%)	0.0912 (51.0%)
Individual pitch control	0.2937 (164.4%)	0.3799 (212.6%)	0.1713 (95.9%)	0.1046 (58.5%)
Tower damping control	0.1890 (105.8%)	0.1730 (96.8%)	0.1356 (75.9%)	0.0974 (54.5%)

Table 6-4: root-mean-square of the errors between reference and actual signals
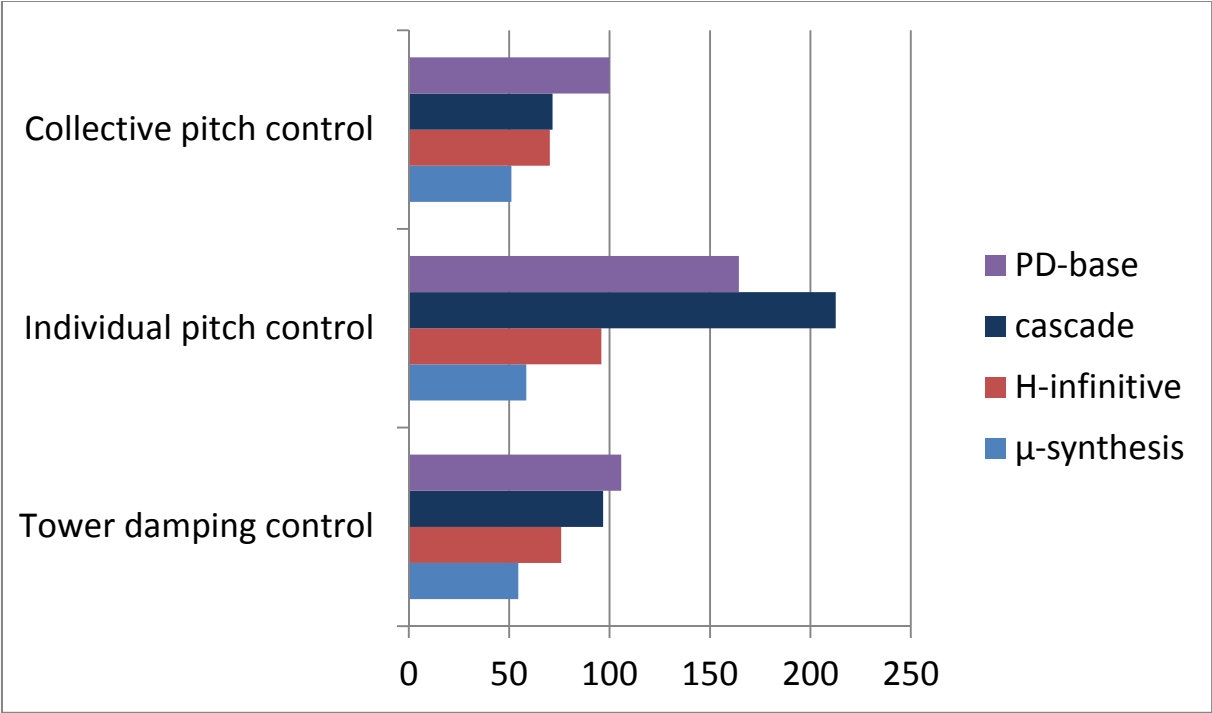
Figure 6-45: root-mean-square of the errors between reference and actual signals, collective pitch control with PD-base is set to be 100%.

Figure 6-46: Pitch angle, collective pitch control, 12m/s turbulence, with load simulation

Figure 6-47: Pitch angle, individual pitch control, 12m/s turbulence, with load simulation
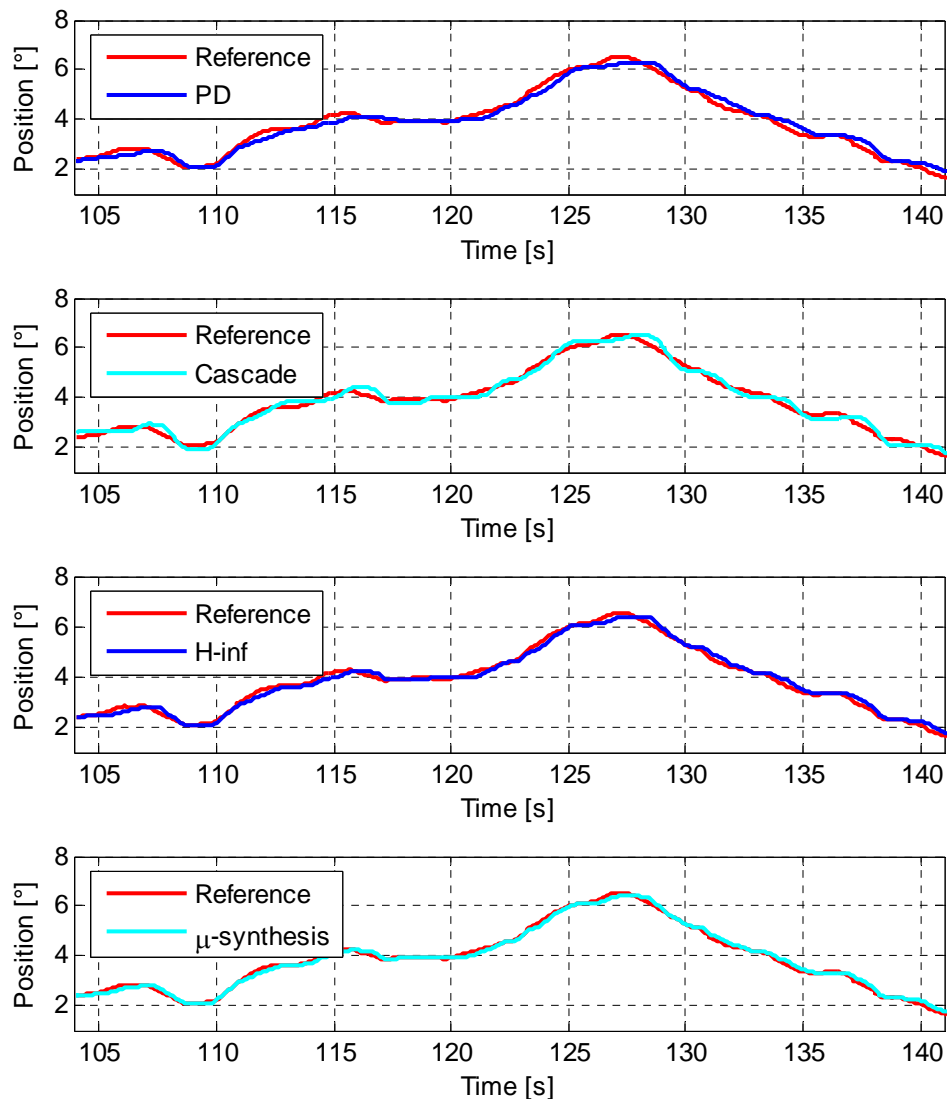
Figure 6-48: Pitch angle, tower damping control, 12m/s turbulence, with load simulation

Experiments without load simulation

It is worth to find how much the four problems among sinusoidal reference value, blade's load around pitch axis, nonlinearities of the pitch actuation system, and viscous friction coefficient affect the tracking performances of the pitch angle controller. Sinusoidal reference value is one of the reasons that the tracking performances of the two robust controllers are good with individual pitch control. Coulomb/sliding friction and viscous friction change is implied in the test rig, so these effects cannot be excluded in the test rig. In contrast, blade's load around pitch axis is given to the two load

motors in the test rig. Thus load simulation is excluded and the performances of the four controllers are tested. Since the two load motor sets have gear play, they are tensed with ±5Nm.

Table 6-5 shows that the errors between reference and actual signals are reduced regardless of the pitch angle controllers and the pitch controllers. These are also shown in Figure 6-49 for collective pitch control and Figure 6-50 for individual pitch control. RMS of PD-controller with collective pitch control and load simulation is defined as 100% and the other RMSs are calibrated to the default value. Because the tracking performances with tower damping control is similar to with collective pitch control, only collective pitch control and individual pitch control without load simulation are tested.

In Figure 6-49, the RMS of error for collective pitch control is decreased in the order of PD-controller, cascade controller, H-infinitive and μ-synthesis. In all the four pitch angle controllers, the RMS without load simulation is smaller than that with load simulation. The difference is between 3.1% in H_∞ controller and 34.5% in cascade controller.

The changes in case of no load simulation are found obviously with individual pitch control (see Figure 6-50). The position errors of base PD-controller and cascade controller are reduced from 0.2937 and 0.3799 to 0.1809 and 0.2376. This, in reverse, indicates that the blade's load around pitch axis takes 37.5-38.4% of the RMS. The effects of the blade's load around pitch axis in the H_∞ controller and the μ-synthesis are 22.4% and 32.0%. Therefore, it is found that the blade's load around pitch axis is an important hindrance to the pitch angle controllers. Because the difference is less than 50% and the effects of the other three problems are not known, blade's load cannot be decided to be the biggest hindrance to the pitch angle controllers.

All the pitch angles for collective and individual pitch control without load simulations are found in Figure 6-51 and Figure 6-52.

		PD-controller	Cascade	H_∞ controller	μ-synthesis
Collective pitch control	with load simulation	0.1787	0.1280	0.1255	0.0912
	without load simulation	0.1638	0.0839	0.1216	0.0696
	difference	0.0149 (8.3%)	0.0441 (34.5%)	0.0039 (3.1%)	0.0216 (23.7%)
Individual pitch control	with load simulation	0.2937	0.3799	0.1713	0.1046
	without load simulation	0.1809	0.2376	0.1329	0.0711
	difference	0.1128 (38.4%)	0.1423 (37.5%)	0.0384 (22.4%)	0.0335 (32.0%)

Table 6-5: root-mean-square of the errors between reference and actual signals

Figure 6-49: root-mean-square of the errors between reference and actual signals, collective pitch control, PD-controller with load simulation is 100%
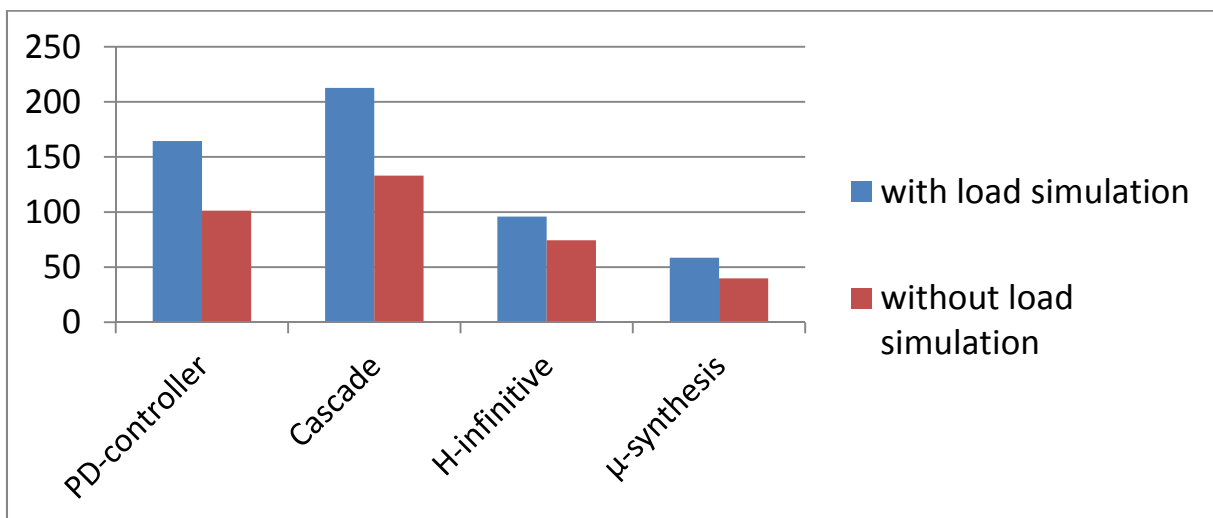
Figure 6-50: root-mean-square of the errors between reference and actual signals, individual pitch control, PD-controller with load simulation and collective pitch control is 100%
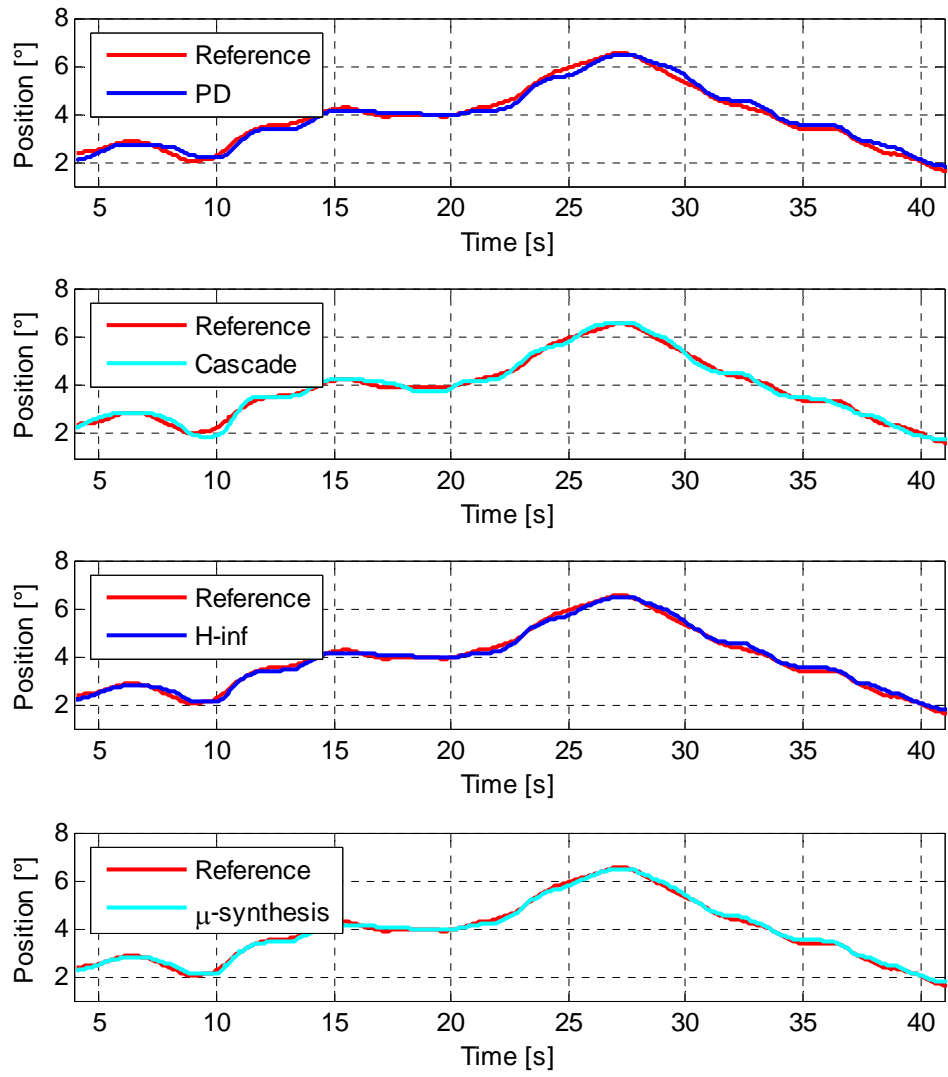
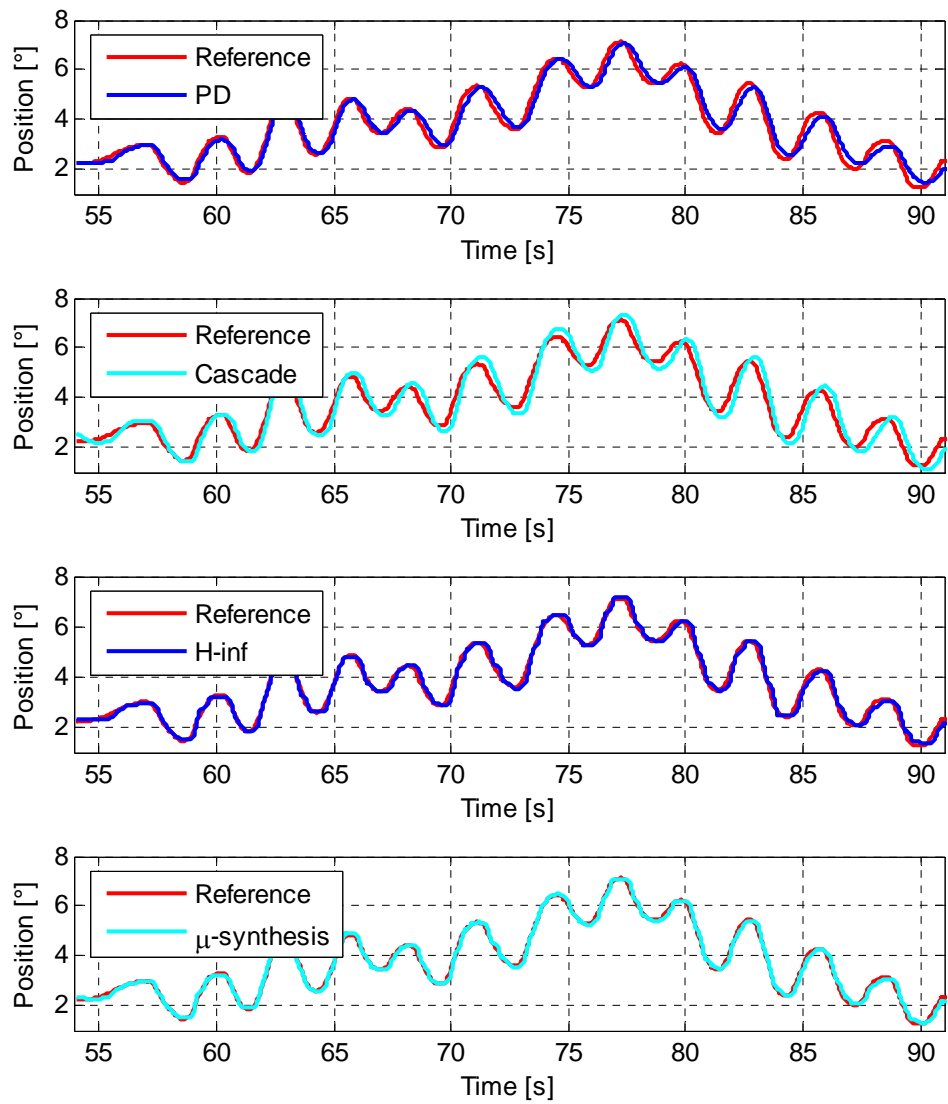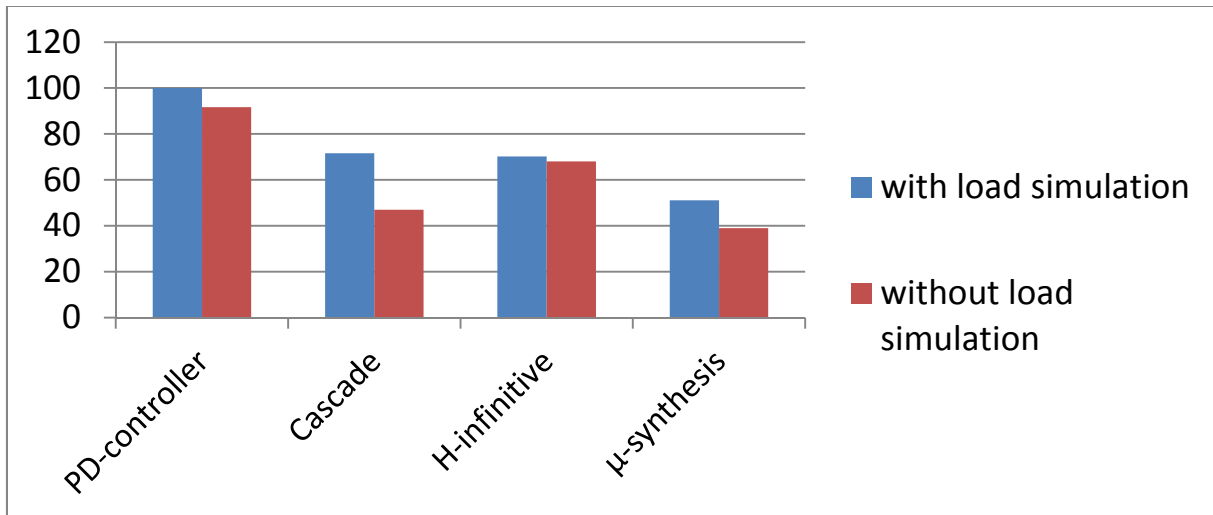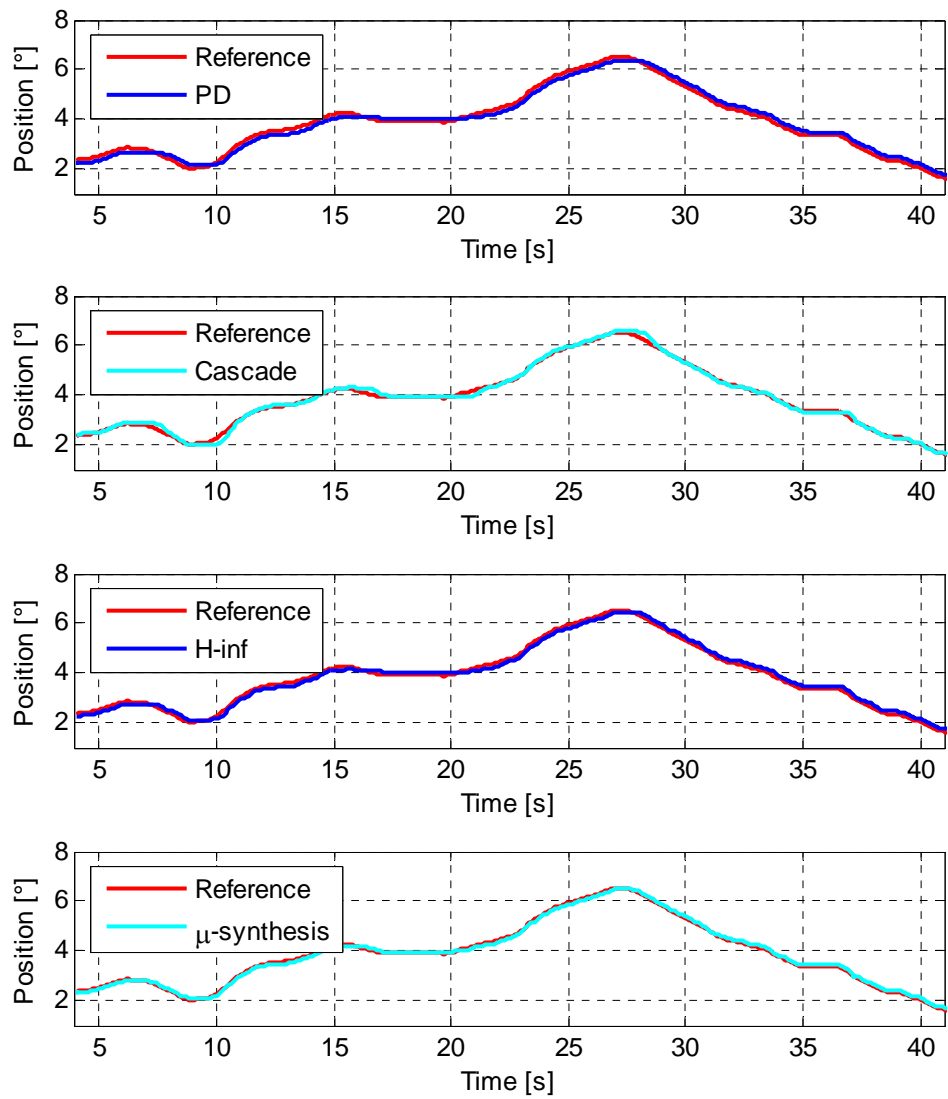**Figure 6-51: Pitch angle, collective pitch control, 12m/s turbulence, without load simulation**
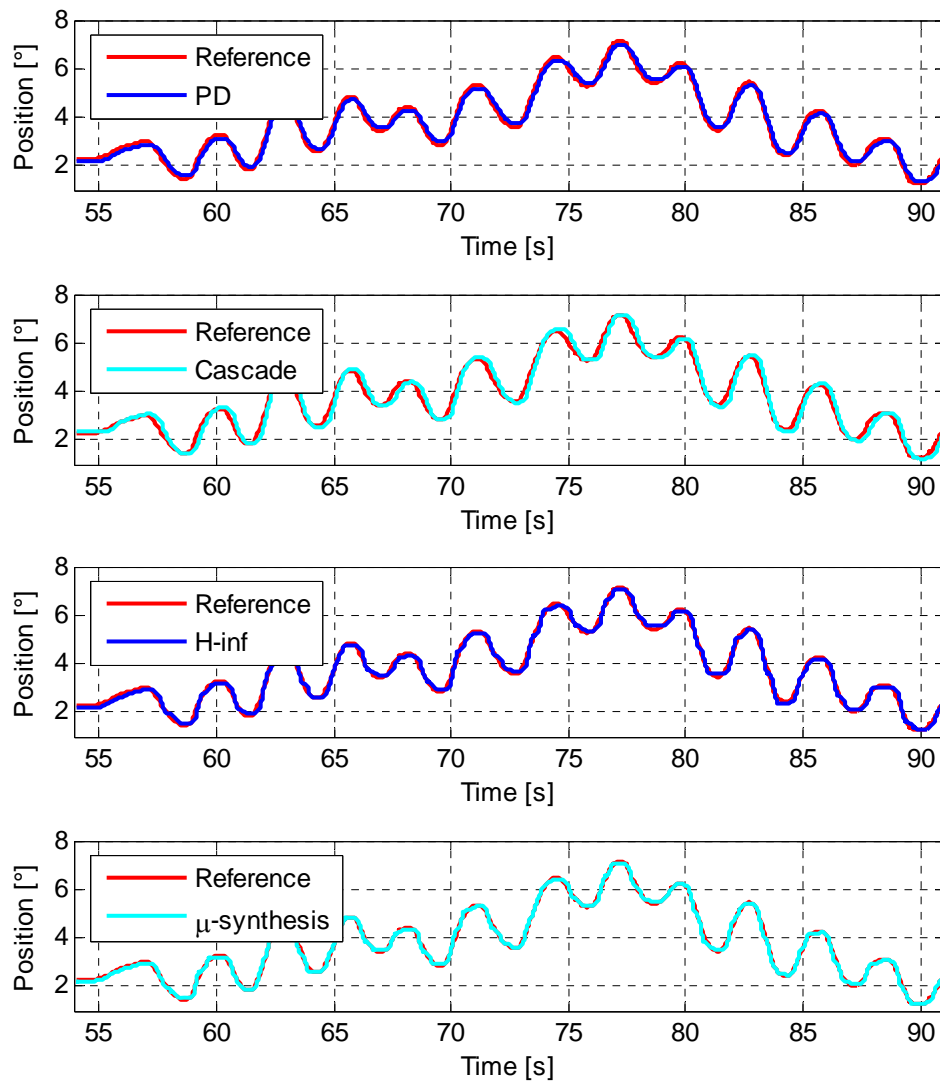
Figure 6-52: Pitch angle, individual pitch control, 12m/s turbulence, without load simulation

Discussion

The H$_\infty$ controller and μ-synthesis track the reference signal more precisely than the PD-controller and the cascade controller regardless of the pitch controllers and load simulations. The differences in tracking performance are found especially in individual pitch control case because the problems such as sinusoidal reference value, blade's load around pitch axis, and nonlinearities of the pitch actuation system are applied especially in individual pitch control. PD-base and cascade controllers are designed on a linear model and only a few parameters can be adjusted. The four problems can be considered in simulations or experiments after the classical controller is designed. Instead, robust controller takes the four problems into account in the designing step. The tracking performances of

the robust controllers are seen obviously especially with individual pitch control because sinusoidal reference value, blade's load around pitch axis, and nonlinearities of the pitch actuation system are applied more strongly with individual pitch control.

By comparing the experiments with and without load simulation, it is found that blade's load around pitch axis is one of the main hindrances to the tracking performances of the controllers.

Two-motor-pitch-system is developed for new developing pitch controllers, especially for individual pitch control. With the experiments in this chapter, it is concluded that the pitch actuation system shows the best tracking performance in case the two-motor-pitch-system is combined with a robust pitch angle controller.

7. Conclusion and further studies

In the development of large wind turbines, a great load on their elements has to be taken into account. In order to alleviate this load, new pitch control strategies are required such as individual pitch control or tower damping control. Whereas the new pitch controllers lessen load on the elements, e.g. main bearing or blade root bearing, load on the pitch actuation system increases because pitch action is performed also in low wind speed and pitch reversal occurs much more frequently. Since the gear play in the gearbox and between the pinion and ring causes fatigue increment, a two-motor-pitch-system is proposed to compensate for gear play. Three methods are compared to distribute torque into the two pitch motors.

A profile generator is currently used as a pitch angle controller. However the profile generator is not suitable for individual pitch control because of phase delay at sinusoidal reference values. As an alternative, two robust controllers are suggested and compared to PD and cascade controllers.

A test rig is built to test the two-motor-pitch-system and the pitch angle controller. Since no sensor is equipped on the ring of the test rig, an observer is used to calculate the ring position. However, the ring position itself is an output of the test rig model. Thus the proposed observer designates its output in a different way from the Luenberger observer.

Large wind turbines endure great loads. New pitch controllers increase load on the pitch actuation system. A two-motor-pitch-system and robust control are hardware and software which guarantee a long lifetime and good performance of large wind turbines.

7.1. Fatigue on the pitch actuation system

As the pitch angle direction changes, gear teeth hit each other and torque soars with a one-motor-pitch-system. The torque peak does not occur with a two-motor-pitch-system. Because torque peak increases fatigue, a two-motor-pitch-system alleviates fatigue on the pitch actuation system.

Advantages of the two-motor-pitch-system are:

- Lifetime of the pitch actuation system increases. Thus maintenance and replacement cost can be saved.
- Gear teeth in the gearbox, pinion and ring may have larger tolerance, thus the manufacturer can save cost.

Disadvantages of the two-motor-pitch-system are:

- Pitch action requires energy not only to rotate blade but also to overcome friction and inertia of the pitch actuator. The two-motor-pitch-system has larger inertia and Coulomb/viscous friction in comparison to the one-motor-pitch-system. Thus the two-motor-pitch-system leads to more energy consumption.

- In the two-motor-pitch-system, torques of the two motors are applied in the opposite direction. It causes the sliding friction to increase. Thus more electricity is consumed.
- Two pitch actuators are equipped instead of one, thus manufacturing cost for pitch actuation system increases.

It is not known if the total cost inclusive manufacturing cost, maintenance cost, replacement cost and electricity can be saved. This is explained in section 7.3 in detail.

7.2. Pitch angle controller

A large overturning moment is given to a large wind turbine. Nonlinear friction due to the overturning moment and gravity force of a blade mass are hindrances to pitch action. Pitch actuation system itself has also nonlinear frictions. Mechanical characteristics such as viscous friction coefficient vary during pitch action. Tracking sinusoidal reference value requires an additional consideration in controller design. The proposed two robust controllers show satisfactory results in comparison to a PD and cascade controllers.

Advantages of the two robust controllers in comparison to PD and cascade controllers are:

- A robust controller guarantees robust performance in the situation of blade load simulation and nonlinear frictions.
- Estimated parameters of the model may have some tolerances. Viscous friction coefficient is not fixed, thus the parameter does not exist as a constant but in a range. Robust controllers operate sufficiently well in the range of certain parameter uncertainties.
- The user designates amplitudes and frequencies of disturbance, noise, performance and control weighting functions. A reference model is also designed by the user. Thus several criteria e.g. robustness against disturbance, robustness against uncertainty, tracking performance and energy consumption can be satisfied at the controller design step.

However, the robust controllers in this study have also a few disadvantages compared to cascade and PD controllers:

- A robust controller requires many weighting functions. In this study, 4 weighting functions and one reference model are designed. The user should have a thorough understanding of the system. It requires much more effort and time than designing PD or cascade controller.
- Since a robust controller is made based on the model, the model has to be correct. Small errors in the model can harm performance and stability of the closed-loop system.
- A robust controller is in high order. The PLC in the test rig can support a controller with 20 orders of the H_∞ controller and 60 orders of the μ-synthesis, but the computing duration can be longer than the time interval in a computer with low performance. The order of a controller can be reduced, but it may cause unsatisfactory performance.

- The structure and parameters of the robust controllers are not straightforward. Thus the robust controllers are not preferred in technical fields.

7.3. Further studies

Two advantages and three disadvantages of two-motor-pitch-system are written in section 7.1. However, it is not known if the total cost can be saved and how much. This can be solved with the electricity consumption and price, maintenance and replacement cost for pitch actuator, the price data of the components in the pitch actuation system and the lifetime calculation. The lifetime calculation can be performed by means of a simulation code. Fatigue load cases such as dlc1.2 and dlc6.4 in GL certification are used to calculate fatigue on the pitch actuation system.

H_∞ control and μ–synthesis are studied in this research. For further studies, another robust controller such as H_∞ - Loop shaping or sliding mode control can be designed. Adding a feed-forward controller besides a feed-back controller may enhance tracking performance of sinusoidal reference values. A combination of an adaptive control and a robust control is also reported [62]. Viscous friction coefficient change may be adapted with a robust adaptive control.

The blade root bearing diameter of a large wind turbine ranges up to 3.2m for 6MW wind turbine [63]. However, the diameter of the ring in the test rig is less than 1m. Thus, gearboxes with high gear ratio are used in the real wind turbines in comparison to the test rig. Parameters of the controllers in this research must be tuned for the real wind turbines.

Load on the pitch bearing is simulated and transferred to the two load motors. Their inertia and friction have influence on the load simulation. An algorithm can be made to extract the influences. A field test does not require the load motors, so that it is another option.

8. References

[1] Tony Burton, David Sharpe, Nick Jenkins, and Ervin Bossanyi, *Wind Energy Handbook*, John Wiley&Sons, Chichester, UK, 2001

[2] K. Selvam, *Individual pitch control for large scale wind turbines*, ECN, 2007

[3] C.L.Bottasso, F.Campagnolo, A.Croce, C.Tibaldi, *Integrating active and passive load control in wind turbines*, EWEA conference, Copenhagen, 2012

[4] S.J.Johnson, *Active load control techniques for wind turbines*, Sandia report, 2008

[5] E.A.Bossanyi, *Wind turbine control for load reduction*, Wind Energy, 2003

[6] M. Geyler, P. Caselitz, *Individual blade pitch control design for load reduction on large wind turbines*, EWEC, Milan, Italy, 2007

[7] R. Gasch, *Windkraftanlagen*, 3. Auflage, B.G. Teubner Stuttgart, 1996

[8] M. Geyler, P. Caselitz, *Regelung von Windenergieanlagen*, Automatisierungstechnik, Oldenbourg Verlag, 2008

[9] E. Hau, *Windturbines*, Springer, 2000

[10] *Servoregler, SE-Power 1kVA*, Afag Automation AG, 2012

[11] *Schlussbericht: Lastreduzierende Regelungssysteme für Multimegawatt-Windkraftanlagen im Offshore-Bereich*, Fraunhofer IWES, Areva, Moog, 2011

[12] N. Erdmann, *Multibrid M5000 – Alpha-Ventus site Project Certification Load Calculations GL 2005 Regulation*, Multibrid GmbH, 2008

[13] M. Hackl, *Verfahren zur Betätigung eines Steer-by-Wire-Lenkantriebs*, *Patent: DE 197 54 258 A 1,* Robert Bosch GmbH, 1999

[14] A. Wobben, *Windenergieanlage*, Patent: DE 101 16 011 B4, 11.2005

[15] SSB-Antriebstechnik GmbH&Co., *Windenergieanlage, Patent: DE 20 2005 005 694 U1*, 09.15.2005

[16] P. Rogall, P. Achenbach, *Pitch drive system for a wind turbine, Patent: US 2006/0083615 A1*, 04.20.2006

[17] T. Jukic, N. Peric, *A comparative study of backlash compensation methods*, European control conference, 2003

[18] T. Jukic, N. Peric, *Model based backlash compensation*, American control conference, 2001

[19] C. Lindenburg, H.B. Hendriks, *Load set for NM3000 – LMH46-5-X00*, ECN-CX-00-077, ECN, 2001

[20] *Bonfiglioli Trasmital broschure*, Bonfiglioli

[21] Rules for classification of ships/ high speed, light craft and naval surface craft, Det Norske Veritas, 2007

[22] M.Wecker, M.Shan, *Vorstudie 2-Motor-Pitchsystem Rev.05*, Fraunhofer-IWES, 05.2012

[23] J. Choi, *Optimizing the mechanical characteristics of pitch systems for wind turbines*, Diploma thesis, University of Stuttgart, 2008

[24] J. Kuria, J. Kihiu, *Prediction of overall efficiency in multistage gear trains*, International journal of aerospace and mechanical engineering, 2011

[25] A. Csobán, M. Kozma, *Tooth friction loss in simple planetary gears*, 7th international multidisciplinary conference, Romania, 2007

[26] T. T. Petry-Johnson, A. Kahraman, N.E. Anderson,, D.R. Chase, *Experimental investigation of spur gear efficiency*, Proceedings of the ASME 2007 international design engineering technical conference&computers and information in engineering conference, Las Vegas, USA, 2007

[27] R. Martins, J. Seabra, A. Brito, C. Seyfert, R. Luther, A. Igartua, *Friction coefficient in FZG gears lubricated with industrial gear oils: Diodegradable ester vs. mineral oil*, Tribology international 39, 2006

[28] M. Abdulhadi, Irbid, *Stiffness and damping coefficients of rubber*, Ingenieur-Archiv 55, 421-427, 1985

[29] Morten H. Hansen, Anca Hansen, Torben J. Larsen, Stig Øye, Poul Sørensen, and Peter Fuglsang, *Control design for a pitch-regulated, variable speed wind turbine*, Risø National Laboratory, Roskilde, Denmark, January 2005

[30] E.A.Bossanyi, P. Jamieson, *Blade pitch system modeling for wind turbines*, 1999 EWEC, France

[31] M. Kühn, *Dynamics and design optimisation of offshore wind energy conversion systems*, PhD-Thesis, TU Delft, 2001

[32] Rothe Erde, *Großwälzlager*, Produktbrochüre

[33] M. Geyler, *Auswertung zur Messung der Pitchmomente an der M5000*, ISET 2009

[34] R.Gasch, K.Knothe, *Strukturdynamik Band-2*, Springer Verlag, 1989

[35] E.A.Bossanyi, *GH Bladed User Manual version 3.81*, Garrad Hassan and Partners, 2009

[36] R. W. Clough, J. Penzien, *Dynamics of structures*, McGraw Hill, New York, USA, 1993

[37] Martin O.L. Hansen, *Aerodynamics of Wind Turbine*, James and James, London, UK, 2000

[38] Tony Burton, David Sharpe, Nick Jenkins, and Ervin Bossanyi, *Wind Energy Handbook*, John Wiley&Sons, Chichester, UK, 2001

[39] Peter Caselitz, Martin Geyler, Jochen Giebhardt, Bahram Panahandeh, *Hardware-in-the-loop development and testing of new pitch control algorithms*, ISET, Kassel, Germany

[40] J. –P. Hauschild, G. R. Heppler, J. J. McPhee, *Friction compensation of harmonic drive actuators,* Proceedings of 6th international conference on dynamics and control of systems and structures in space, pp683-692, 2004

[41] F. Altpeter, *Friction modeling, identification and compensation*, PhD thesis, École polytechnique fédérale de Lausanne, 1999

[42] C. Canudas de Wit, H. Olsson, K. J. Åström, P. Lischinsky, *A new model for control of systems with friction, IEEE transactions on automatic control*, Vol. 40, No. 3, 1995

[43] Y. Zhu, P. R. Pagilla, *Static and dynamic friction compensation in trajectory tracking control of robots*, IEEE International conference on robotics & automation, 2002

[44] L. L. Tien, A. Albu-Schäffer, A. De Luca, G. Hirzinger, *Friction observer and compensation for control of robots with joint torque measurement*, IEEE International conference on intelligent robots and systems, 2008

[45] N. Mallon, N. van de Wouw, D. Putra, H. Nijmeijer, *Friction compensation in a controlled one-link robot using a reduced-order observer*, IEEE Transactions on control systems technology, Vol 14, No. 2, 2006

[46] Ji-Ho Park, Hyun-Cheol Cho, *Adaptive control of flexible robot actuators with time-varying parameters*, Trans KIEE, Vol. 57P, 2008

[47] C. Pirie, G. E. Dullerud, *Robust controller synthesis for uncertain time-varying systems*, Vol. 40, Society for industrial and applied mathematics, 2002

[48] D. Limon, T. Alamo, D.M. Pena, M.N. Zeilinger, C.N. Jones, M. Pereira, *MPC for tracking periodic reference signals, Nonlinear model predictive control*, Vol 4, p490-495, Leeuwenhorst, Netherlands, 2007

[49] P.Y. Li, *Advance control systems – lecture script*, University of Minnesota

[50] D. Gu, P. H. Petkov, M. M. Konstantinov, *Robust control design with Matlab*, Springer, 2005

[51] E. Elisante, G. P. Rangaiah, S. Palanki, *Robust controller synthesis for multivariable nonlinear systems with unmeasured disturbances*, Chemical engineering science, 2004

[52] Z. Li, J. Sun, *Disturbance compensating model predictive control with application to ship heading control*, Vol. 20, IEEE transactions on control systems technology, 2012

[53] T. R. Bewley, R. Temam, M. Ziane, *A general framework for robust control in fluid mechanics*, Physica D 138, 2000

[54] K. Ogata, *Modern control engineering, 3rd edition*, Prentice hall, 1997

[55] U.Mackenroth, *Robust control systems*, Springer, 2004

[56] B.Bandyopadhyay, S.janardhanan, S. Spurgeon, *Advances in sliding mode control*, springer, 2013

[57] M. Mirzaei, H. H. Niemann, N. K. Poulsen, *A μ –synthesis approach to robust control of a wind turbine*, IEEE conference on decision and control and European control conference, USA, 2011

[58] A. Mystkowski, *An application of mu-synthesis for control of a small air vehicle and simulation results*, Journal of Vibroengineering, Vol. 14, 2012

[59] G. Spiazzi, P. Mattavelli, L. Rossetto, L. Malesani, *Application of sliding mode control to switch-mode power supplies, Journal of circuits, systems and computers*, Vol 5, 1995

[60] K. Kelley, K. Lai, *Accuracy in parameter estimation for the root mean square error of approximation*, Multivariate behavioral research, 2011

[61] R. J. Hyndman, A. B. Koehler, *Another look at measures of forecast accuracy*, International journal of forecasting, 2006

[62] P.A. Ioannou, J. Sun, *Robust adaptive controls*, Dover Pubn Inc, 2012

[63] D. Miguel, L. Feigl, N. Toft, P. Hansen, *Large rotor development for a new generatin 6MW offshore wind turbine*, EWEA offshore, Amsterdam, 2011